Full-Field Strain Behavior of Friction Stir-Welded Titanium Alloy

Trent A. Greenwell

A thesis
submitted in partial fulfillment of the
requirements for the degree of

Master of Science in Mechanical Engineering

University of Washington

2008

Program Authorized to Offer Degree:
Mechanical Engineering

Report Documentation Page

Form Approved
OMB No. 0704-0188

1. REPORT DATE	2. REPORT TYPE	3. DATES COVERED
01 JUN 2008	**N/A**	**-**

4. TITLE AND SUBTITLE	5a. CONTRACT NUMBER
Full-Field Strain Behavior of Friction Stir-Welded Titanium Alloy	5b. GRANT NUMBER
	5c. PROGRAM ELEMENT NUMBER
6. AUTHOR(S)	5d. PROJECT NUMBER
	5e. TASK NUMBER
	5f. WORK UNIT NUMBER
7. PERFORMING ORGANIZATION NAME(S) AND ADDRESS(ES) **University of Washington**	8. PERFORMING ORGANIZATION REPORT NUMBER **CI08-0021**
9. SPONSORING/MONITORING AGENCY NAME(S) AND ADDRESS(ES) **The Department of the Air Force AFIT/ENEL, Bldg 16 2275 D Street WPAFB, OH 45433**	10. SPONSOR/MONITOR'S ACRONYM(S)
	11. SPONSOR/MONITOR'S REPORT NUMBER(S)

12. DISTRIBUTION/AVAILABILITY STATEMENT
Approved for public release, distribution unlimited

13. SUPPLEMENTARY NOTES
The original document contains color images.

14. ABSTRACT

15. SUBJECT TERMS

16. SECURITY CLASSIFICATION OF:			17. LIMITATION OF ABSTRACT	18. NUMBER OF PAGES	19a. NAME OF RESPONSIBLE PERSON
a. REPORT **unclassified**	b. ABSTRACT **unclassified**	c. THIS PAGE **unclassified**	**UU**	**235**	

University of Washington
Graduate School

This is to certify that I have examined this copy of a master's thesis by

Trent A. Greenwell

and have found that it is complete and satisfactory in all respects,
and that any and all revisions required by the final
examining committee have been made.

Committee Members:

Mamidala Ramulu

John Kramlich

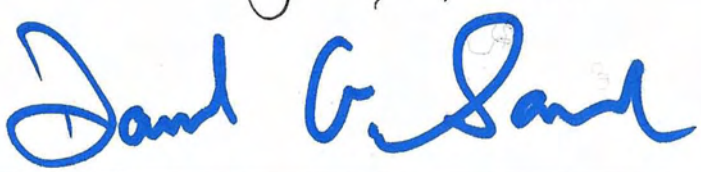

Daniel Sanders

Paul Labossiere

Date: 18 MARCH 2008

In presenting this thesis in partial fulfillment of the requirements for a master's degree at the University of Washington, I agree that the Library shall make its copies freely available for inspection. I further agree that extensive copying of this thesis is allowable only for scholarly purposes, consistent with "fair use" as prescribed in the U.S. Copyright Law. Any other reproduction for any purpose or by any means shall not be allowed without my written permission.

Signature 

Date 18 MARCH 2008

TABLE OF CONTENTS

LIST OF FIGURES

LIST OF TABLES

ACKNOWLEDGEMENTS

Though I undertook this effort as individual research, many others contributed significantly to its success. I would like to thank the following individuals for their contributions to this work:

Professor Mamidala Ramulu, my Advisor and Committee Chair, for taking me on as a graduate student and pointing me down the path of this work. Without him, this work would never have progressed.

Professor Paul Labossiere for his boundless generosity of time, effort, facilities, equipment, materials, expertise, wisdom, and friendship. He should share equal credit for all aspects of this effort as his input was crucial to assuring the success of this endeavor.

Mr. Paul Edwards and Mr. Dan Sanders of the Boeing Company for providing test, reference, and presentation materials as well as a first-hand look at the process of friction-stir welding.

Mr. Russ Noe and Mr. Eamon McQuaide of the Instructional Machine Shop for their time, patience, and expertise in helping me to prepare my test specimens.

Mr. Bill Kuykendall of the Mechanical Engineering Department for his time and assistance in attending to gathering, preparation, and operation of test equipment.

Mr. Kevin Soderlund of the Mechanical Engineering Department for his undeniable and elegant skill in making the maximum possible use of limited materials.

My stepson, for his responsibility, maturity, and consideration in looking out for the family needs while I was busy with this project.

My parents, for instilling in me the fortitude to endure the harder times and the drive and responsibility to overcome all manner of obstacles.

My beautiful Wife, for providing me warm meals, clean clothes, good spirits, and limitless support during this effort as well as providing me an amazing quality of life worthy of the sacrifice required to complete this undertaking in such short time. Our future together is my greatest inspiration for success.

1. Introduction

Titanium is an abundant elemental metal with an exceptional strength-to-weight ratio. Due to properties of high strength, low weight, high heat tolerance, and exceptional corrosion resistance, titanium alloys are used extensively in a number of industries, such as power production, mineral extraction, biomedical, marine, chemical processing, and, of particular interest here, aerospace. The aerospace industry is the single largest user of titanium, particularly Ti-6Al-4V which is considered the 'workhorse' titanium alloy [1]. Unfortunately, the properties that make titanium so attractive for use also make it challenging to machine and join. This difficulty in joining poses particular problems for titanium alloy sheets, which are typically very limited in available sizes. Mechanical joining of titanium sheets requires strict vigilance to assure constant tool integrity and use of high-strength fasteners, which can be heavy and costly. Titanium is a highly reactive material making conventional fusion welding processes very difficult, though possible with proper preparations and precautions.

Friction stir-welding (FSW) is a low-energy, solid-state process in which two material sheets are joined by the mixing action of a rotating pin under the combination of high pressure and rotational friction along the surface a material. Since its invention in 1991, FSW has proven highly effective in joining aerospace metallic alloys for which conventional fusion welding is poorly suited [2]. Much has been accomplished in characterizing FSW joints in 2XXX and 7XXX series aluminum alloys for aerospace use, but little published research exists regarding FSW joints in titanium alloys; however,

preliminary research indicates FSW of titanium alloys results in a robust weld with strength equal to or greater than the base metal and capable of further post-processing. Review of currently available research finds global stress response and microstructural characterization of friction stir welded Ti-6Al-4V available, but no data is found describing the stress response of the weld region.

Digital Image Correlation (DIC) is a recently developed optical full-field strain analysis method which examines pixel shifts of distinct contrast patterns, such as paint speckles on smooth finishes or surface texture variations in rough finishes, to measure displacement and strain in a series of digital images [3]. Moiré interferometry is another optical full-field stress analysis technique which uses coincident laser reflection from a grid pattern of valleys and peaks on the surface of a polished specimen to generate a reflected fringe pattern to determine displacements, strains, and stresses [4].

1.1. Objective and Motivation

The objective of this thesis project is to examine, evaluate, and characterize the fundamental elastic-plastic stress/strain response of friction stir-welded butt joints in thin-sheet, fine grain Ti-6Al-4V titanium alloy under normal tensile loading using the full-field optical stress analysis techniques of Digital Image Correlation (DIC) and moiré interferometry. Using titanium sheets cut into dogbone specimens with friction stir-welds transverse to and centered within the narrow gage, the above objective will be met in three distinct tasks:

First, evaluate the stress-strain response of the specimens using traditional/global measurements, full-field Digital Image Correlation measurements, and full-field moiré interferometry measurements.

Second, compare and attempt to determine a correlation between DIC and moiré interferometry.

Third, and finally, develop, if possible, a robust finite element model of the stress behavior of the friction stir weld within titanium.

The motivation for this thesis project is to develop a better understanding of the nature of stress development in friction stir-welded titanium sheets under tensile loading transverse to the direction of the weld. It is hoped that a better understanding of the nature of the weld under elastic and plastic loading will help in further understanding and creating effective design of titanium structures, particularly in aerospace applications as distinct advantage exists for the aerospace industry in using FSW of titanium in order to maintain high strength and low weight.

1.2. Scope

The scope of this research effort is limited to examining the full-field strain behavior of a friction stir-weld within titanium under tensile load in order to develop a notional understanding of behavioral variations. Along with developing this qualitative

assessment, this research demonstrates the feasibility of using the full-field strain analysis methods of Digital Image Correlation and moiré interferometry as means of developing analytical models, without actually developing a refined material model or characterizing either analytical technique. Because of this limited scope, the number of analyzed specimens is limited to eight for each analytical technique in order to develop an adequate sample size to establish behavioral trends.

1.3. Thesis Organization

This thesis is organized in a manner to build a basic motivation for the reader to develop interest in the subject of the research in Chapter 1. Chapter 2 then provides more specific and detailed background information on titanium, friction stir-welding, published research on the friction stir-welding of titanium, and full-field optical stress-strain measurement techniques. Next, in Chapter 3, the specific approach of this research project is explained with the results presented in Chapter 4. Chapter 5 presents a discussion of the research results and Chapter 6 provides conclusions and recommendations.

2. Background

This chapter presents detailed and comprehensive description of the topic areas and applications fundamental to FSW research. The chapter begins with the history and applications of titanium and friction stir-welding and then discusses the results of current research on FSW of titanium. The presented discussion concludes with an overview of the principles and theory behind Digital Image Correlation and moiré Interferometry.

2.1. Titanium and its Applications

Titanium is the fourth most abundant elemental metal in the earth's crust [5]. Discovered in 1791 and identified as an element in 1795 in Austria, titanium didn't come into structural use until the 1950s when it began use in aerospace applications [5,6]. Since then it has been adapted to other industries such as power production, mineral extraction, biomedical implants, marine structures, chemical processing, and jewelry due to its inherent properties of high strength, low weight, high heat tolerance, and exceptional corrosion resistance. These properties are particularly attractive to the aerospace industry as they allow for relatively lightweight yet robust structures capable of withstanding rigorous applications, such as the engine cowlings on the F-15E fighter jet shown in Figure 2-1.

Figure 2-1: Titanium engine cowlings on US Air Force F-15E fighter aircraft – Reprinted from open-source USAF photo

The aerospace industry remains the single largest user of titanium, particularly the 'workhorse' Ti-6Al-4V alloy, also known as Grade 5 titanium, which incorporates 6% aluminum and 4% vanadium in addition to trace levels of iron and oxygen [7,8]. Titanium exists in three distinct phases: alpha, beta, and alpha-beta. Alpha phase titanium has a hexagonal close-packed (HCP) lattice structure, shown in Figure 2-2, which exists up to about 1625°F where it undergoes an allotropic change to the beta phase of body-centered cubic (BCC) lattice structure, shown in Figure 2-3 [9]. Addition of alloying elements causes preferential stabilization of either the alpha or beta phase allowing for a variety of stable combinations of alpha-beta phases. Alpha-beta titanium

alloys include most titanium alloys in use today along with the subject alloy of this research, Ti-6Al-4V.

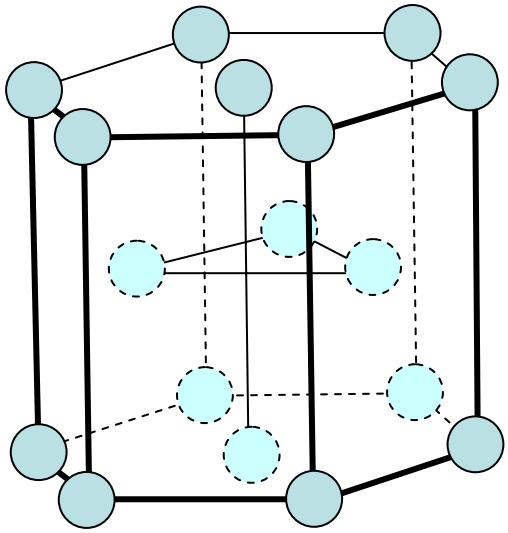

Figure 2-2: Hexagonal close-packed lattice structure of α-phase titanium

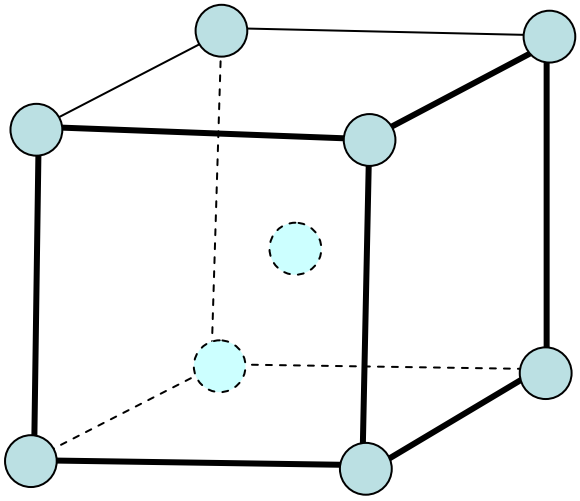

Figure 2-3: Body-centered cubic lattice structure of β-phase titanium

With the highest strength-to-weight ratio of any modern structural metal, titanium has particularly attractive properties for structural applications in the aerospace industry [9].

Titanium's specific weight is approximately two thirds the magnitude of steel and roughly two thirds higher than aluminum. The tensile stiffness of titanium sheet is between that of steel and aluminum, but titanium's strength, particularly in alloy form, is significantly higher than many steel alloys. A comparison of fundamental properties titanium and other common aerospace metals is shown in Table 2-1.

Table 2-1: Titanium mechanical properties compared to other metals [8, 10-14]

	C.P. Grade 1 Ti	Ti-6Al-4V Grade 5 Ti	7075 T-6 Aluminum	2024-T4 Aluminum	Type 316 Stainless	Type 4130 Steel
Density (lb/in^3// g/cc)	0.163//4.50	0.160//4.43	0.102//2.81	0.100//2.78	0.289//8.00	0.284//7.85
Specific Heat (BTU/lb-°F //J/g-ºC)	0.126//0.528	0.126//0.526	0.229//0.960	0.209//0.875	0.120//0.500	0.114//0.477
Hardness (Brinell)	70.0	334	150	120	187	197
Ultimate Tensile Strength (ksi//MPa)	31.9//220	138//950	83.0//572	68.0//469	84.1//580	97.2//670
Yield Strength (ksi//MPa)	20.3//140	128//880	73.0//503	47.0//324	42.1//290	63.1//435
Modulus of Elasticity (Msi//GPa)	16.8//116	16.5//113.8	10.4//71.7	10.6//71.3	28.0//193	29.7//205
Poisson's Ratio	0.34	0.34	0.33	0.33	0.25	0.29

Titanium's desirable properties are not without cost and difficulty to attain. Because of its highly reactive nature, titanium post-processing involving heat and liquid state operations can be exceptionally difficult. Titanium castings, for example, are possible, but must be conducted in a vacuum [15]. Fusion welding of titanium is extremely difficult as well and is limited to arc welding as it is not possible to use oxyacetylene welding on titanium or titanium alloys [16]. Effective welding of titanium can be

achieved with Gas Tungsten-Arc welding, also known as TIG welding, and Gas Metal-Arc welding, also known as MIG welding, as long as proper inert gas shielding techniques are used to prevent introduction of oxygen, nitrogen, and hydrogen reactants which can cause embrittlement [16,17]. Resistance, plasma arc, electron beam, and friction welding have also been used with great effect on titanium and its alloys.

2.2. Friction Stir-Welding

Friction stir-welding, shown in Figure 2-4 and described in Figure 2-5, is a welding process which has demonstrated great success with titanium and its alloys.

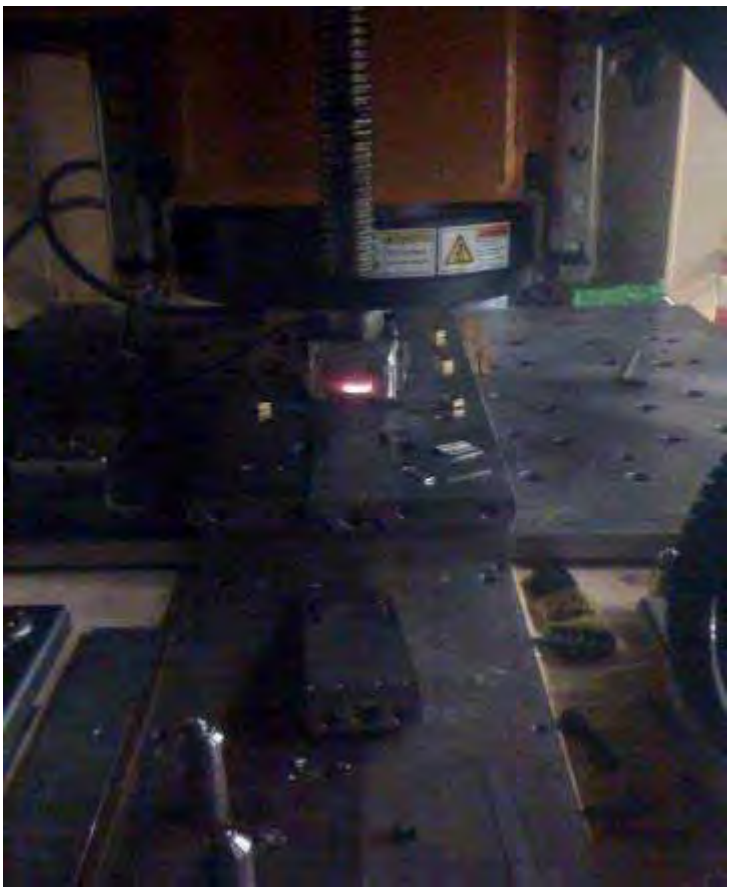

Figure 2-4: Friction stir-welding in action – courtesy of Paul Edwards, Boeing Co.

Friction stir-welding is a recent invention having been discovered and patented at The Welding Institute (TWI) in the United Kingdom in 1991 [7]. FSW is a relatively simple, solid-state process which uses a non-consumable rotating tool under great pressure to 'mix' two relatively thin-section plates or sheets of material along abutting edges. The FSW tool consists of a flat or nearly flat circular shoulder pressed against the material seam with great force and rotated to generate friction which causes material softening while a material-specific pin plunged into the material seam promotes the mixing action. Figure 2-5 shows a diagram of the process.

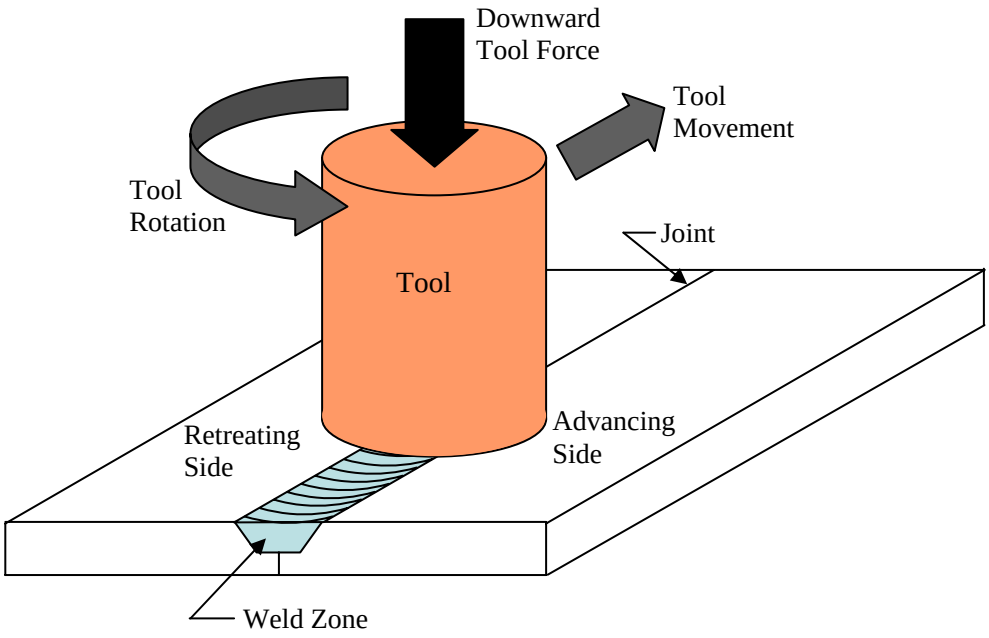

Figure 2-5: Friction stir-welding process diagram – Redrawn from [1].

FSW offers many advantages over conventional fusion welding due to the material remaining in the solid-state, such as low distortion and shrinkage, excellent material

properties, no porosity in the weld, and no arc, fumes, or spatter. Other advantages include the capability to weld materials otherwise difficult or impossible to weld using conventional fusion welding processes, such as 2XXX and 7XXX series aluminum alloys, and without use of gas shielding; an energy-efficient process with a non-consumable tool and no filler wire; and a machine-driven process capable of automation and robotic application, thus eliminating the necessity for welder certification. FSW is not without its disadvantages, however; because of the weld force required, the workpiece must be rigidly clamped to a fixture or working surface and a backing bar must be used to support tool forge loads; pin extraction leaves a 'keyhole' in the shape of the FSW tool at each end of the weld which must be removed or post-processed; and, the process does not accommodate use of filler material leaving some weld geometries, such as fillet welds, difficult to achieve [18].

Because of the complexity of the plastic deformation, material movement, and heat generation in FSW, process parameters such as tool geometry, welding parameters, and joint design play a critical role. Tool geometry is the predominant factor in FSW process development due to its critical role in determining material flow characteristics which determine tool rotation speed and traverse rate [2]. FSW tools consist generally of a shoulder and a pin, though the specific geometries of each can vary considerably. The tool has two fundamental functions: localized heating and material flow [2]. Heating initially results from the pin due to friction and workpiece material deformation during the initial tool plunge into the workpiece, but friction between the shoulder and the

workpiece is the primary means of heating. Because of this, only the relative size of the tool pin compared to the shoulder plays an important role in determining localized heating characteristics.

The geometry of the pin and shoulder both play a critical role in material flow, hence they are the influencing parameters for microstructural uniformity and mechanical properties [2]. Typical FSW tools for aluminum are made from tool steel and can have fairly elaborate geometries, including scrolled shoulders as well as threaded and fluted pins. The purpose the scrolled shoulder is to cause material to flow in towards the center of the tool to avoid material flow outside of the weld zone causing burrs or thinning. The purpose of the threaded pin is to drive material down into the weld zone to maintain uniform microstructure with a minimum of voids or defects [19]. Typical FSW tools for titanium are made from tungsten which is too brittle to accommodate machining of elaborate geometries like threaded pins or scrolled shoulders, so titanium FSW tools use smooth cylindrical shoulders and smooth, conical pins. Tungsten tools, though strong and resistant to high heat, are prone to deformation when used on titanium due to its high strength. Two typical FSW tool geometries described in literature on FSW are shown in Figure 2-6.

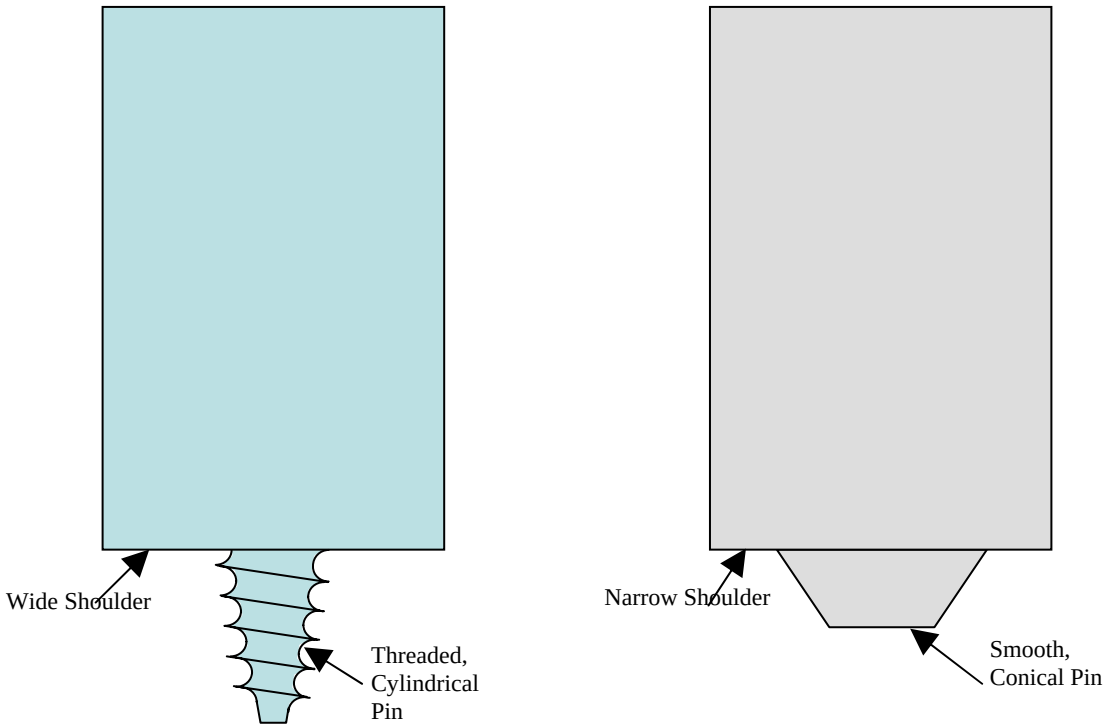

Figure 2-6: Friction stir-welding tool geometries

The two welding parameters of primary concern in FSW are tool rotation rate, measured in revolutions per minute, and the tool traverse speed, measured in distance traveled over time. Tool rotation rate determines the extent of mixing and the amount of friction heating which occurs in the workpiece, both of which directly affect the resulting microstructure of the weld zone. Tool traverse speed is an important consideration to assure adequate mixing while preventing overheating. Typically, FSW of aluminum is conducted with a rotation rate between 200 and 1000 rpm with traverse rates of 2 to 12 inches per minute (ipm) (51 to 305 mm/min), while FSW of titanium uses rotation rates between 80 and 500 rpm with traverse rates from 3 to 6 ipm (76 to 152 mm/min) [19].

Rotation direction, either clockwise or counterclockwise relative to the direction of travel, is another weld parameter of consideration as weld characteristics vary between the advancing and retreating sides. Other welding parameters of consideration are tool tilt angle relative to the workpiece; the pin height and pin insertion depth, which determines shoulder contact; the downward force on the tool, known as the forge load; and workpiece heating, to include preheating, and cooling, to include precooling [2].

Joint design is the final critical process parameter in FSW. Due to the inherent concept of FSW, it is exceptionally well-suited to butt joints and lap joints and a number of variations based on these two basic weld joints, shown in Figure 2-7. For standard butt joints, two material plates of roughly equal thickness are placed side by side on a backing plate and clamped into position to prevent separation of the workpiece seam, also called an abutment, during the welding process. The FSW tool is plunged into the center of the abutment and traversed along the seam in the desired direction. For simple lap joints, two overlapping plates are clamped onto a backing plate and the FSW tool is plunged through the upper plate and into the lower plate and traversed along the desired direction, joining the two plates together. Other joint designs, such as fillet welds, are possible but with added difficulty.

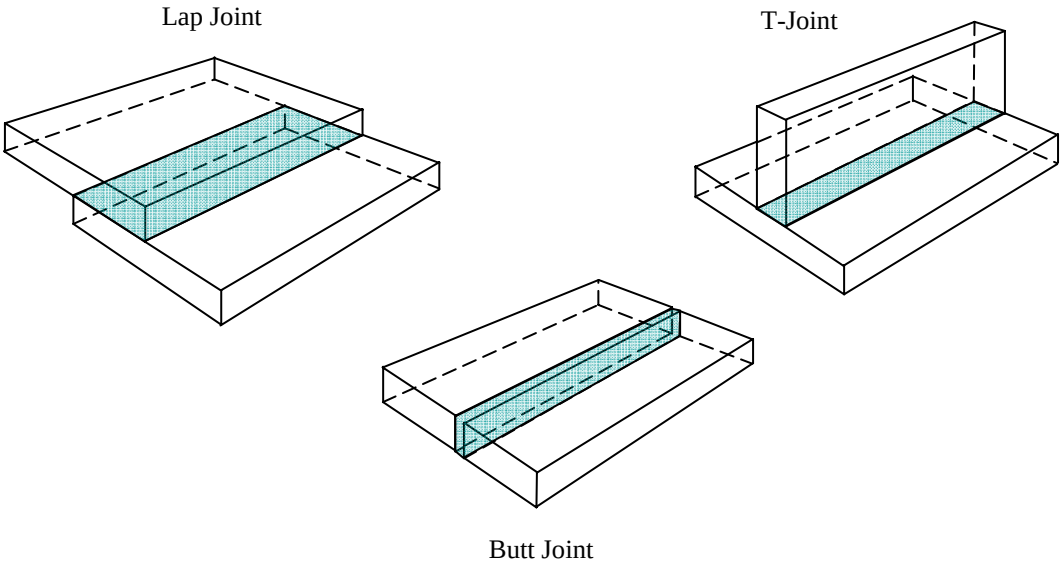

Figure 2-7: Weld joints possible using friction stir-welding

The distinct advantages of FSW are clearly realized in aerospace applications which normally rely on riveting to join large sheets of aircraft skins. The recently developed Eclipse 500 aircraft incorporated FSW to replace 60% of its rivets for substantial weight savings and elimination of roughly 97% of the re-work required for riveting operations [20]. This illustrates the advantages of the FSW process itself, in addition the finished joint which can be roughly three times stronger at a fraction of the weight. The ability to automate the FSW process in lieu of the variable nature of riveting results in drastic reduction of labor hours, as realized by the ability to produce approximately 5300 in (134.6 m) of weld in two shifts per day on the Eclipse 500 aircraft assembly line [20].

Because FSW is capable of easily joining materials which are difficult or impossible to weld using conventional methods, much research has been done to characterize FSW joints, mechanics, and microstructural properties in common aerospace aluminum alloys,

such as the 2XXX and 7XXX series alloys. FSW of titanium and its alloys is a relatively recent endeavor. As much of what is known about friction stir welding is empirically derived by trial and error, FSW tooling and techniques for titanium are largely based upon what has proven effective for aluminum alloys [21]. Due primarily to differences in hardness, strength, and reactivity to heat and oxidation, titanium does not behave in the same manner as aluminum, however, and a number of unique FSW process considerations for titanium have been determined.

2.3. Friction Stir-Welding of Ti: Mechanics and Microstructure

Friction stir-welding of titanium promises great advances in manufacturing. As titanium alloy sheets are generally limited in available size, the aforementioned advantages of FSW over riveting are exceptionally attractive. Figure 2-8 shows FSW of Ti-6Al-4V.

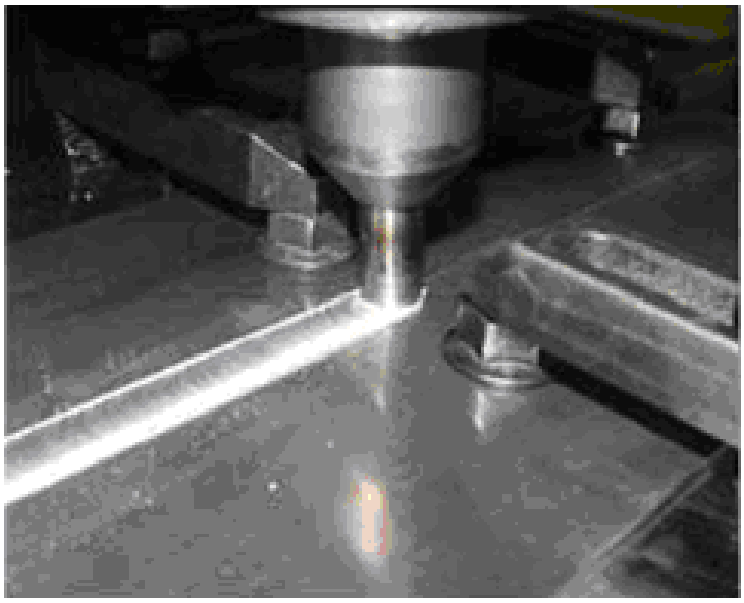

Figure 2-8: FSW of Ti-6Al-4V sheet – Courtesy of Paul Edwards, Boeing Co.

Preliminary research indicates FSW of titanium alloys results in a robust weld with strength equal to or greater than the base metal and capable of further post-processing. Lienert, et al, conducted comprehensive research of FSW using a smooth-pinned commercially pure tungsten tool on mill-annealed Ti-6Al-4V plates [7]. The tool had a shoulder diameter of 0.75 in (19.1 mm), a pin diameter of 0.31 in (7.9 mm), and a pin length of 0.25 (6.4 mm). Tool rotation speeds were held constant at 275 rpm with tool and workpiece in an inert gas chamber to prevent surface oxidation. The tool and workpiece were both instrumented with thermocouples to characterize heat distribution during welding. Microstructures were evaluated with optical light and scanning electron microscopy and mechanical properties were evaluated by means of microhardness and tensile testing [7].

FSW of titanium results in three distinct regions within the weld zone: the weld nugget, a heat affected zone (HAZ), and base metal. FSW of aluminum demonstrates an additional region called the thermo-mechanically affected zone (TMAZ), but this region is not present in titanium due to titanium's inherent ability to recrystalize under severe plastic deformation.

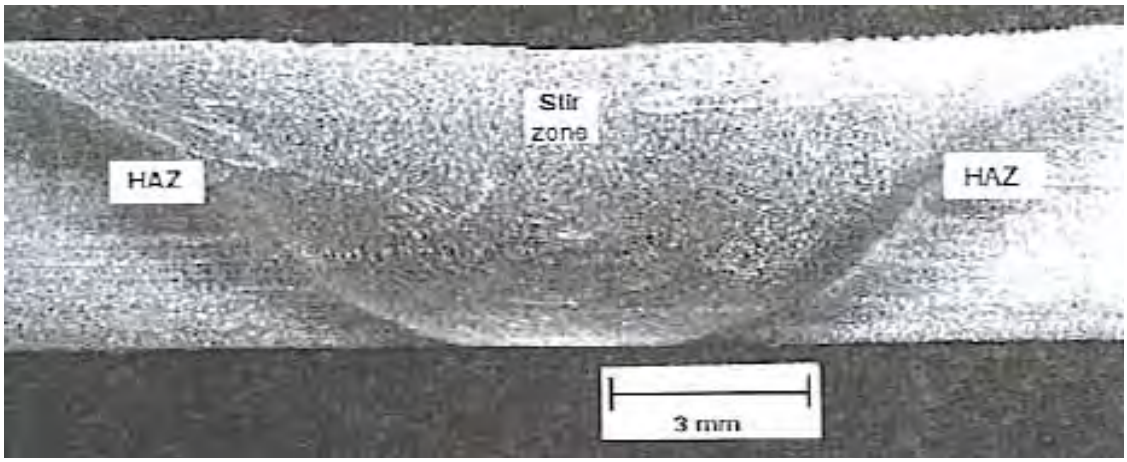

Figure 2-9: Weld Regions in Friction Stir Welded Ti-6Al-4V – courtesy of Paul Edwards, Boeing Co.

From Lienert, et al's research, the mixed alpha-beta phase of Ti-6Al-4V undergoes a phase change within the weld nugget to become completely beta phase, indicating sustained temperatures above the beta transus. Indications within the HAZ, as well as the nearly non-existent TMAZ, show peak temperatures that do not exceed the beta transus. Results of this research also indicated grain size reduction in the weld zone from the base metal, from an average of 18 μm to 15.5 μm [7]. Their research indicates an increase in microhardness from approximately 340 vickers hardness number (VHN) in the base metal and weld nugget to 370 VHN in the HAZ [7].

Lienert's study showed 100% joint efficiency for yield and ultimate tensile strength as well as an identical average strain to failure between weld samples and base metal samples [7]. Review of currently available research finds global stress response and microstructural characterization of friction stir welded Ti-6Al-4V available, but no data is found describing the stress response of the weld-base metal interface.

2.4. Full-Field Strain Measurement

Stress-strain measurement is typically local in nature, either by point-to-point extensometers or resistance strain gauges. Unfortunately, these local measurements are limited to providing either ‘snapshots’ or averages of a stress state, which do not provide a full picture of the actual stress state. Full-field stress-strain measurements on the other hand provide a means of examining a complete state of stress, either in-plane or out-of-plane, such as across a three-dimensional contoured surface. A common thread of full-field stress-strain measurement techniques is their use of imagery and optics. Another feature of most full-field stress-strain measurement techniques is their use of the moiré effect to develop a visible pattern of dark lines or ‘fringes’, also called moiré patterns, which manifest based on the relative displacement between two line or grid patterns.

2.4.1. Digital Image Correlation

Digital Image Correlation (DIC) is a relatively new, software driven method of evaluating full-field displacement and strain by comparing the variations of unique surface features between two digital images [22]. DIC relies on a surface roughness and imperfections to create discrete and identifiable landmarks on an image. In cases where specimens are too smooth to offer distinct surface features, paint speckling can be used to provide unique and identifiable surface features.

Because it is a software driven process, DIC is simple to perform as it only requires a computer and a means of importing a number of scalable specimen surface images at an

appropriate resolution. Each digital image converts the true image of the specimen and its unique surface pattern, be it surface features or paint speckles, into an array of monochromatic pixels, each with a unique shade relative to adjacent pixels. DIC software maps the intensity of each pixel in this array and then compares that map to the initial image of the unstressed specimen. Displacements within the surface pattern are determined by measuring the change in separation, in pixels, of selected baseline pixel subgroups within the array from one image to the next. With DIC software, it is possible to evaluate displacement and strain trends over a series of images.

DIC has already been demonstrated as a useful tool in industrial packaging, aircraft non-destructive inspection, and tire analysis [23, 24]. DIC techniques have been applied to optical stereo-microscopy, scanning electron microscopy, and atomic force microscopy demonstrating its utility in micro- and nano-scale applications where displacement and strain measurements may not otherwise be possible [24]. DIC is earning more and more favor as a full-field displacement and strain measurement tool which requires little to no specimen preparation depending on inherent surface roughness and has an exceptional ease of accomplishment given the software to perform the analysis.

DIC has also already found use in measuring strain across friction stir welded aluminum. S. Adapa in his research at Southern Illinois University Carbondale, demonstrated the utility of measuring strain difference at three distinct locations on dissimilar aluminum alloy friction stir welds [25]. Unlike the purpose of this research to demonstrate a general

nature of strain behavior over the entire region of a friction stir weld, Adapa's research focused on using DIC as a means of sampling strains at distinct locations in the respective parent materials outside of the weld and at the center of the weld. Where Adapa's research evaluated each distinct material for discrete variations in strain values, this research evaluates the entire weld region to develop a general pattern of strain behavior [25].

2.4.2. Moiré Interferometry

Moiré interferometry is an optical full-field analysis technique which combines geometrical moiré and optical interferometry to achieve high fidelity in-plane surface displacement measurements [4]. Moiré patterns are series of light and dark bands called fringes which form when two superimposed line or grid patterns of equal or roughly equal amplitude are displaced relative to one another, either by translation, rotation, or deformation. Figure 2-10 shows moiré patterns produced by rotating and deforming one of two superimposed line patterns. In order to achieve highly visible fringes, the grating pattern should be well-

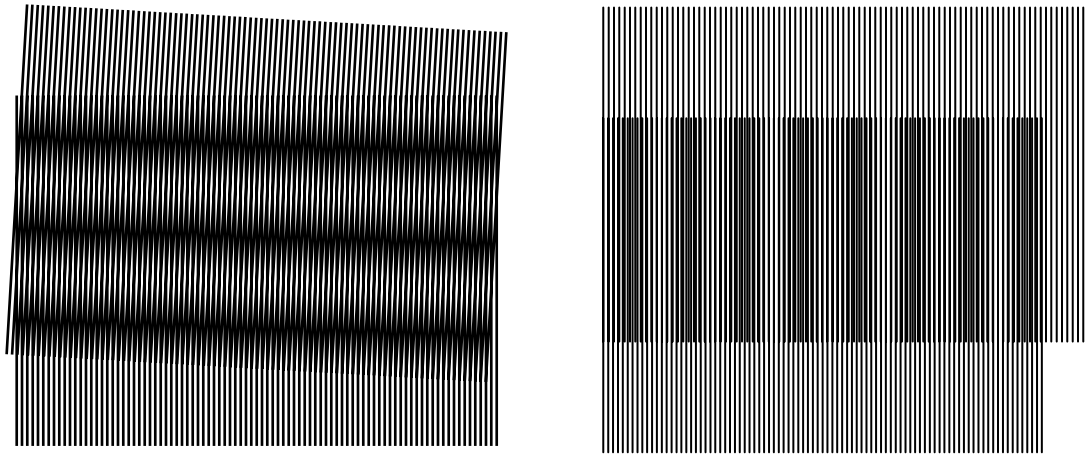

Figure 2-10: Simple moiré patterns from rotation and linear deformation

defined, with roughly equal sized lines and spaces. Also, the angle of intersection of the two gratings should be small (approximately 3° or less) and the line pitch ratio of the two gratings should be small (approximately 1.05:1) [4]. The analytical value of moiré fringes in stress-strain studies derives from the simple geometric relationship between the gratings and the fringes. In the case of pure extension, which is of interest in this research effort, the frequency of fringe patterns, F, is simply described by the frequency of the two superimposed grating patterns, f_1 and f_2, by the relationship:

$$F = f_1 - f_2$$

This relationship shows that one fringe develops for every additional grating line in a given frequency range. For example, if the two superimposed gratings began as 100 lines/mm and only one grating, f_2, was extended such that its frequency became 98

lines/mm, then two fringes would appear over every one mm of grating overlap. Analysis of fringe images is governed by the elegant simplicity of converting the fringe values to strain values, for if the grating frequency is known to start at 100 lines/mm, or 0.01 mm between lines, and the stretched grating is longer than the original grating, also termed the ‘reference grating’, such that two fringes appear, that is easily determined to be a difference of two lines between the strained grating and the reference grating. Examining a given frequency range, such as 1 mm in this case, the displacement over that range is 0.02 mm for a strain of 0.02 mm. Hence, if the grating frequency is known, it is possible to evaluate pure extensional strains, both locally and overall, by simply counting the number of visible fringes over a given distance. Unlike global stress-strain evaluations which use either an extensometer or strain gauge to measure an average displacement over a fixed distance, moiré patterns allow for identifying localized strain variations, due to material differences or stress concentrations, and further allow measurement of these localized strains.

Moiré interferometry is a specialized application of moiré patterns which uses two or four beams of coherent light to illuminate a reflective grating which has been firmly applied to the surface of a specimen, either by etching or bonding, in order to create both a ‘virtual’ reference grating as well as a deformable ‘specimen’ grating. Two-beam moiré interferometry is capable of generating fringe patterns only in a single dimension to achieve either u, in the x-direction, or v, in the y-direction, displacements, but not both. Four beam moiré interferometry is capable of generating u and v displacements

simultaneously and, hence, can be used to determine shearing strains in addition to axial strains. Figure 2-11 shows a schematic of four beam moiré interferometry.

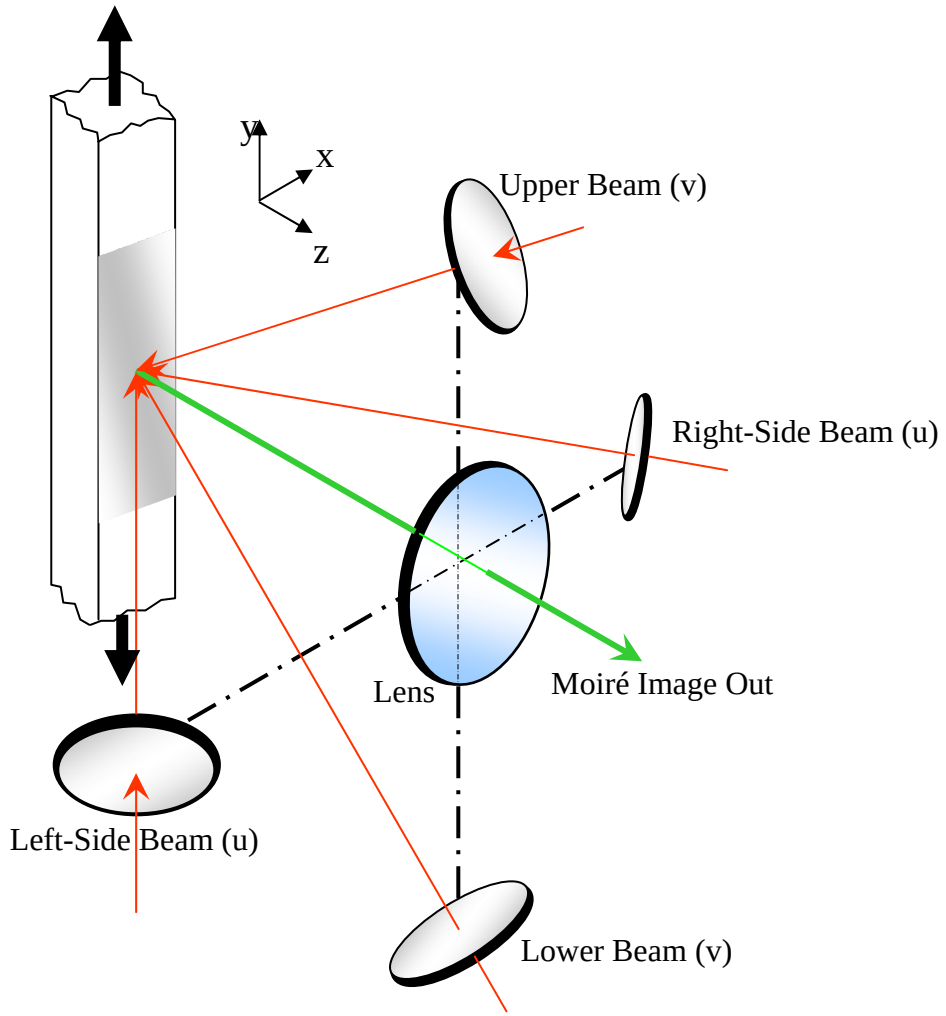

Figure 2-11: Four-Beam moiré interferometer schematic diagram – redrawn from [4]

The virtual reference grating is created by directing the lasers into the specimen grating at equal and opposite angles to create areas of constructive and destructive interference within the area of their intersection which appear to a properly placed eye or camera as a

grating pattern; see Figure 2-12 for a schematic diagram with w_1 and w_2 as the wave of coherent light from the first and second beam, w_1 and w_2 respectively; f as the frequency of the virtual reference grating, and f_s as the frequency of the deformable specimen grating. When viewed through the properly placed eye or camera, this virtual grating interacts with the actual deformable grating on the surface of the specimen to create moiré fringes when the specimen is deformed or displaced.

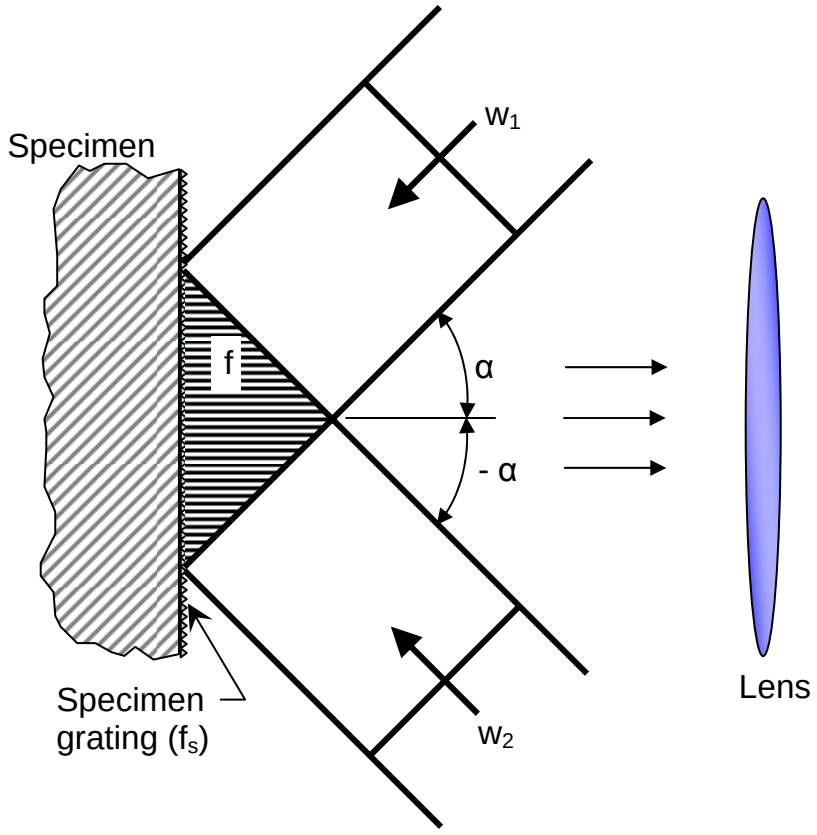

Figure 2-12: Schematic diagram showing creation of virtual reference grating – redrawn from [4]

The schematics and information above is somewhat simplified to provide a general idea of moiré interferometry.

3. Experimental Set-Up and Procedure

3.1. Materials

This research focused on friction stir welds of identical fine grain Grade 5 (Ti-6Al-4V) titanium alloy sheets. The original material base sample from which all research test specimens were generated was made from two 0.071 in (1.8 mm) thick by 4 in (101.6 mm) wide by 24 in (699.6 mm) long sheets of identical alloy butt welded together along their respective long edges, as shown in Figure 3-1. Fundamental material properties for this alloy are shown in Table 2-1. A typical stress-strain curve for the material is shown in Figure 3-5. The specific material used was provided by the Boeing Company.

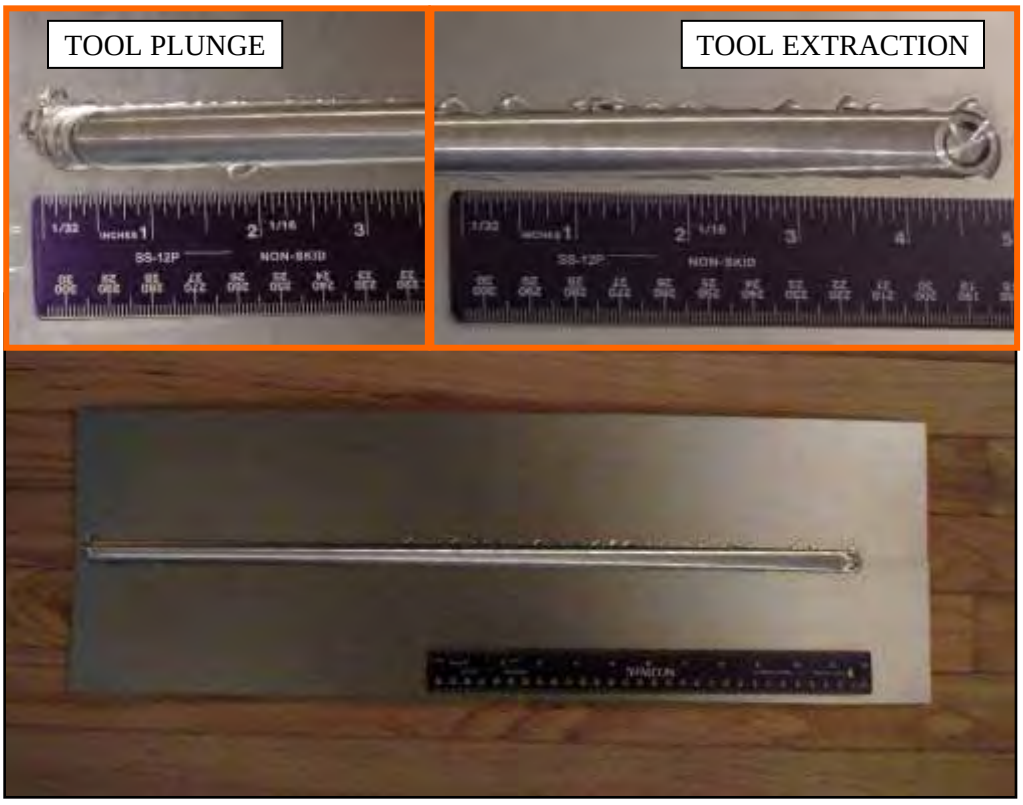

Figure 3-1: Welded titanium sheet base sample

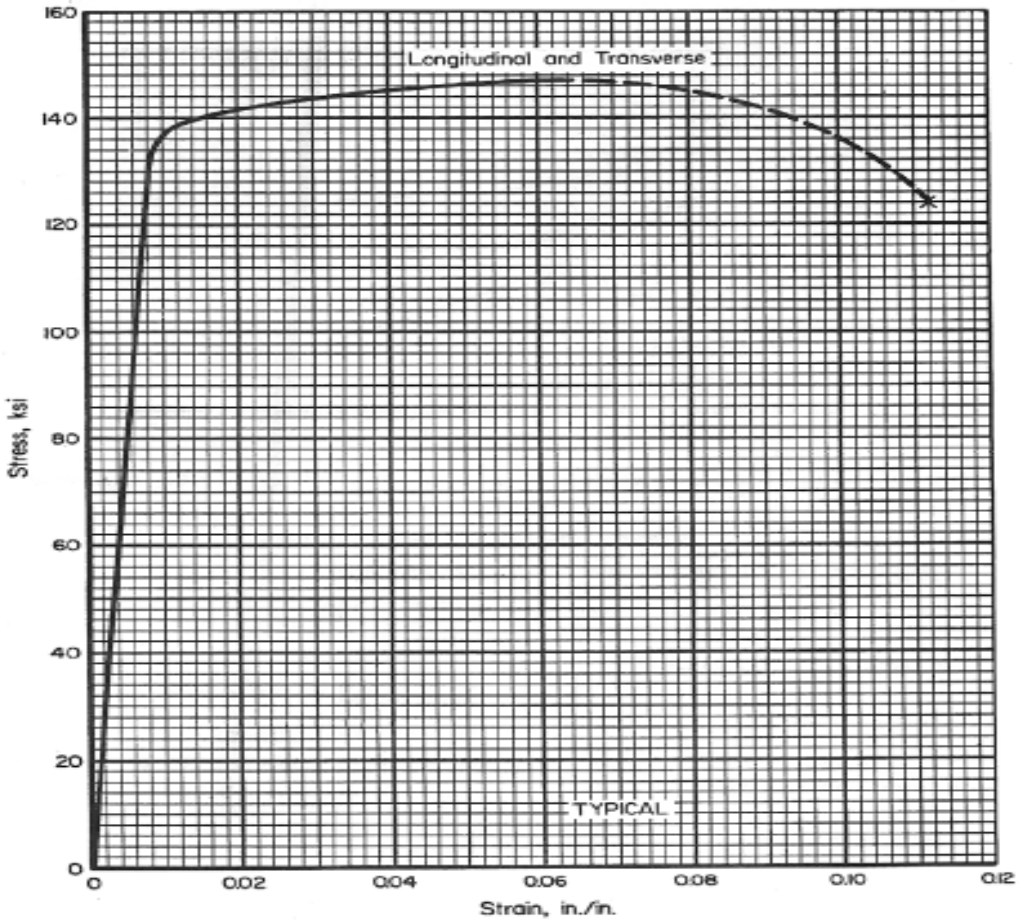

Figure 3-2: Typical Ti-6Al-4V Stress-Strain Curve – reprinted from Mil-Hdbk 5H [26]

3.2. Friction Stir-Weld Parameters

As with the specific material used, the friction stir-welding of the base sample was accomplished by the Boeing Company using its own FSW machine. Typical weld parameters used are shown in Table 3-1. While the specifics of the tool geometry are proprietary, the tool had the same conical pin and narrow shoulder typical of tungsten FSW tools intended for use on titanium.

Post-processing evaluation of the weld parameters used on the base sample indicated the material used in this research did not achieve full weld penetration, as shown in Figure 3-3; however, that did not adversely affect this research as the focus of the full-field strain evaluation is a the material surface. In order to further assure viability of this material for the purpose of this research, the remaining seam at the sheet abutment where the weld failed to penetrate, shown in Figure 3-4, was laser welded to prevent premature failure due to the presence of an existing 'crack'.

Table 3-1: Subject Research Welding Parameters

Spindle Speed:	550 RPM
Spindle Rotation:	Counter-Clockwise
Tool Travel Speed:	5 inches/minute
Forge Load:	~3500 lbf (15.6 KN)
Tool Plunge Depth:	~0.062 in (1.6 mm)
Tool Tilt:	3° from direction of travel
Tool Material:	Tungsten Pin and Anvil
Tool Pin Length:	~0.06 in (1.4 mm)
Tool Pin Diameter:	~0.34 in (8.6 mm)
Tool Shoulder Diameter:	~0.63 in (15.9 mm)

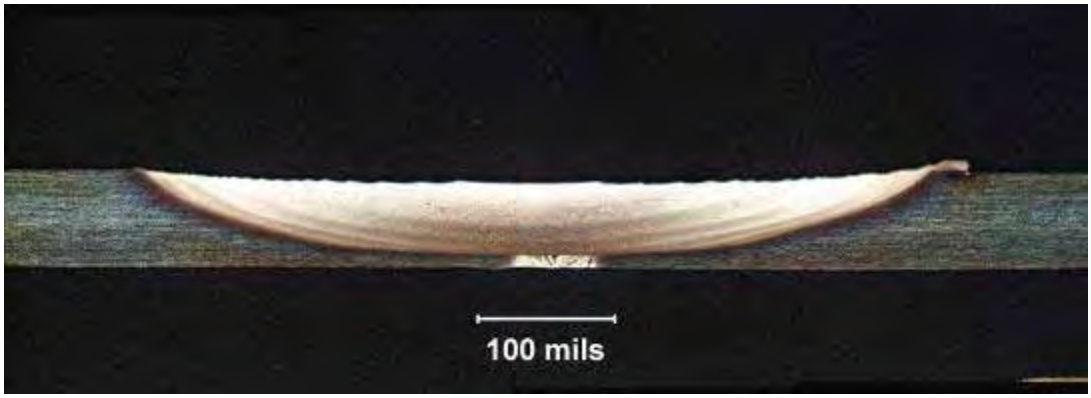

Figure 3-3: Cross-sectional view of similarly welded material showing lack of weld penetration – courtesy of Paul Edwards, Boeing Co.

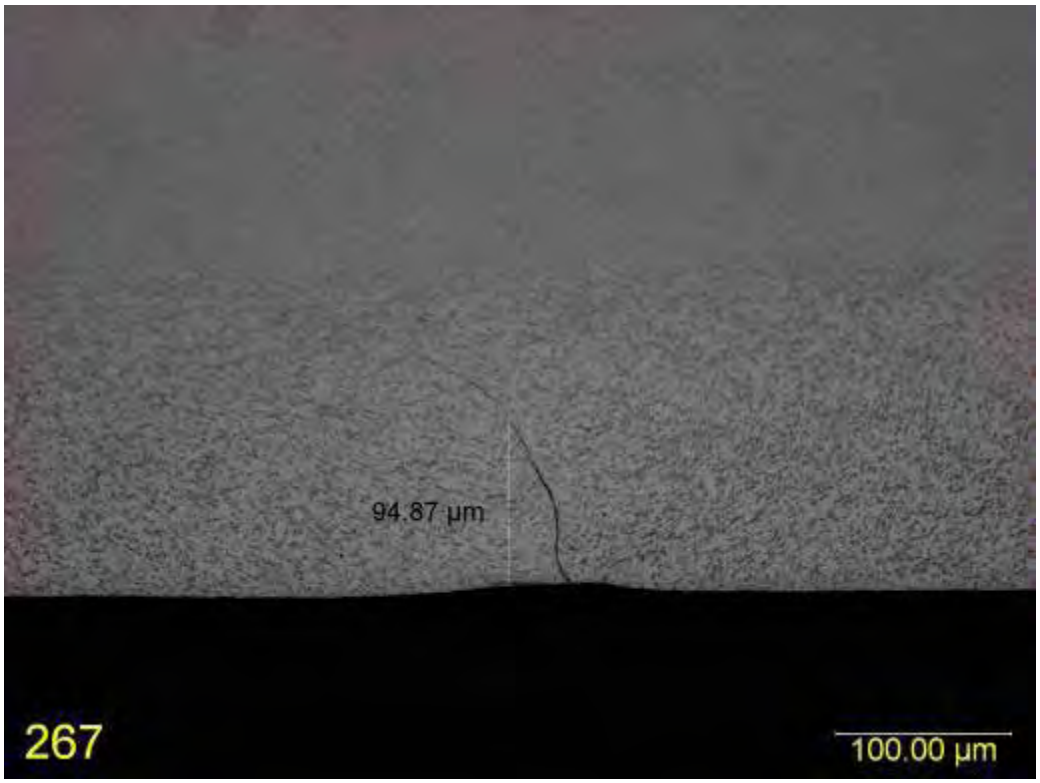

Figure 3-4: Micrograph showing seam separation due to lack of full weld penetration – courtesy of Paul Edwards, Boeing Co.

3.3. Specimen Geometry

This research used uniquely designed tensile test 'dogbone' specimens made from friction stir-welded Ti-6Al-4V sheet. The specimens were designed such that the weld runs transverse to the direction of loading through the center of the specimen gage section. The geometry of the tensile test specimen is shown in Figure 3-5. All dimensions are in millimeters. The dimensions of the specimen were not held in accord with ASTM E8-04 standards for tensile test specimens for three reasons: first, the laboratory containing the optical equipment necessary to conduct the moiré interferometry would not accommodate a large load frame, so the specimen was required to fail at loads below 1000 lbf (4448 N); second, the resolvable field of view of the

camera used in the moiré interferometry apparatus is on the order of 0.118 in (3.0 mm), so larger specimens would not present any value in this research; and, third, during the course of planning this research effort, materials were extremely limited so conservation of available materials was of paramount concern.

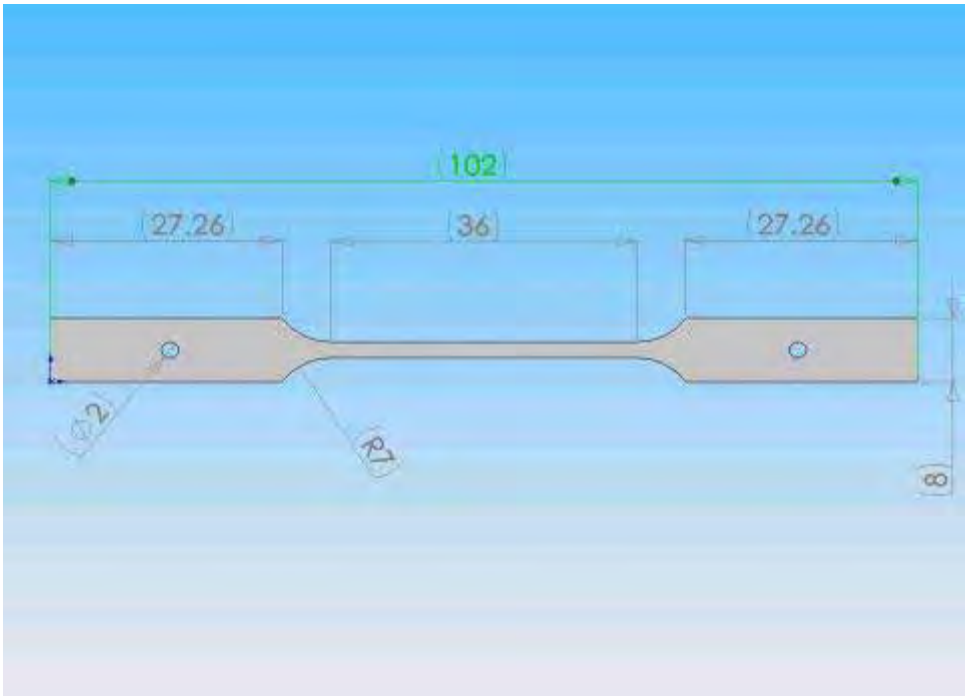

Figure 3-5: Tensile Test Specimen Geometry and Dimensions

3.4. Specimen Preparation

Specimen preparation consisted of a set of common processing steps followed by unique processing steps for each of the two full-field strain measurement processes. All research test specimens were first cut from the base sample by a high-pressure abrasive waterjet cutter owned and operated by the University of Washington Mechanical Engineering Department; see Figure 3-6. Waterjet cutting was chosen due to the very narrow

thickness of cut of less than 0.039 in (1.0 mm) which maximized the number of specimens attainable over a given length of base material.

Figure 3-6: Abrasive waterjet cutting of specimens from raw sheet material

Once cut to shape, the burrs and slag formed on the upper weld surface by the FSW process and the remnant laser weld bead on the underside of the FSW surface were removed from each specimen using a grinding wheel. No clean up was conducted on the waterjet cut edges in order to preserve the desired gage width. Each specimen was then polished to achieve a mechanically flat surface by adhering three to six specimens at a time to the finished face of an aluminum block using 3M brand 'Super 77' spray adhesive and then hand sanding against a mechanically flat ceramic backing surface using silicon

carbide sandpaper with a sequence of grit ratings from 60 to 80 to 120 grit until the friction stir-weld was no longer visible and the specimen gage had a uniform thickness. This level of initial processing left each specimen with typical final gage dimensions of 0.079 in (2.0 mm) wide by 0.063 in (1.6 mm) thick. Specimens processed to this extent were used for global stress-strain tensile tests; full-field strain tests required further unique post-processing.

3.4.1. Preparation of Digital Image Correlation Specimens

DIC specimen preparation consisted of applying a speckle pattern to the gage surface, as shown in Figure 3-7. The DIC speckle pattern was applied by directing a cloud of printer toner 'dust' onto wet white enamel spray paint applied to the specimen gage. A speckle pattern of black spray paint droplets would have also been acceptable, but using a toner dust speckle pattern resulted in a finer pattern of discernable surface features at higher camera magnification levels. As the DIC tests were performed using wedge-style load frame grips, no further preparation was required.

Figure 3-7: DIC specimen with speckling applied to gage

3.4.2. Preparation of Moiré Interferometry Specimens

Preparation of moiré interferometry specimens, or simply moiré specimens, required further polishing to achieve as uniformly flat and smooth of a surface finish as possible to prevent distortion that could affect the moiré fringes. To this end, hand polishing continued from the initial common preparation through successively finer grit silicon carbide sandpaper from 150, 220, 400, 600, 800, 1200 to 2000 grit. Once polished, each moiré specimen was drilled with a 0.0787 in (2.0 mm) diameter pin-hole in each tab to secure the specimens into the custom-made pin-secured load frame grips used during moiré testing.

The final, and most precarious, step in moiré specimen preparation was the application of the specimen surface grating. This research used previously fabricated evaporated-aluminum dual-field gratings with symmetric and perpendicular patterns of 300 lines/mm. The aluminum grating was applied to the moiré specimen by bonding the aluminum film grating to the polished weld surface using Loctite brand “5-minute Epoxy” and allowing to cure. Following the required cure period, the aluminum grating glass backing was carefully separated from the weld surface. If successful, this left a continuous thin-film of aluminum with an intact grating pattern across the area of interest containing the entire weld region on the gage surface of the moiré specimen. Once a successful grating was achieved, the grating surface was marked with at the weld boundary to provide a landmark for the imaging the weld area of interest. A completely prepared moiré specimen is shown in Figure 3-8.

Figure 3-8: Moiré specimen with grating applied to gage

3.5. Experimental Set-Up and Analysis

Each of the three separate experiments conducted in this research relied on the same basic test specimens. A summary test matrix for all experiments is shown in Table 3-2.

Table 3-2: Experimental Test Matrix

		Specimen Dimensions			
Empirical Method	Specimen Number	Gage Length (in//mm)	Gage Width (in//mm)	Gage Thickness (in//mm)	Gage Area (in^2//mm^2)
Global Stress-Strain Measurement	TAG GS 1	1.42//36.0	0.079//2.00	0.062//1.57	0.005//3.14
	TAG GS 2	1.42//36.0	0.078//1.99	0.062//1.57	0.005//3.12
	TAG GS 3	1.42//36.0	0.078//1.98	0.062//1.58	0.005//3.13
	TAG GS 4	1.42//36.0	0.080//2.02	0.061//1.56	0.005//3.15
Digital Image Correlation Measurement	TAG DIC 1	1.42//36.0	0.077//1.96	0.065//1.64	0.005//3.21
	TAG DIC 2	1.42//36.0	0.079//2.01	0.062//1.58	0.005//3.18
	TAG DIC 3	1.42//36.0	0.077//1.96	0.064//1.62	0.005//3.18
	TAG DIC 4	1.42//36.0	0.077//1.96	0.063//1.60	0.005//3.14
	TAG DIC 5	1.42//36.0	0.076//1.94	0.065//1.65	0.005//3.20
	TAG DIC 6	1.42//36.0	0.078//1.97	0.062//1.58	0.005//3.11
	TAG DIC 7	1.42//36.0	0.079//2.01	0.063//1.60	0.005//3.22
	TAG DIC 8	1.42//36.0	0.080//2.04	0.062//1.57	0.005//3.20
Moiré Interferometry Measurement	TAG MS 1	1.42//36.0	0.080//2.04	0.061//1.55	0.005//3.16
	TAG MS 2	1.42//36.0	0.079//2.01	0.063//1.61	0.005//3.22
	TAG MS 3	1.42//36.0	0.080//2.02	0.064//1.63	0.005//3.29
	TAG MS 4	1.42//36.0	0.080//2.04	0.055//1.40	0.004//2.86
	TAG MS 5	1.42//36.0	0.080//2.04	0.062//1.58	0.005//3.22
	TAG MS 6	1.42//36.0	0.080//2.03	0.062//1.57	0.005//3.19

3.5.1. Global Strain Measurement Set-Up

Though, the Ti-6Al-4V base material is a well-established and thoroughly characterized aerospace material, the stress-strain behavior of friction stir-welded titanium remains limited to specific weld and material parameters In establishing the mechanical behavior of the friction stir-welded titanium alloy, it was first necessary to establish the global stress-strain character of the subject welded material. . To establish a baseline for the global-stress strain behavior of the subject material, four initially prepared specimens, or global specimens, were dedicated to global stress-strain tensile tests. Additionally, the eight DIC specimens were tested with the same global stress-strain apparatus to collect additional global stress-strain data.

The global stress-strain test apparatus consisted of an Instron 5585H Floor Model Test System (load frame) capable of 56,250 lbf (250 kN) with 0.00004 – 20 in/min (0.001 – 500 mm/min) speed range and a 49.4 in x 22.6 in (1256 mm x 575 mm) usable test area. The Instron 2716 series mechanical wedge style grips used had a load capacity of 30 kN. The built-in load cell was capable of a 250:1 force measurement range with a load accuracy of ± 0.5% of the indicated load. The data acquisition system was capable of 500 Hz synchronous across all available channels, used in this research to capture load, load frame internal extension, and accessory strain gauge extensometer data. The Instron 2630-106 strain gauge extensometer used had a gauge length of 0.984 in (25 mm) and travel of -0.091 in to 0.492 in (-2.3 mm to 12.5 mm) with ± 0.5% accuracy.

Global specimen test data was collected on a personal computer using Instron BlueHill 2 software, which also served as the test control console and program [27]. The test program parameters used in this testing were for an extension-controlled increase of load 0.001 in/sec (0.03 mm/sec) over a steady rate to a load-controlled maximum of 1000 lbf (4448 N).

3.5.2. Full Field Strain Measurement Set-Up

The two full field strain measurement methods explored in this research rely on substantially different approaches and associated equipment. A comprehensive description of the methods and equipment used for each full field strain measurement technique is provided in the following sections.

3.5.2.1. Digital Image Correlation Set-Up

Digital Image Correlation data was collected by capturing successive digital images of prepared specimens undergoing tensile loading on the same Instron 5585H load frame described in section 3.5.1. All set up related to the load frame, load frame grips, load cell, strain gauge extensometer, data acquisition, and control/data capture software is identical to the global stress-strain tests. The only difference for the DIC specimen test profile was to alternately load the specimen to a relative displacement of 0.00394 in (0.10 mm) and hold the displacement for a 15 second pause to capture image data. This profile was run until reaching an absolute displacement of 0.118 in (3 mm), corresponding to roughly 8% elongation, or visible necking; whichever came first.

Digital images were captured using a Sony HD-HC5 combination 1080p video/4.0 Megapixel digital still camera equipped with a 1.7X telephoto lens. The camera captured .jpg format images at a resolution of 2304 x 1728 and total pixel count of roughly 1,990,000 per image. Photographs were taken using the "telemacro" setting for maximum zoom on the specimen gage area of interest.

3.5.2.2. Moiré Interferometry Set-Up

The moiré interferometry apparatus used in this research was comprised of several major components, including a load frame to induce strain in the specimen; a moiré interferometer to generate moiré fringes on the strained specimen; a camera and personal computer to capture the moiré fringe imagery; and a load cell, data acquisition device, and additional personal computer to measure applied load.

The load frame used was an Instron model TM-M-L table-top model owned by the University of Washington Mechanical Engineering Department. Technical specifications for this load frame and its associated load cell were and remain unavailable. Though notionally capable of loads approaching 3000 lbf (13.34 kN), this research confirmed load frame capacity in excess of 740 lbf (3.29 kN). Load frame control was performed by manual load frame adjustment coupled with real-time monitoring of the load cell.

This research utilized a custom-built, four-beam, dual-field, fiber optic, piezoelectrically phase-shifted moiré interferometer for purposes of strain measurement. This moiré

interferometer was assembled and is maintained by Dr. Paul Labossiere at his lab on Bainbridge Island, Washington. Figure 3-9 shows the physical set up while Figure 3-10 shows the schematic diagram of the major components.

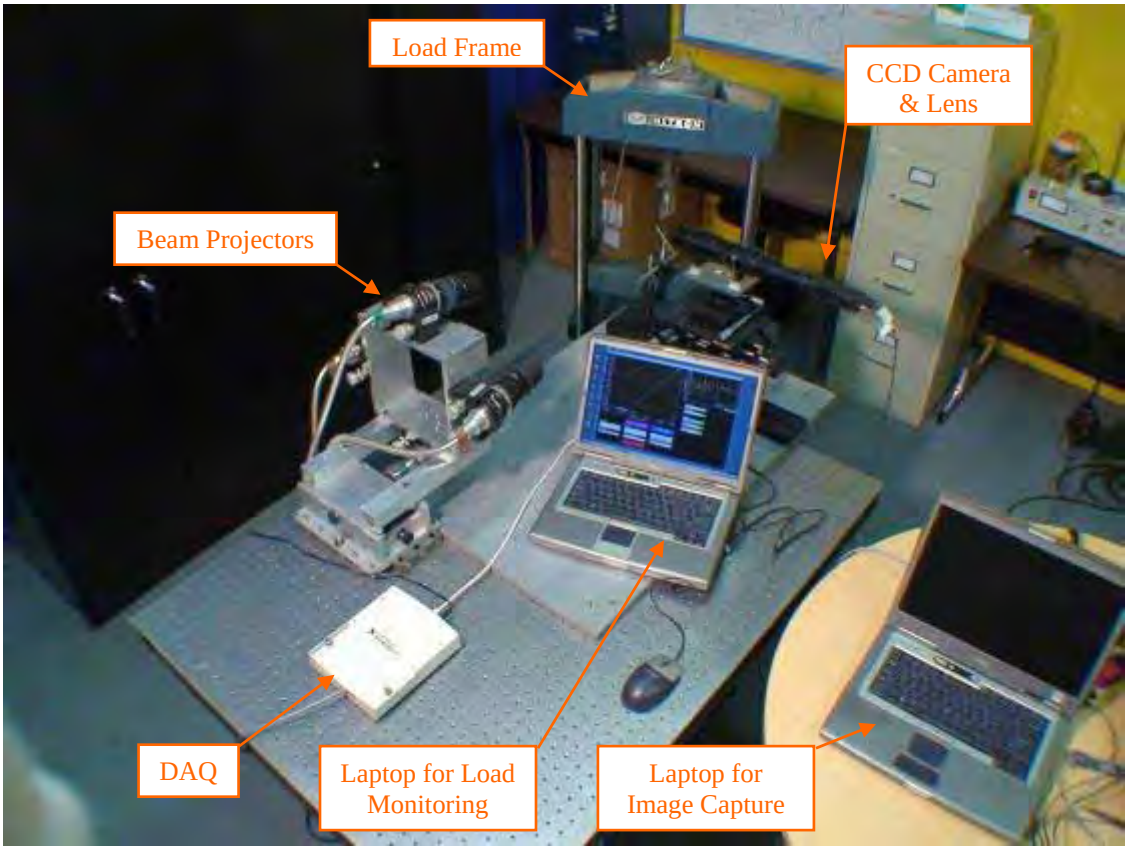

Figure 3-9: Moiré interferometry experimental set-up

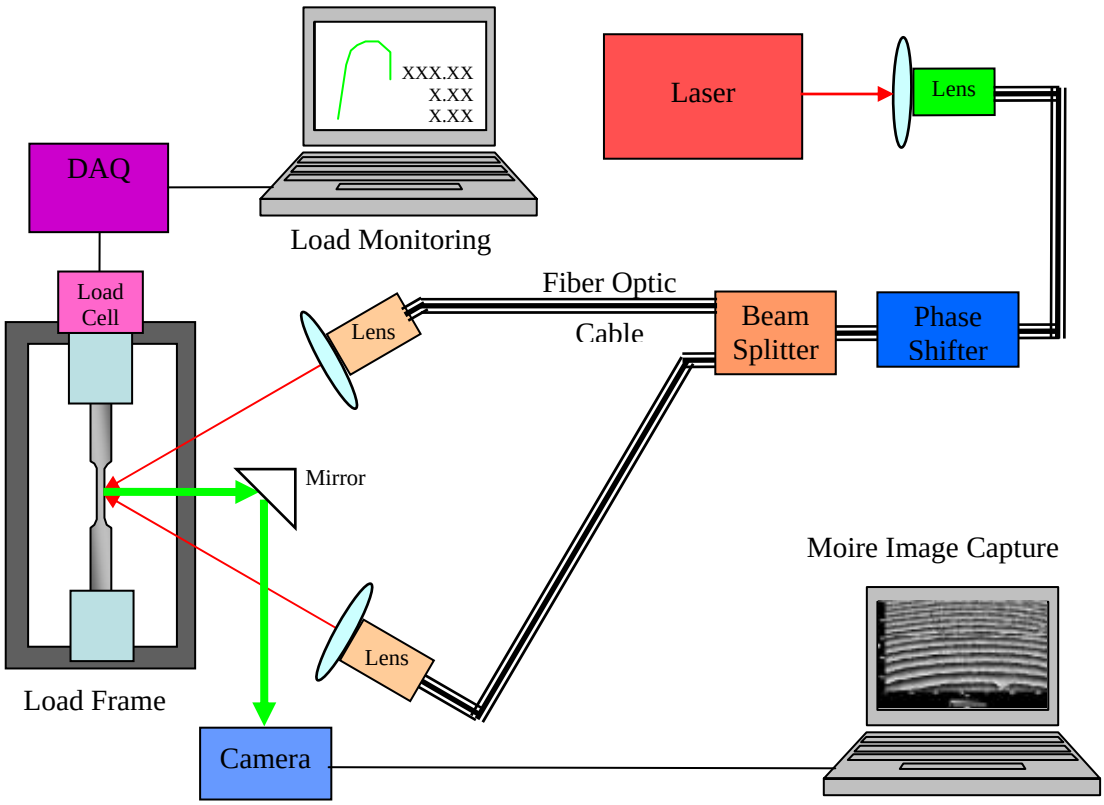

Figure 3-10: Phase-shifted moiré interferometry schematic diagram

The subject moiré interferometer used a 620 nm wavelength Helium-Neon laser passed through a phase-shifter and then split into four separate beams and transmitted through fiber optic cables into four separate collimator projector lenses set at angles to produce separate v-field and u-field reference gratings of 600 lines/mm. Figure 3-11 shows the collimator projector lens and mount. Because aligned collimated beams are necessary to produce the virtual reference grating, simultaneous capture of v-field and u-field imagery is impossible due to the destructive action of perpendicularly aligned collimated beams upon each other. The four-beam, dual-field apparatus used in this research simplified sequential capture of v-field and u-field imagery by allowing quick switching between v-

and u-fields by blocking the horizontally aligned u-field or the vertically aligned v-field projector lenses, respectively. Each lens was individually adjustable in focus and rotation and the mounting frame was also adjustable in rotation to correct for misalignment of the specimen grating or specimen misalignment in terms of axial rotation to provide horizontal or vertical moiré fringes for v-field or u-field imagery, respectively. Though one adjustment of fringe alignment may have been sufficient for a number of image captures, particularly after the specimen was loaded and the camera held in a fixed position, any movement of the camera or specimen typically required readjustment of the collimator lenses to align the fringes.

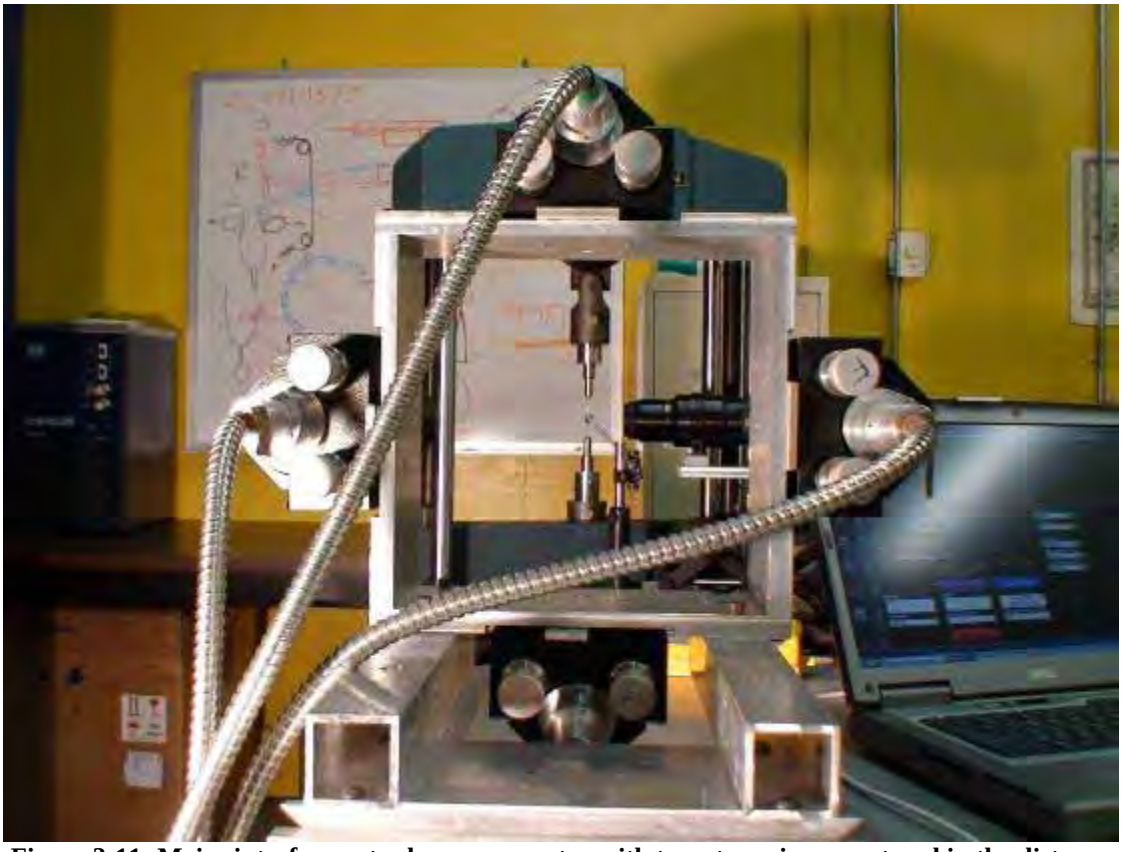

Figure 3-11: Moire interferometer beam apparatus with target specimen centered in the distance

Moiré imagery data was collected by a Sony 1289 x 960 pixel 10-bit resolution XCD-SX910 monochromatic charge-coupled device (CCD) camera using a 10X manual zoom lens with fixed focal length. A 45º first surface optically flat turning mirror was used to direct specimen and moiré fringe imagery into the camera. Image data was captured and phase-shifted on a personal computer by means of an IEEE 1394 “FireWire” interface using custom software programmed by Kenneth E. Perry [28].

Load data was collected for each test using a custom-programmed LabView version 8.5 data collection routine [29]. This program captured load response data from the built-in load cell in the Instron TM-M-L load frame. No specification data remained for this load frame or load cell, but the professor who originally procured the set remembered it to be notionally rated at 1000 lbf (4.45 kN) channeled through a National Instruments DAQPad model 6015 USB multi-function data acquisition device (DAQ). Load data for each specimen was recorded manually.

3.5.3. Analysis Procedure

Each method of analysis used in this research differed significantly in the type of data collected and the available tools for analysis. The individual and unique methods of analysis for global stress-strain, DIC, and moiré interferometry are discussed in the following sections.

3.5.3.1. Global Strain Measurement Analysis

Global specimen data for each test was collected by the Instron BlueHill 2 software as a standard comma-separated value (.csv) file. The BlueHill 2 software also generated a raw data plot of stress vs strain. Refined analysis and normalizing of the global specimen data was performed with Microsoft Excel.

3.5.3.2. Digital Image Correlation Analysis

Following capture of image data, each specimen's series of digital images were rotated to a vertical gage alignment and cropped to a common final size and framing using IrfanView version 4.10 image viewing and editing software [30].

Finally, once all digital images had been properly prepared, this research utilized Vic-2D version 4.4.2 DIC software to process the digital images for displacement and strain data [31]. As DIC software is not available to the general student body at the University of Washington, the DIC portion of this research was conducted with the trial version of Vic-2D obtained by the author. Though further refinement of analysis parameters is warranted to fully characterize the DIC results, reasonably optimal software settings for purposes of this research were achieved by an iterative approach of successively refined analyses. The best convergence of relative strain results to the expected strain behavior was achieved with the software specific settings shown in Table 3-3.

Table 3-3: Vic-2D Software Settings for this research

Correlation Option	Selection
Interpolation	Cubic B-Spline
Filter	None
Subset Shape Function	Affine Transformation
Correlation Criterion	NSSD (Normalized Sum of Squared Differences)
Thresholding	None

3.5.3.3. Moiré Interferometry Analysis

The first and inherent step in moiré data analysis was conversion of raw moiré imagery into high-fidelity gray scale moiré fringe imagery. In order to achieve high-fidelity moiré fringe images, each image capture underwent software-driven phase-shifting to improve resolution and reduce noise from surface imperfections. The phase shifting also converted each raw black and white photographic image to a 10-bit gray scale refinement of fringe imaging allowing for more precise counting of fringes. A 10-bit image has 1,024 shades of gray for distinct imagery of fringe transitions. Figure 3-12 shows the raw image and phase shift mask required to achieve a high-quality phase-shifted moiré image.

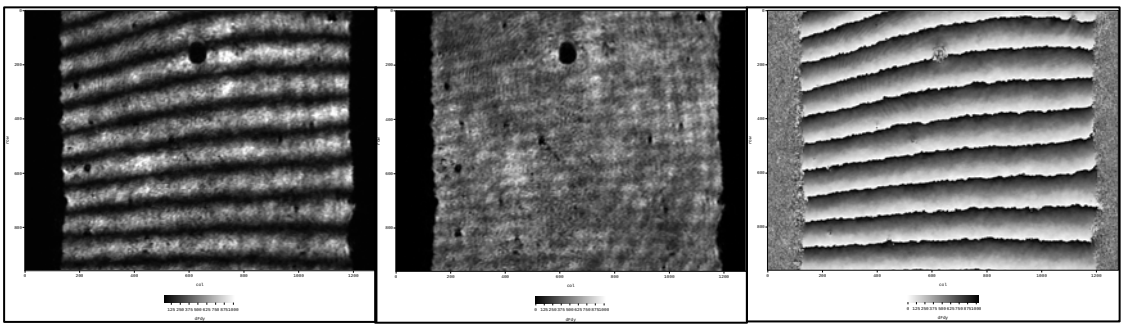

Raw Image Phase Shift Mask Final Phase-Shifted Image

Figure 3-12: Image sequence to achieve good fidelity phase-shifted moiré image

In addition to a high sensitivity to specimen rotation and grating alignment, phase shifting of the moiré image capture was extremely sensitive to vibration of any kind. In order to reduce ambient vibration, the optical table had to be completely free of machinery, such as laptop computers with cooling fans, the room had to be free of air flow, to include forced air heating and human breathing, and the immediate surrounding area had to be free of foot and vehicle traffic. Even under the best conditions achievable, each image capture often required several attempts to achieve a good quality phase shifted image. Figure 3-13 shows the raw image and phase shift mask to achieve a poor fidelity phase-shifted image.

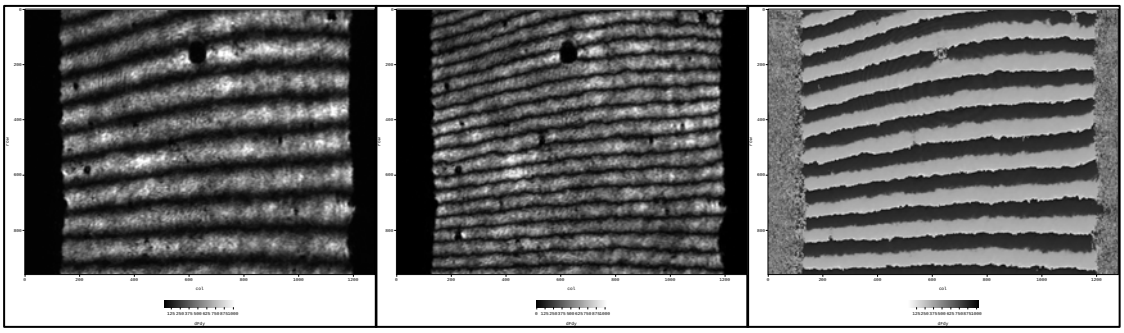

Raw Image Phase Shift Mask Final Phase-Shifted Image

Figure 3-13: Image sequence resulting in poor quality phase-shifted moiré image

With the known reference grating frequency and the specimen grating frequency, each single fringe represented 1.667 μm of displacement. Dividing the calculated displacement value by the known distance they spanned, approximately scaled from the presumed uniform specimen width of 2.0 mm, resulted in an approximate strain. Strain was calculated at areas of interest which included the weld nugget (WN) beginning 0.039 in (1.0 mm) inside the weld border and moving in toward the center, the thermo-

mechanically affected zone (TMAZ) spanning from the weld border to the WN, the heat affected zone (HAZ) spanning from the weld boundary to 0.039 in (1.0 mm) outside of the weld border, and the parent material (PM) beginning at the other side of the HAZ and moving out from the center. With the exception of the HAZ or TMAZ, the full length of these regions was rarely captured leaving only approximations of regional strain based on available data near the regional interfaces. This approximation data is sufficient for purposes of demonstration of capability and technique, which defined the scope of this research.

With achievement of a good quality phase-shifted image, the gradient shading for each fringe provided sufficient fidelity to allow visual counting of fractional fringes for more precise displacement data than counting only whole number fringes. Counting fractional moiré fringes posed some challenges in terms of resolving gradient levels and applying a uniform and accurate scale. Two methods of counting fringes were applied to the moiré fringe data: computer counting and paper counting.

Computer counting was performed using Microsoft PowerPoint software. Raw moiré fringe images were imported into PowerPoint and the drawing features inherent in the software were used to apply mark-ups and scales. Figure 3-14 and Figure 3-15 show a typical image analysis to determine localized strain. First, the presumed 2.0 mm width of the null specimen is used to generate a scale of 0.1 mm increments in the axial and transverse directions of the specimen gage, as shown in Figure 3-14. Next, this same

scale was applied to an image of the loaded specimen to determine the number of fringes in a known distance. Fringes are counted starting from one shade of gray to the next matching shade of gray. As shown in Figure 3-15, a 1.0 mm length of the gage section is arbitrarily selected and the fringes within are counted as slightly more than five fringes, or approximately 5.1 fringes. The displacement and, subsequently, the strain in this region are approximated as 0.000335 in (0.0085 mm) and 0.000335 in/in (0.0085 mm/mm), respectively, using the below relationships:

$$\frac{5.1\,fringes}{600 lines/mm} = 0.0085 mm; \qquad \frac{0.0085 mm}{1.0 mm} = 0.0085 mm/mm$$

In this manner, the displacement fields shown in the moiré image can be used to determine areas of localized strain and approximate strain values over any distance on the specimen surface.

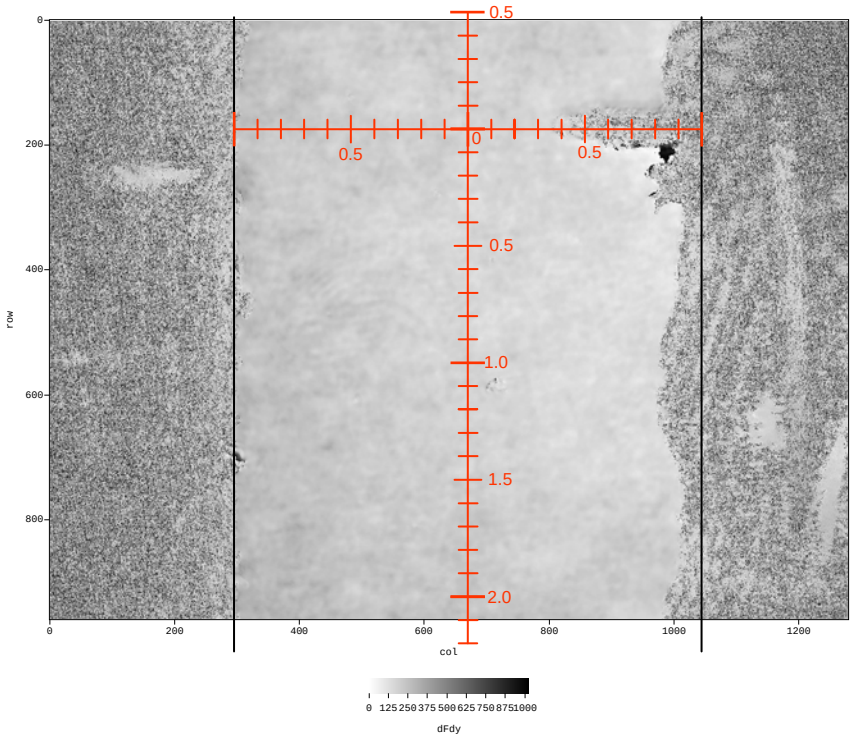

Figure 3-14: First step in moiré image analysis – applying scale

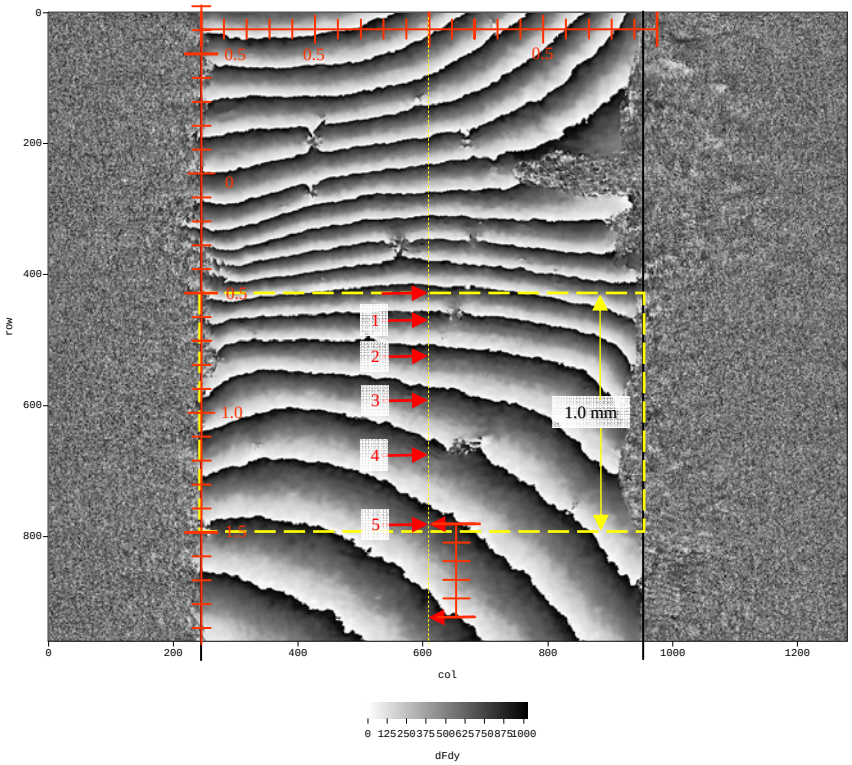

Figure 3-15: Next step in moiré image analysis – count fringes and approximate displacement/strain

In the paper counting method, each moiré image was printed at 1200 dpi resolution onto regular bond paper using a Brother 5250N LaserJet printer. Once printed, the width boundaries of the specimen were drawn onto the null load image. Next, a scaling factor was determined from these boundaries based on their assumed uniform 1:1 separation distance of 0.787 in (2.0 mm) and an equivalent scale was applied to the image, as shown in Figure 3-14. The scaling factor was subsequently applied to each image taken at the same magnification. Changes in magnification required altering the scaling factor, typically by use of visible 'landmarks' such as surface flaws, the weld boundary marker, or unique patterns along the grating edges. Using this scaling factor, distances on the paper image were measured with a rough visual accuracy of 1.0 ± 0.5 mm using a standard metal 12 in/300 mm scale. These distances were scaled with the appropriate factor to provide final data values.

Comparison of paper counting vs computer counting for one specimen's stress-overall strain values for a series of loading and unloading steps resulted in the chart in Figure 3-16. While both methods of counting are tedious, it appeared that paper counting, which takes slightly less time to accomplish, results in more accurate data. The only problem with paper counting is that the hardcopy analyzed images are not as easily reproduced and shared as the digital analyzed images resulting from computer counting. For this research, each of the two methods was used in different cases and often both methods were used with the best results presented.

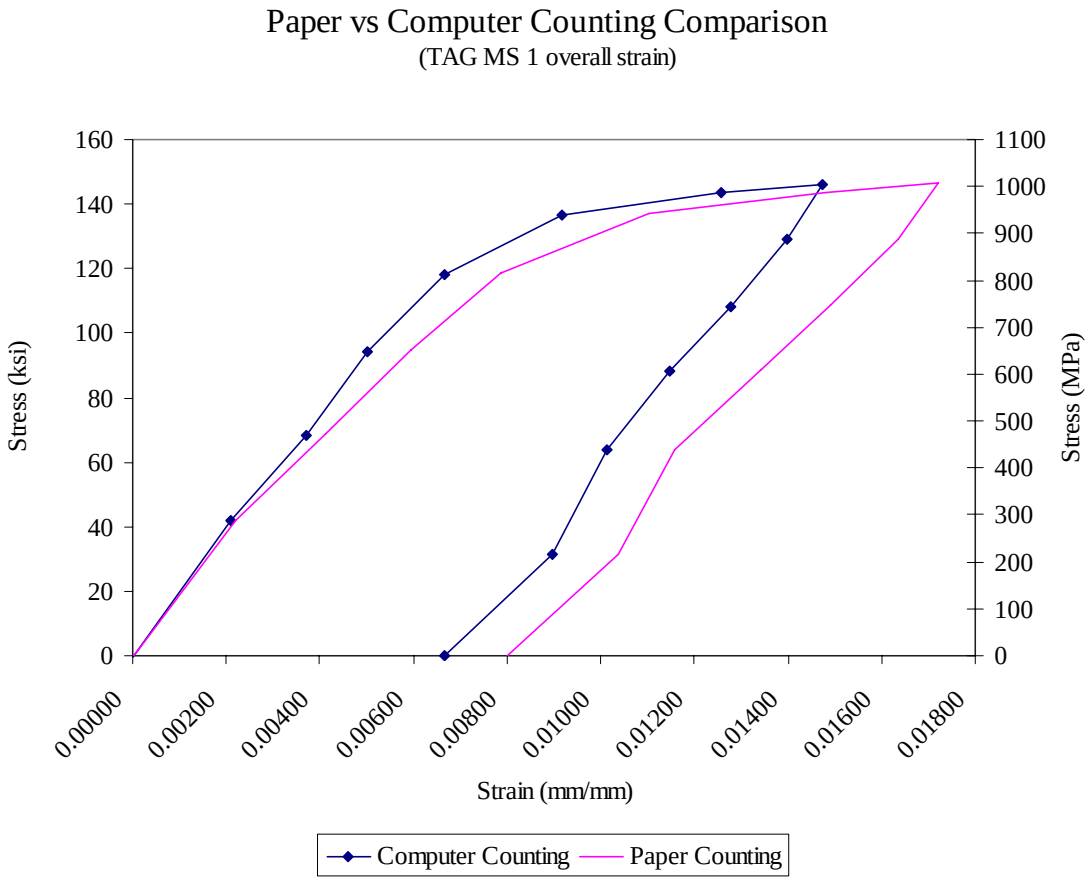

Figure 3-16: Comparison of computer and paper counting values for the same imagery

3.5.4. Numerical Modeling

Using the results of the full field strain analyses, a numerical model was developed to demonstrate the capability and utility of DIC and moiré interferometry in regards to modeling friction stir weld behavior. A non-linear large deformation analysis using a finite element model was chosen for this effort and created using ABAQUS version 6.7.1 finite element analysis (FEA) software [32].

As the specimen is symmetrical about the transverse midsection of the gage, only half of the geometry was modeled, as shown in Figure 3-17. The specimen is also symmetrical about the axial midsection of the gage allowing for further reduction to only a quarter of the geometry to further refine the finite element mesh. The half model was chosen to allow better visualization of behavior as well as capture any asymmetry in the plastic behavior.

The weld region was modeled as three simplified block regions at the base of the model, as visible in Figure 3-17(b). A trapezoidal geometry of these regions could also be used to further refine the fidelity of the modeling, but as this model is for demonstration purposes, the block geometry was sufficient. The four distinct regions of the model included a 0.236 in (6 mm) weld nugget, a 0.0394 in (1 mm) TMAZ, a 0.0394 in (1 mm) HAZ, and the remainder of the model as parent material. These regions were named for purposes of easy identification with the unique weld regions they contained. The dimensions of the modeled regions held no correlation with the actual dimensions of the weld regions they represented in friction stir welded Ti-6Al-4V, but were used for solely to simplify the model and analysis. The variation of material properties was simplified to a uniform 1% decrease in yield strength from one region to the next starting at the weld nugget.

Pin loading of the specimen was modeled to increase the fidelity of model. This was accomplished by defining a contact interaction of the half model with a translating,

analytically-defined rigid cylinder at the pin hole. For this effort, the pin displacement was limited to 2.0 mm in order to achieve strain localization without ultimate failure.

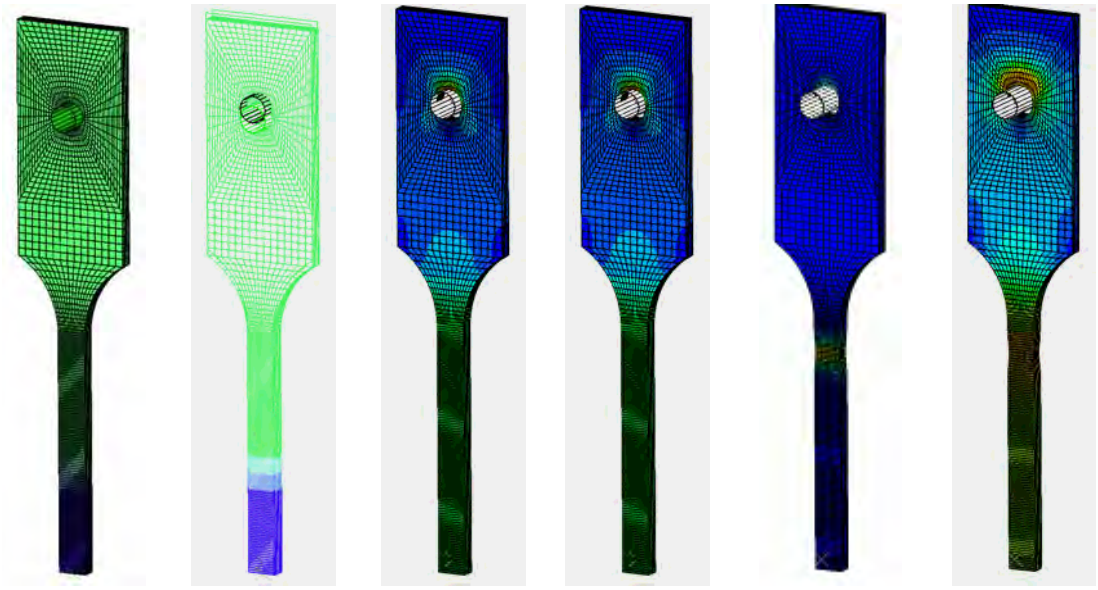

Figure 3-17: Finite element mesh and solutions for a homogeneous linear elastic and homogeneous elastic plastic material

The half model was meshed using three-dimensional eight-noded brick elements, identified as "C3D8" in ABAQUS, with full mapping, as shown in Figure 3-17(a). Mesh density was refined to a sufficiently fine level to capture strain localization in the model. The final mesh used contained slightly over 18,000 nodes with over 55,000 degrees of freedom. Full three-dimensional analysis was chosen since neither plane stress nor plane strain conditions apply to the specimen geometry. The model behavior was evaluated under linear elastic and elastic plastic conditions for rough validation, as shown in Figure 3-17 (c) and (d), respectively.

4. Experimental Results

In this chapter, experimental results of friction stir welded Ti-6Al-4V under tensile loading is presented. Mechanical behavior results obtained from the three methods of strain measurement are described in the following sections.

4.1. Global Stress-Strain Measurements

While typical global stress strain results are limited to presentation of stress-strain curve data, it is important in this research to also consider the details of the specimen failure. Figure 4-1 shows the stress-strain data taken from the four dedicated global specimens. The yield and ultimate stresses show good accord with the accepted values shown in Figure 3-2, though the failure strain values of 2.2 – 5.5% are significantly less than the Ti-6Al-4V expected 10 – 14% elongation at break [19,8]. Adding the global stress-strain results from the DIC tests, shown in Figure 4-2, maintains good accord with expected yield and ultimate stresses and also increases the elongation range to 2.2 – 6.2%. Comparison of the empirical data obtained in this research with previous research conducted at the University of Washington by Paul D. Edwards on similarly friction stir-welded Ti-6Al-4V material shows correlation of yield stress values within 9% [19]. Experimental percent elongation from Mr. Edwards' research, however, resulted in values from 4.4% to 12.1% versus the 2.2 % to 6.2% elongation shown in Figure 4-2. Given that only 12 specimens were evaluated for this research effort and that their values for yield and ultimate strength were in accord with accepted and previous empirical data, the relatively low values for percent elongation may be indicative of the effects of the

weld on the material properties and reflect the unique behavior of the particular samples of Ti-6Al-4V used. The difference from expected elongation may also be due to the presence of the FSW spanning most of the gage region covered by the strain-gage extensometer.

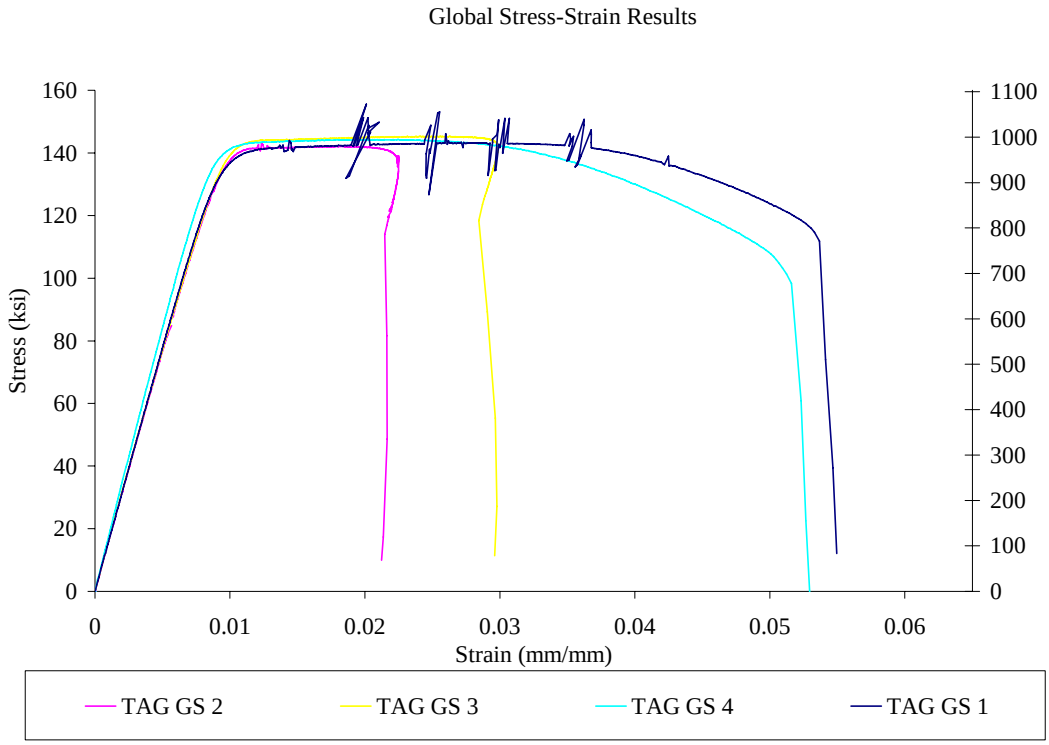

Figure 4-1: Global specimen stress-strain results

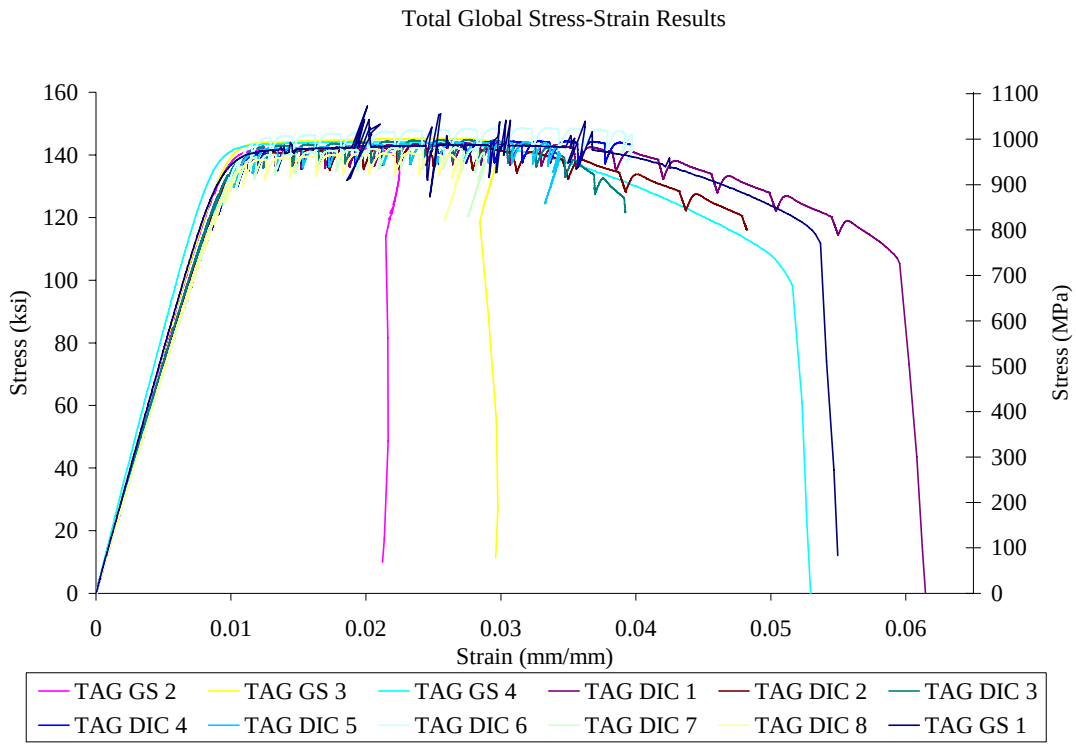

Figure 4-2: Total combined global stress-strain results

4.2. Digital Image Correlation Results

Twelve total DIC specimens were prepared for this research with a goal of achieving eight successful tensile tests. Two specimens out of the twelve failed to properly test due to the inadequate grip torque resulting in specimen slippage within the load frame grips. Once the eight successful tests were achieved, the remaining two DIC specimens were left untested. The complete sets of DIC data are presented in Appendix A. To summarize the findings, the DIC data for all of the DIC specimens shows a broad scattering of areas of localized strain for specimen loads from null through elastic strain values. Though seemingly random, there are areas of increased localized strain that manifest in this region and remain throughout the duration of the test. These areas are at

the weld boundaries and at the ends of the specimen gage, where stress concentration due to the specimen fillet is expected to cause an increase in local strain. The localized strain at the weld boundaries generally increases significantly once the specimen enters plastic strain and remains the dominant localized strain until overtaken by localized strain near the fillets and particularly within the area of ultimate failure. This trend can be seen in the down-sampled sequence of images in Figure 4-3. Strain is distributed fairly evenly with small random localizations until (c) which shows definite localizations developed at the weld boundaries after yield strength is reached. These localizations remain, but are eventually overtaken in magnitude by the strain in the area of the fillet stress concentrations, shown in (e) – (f). The arrow in (f) indicates the area of ultimate failure. Though varied in strain magnitudes and ultimate failure locations, the remainder of DIC specimens showed the same post-yield pattern of relatively high strain localization at the weld boundaries with substantially lower relative strain intensity across the weld nugget. All DIC specimens demonstrated ultimate failure, with the associated strain localization ultimately developing to the expected peak magnitude, outside of the weld boundaries. Table 4-1 summarizes the DIC failure data.

Table 4-1: DIC specimen failure strain summary

			Indicated Strain at Failure				
Specimen	**Ultimate Stress (ksi//MPa)**	**Failure from Weld (in//mm)**	**Retreating Boundary**	**Weld Center**	**Advancing Boundary**	**Failure Point**	**Strain Gauge Extens.**
TAG DIC 1	143.7//991	0.157//4.0 A	0.027*	0.012*	0.064*	0.069*	0.0306*
TAG DIC 2	142.4//982	0.122//3.1 A	0.019	0.006	0.050	0.325	0.0482
TAG DIC 3	114.9//999	0.185//4.7 A	0.035	0.013	0.057	0.354	0.0392
TAG DIC 4	144.4//996	0.331//8.4 A	0.056	0.007	0.104	0.122	0.0396
TAG DIC 5	144.2//994	0.346//8.8 A	0.054	0.009	0.065	0.314	0.0344
TAG DIC 6	148.5//1024	0.335//8.5 A	0.068	0.011	0.091	0.256	0.0398
TAG DIC 7	142.3//981	0.343//8.7 A	0.028	0.012	0.081	0.327	0.0288
TAG DIC 8	140.7//970	0.335//8.5 A	0.022	0.008	0.047	0.327	0.0271

A = advancing side of weld (no DIC failures on retreating side); * max stress data available

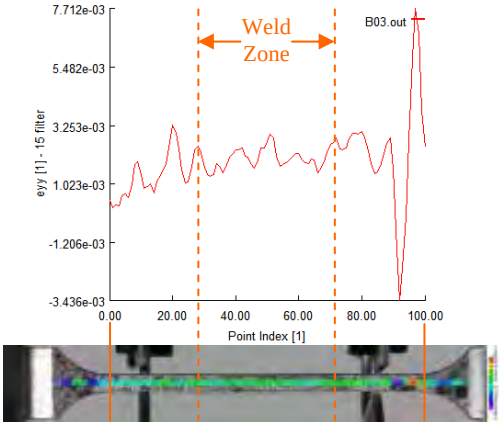

(a) Load Step 3: 51. 8 ksi (357 MPa)

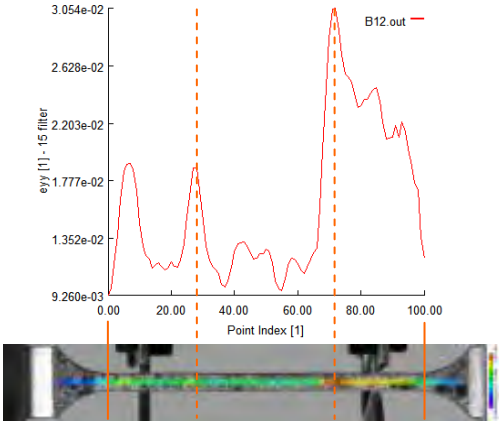

(d) Load Step 12: 142.3 ksi (981 MPa)

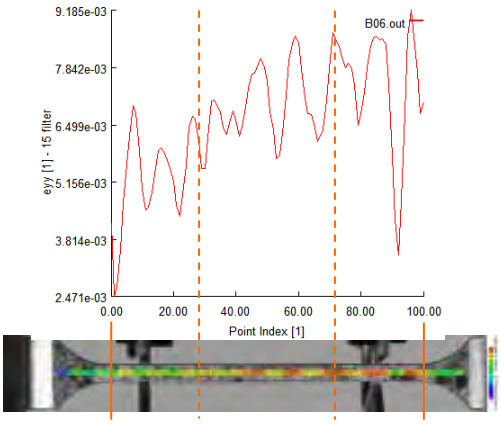

(b) Load Step 6: 110.1 ksi (759 MPa)

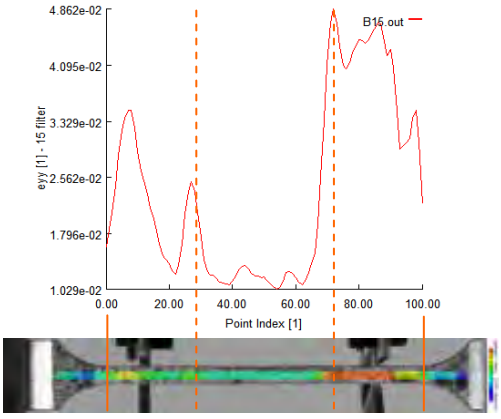

(e) Load Step 15: 143.2 ksi (987 MPa)

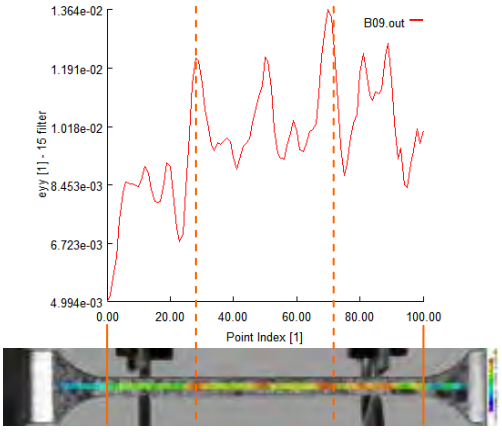

(c) Load Step 9: 139.2 ksi (960 MPa)

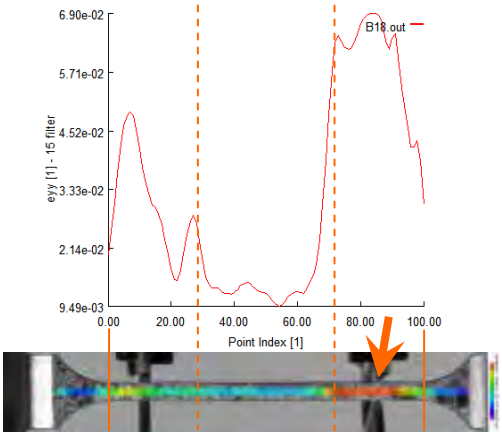

(f) Load Step 18: 143.3 ksi (988 MPa)

Figure 4-3: Representative down-sampled DIC specimen data spectrum

4.3. Moiré Interferometry Results

Nine moiré interferometry specimens were prepared for this research effort with a goal of achieving eight viable sets of moiré test data. It should be noted that though nine specimens were set aside specifically for moiré testing, a number of specimens required multiple moiré-specific preparation due to failed initial attempts to apply the surface grating. Of the nine successfully prepared moiré specimens, two were used in setting up and verifying the experiment apparatus and were not dedicated to data collection. The first of these set-up specimens experienced application of repeated loading/unloading cycles which might have altered its strain behavior under load. The second of the set-up specimens was used to collect moiré fringe evidence of strain, but without any accompanying load information; information from this specimen is presented in Appendix B, section 1. Six of the remaining seven specimens produced sufficient data to hold the last specimen as reserve material for further testing if needed.

The moiré experiments followed a flexible approach to explore the strain behavior in elastic and plastic loading at the surface of a friction stir weld for variations at each of the different weld interface regions and to explore the strain behavior in both the axial (v-field) and transverse (u-field) directions for variations in transverse strain behavior. The results of all six successful tests show distinct areas of elevated localized strain near the weld boundary developing near the yield strength and continuing through plastic loading. In two cases, the moiré tests continued until necking developed which showed weld

boundary strain localization at a maximum until overtaken as the maximum by the necking region associated with the point of ultimate failure.

Table 4-2: Moiré specimen failure strain summary

			Calculated Maximum Strain				
Specimen	**Maximum Stress (ksi//MPa)**	**Failure from Weld (in//mm)**	**PM**	**HAZ**	**TMAZ**	**WN**	**Total**
TAG MS 1	146.1//1007	N/A	N/A	0.0173	0.0203*	0.0116	0.0172
TAG MS 2	139.5//961	N/A	N/A	0.0115	0.0153	0.0213*	0.0198
TAG MS 3	146.1//1007	N/A	N/A	0.0173	0.0194*	0.0110	0.0163
TAG MS 4	125.6//866	N/A	0.0094	0.0257	0.0317*	0.0095	0.0124
TAG MS 5	146.4//1009	0.165//4.2 R	0.0167	0.0200	0.0233*	0.0233	0.0344
TAG MS 6	146.4//1009	0.039//1.0 R	0.0123	0.0167	0.0283*	0.0110	0.0129

R = retreating side of weld; * first region of visible strain localization

Image and associated stress data for all of the six moiré specimens is included in Appendix B. A summary of the strain data from these specimens is presented in Table 4-2.

Figure 4-4 presents a down-sampled typical sequence of moiré specimen data. The moiré fringes in the image progression indicate relative changes of grating displacements that correspond to relative changes in strain on the specimen surface. Figure 4-4(a) shows a typical null image without any discernable fringes. Figure 4-4(b) shows a typical elastic fringe pattern with consistent fringe spacing across the entire length of the specimen gage. Figure 4-4(c) shows the advent of strain localization in the area of tighter fringe spacing as the applied stress exceeds the yield stress. This localization continues to increase to a maximum shown in Figure 4-4(d), which corresponds to the maximum

applied stress before the specimen was unloaded. Figure 4-4(f) shows the residual plastic strain in the fully unloaded specimen. Note the change in fringe spacing from the maximum applied stress image; the area of maximum localization, corresponding to the weld boundary, remains highly strained while the areas above and below, corresponding to the parent material and weld nugget, relax considerably.

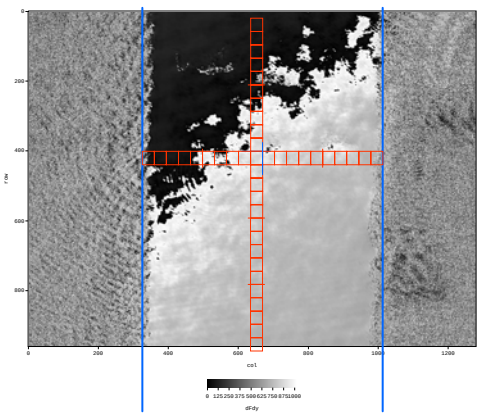

(a) Load Step 1: null

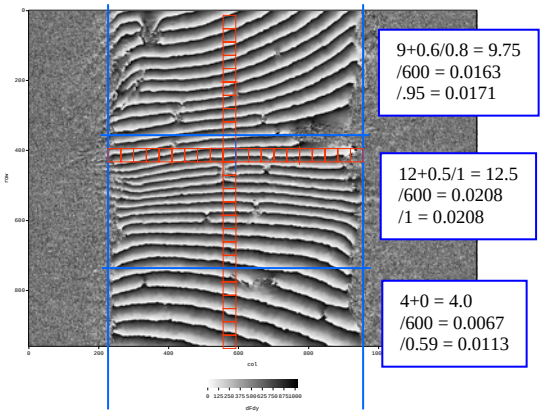

(d) Load Step 8: 146.1 ksi (1007 MPa)

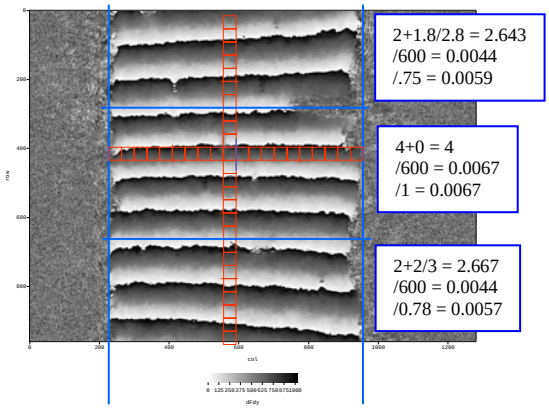

(b) Load Step 4: 94.3 ksi (650 MPa)

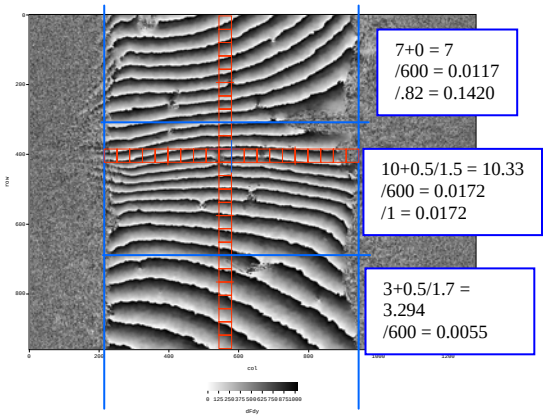

(e) Load Step 11: 88.4 ksi (610 MPa)

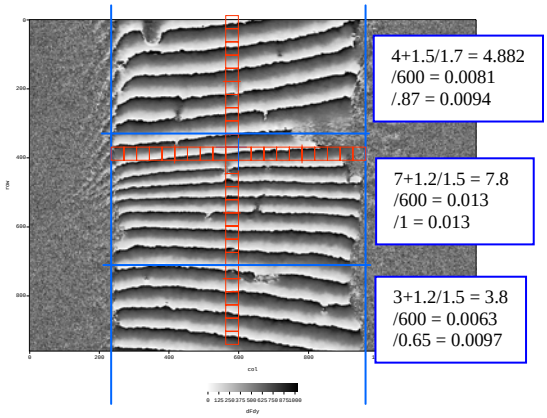

(c) Load Step 6: 136.5 ksi (941 MPa)

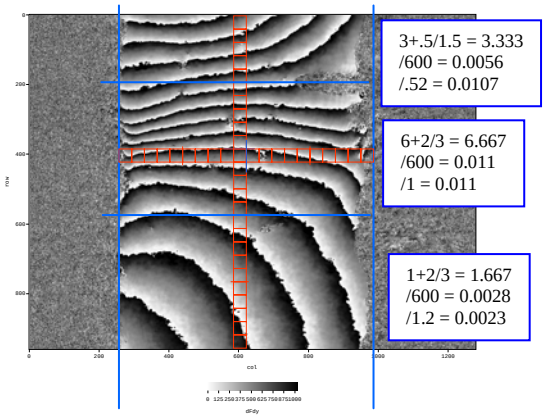

(f) Load Step 14: 0.2 ksi (1 MPa)

Data Key:

full fringes + fractional fringes = total fringes
/600 lines/mm = displacement (mm)
/length of interest = strain (mm/mm)

Figure 4-4: Representative down-sampled moiré specimen data

4.4. Numerical Modeling

Following verification of the proper fundamental behavior of the finite element model under elastic and plastic loading, the strain behavior was modeled by displacing the rigid pin 0.0787 in (2 mm) away from the gage to put the specimen under tension. Figure 4-5 shows a progression of the model results for maximum principal strain starting with uniform elastic loading on the left and moving into localization behavior and ultimate failure. This rough model shows necking occurring at the interface between the region representing the TMAZ and the region representing the HAZ, which is in accord with empirical results showing initial strain localization consistently manifesting at or near the visible weld boundary. Figure 4-6 shows the corresponding von Mises stress progression for the same modeled conditions.

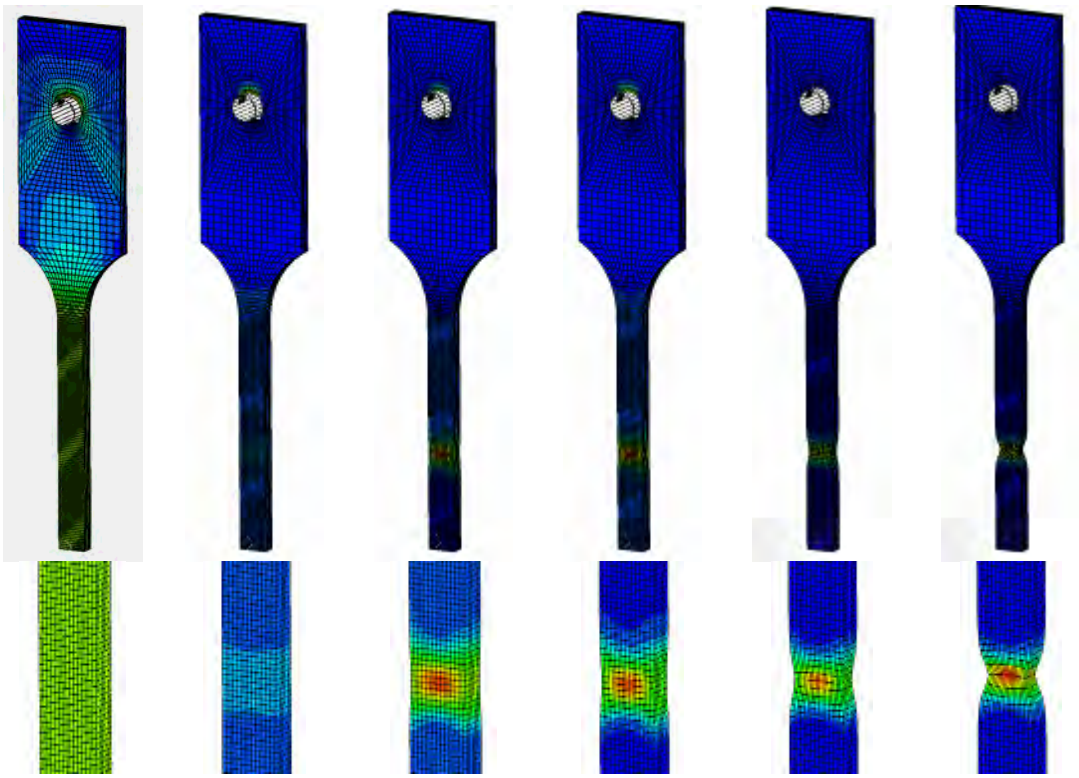

Figure 4-5: Maximum principal strain progression from uniform elastic loading to localized failure

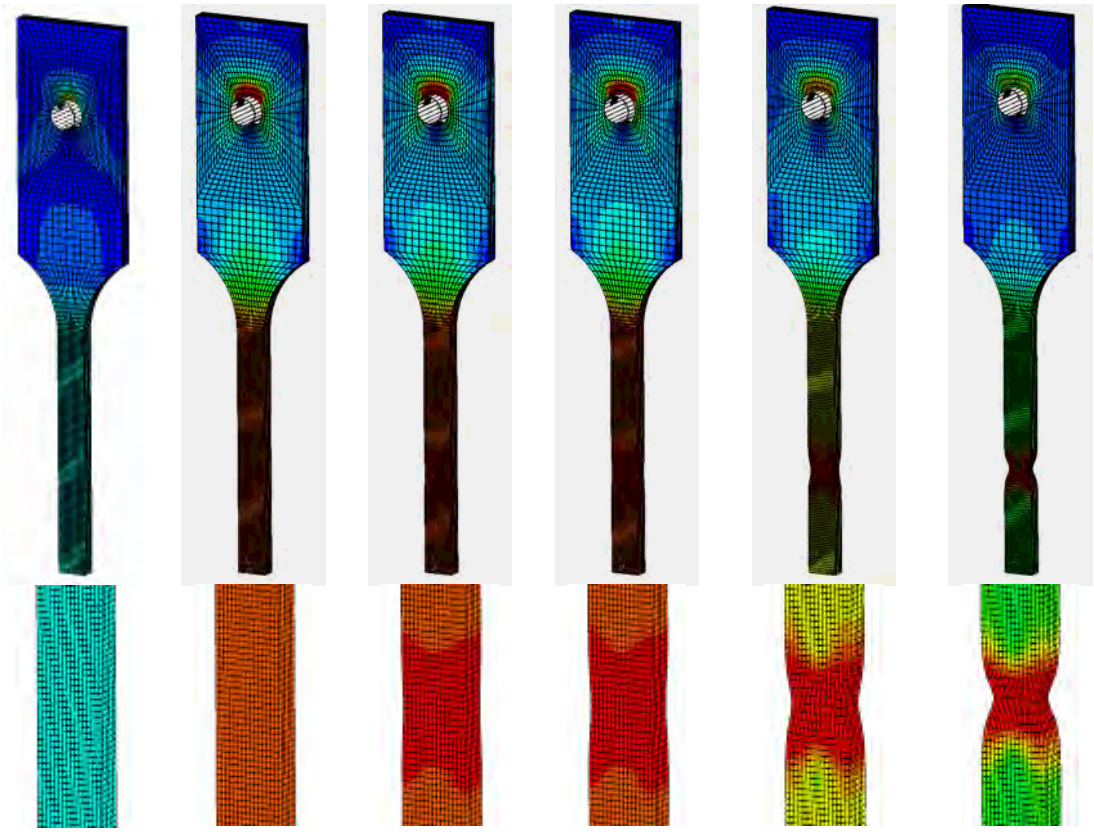

Figure 4-6: von Mises stress progression from uniform elastic loading to localized failure

In addition to the traditional contour plots shown in Figure 3-17, Figure 4-5, and Figure 4-6, it is possible to model moiré fringe behavior in the finite element model. Figure 4-7 shows simulated moiré fringe modeling and growth under loading using FEA. Keeping within the scope of this research, these FEA-simulated moiré fringes are demonstrated for the utility of the process and do not correspond to the actual fringe behavior observed in the moiré interferometry portion of this research. Although not demonstrated here, it is possible to attenuate the finite element model to reproduce simulated fringes at the same displacement intervals in which they would actually appear if using moiré interferometry. This capability would allow the use of moiré interferometry as a means of characterizing

localized displacement and strain behavior or any material discontinuity, such as weld regions or material interfaces, to refine the FEA accuracy.

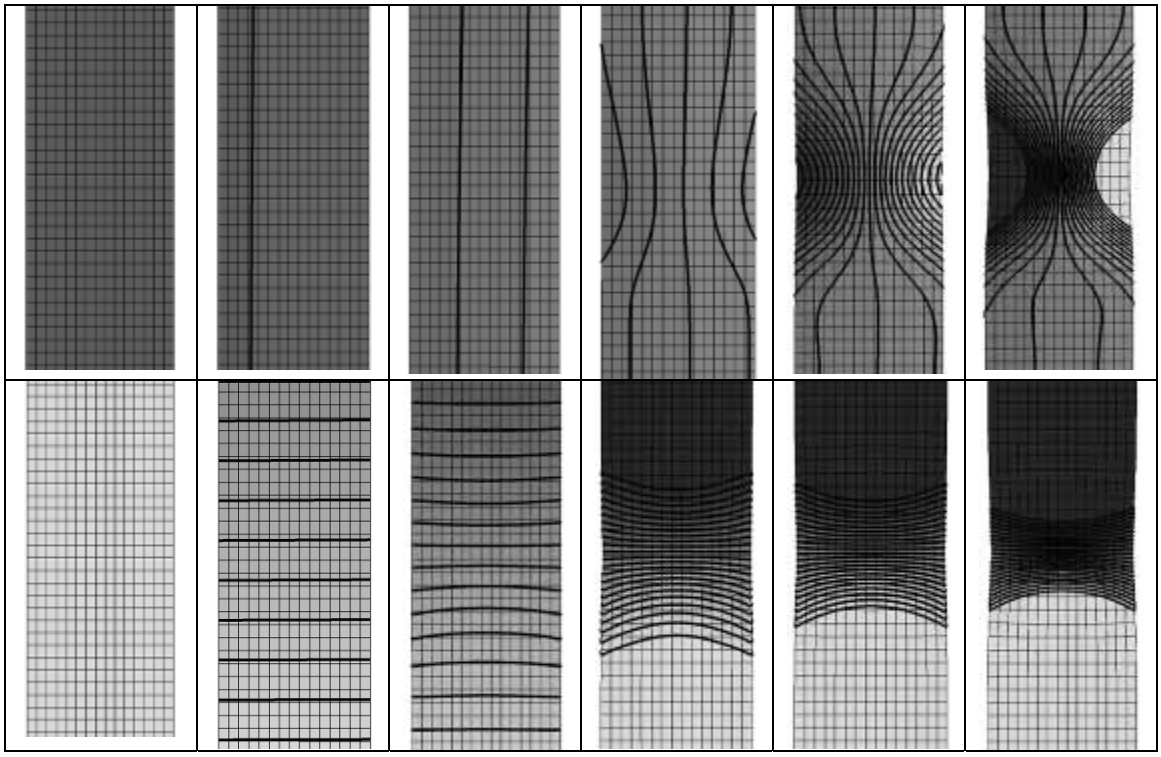

Figure 4-7: FEA simulated moiré fringes

5. Discussion

This research set out to accomplish three separate research objectives, outlined in Section 1.1. This chapter scrutinizes the results of the research described in the previous chapters in the context of accomplishing the three stated objectives.

5.1. Global and Full-Field Stress-Strain Behavior

The foremost purpose of this research was to evaluate the stress-strain response of friction stir-welded Ti-6Al-4V in elastic and plastic loading conditions using global and full-field strain measurement techniques in order to demonstrate utility in determining variations in strain behavior due to the presence of the weld. Each of the three methods used to evaluate the strain response demonstrated that consistent variations in strain behavior within each of the four unique weld regions definitely exist. The data in Table 5-1, which summarizes the global specimen failure data, shows a distinct difference in the total strain depending on the location of the ultimate failure with respect to the weld boundary.

Table 5-1: Global specimen failure strain summary

Specimen	Maximum Stress (ksi//MPa)	Failure from Weld (in//mm)	Extensometer Indicated Strain
TAG GS 1	146.1//1007	0.0 A	0.0550
TAG GS 2	139.5//961	0.248//6.3 R	0.0225
TAG GS 3	146.1//1007	0.315//8.0 A	0.0299
TAG GS 4	125.6//866	0.051//1.3 R	0.0530

A = advancing side of weld; R = retreating side of weld

The global specimen tests represent the lowest fidelity of the three measurement techniques used in this research and only present an average of the total strain across the entire weld region. When evaluated with the specific failure behavior of each specimen, however, the global specimen tests demonstrated that the stress-strain behavior differs substantially between specimens which failed in or near the weld region vs those which failed well away from the weld boundary in the parent material. Noteworthy in the stress-strain behavior shown in Figure 4-1 and Figure 4-2 are two distinct curve shapes. The first shape, shown isolated from the other data in Figure 5-1, is indicative of a more ductile failure and represents the specimens which failed near the weld interface, defined in this research as within 0.197 in (5 mm) of the visible weld boundary. These stress-strain curves demonstrated a gradual decline in stress magnitude and higher elongation in general before reaching ultimate failure.

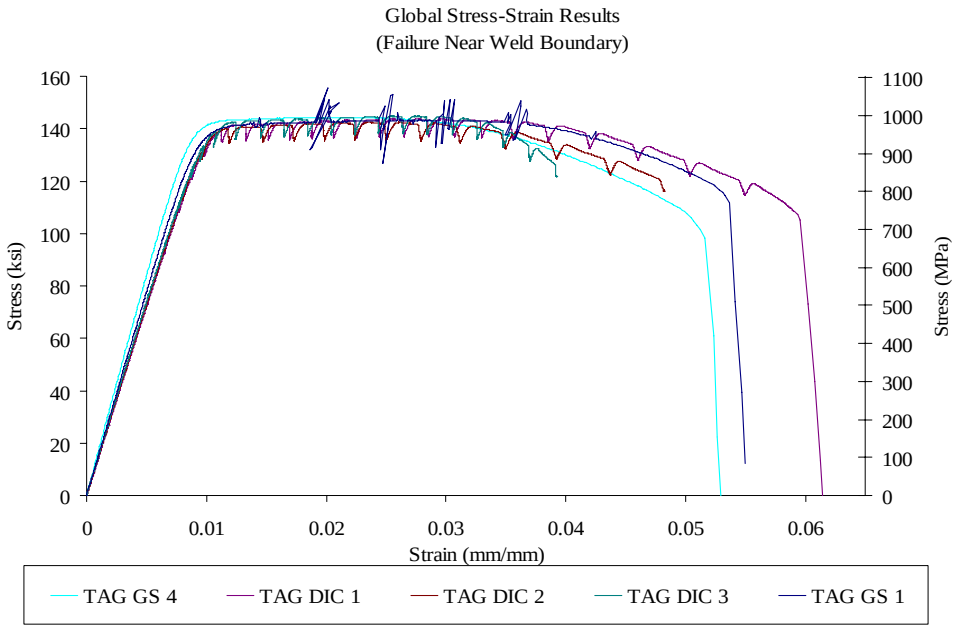

Figure 5-1: Stress-strain behavior of weld interface failures

The second curve shape, shown in Figure 5-2, is indicative of a less ductile failure and represents the specimens which failed well into the parent material, arbitrarily defined in this research as more than 0.197 in (5 mm) away from the weld boundary. Though this change in global strain behavior does not provide sufficient insight into material behavior to support specific conclusions, it does indicate changes in material properties based on proximity to the friction stir-weld. These results suggest that the region near the weld interface, which has been affected by the FSW process, is more ductile than the parent material.

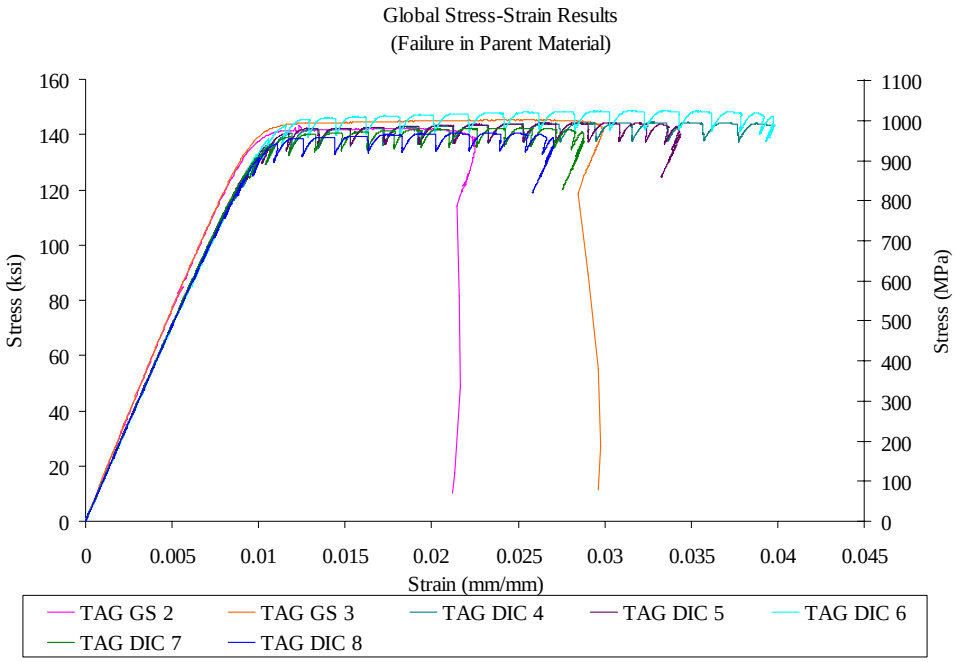

Figure 5-2: Stress-strain behavior of parent material failures

Further scrutiny into this difference in behavior using DIC shows a more elaborate behavioral response across the interface between the weld and parent material. In all DIC

specimen tests, the results of which are shown in Appendix A, a consistent pattern of strain behavior is visible across the gage length. Under elastic loading, the strain pattern shows no consistent pattern. Once yielding is reached, strain localization initiates near both weld boundaries simultaneously, typically with one side showing a higher strain than the other. As the specimen is extended further, the weld boundary localizations continue to grow without consistency; sometimes the lower magnitude localization outgrows the larger, both grow consistently, or the larger magnitude localization continues to increase relative to the lower. In all cases, as stress increases, the strain localizations which manifest at the weld boundaries are eventually surpassed by the strain localization manifesting at the point of ultimate failure. Often, the weld boundary localizations are also surpassed by the strain manifesting at the ends of the specimen gage due to stress concentrations at the fillets between the specimen gage and tabs. Observation of this expected elevated stress at the fillets within the test data indicates future specimen dimensions would be improved by lengthening the gage with respect to the weld width. As shown in the results for the global specimen testing, the magnitude of the resultant ultimate strain localization and the behavior of that localization relative to the initial strains at the weld boundaries varied depending on the location of the ultimate failure location relative to the different weld regions.

One hypothesis for this observed behavior is that as the stress increased, the strain initially manifested to a higher intensity in the area of higher ductility around the weld boundaries, but the material in this area proved to be ultimately stronger than the parent

material which experienced fracture. This difference is believed to be due to the greater number of impurities or flaws remnant in the grain structure of the unstirred parent material as compared to the refined grain structure of the stirred material.

The moiré specimens confirmed the strain behavior observed in the DIC specimens. Due to limitations in adjusting camera elevation, zoom, and focus, the moiré experiments were not used to extract full-field strain imagery to the same extent across the entire gage length as was done in DIC. Moiré specimens were instead used to evaluate specific narrow areas of interest around the weld region. In a few instances, to provide a notional understanding of the strain manifestations at the different weld regions, multiple panned images were captured along the gage length to create a composite image of strain localization behavior across larger portions of the gage, as shown in Figure 5-3.

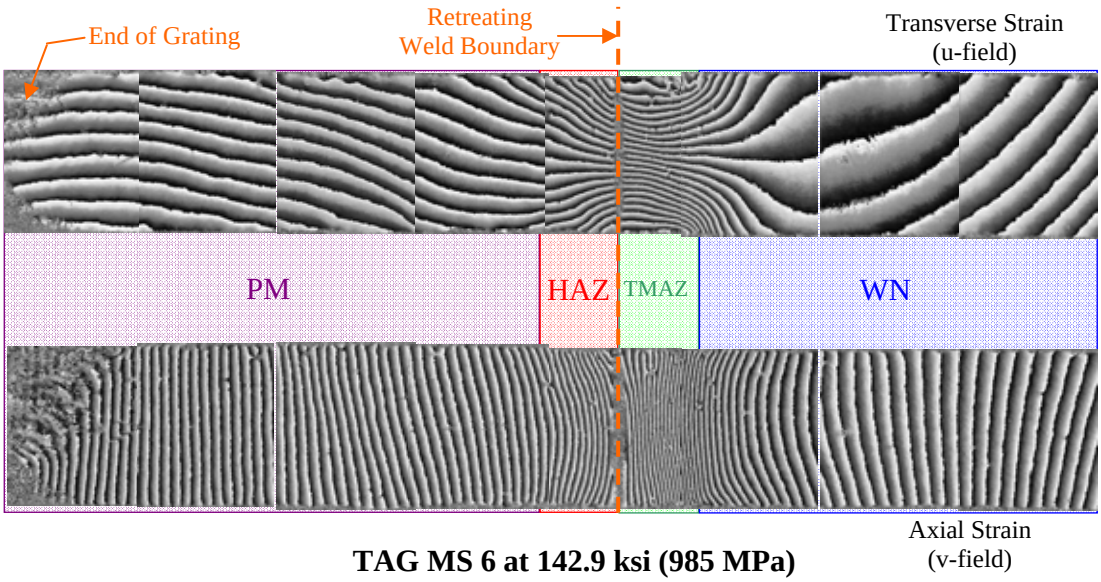

Figure 5-3: Composite moiré images of axial and transverse strain localizations

5.2. Comparison of Measurement Methods

The secondary purpose of this research was to compare and attempt to correlate the full-field strain measurement techniques of DIC and moiré interferometry. It was found that both methods captured the same fundamental strain localization behavior across the friction stir weld. Unfortunately, the captured moiré data is limited and only a few full gage composite images were captured to show strain localization behavior at a number of successive load steps. The DIC data was able to capture behavior across the entire gage length every time. The limited scope of this research, however, did not accommodate capturing the quantity of data at the level of accuracy necessary to determine a rigorous quantitative correlation between the two methods, though it did qualitatively support a general relationship between the two measurement techniques.

Figure 5-4 shows a qualitative comparison of moiré and DIC imagery data. The moiré images are of specimen TAG MS 6 and the DIC images are of specimen TAG DIC 2. The moiré image can be interpreted by the relative fringe spacing while the DIC image displays an overlaid contour plot of relative strain intensity with red being the highest and purple being the lowest. It is important to note that unlike the sequential moiré images, the contour coloration in the DIC images is unique to each image and not based on an absolute scale. Both of these specimens exhibited similar failure behavior of necking outside of the weld boundary, but close enough to be within the general area of the weld. Also in both cases, imagery shows similar full-field strain behavior. Figure 5-4(a) shows strain localization at the weld boundary shortly after yielding occurred. Figure 5-4(b)

shows behavior after additional loading where the strain localization began to manifest more or less uniformly out from the weld boundary away from the center of the specimen. Figure 5-4(c) shows the behavior after additional loading just before visible necking occurred at the point indicated by the green line. At the necking line in the moiré image, the fringe pattern 'washes out' due to the inability of the camera to resolve the individual closely spaced at its current magnification level. While this doesn't allow for calculation of strain by fringe counting, it does indicate the spacing between fringes in the unresolved area is much smaller than in the surrounding areas where individual fringes can still be counted.

Ultimately, in both the moiré and DIC images presented in Figure 5-4, the peak strain localization "migrated" (reference the hypothesis offered in section 5.1.) away from the weld boundary to the point of ultimate failure demonstrating a qualitatively high degree of correlation.

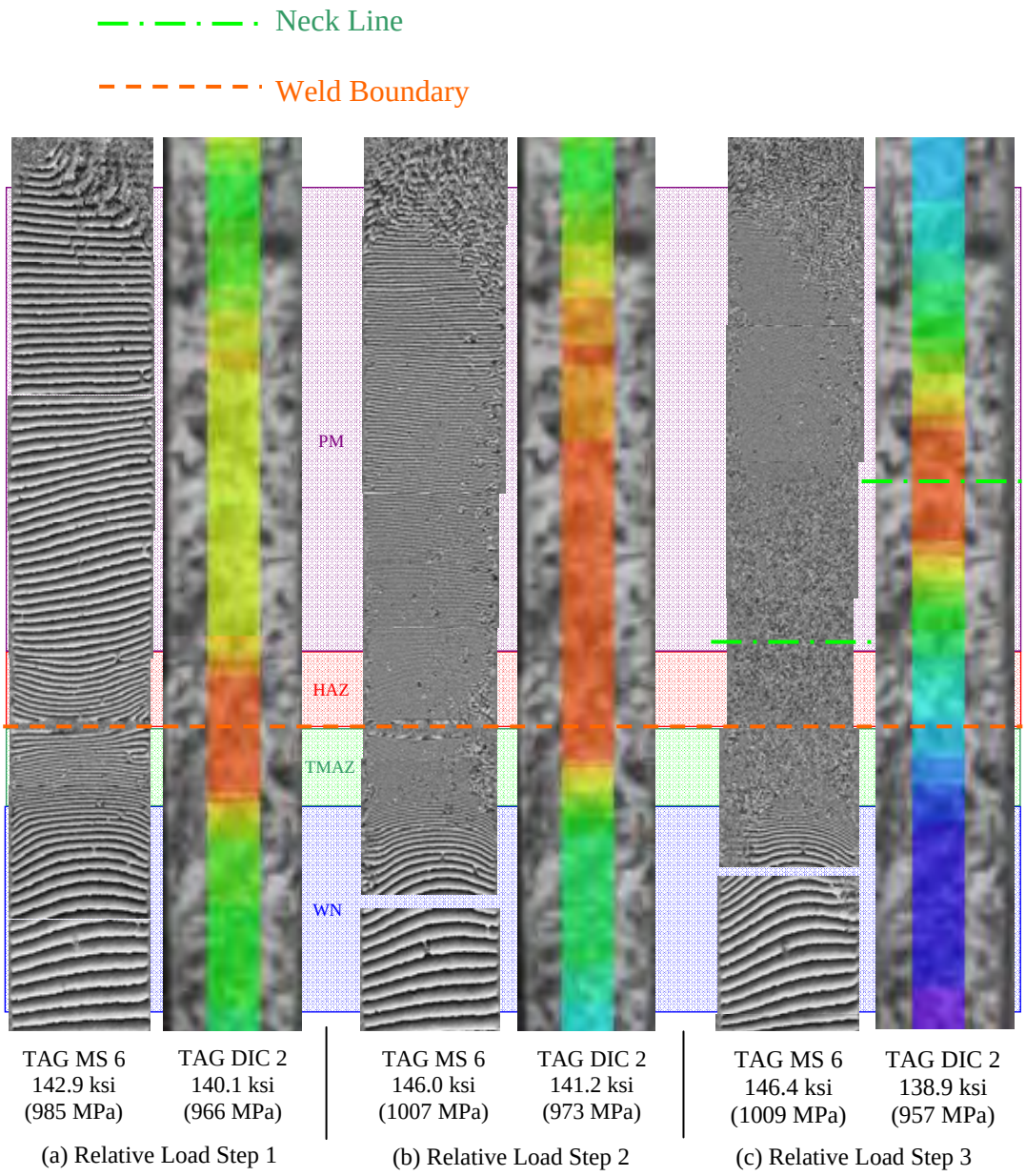

Figure 5-4: Comparison of moiré and DIC imagery for similar failure behavior

Further evidence of correlation is shown in Figure 5-5 which shows highly similar local strain data captured be means of both moiré interferometry and DIC. Figure 5-5(a) shows the full-field axial strain curve for TAG MS 5 plotted along the specimen gage

length indexed at equal spacing from 0 to 100 to allow direct comparison with the Vic 2D strain plot shown in Figure 5-5(b). The curves are mirror images of the same pattern of strain localization due to TAG MS 5 failing at the retreating side of the weld and TAG DIC 3 failing at the advancing side. Figure 5-5(a) was constructed by using moiré fringe data to calculate the average strain over separate increments of approximately 0.020 in (0.5 mm) over the length of the weld region and then plotting those values over a gage distance scale normalized to correspond to the DIC index scale. The flat peak of the moiré curve is due to the fringe spacing in the area of necking being too close to resolve; strain values for unresolved regions were approximated at slightly greater than the strain at the smallest resolved fringe spacing. Figure 5-5(b) was automatically generated by the Vic 2D software by designating a line area of interest from one end of the specimen gage to the other, starting with the retreating side of the weld. Note the correlation between the two data sets of elevated local strains in the vicinity of the weld boundaries and outside of the weld boundaries in the parent material.

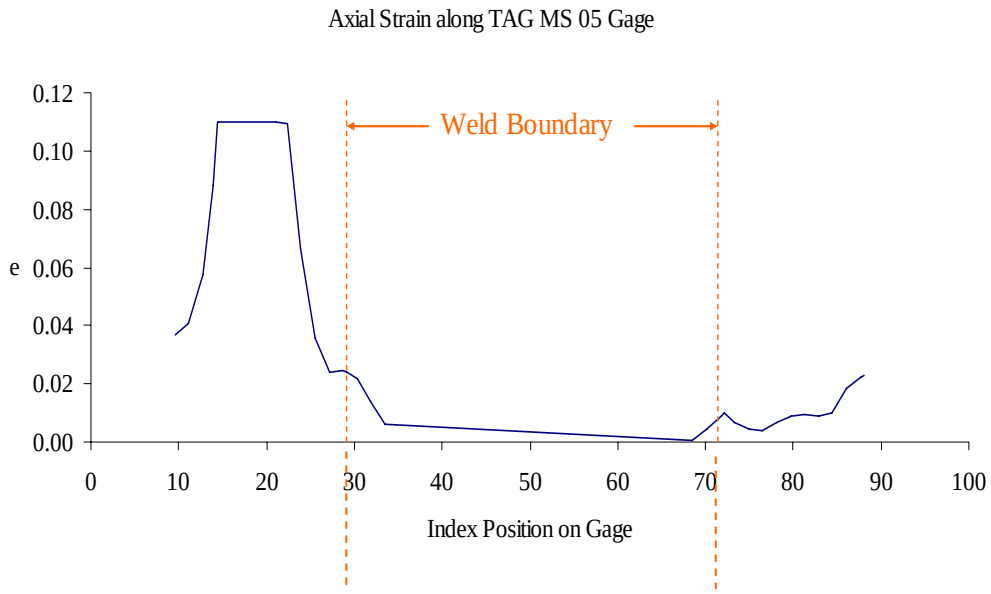

(a) TAG MS 5 axial strain data

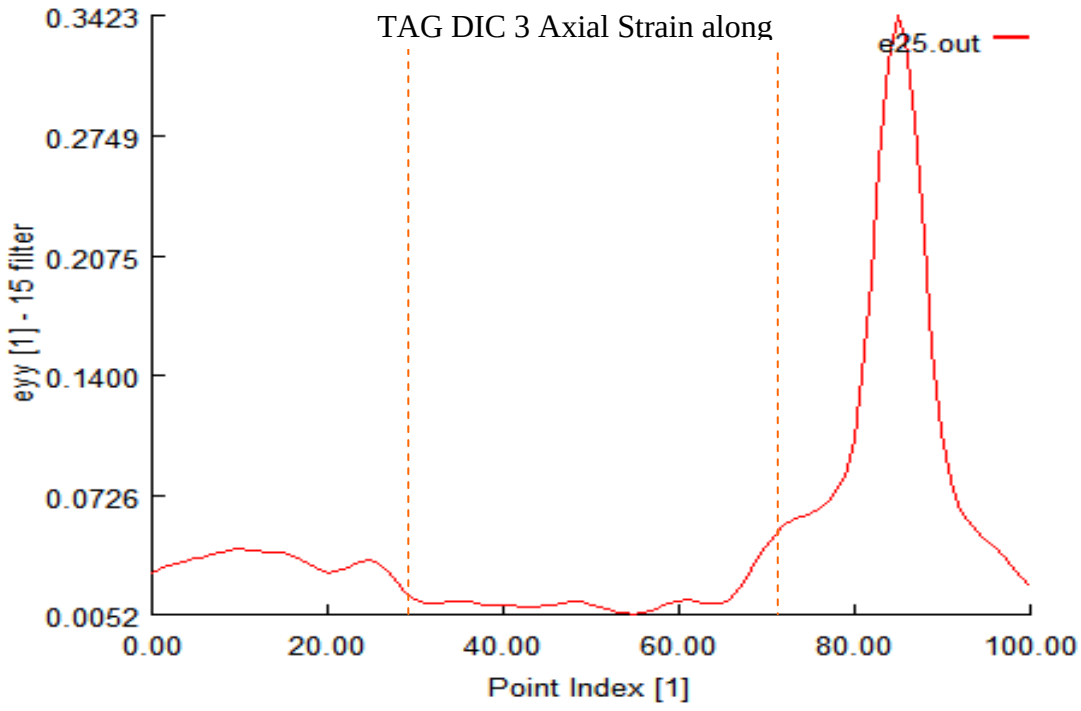

(b) TAG DIC 3 axial strain data

Figure 5-5: Comparison of axial strain results along gage length obtained by moiré interferometry (a) and digital image correlation (b).

Comparison of stress-strain behavior variations between the three distinct regions of the weld from both moiré interferometry and DIC results provided an additional means of correlating the general agreement of the two techniques. The three distinct regions evaluated were the weld nugget (WN), weld boundary (WB), and parent material (PM). In the DIC results, shown in Figure 5-6, strain values for each of the regions was roughly approximated by examining the plots of strain across the gage length and finding a consistent index point per specimen for the value of interest. In both specimens shown in the figure, the WB yields at lower stress than the WN and PM, which exhibit approximately the same yield character. It is important to note the DIC data is very "noisy" and exhibits frequent and substantial scatter in the data, particularly in the range of elastic loading. For this reason, each of the two sets of DIC data include a detail of the yield area with only data points plotted to illustrate the scatter. Also note the variation in dominant yielding from one specimen to the next. TAG DIC 2 ultimately failed nearer to the weld boundary so the WB region manifested as the dominant strain localization. TAG DIC 3, on the other hand, failed further into the parent material and away from the weld boundary, so the PM region manifested as the dominant strain localization.

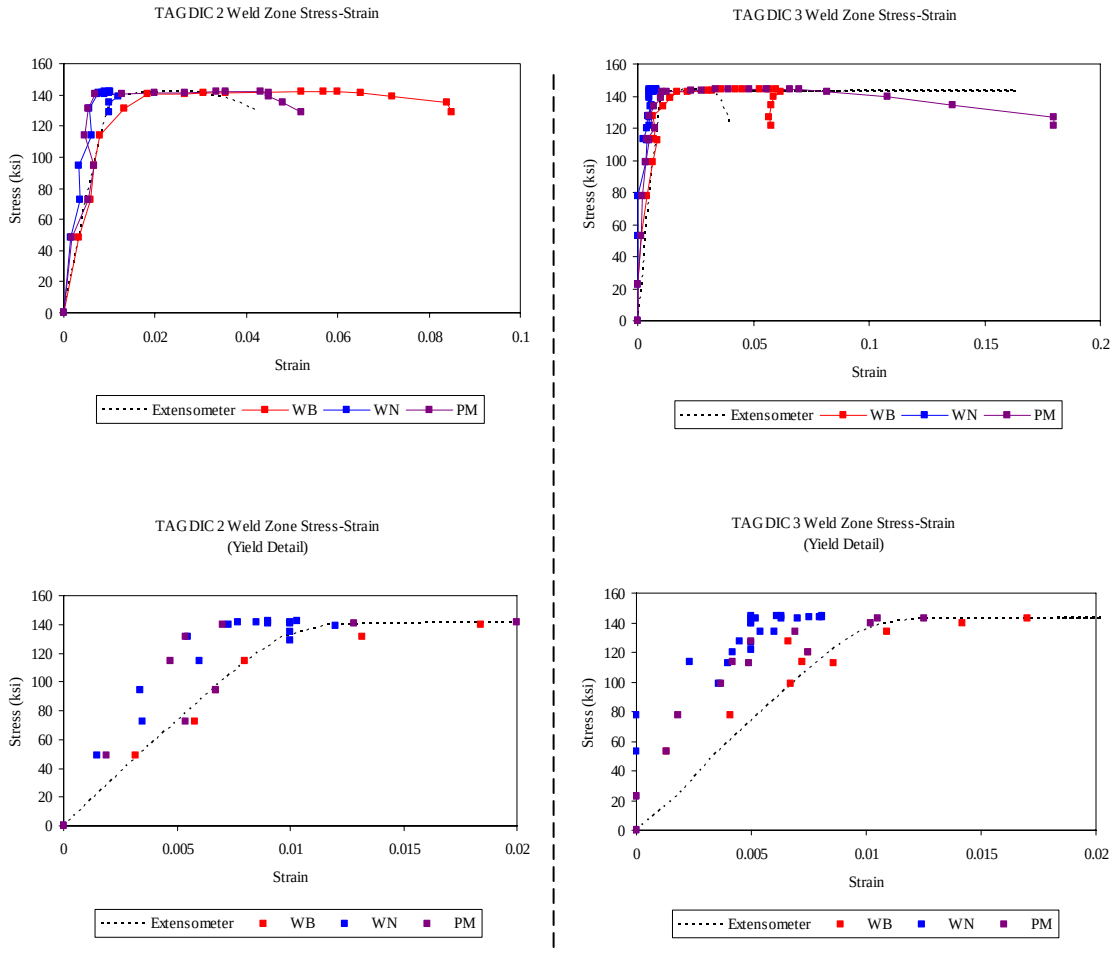

TAG DIC 2 TAG DIC 3

Figure 5-6: Typical DIC weld region stress-strain plots

Comparison of the above plots with typical stress-strain curves derived from moiré interferometry data, shown in Figure 5-7, shows agreement in yielding in the WB vs WN regions. PM stress-strain behavior data from the moiré measurements is very limited due to the limited scope of the moiré evaluation which concentrated on the known areas initial localization near the weld boundaries. For this reason, only a small segment of PM stress-strain behavior was captured during a single moiré specimen test, shown in Figure

5-8. Typically, the narrow frame region of the moiré images allowed capture of the weld boundary and one other region without panning for composite images. Composite images were only captured at plateau loading or fully unloaded, which left no data that captured both WN and PM behavior for a single specimen in the range of yielding.

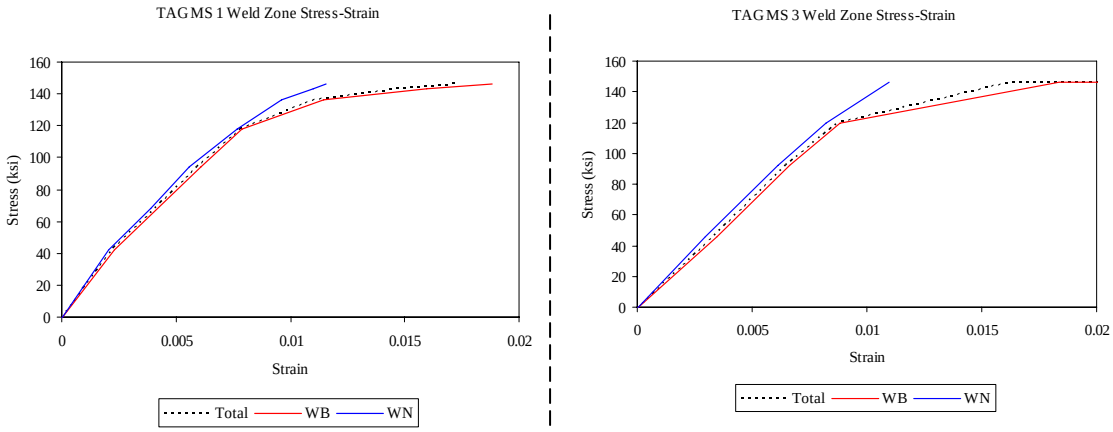

TAG MS 1 TAG MS 3

Figure 5-7: Typical weld region moiré stress-strain plots

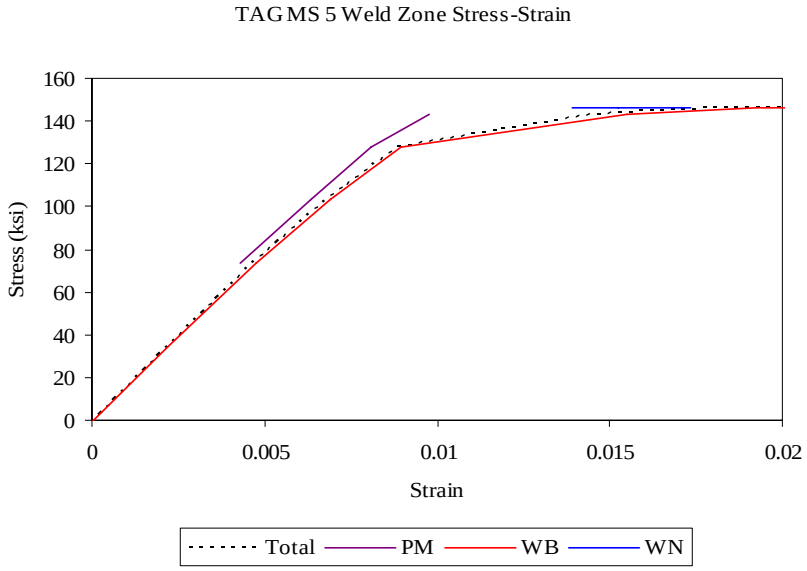

Figure 5-8: TAG MS 5 weld region stress-strain plot showing limited PM and WN values

Though the stress-strain plots shown in Figure 5-6, Figure 5-7, and Figure 5-8 do not show the same amount of comparative data, when considered with Figure 5-3, which shows typical moiré fringe distribution around the weld region, a qualitative pattern of behavior is clearly illustrated: the WN and PM regions exhibit similar strain behavior until ultimate failure begins and the WB consistently exhibits lower yielding onset and higher localized strain. Both methods of full-field strain measurement support this conclusion.

5.3. Finite Element Modeling

The tertiary purpose of this research was to apply the observed full-field strain behavior from this experimentation to develop a robust finite element model of the stress behavior within a Ti-6Al-4V friction stir-weld. A finite element model reflecting the empirical results of this research, including the ability to model moiré fringes with FEA, was demonstrated in Section 0. This 'rough' modeling, while not accurately representative of the actual weld geometry tested, showed the capability exists to refine a finite element model to accurately reflect the actual behavior of a friction stir-weld in Ti-6Al-4V.

6. Conclusions and Recommendations

The general nature of friction stir-welded Ti-6Al-4V under elastic and plastic loading was demonstrated by experimental methods including traditional tensile specimen testing along with the full-field strain measurement methods of digital image correlation, and moiré interferometry. An understanding of this general nature of the weld region will provide valuable insight to failure mechanisms and aid in the design and development of structures that utilize friction stir welding. Additionally, a numerical analysis in the form of a finite element model demonstrated the capability to incorporate full-field strain behavior into finite element analyses which include friction stir welded parts. This will provide exceptional utility in developing computational models with exceptional accuracy, which is particularly important in the design of aerospace structures where margins of safety are particularly low. Though limited in scope, the experimental and numerical analyses presented in this research will form the foundation of an increased level of refinement in the design and analysis of friction stir-welded joints in Ti-6Al-4V.

6.1. Conclusions

Experimental and numerical results of this research support the following conclusions:

Global Stress-Strain Behavior of Friction Stir-Welded Ti-6Al-4V:

- Overall strength of friction stir-welded Ti-6Al-4V is comparable to the accepted values for pure mill-annealed Ti-6Al-4V.

- Overall strain performance of friction stir-welded Ti-6Al-4V is roughly half that of the accepted values for pure mill-annealed Ti-6Al-4V.
- Failure in friction stir-welded Ti-6Al-4V will likely occur at or outside of the weld boundary with no apparent preference for advancing or retreating side of the weld.
- The material properties of friction stir-welded Ti-6Al-4V vary across the different regions of the weld, and are apparently more ductile yet ultimately higher or equivalent in strength within the area of the weld boundary as they are within the parent material.

Full-Field Strain Characterization of Friction Stir-Welded Ti-6Al-4V:

- Friction stir-welded Ti-6Al-4V demonstrates a consistent pattern of strain localization between the onset of yielding and ultimate failure.
- Following yielding, strain localizations develop at the weld boundaries and dominate the strain response during the initial stages of plateau loading.
- During plateau loading, strain localizations migrate away from the weld boundary and into the parent material, where ultimate failure typically occurs.
- Even under plastic loading to near ultimate failure, the entire central portion of a friction stir-weld (the weld nugget) does not manifest significant strain when compared to the weld boundaries and parent material, nor does significant residual strain remain in the weld nugget after unloading as compared to the weld boundaries and parent material.

- The full-field strain measurement methods of digital image correlation and moiré interferometry show good agreement with one another in terms of determining relative strain localizations.
- Digital image correlation provides an excellent means of refining global stress-strain behavior data to determine general areas of localization and atypical behavior.
- Moiré interferometry provides a good means of refining digital image correlation stress-strain behavior data to characterize specific areas of localization and quantify atypical strain behavior

Numerical Analysis of Friction Stir-Welded Ti-6Al-4V

- Empirical full-field strain measurement techniques such as digital image correlation and moiré interferometry are of great value in refinement and validation of finite element modeling of friction stir-welded behavior.
- It is possible to model accurate moiré fringe development within finite element analysis.

6.2. Recommendations

This research presents a qualitative demonstration of the utility of full-field strain measurement techniques in determining and modeling the strain behavior of specific areas of interest in a friction stir-weld applied to Ti-6Al-4V. Having demonstrated only the applicability of the empirical methods, utility of the numerical analysis, and relative

behavior of the weld region, this research provides an impetus for further research along these same lines, recommended below:

- Conduct more comprehensive research on the global and full-field strain behavior of friction stir-welded Ti-6Al-4V using a greater sample size in order to characterize typical behaviors of strain across the weld, as opposed to suggesting possible behaviors as this research has done.
- Investigate and fully characterize the material properties, beyond basic microhardness, of each region of a friction stir-weld.
- Further refine and enhance the basic finite element model presented in this research to accurately model friction stir-weld stress-strain behavior.

BIBLIOGRAPHY

1. Titanium Industries, Inc [online]. "Aerospace Applications". 15 November 2007. < http://www.titanium.com/titanium/aerospac.cfm>

2. R.S. Mishra and Z.Y. Ma, "Friction stir welding and processing" *Materials Science and Engineering*, R 50, 2005, pp.1-78

3. P.C. Hung and A.S.Voloshin, "In-plane Strain Measurement by Digital Image Correlation". *Journal of the Brazillian Society of Mechanical Science and Engineering*, v 25, n 3, July 2003, pp. 215 – 221

4. D. Post, B. Han, and P. Ifju, High Sensitivity Moiré: Experimental Analysis for Mechanics and Materials. New York, New York: Springer-Verlag, 1994.

5. Titanimium Industries, Inc [online]. "History and Production of Titanium". 23 Nov 2007. <http://www.titanium.com/titanium/tech_manual/tech1.cfm>

6. International Titanium Powder [online]. "Titanium History". 23 Nov 2007. <http://www.itponline.com/index_files/TiHistory.htm>

7. R.S. Mishra and M.W. Mahoney, Friction Stir Welding and Processing. Materials Park, Ohio: ASM International, 2007.

8. MatWeb [online]. "Titanium Ti-6Al-4V". 4 Dec 2006. <http://www.matweb.com/search/datasheet.aspx?bassnum=MTP642&ckck=1>

9. Titanium Industries, Inc [online]. "Machining Titanium Alloys". 23 Nov 2007. <http://www.titanium.com/titanium/tech_manual/tech2.cfm>

10. MatWeb [online]. "Titanium, Ti". 1 Feb 2008. <http://www.matweb.com/search/DataSheet.aspx?MatID=115&ckck=1>

11. MatWeb [online]. "Aluminum 7075-T6; 7075-T651". 1 Feb 2008. <http://www.matweb.com/search/DataSheet.aspx?MatID=9595>

12. MatWeb [online]. "Aluminum 2024-T4; 2024-T351". 1 Feb 2008. <http://www.matweb.com/search/DataSheet.aspx?MatID=8867>

13. MatWeb [online]. "AK Steel 316 Austenitic Stainless steel". 1 Feb 2008. <http://www.matweb.com/search/DataSheet.aspx?MatID=14715>

14. MatWeb [online]. "AISI 4130 Steel, normalized at 870°C (1600°F)". 1 Feb 2008. <http://www.matweb.com/search/DataSheet.aspx?MatID=7503>

15. Matthew J. Donachie, Jr., Titanium: A Technical Guide. Metals Park, Ohio: ASM International, 1988.R.S. Mishra and Z.Y. Ma, "Friction stir welding and processing" *Materials Science and Engineering*, R 50, 2005, pp.1-78

16. Welding Advisors.com [online]. "Welding-titanium and titanium alloys". 15 Nov 2007. <http://www.welding-advisers.com/Welding-titanium.html>

17. Azom.com [online]. "Titanium – welding and heat treating". 24 Nov 2007. <http://www.azom.com/details.asp?ArticleID=1245>

18. The Welding Institute [online]. "Friction Stir Welding – process advantages". Retrieved 25 Nov 2007. <http://www.twi.co.uk/j32k/unprotected/band_1/fswproc.html>

19. P.D. Edwards, "Experimental and Numerical Characterization of Friction Stir Welded and Superplastically Formed Friction Stir Welded Titanium" (MS thesis, University of Washington, 2006)

20. R. Olexa, "Stirring up a New Airplane". *FFJournal*, Oct 2007, pp 1 – 4.

21. M.J. Russell and R. Freeman, "FSW for Titanium". *Metalworking Production*, May 2007, pp 30.

22. F.T. Duvall, "Full Field Strain Measurement in Welds" (MS Thesis, University of South Carolina, 1998).

23. V. Srinivasan, S. Radhakrishnan, X. Zhang, G. Subbarayan, T. Baughn, and L. Nguyen. "High Resolution Characterization of Materials Used in Packages through Digital Image Correlation". Proceedings of IPACK 2005, ASME InterPACK 05, July 2005, pp 1 – 8.

24. Development of a Digital Image Measurement System. National Aeronautics and Space Agency Scientific and Technical Information Site. 12 March 2008. < http://www.sti.nasa.gov/tto/Spinoff2004/p_9.html>

25. S. Adapa, "Evaluation of Friction Stir Weld Samples Using Digital Image Correlation" (MS thesis, Southern Illinois University Carbondale, 2006)

26. United States. Department of Defense. Military Handbook 5H, Change Notice 1: Metallic Materials and Elements for Aerospace Vehicle Structures. Washington: Department of the Air Force, October 2001.

27. Instron. 2007. *BlueHill 2*. Norwood, Massachusetts.

28. Kenneth E. Perry. Bainbridge Island, Washington: EchoBio.

29. National Instruments. 2008. *LabVIEW, version 8.5*. Austin, Texas

30. Irfan Skiljan. 2007. *IrfanView, version 4.10*. Jajce, Bosnia

31. Correlated Solutions, Inc. 2006. *VIC 2D, version 4.4.2*. Columbia, South Carolina

32. Dassualt Systemes. 2007. *ABAQUS, version 6.7.1*. Providence, Rhode Island: SIMULIA

Appendix A: Digital Image Correlation Data

7. TAG DIC 1: test article B

Reference Image	Post Test Image	Global Stress-Strain Behavior of Specimen
		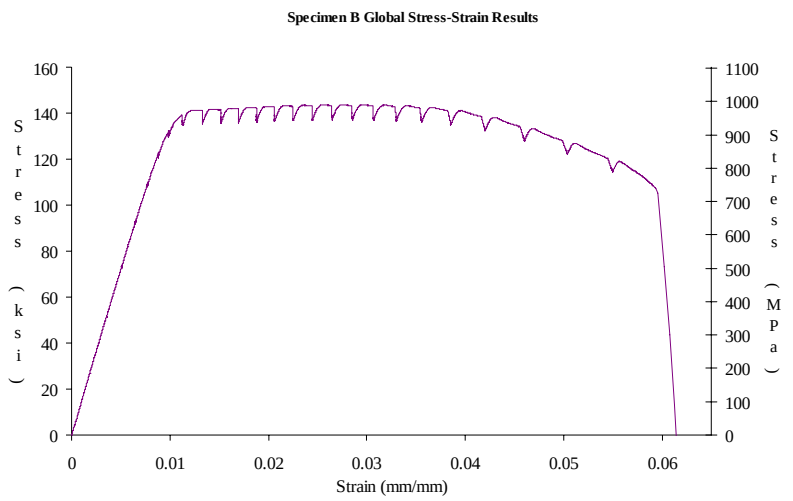 Reference Load (T): 256.8 lbf (1142 N) Reference Stress (σ): 51.8 ksi (357 MPa) Reference Extensometer Strain (ε_{EXT}): 0.00357

Raw Image	e_{yy} Contour	TAG DIC 1
		e_{yy} (Point 0 = Top of Gage; Point 100 = Bottom of Gage)
		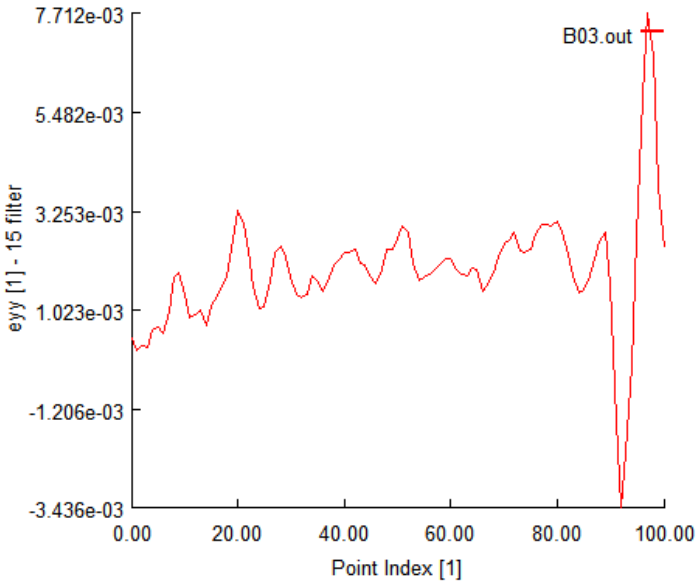
Step	3	T: 256.8 lbf (1142N); σ: 51.78 ksi (357 MPa) e_{EXT}: 0.00354
		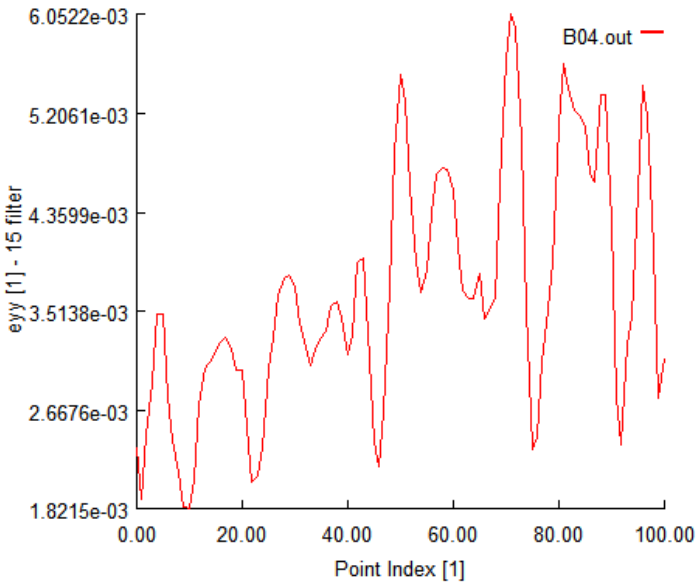
Step	4	T: 367.6 lbf (1635N); σ: 74.1 ksi (511 MPa) e_{EXT}: 0.00515

Raw Image	e_{yy} Contour	TAG DIC 1
		e_{yy} (Point 0 = Top of Gage; Point 100 = Bottom of Gage)
	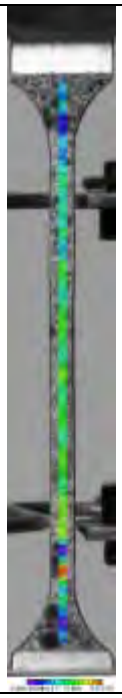	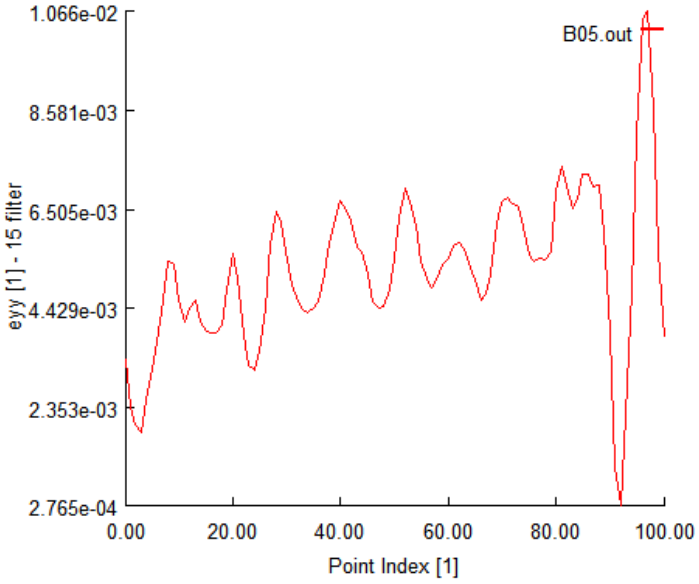
Step	5	T: 464.1 lbf (2064N); σ: 93.6 ksi (645 MPa) e_{EXT}: 0.00655
		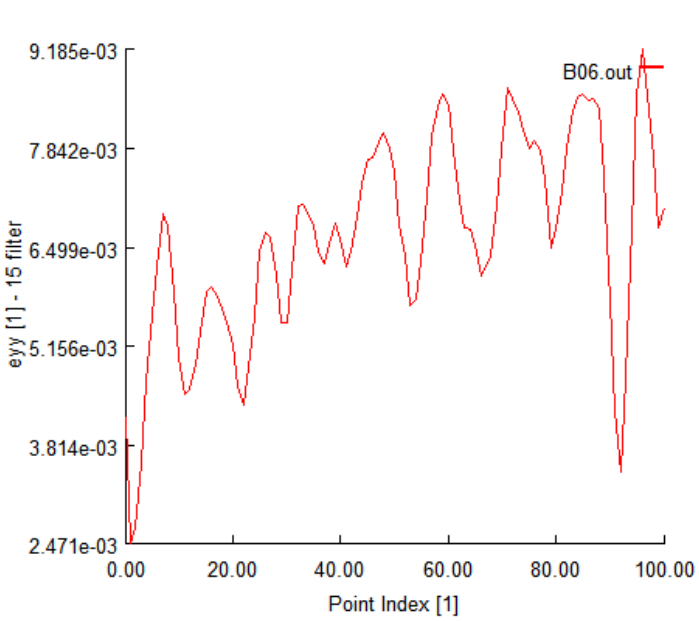
Step	6	T: 545.9 lbf (2428 N); σ: 110.1 ksi (759 MPa) e_{EXT}: 0.00779

Raw Image	e_{yy} Contour	TAG DIC 1
		e_{yy} (Point 0 = Top of Gage; Point 100 = Bottom of Gage)
		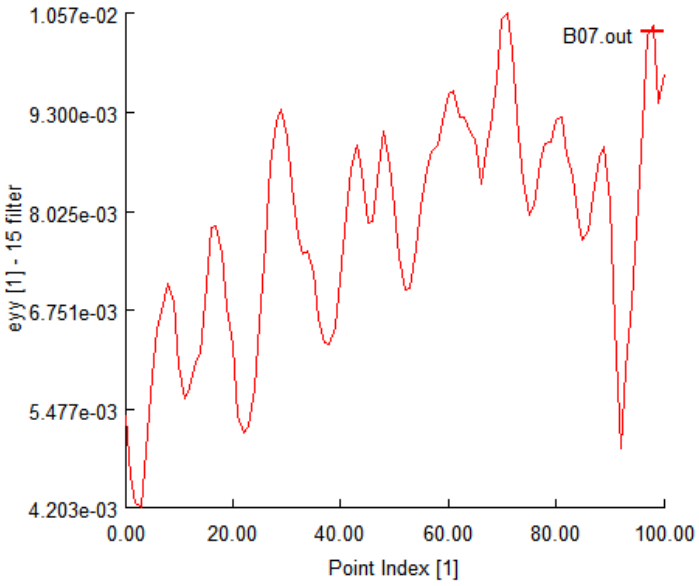
Step	7	T: 610.3 lbf (2715N); σ: 123.1 ksi (848 MPa) e_{EXT}: 0.00888
		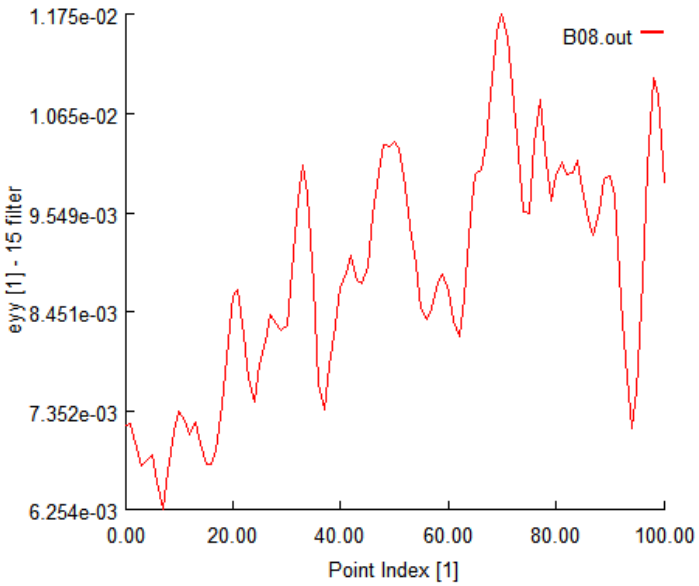
Step	8	T: 657.7 lbf (2925N); σ: 132.6 ksi (914 MPa) e_{EXT}: 0.00993

Raw Image	e_{yy} Contour	TAG DIC 1
		e_{yy} (Point 0 = Top of Gage; Point 100 = Bottom of Gage)
		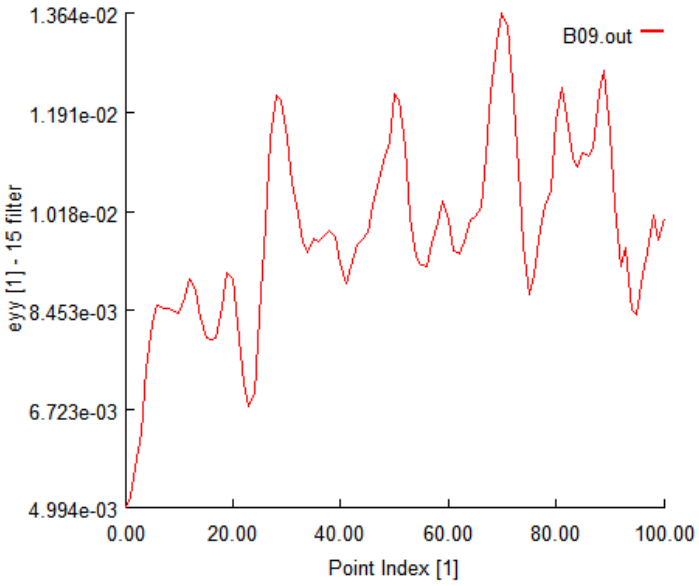
Step	9	T: 690.5 lbf (3072N); σ: 139.2 ksi (960 MPa) e_{EXT}: 0.01124
		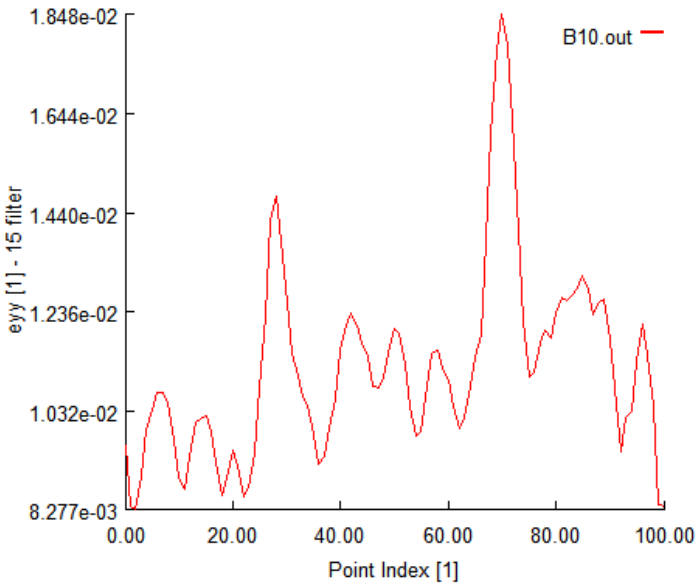
Step	10	T: 700.7 lbf (3117N); σ: 141.3 ksi (974 MPa) e_{EXT}: 0.01322

Raw Image	e_{yy} Contour	TAG DIC 1
		e_{yy} (Point 0 = Top of Gage; Point 100 = Bottom of Gage)
		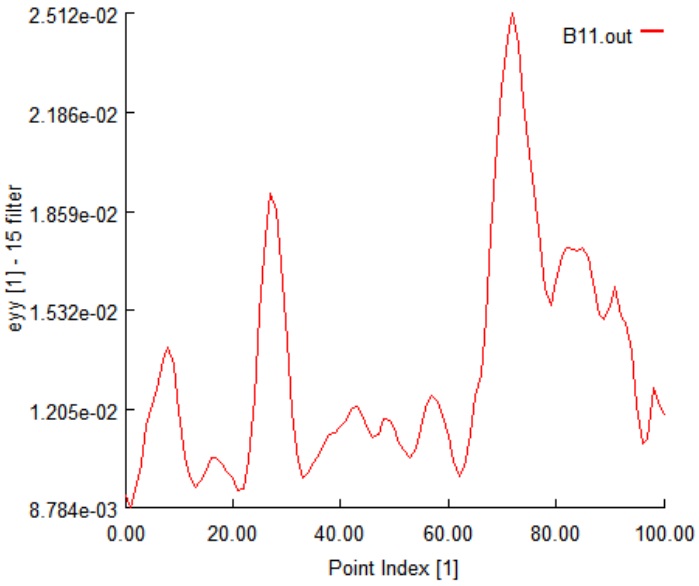
Step	11	T: 704.1 lbf (3132N); σ: 142.0 ksi (979 MPa) e_{EXT}: 0.01695
		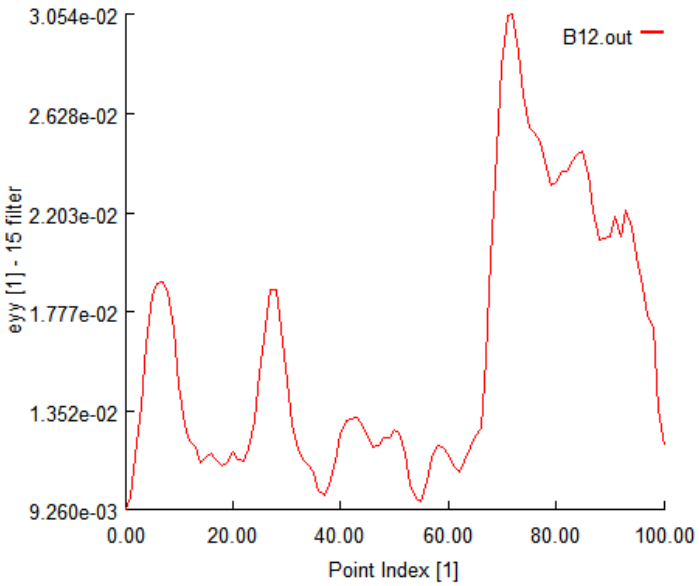
Step	12	T: 705.9 lbf (3140N); σ: 142.3 ksi (981 MPa) e_{EXT}: 0.01871

Raw Image	e_{yy} Contour	TAG DIC 1
		e_{yy} (Point 0 = Top of Gage; Point 100 = Bottom of Gage)
		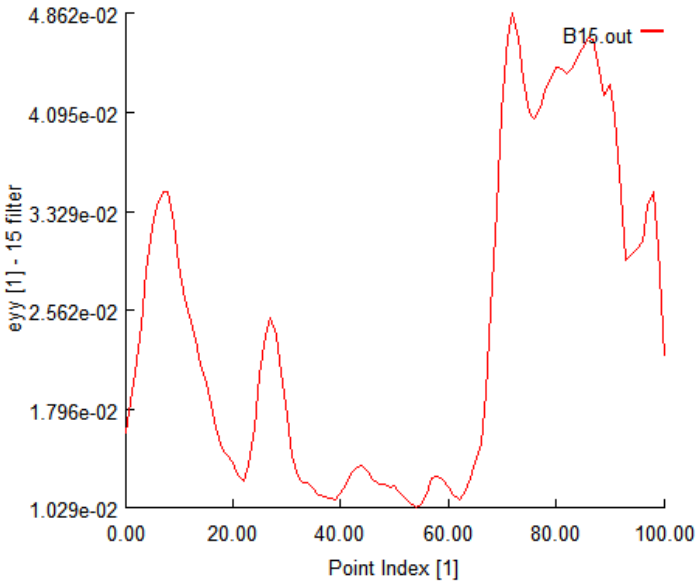
Step	15	T: 710.2 lbf (3159N); σ: 143.2 ksi (987 MPa) e_{EXT}: 0.02437
		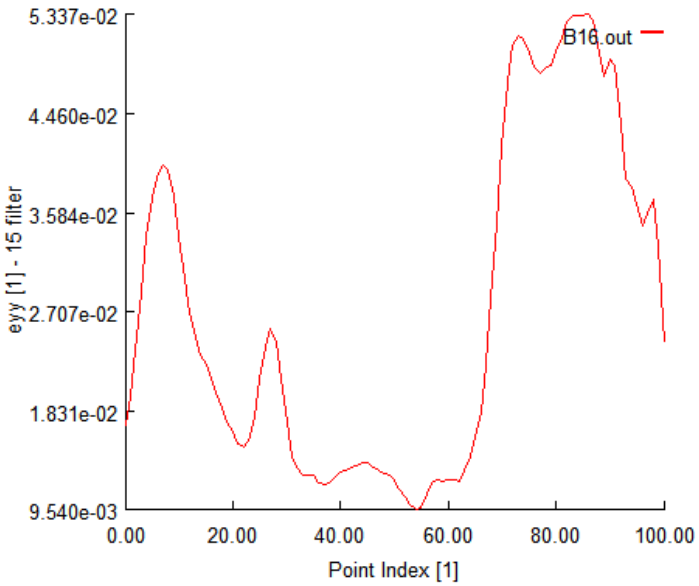
Step	16	T: 710.5 lbf (3160N); σ: 143.2 ksi (988 MPa) e_{EXT}: 0.02641

Raw Image	e_{yy} Contour	TAG DIC 1
		e_{yy} (Point 0 = Top of Gage; Point 100 = Bottom of Gage)
		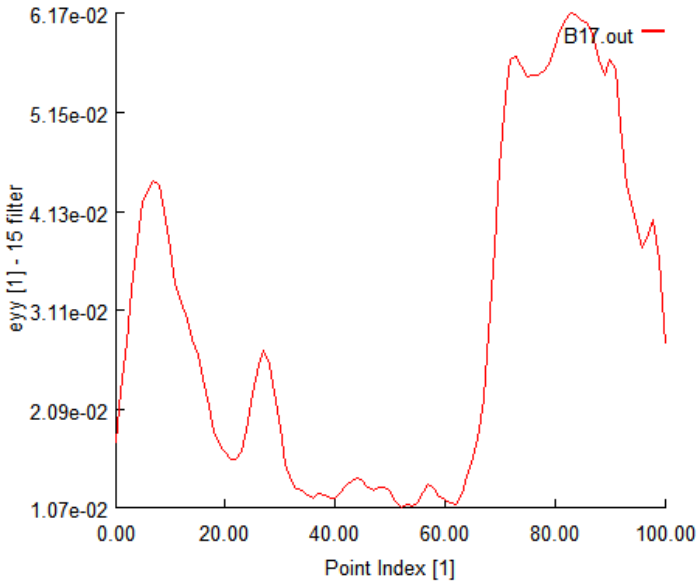
Step	17	T: 710.9 lbf (3162N); σ: 143.3 ksi (988 MPa) e_{EXT}: 0.02841
		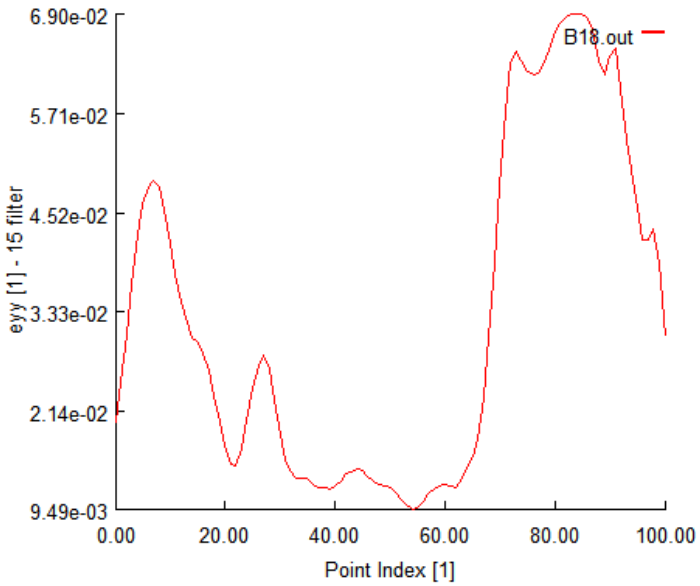
Step	18	T: 710.6 lbf (3161N); σ: 143.3 ksi (988 MPa) e_{EXT}: 0.03058

8. TAG DIC 2: test article C

Reference Image	Post Test Image	Global Stress-Strain Behavior of Specimen
		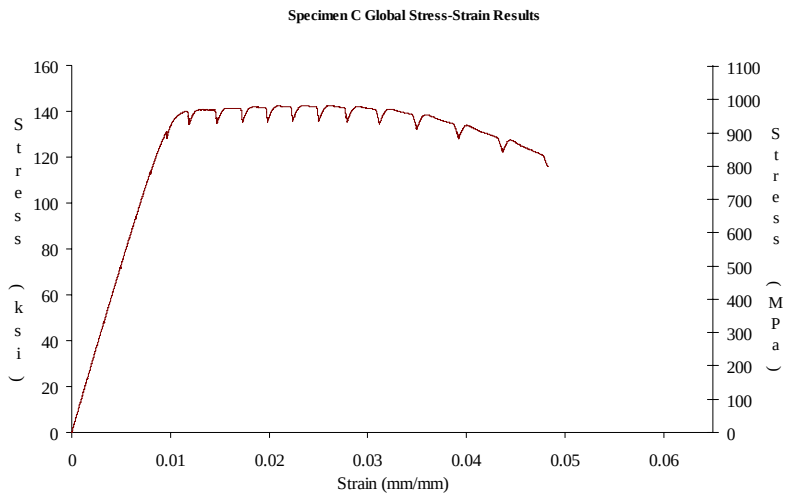 Reference Load (T): 240.5 lbf (1070 N) Reference Stress (σ): 48.5 ksi (334 MPa) Reference Extensometer Strain (ε_{EXT}): 0.00328

Raw Image	e_{yy} Contour	TAG DIC 2
		e_{yy} (Point 0 = Top of Gage; Point 100 = Bottom of Gage)
	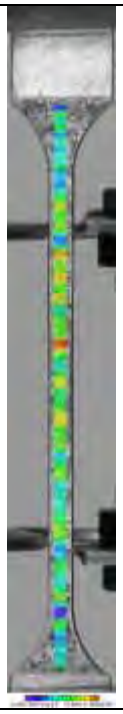	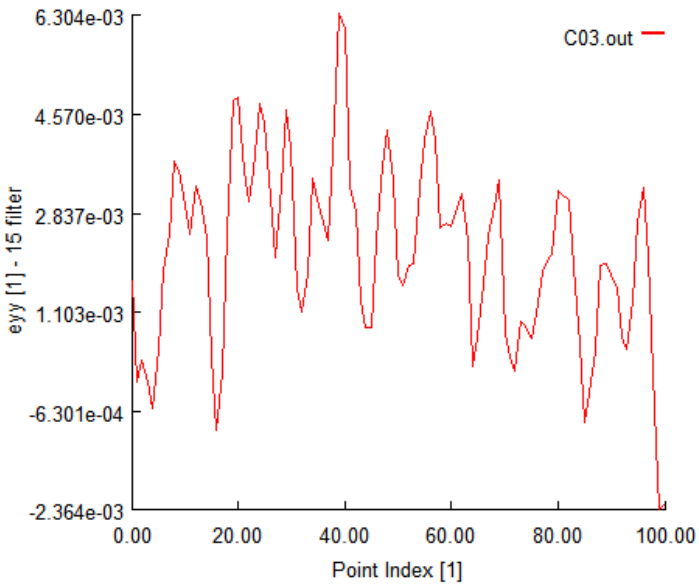
Load Step 3		T: 240.5 lbf (1070N); σ: 48.5 ksi (334 MPa) e_{EXT}: 0.00328
	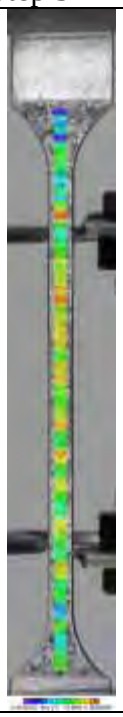	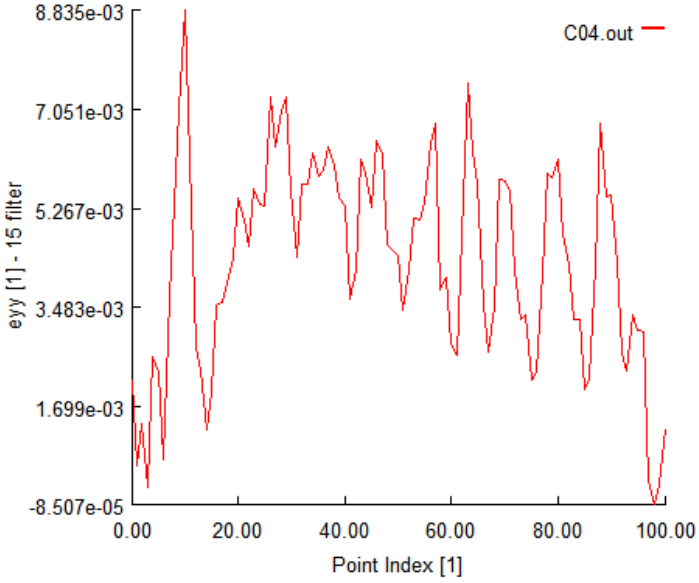
Load Step 4		T: 358.4 lbf (1594N); σ: 72.3 ksi (489 Mpa) e_{EXT}: 0.00495

Raw Image	e_{yy} Contour	TAG DIC 2
		e_{yy} (Point 0 = Top of Gage; Point 100 = Bottom of Gage)
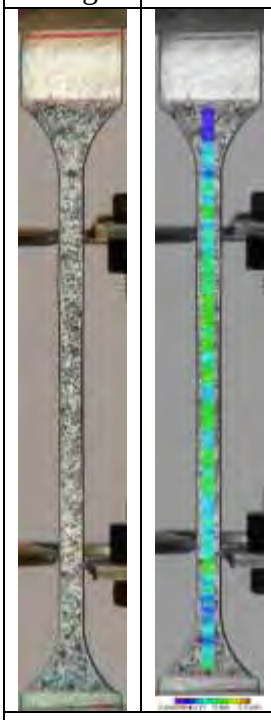		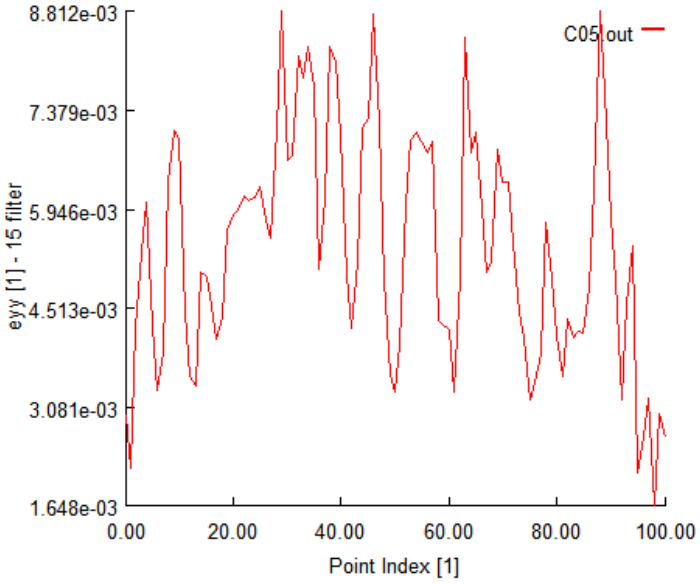
Load Step 5		T: 468.1 lbf (2082N); σ: 94.4 ksi (651 Mpa) e_{EXT}: 0.00653
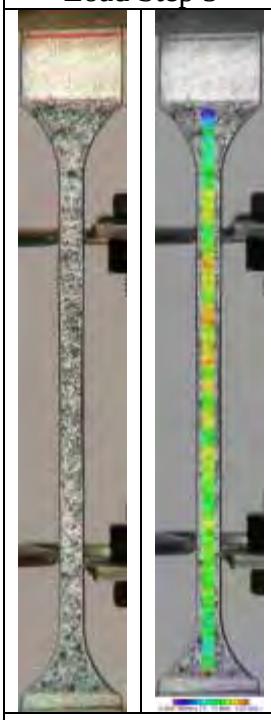		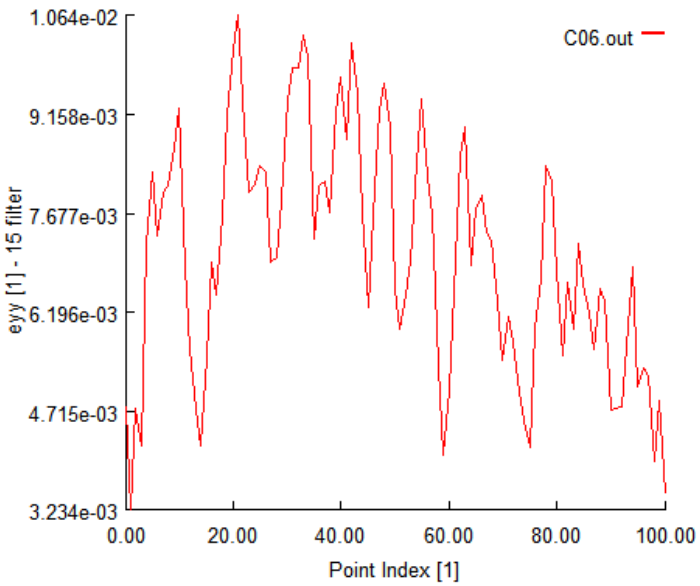
Load Step 6		T:566.7 lbf (2521N); σ: 114.3 ksi (788 Mpa) e_{EXT}: 0.00804

Raw Image	e_{yy} Contour	TAG DIC 2
		e_{yy} (Point 0 = Top of Gage; Point 100 = Bottom of Gage)
	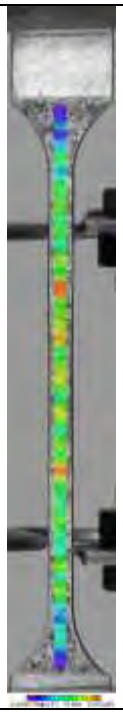	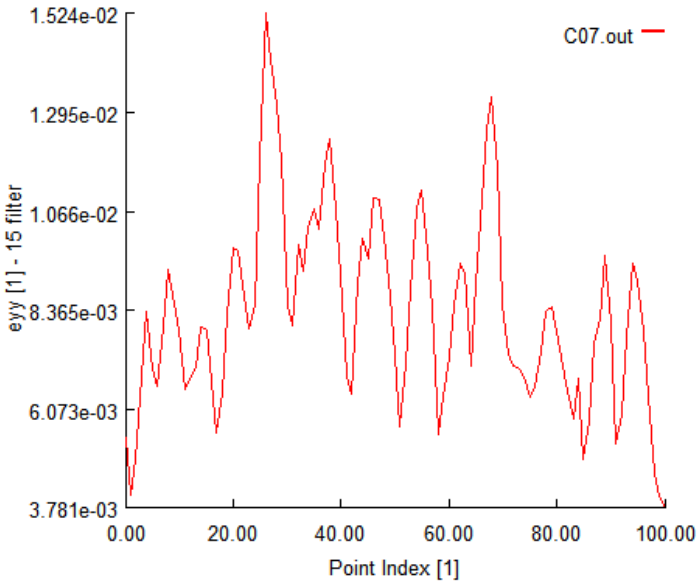
Load Step 7		T:650.4 lbf (2893N); σ: 131.1 ksi (904 Mpa) e_{EXT}: 0.00962
		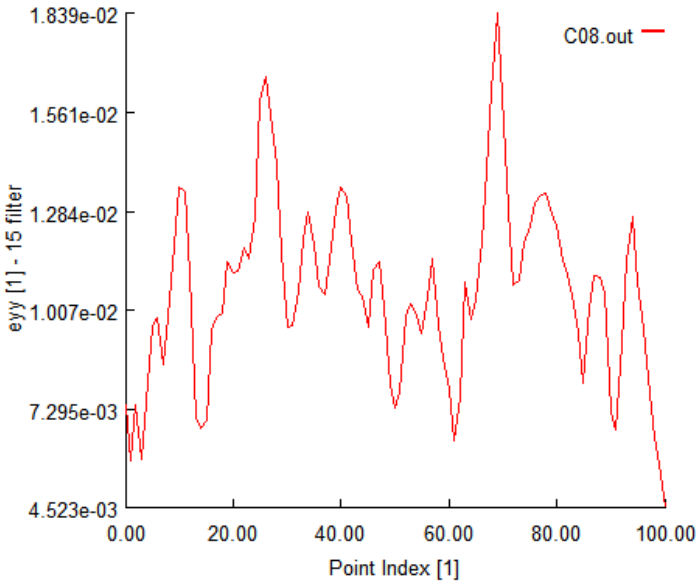
Load Step 8		T:694.8 lbf (3091N); σ: 140.1 ksi (966 Mpa) e_{EXT}: 0.01172

Raw Image	e_{yy} Contour	TAG DIC 2
		e_{yy} (Point 0 = Top of Gage; Point 100 = Bottom of Gage)
		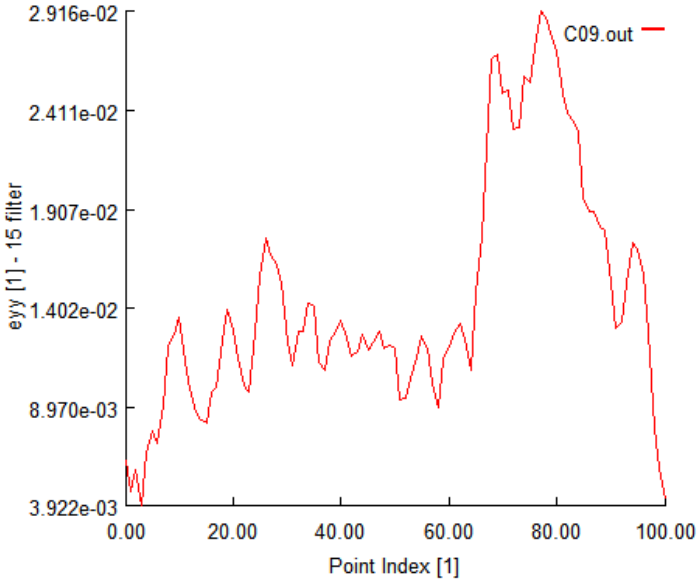
Load Step 9		T:697.8 lbf (3104N); σ: 140.7 ksi (970 Mpa) e_{EXT}: 0.01449
		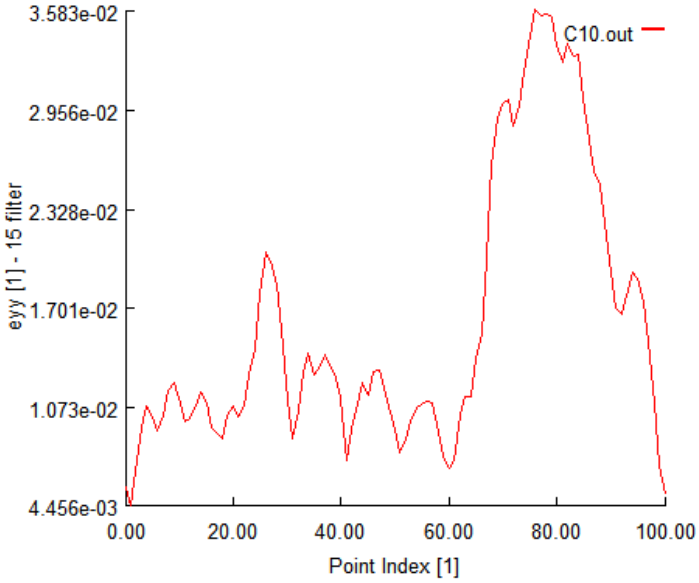
Load Step 10		T:700.1 lbf (3114N); σ: 141.2 ksi (973 Mpa) e_{EXT}: 0.01714

Raw Image	e_{yy} Contour	TAG DIC 2
		e_{yy} (Point 0 = Top of Gage; Point 100 = Bottom of Gage)
		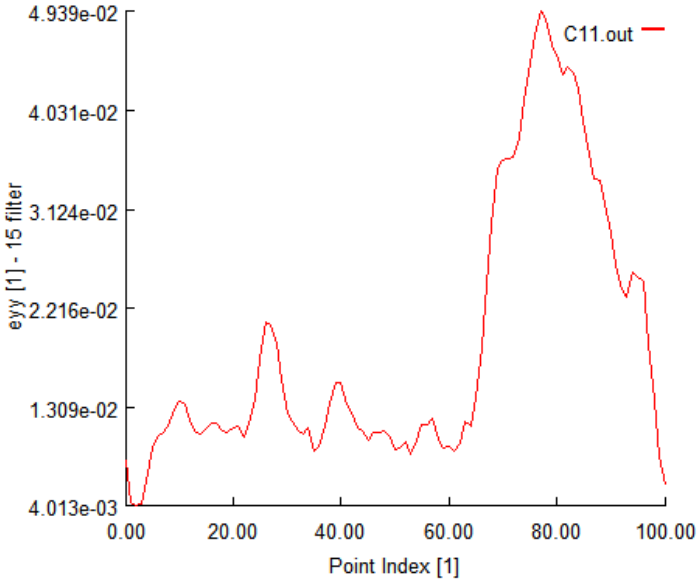
Load Step 11		T:702.4 lbf (3124N); σ: 141.6 ksi (976 Mpa) e_{EXT}: 0.01959
		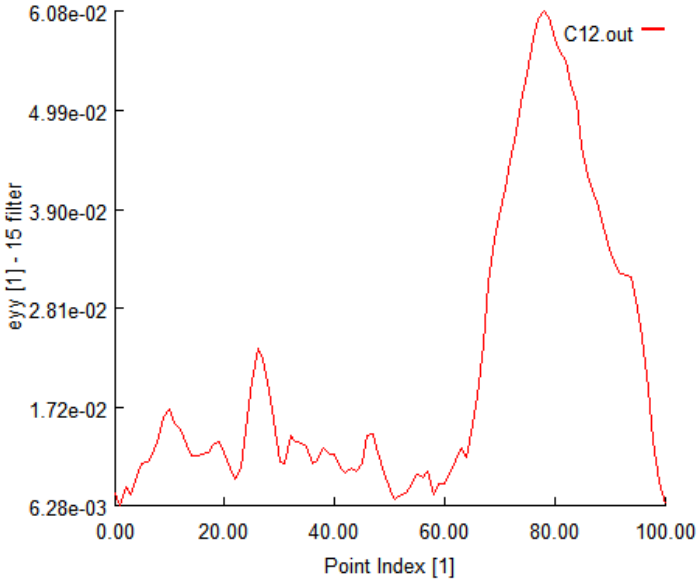
Load Step 12		T:703.8 lbf (3131N); σ: 141.9 ksi (978 Mpa) e_{EXT}: 0.002211

Raw Image	e_{yy} Contour	TAG DIC 2
		e_{yy} (Point 0 = Top of Gage; Point 100 = Bottom of Gage)
		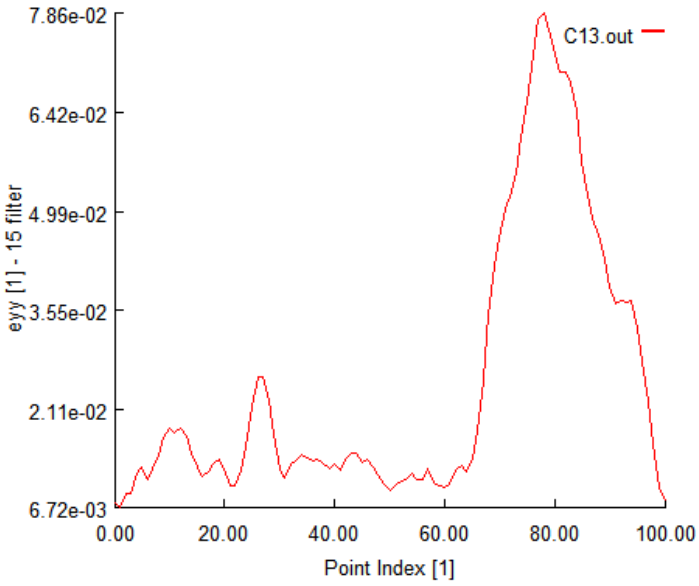
Load Step 13		T:703.8 lbf (3131N); σ: 141.9 ksi (978 Mpa) e_{EXT}: 0.02479
		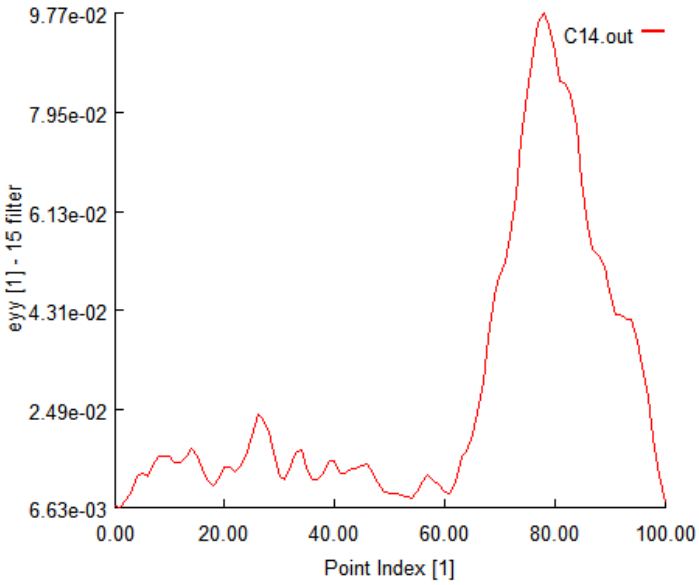
Load Step 14		T:702.8 lbf (3126N); σ: 141.7 ksi (977 Mpa) e_{EXT}: 0.02757

Raw Image	e_{yy} Contour	TAG DIC 2
		e_{yy} (Point 0 = Top of Gage; Point 100 = Bottom of Gage)
		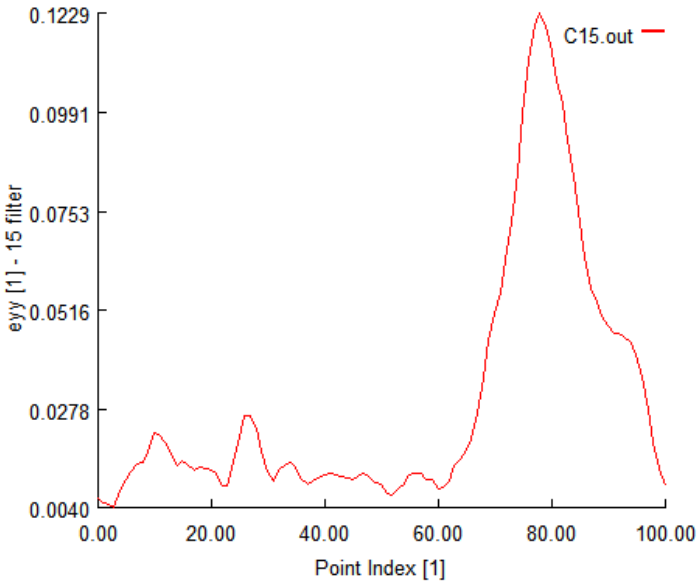
Load Step 15		T:698.7 lbf (3108N); σ: 140.9 ksi (971 Mpa) e_{EXT}: 0.03070
		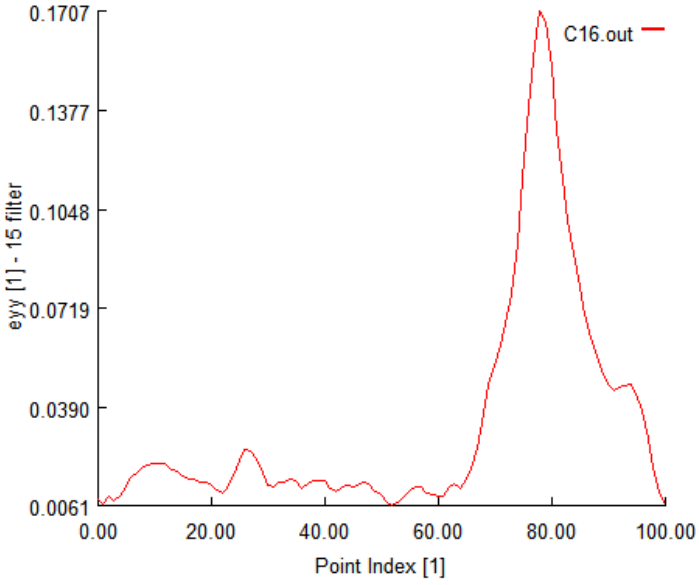
Load Step 16		T:688.8 lbf (3064N); σ: 138.9 ksi (957 Mpa) e_{EXT}: 0.03430

Raw Image	e_{yy} Contour	TAG DIC 2
		e_{yy} (Point 0 = Top of Gage; Point 100 = Bottom of Gage)
		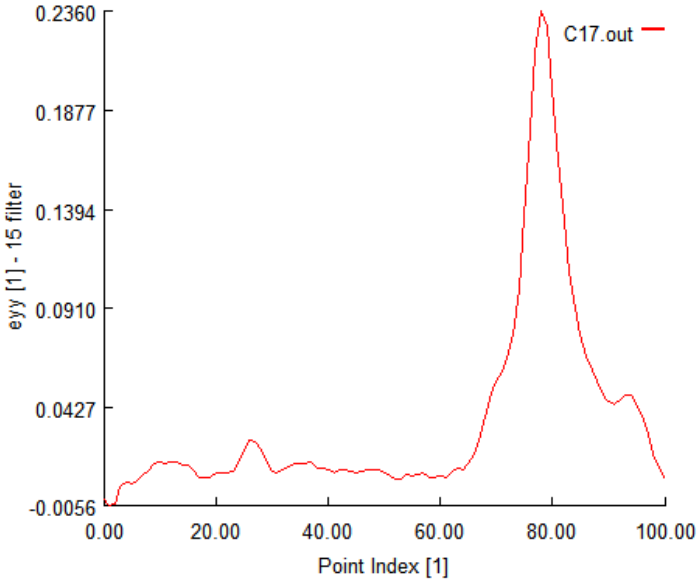
Load Step 17		T:668.6 lbf (2974N); σ: 134.8 ksi (929 Mpa) e_{EXT}: 0.03848
		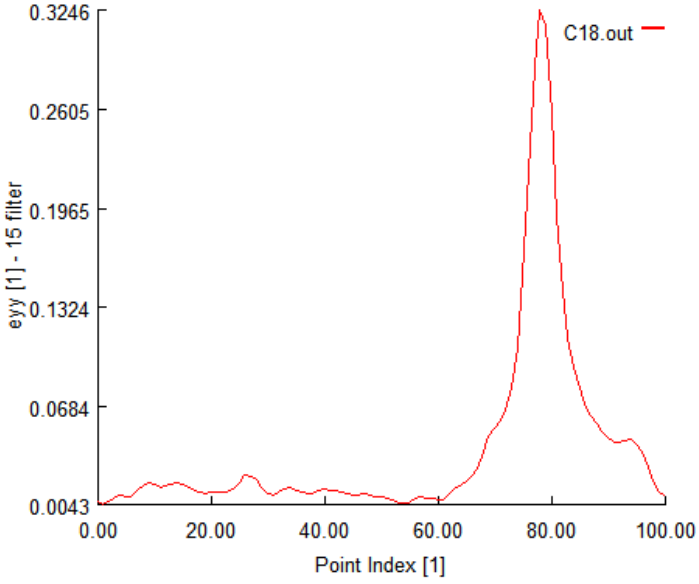
Load Step 18		T:639.2 lbf (2843N); σ: 128.9 ksi (889 Mpa) e_{EXT}: 0.04294

Raw Image	e_{yy} Contour	TAG DIC 2
		e_{yy} (Point 0 = Top of Gage; Point 100 = Bottom of Gage)
		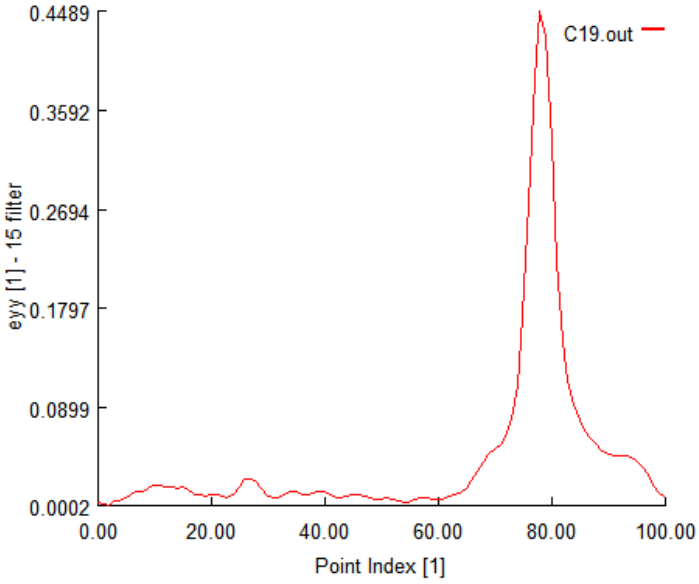
Load Step 19		T:601.1 lbf (2674N); σ: 121.2 ksi (836 Mpa) e_{EXT}: 0.04755

9. TAG DIC 3: test article E

Reference Image	Post Test Image	Global Stress-Strain Behavior of Specimen
		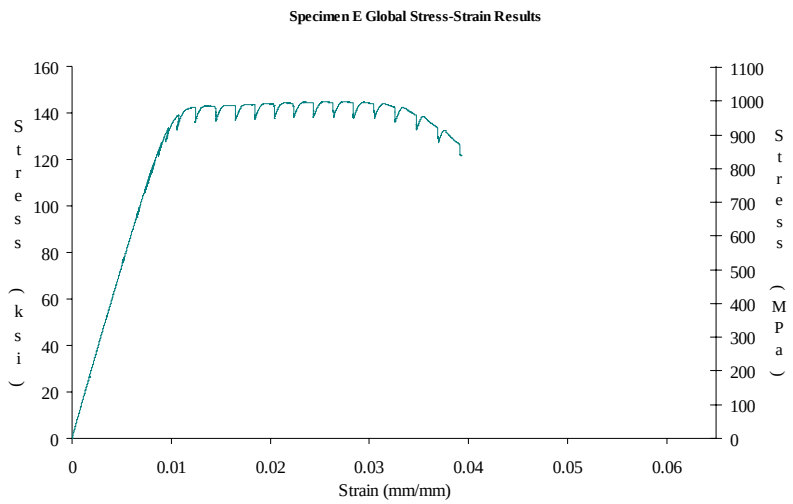 Reference Load (T): 0 lbf (0 N) Reference Stress (σ): 0 ksi (0 MPa) Reference Extensometer Strain (ε_{EXT}): 0

Raw Image	e_{yy} Contour	TAG DIC 3
		e_{yy} (Point 0 = Top of Gage; Point 100 = Bottom of Gage)
	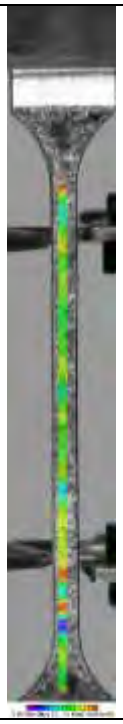	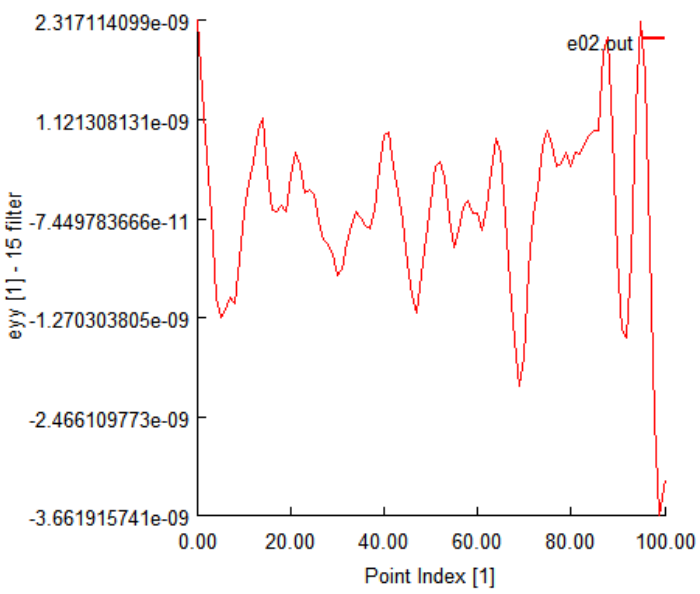
Load Step 2		T:133.2 lbf (593N); σ: 22.9 ksi (185 Mpa) e_{EXT}: 0.00176
		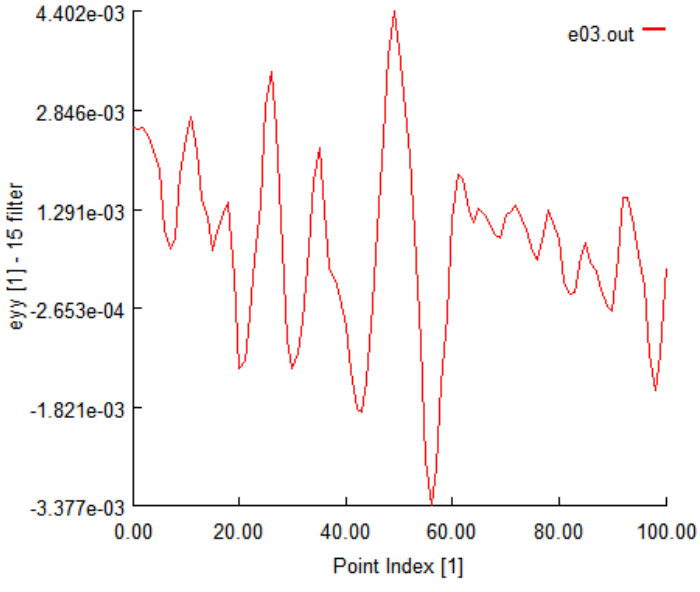
Load Step 3		T:263.2 lbf (1171N); σ: 53.1 ksi (366 Mpa) e_{EXT}: 0.00354

Raw Image	e_{yy} Contour	TAG DIC 3
		e_{yy} (Point 0 = Top of Gage; Point 100 = Bottom of Gage)
		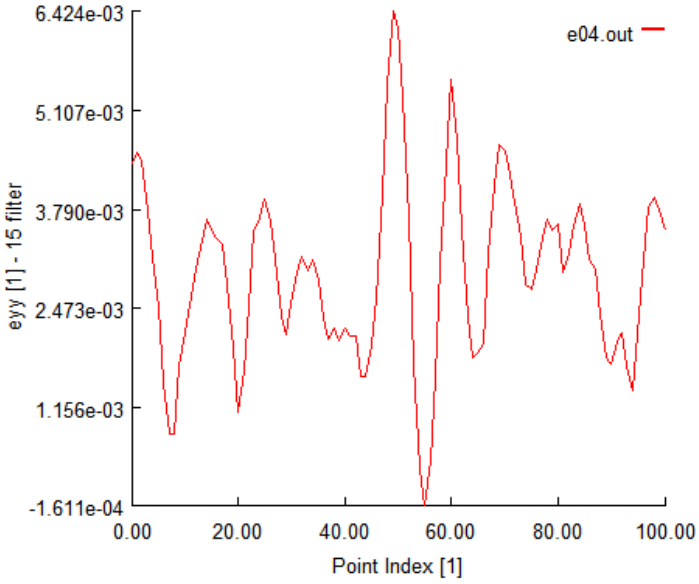
Load Step 4		T:384.6 lbf (1711N); σ: 77.5 ksi (534.6 Mpa) e_{EXT}: 0.00525
		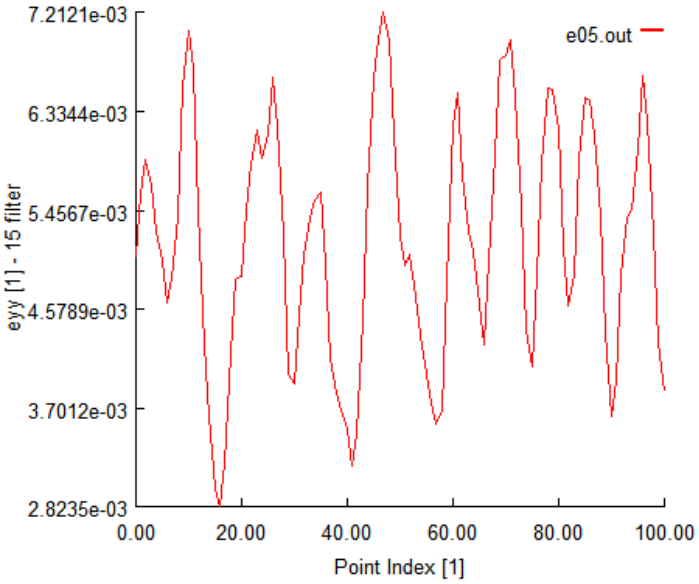
Load Step 5		T:491.1 lbf (2185N); σ: 99.0 ksi (683 Mpa) e_{EXT}: 0.00678

Raw Image	e_{yy} Contour	TAG DIC 3
		e_{yy} (Point 0 = Top of Gage; Point 100 = Bottom of Gage)
		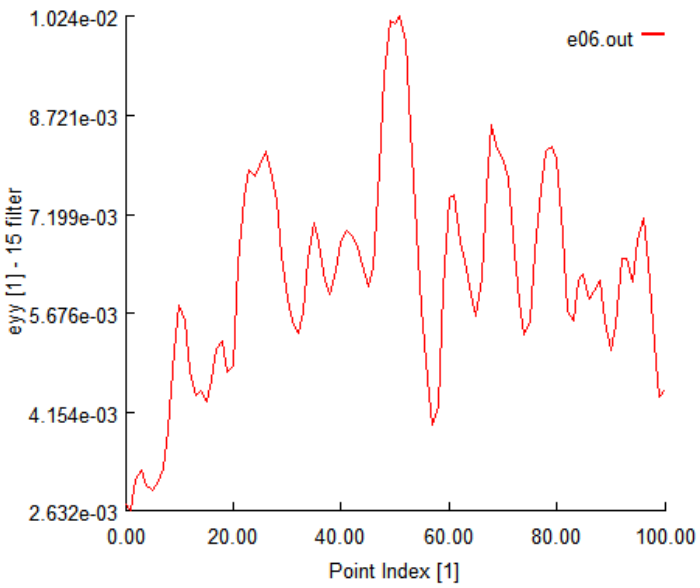
Step	6	T:558.6 lbf (2485N); σ: 112.6 ksi (777 Mpa) e_{EXT}: 0.0078
		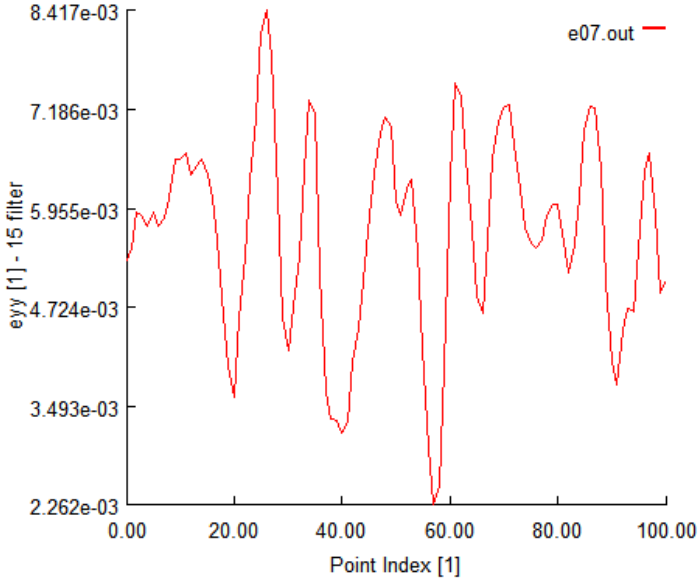
Load Step 7		T:562.6 lbf (2502N); σ: 113.4 ksi (792 Mpa) e_{EXT}: 0.00789

Raw Image	e_{yy} Contour	TAG DIC 3
		e_{yy} (Point 0 = Top of Gage; Point 100 = Bottom of Gage)
	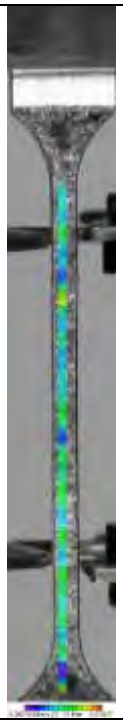	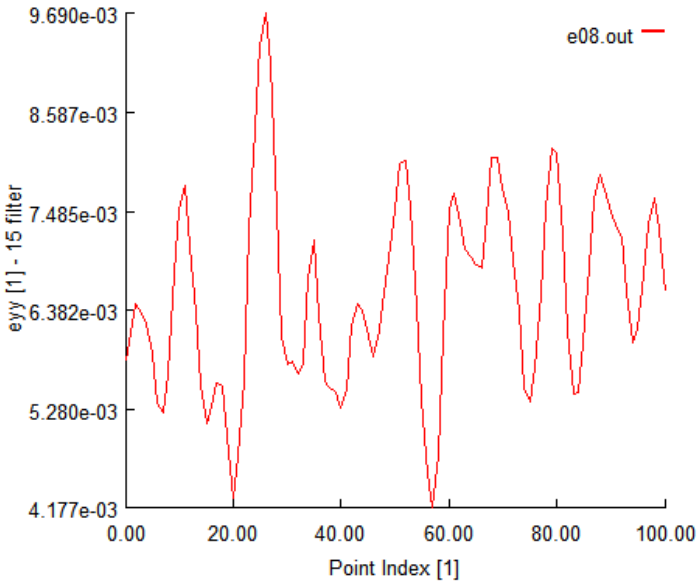
Load Step 8		T:593.6 lbf (2641N); σ: 119.7 ksi (825 Mpa) e_{EXT}: 0.00837
		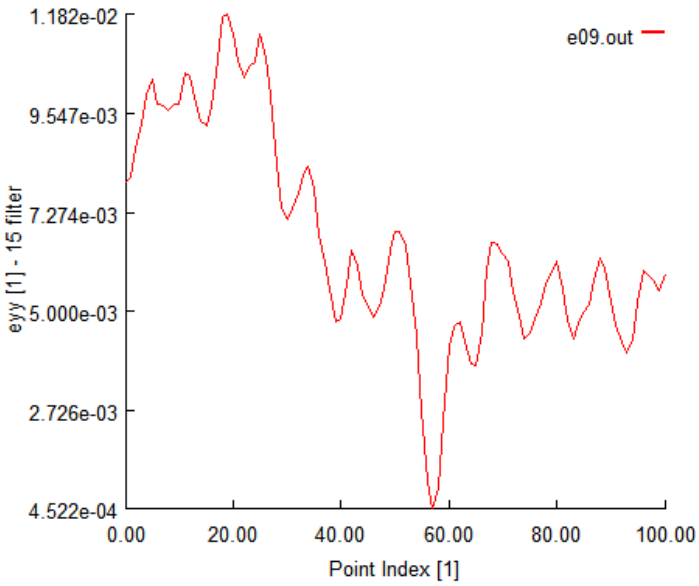
Load Step 9		T:631.6 lbf (2809N); σ: 127.3 ksi (878 Mpa) e_{EXT}: 0.00906

Raw Image	e_{yy} Contour	TAG DIC 3
		e_{yy} (Point 0 = Top of Gage; Point 100 = Bottom of Gage)
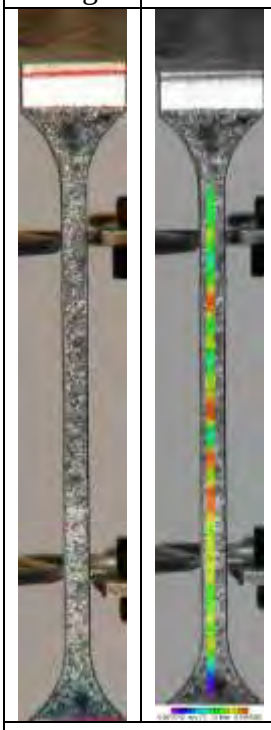		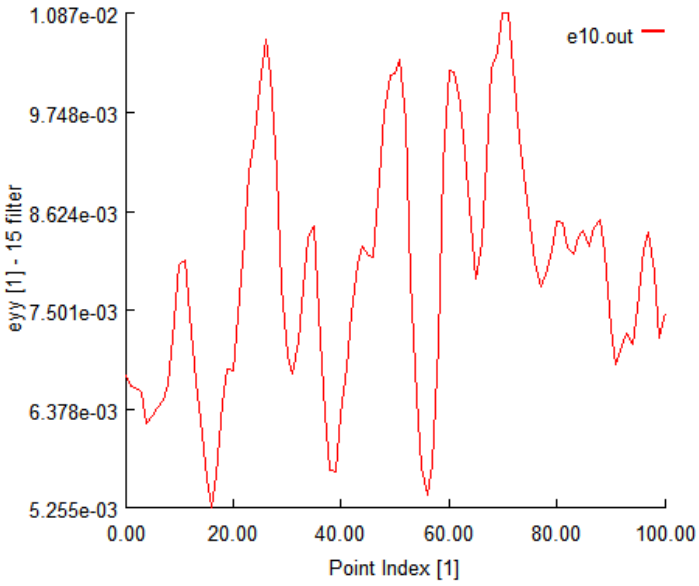
Load Step 10		T:662.5 lbf (2947N); σ: 133.6 ksi (921 Mpa) e_{EXT}: 0.00977
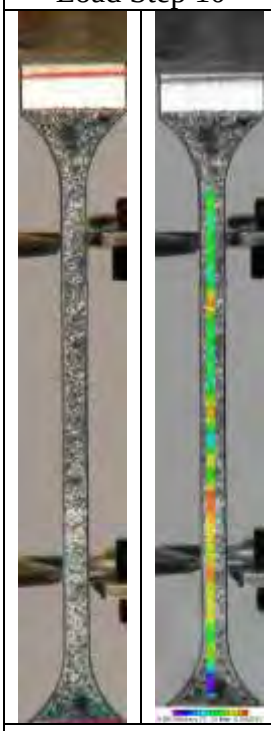		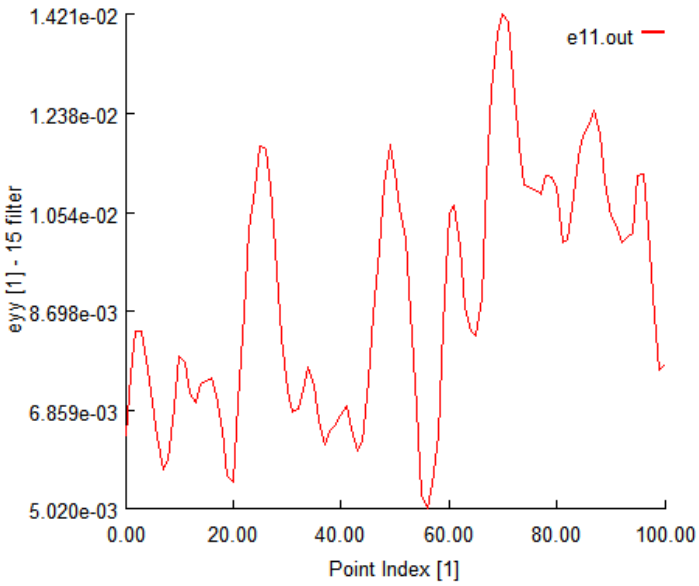
Load Step 11		T:690.4 lbf (3071N); σ: 139.2 ksi (960 Mpa) e_{EXT}: 0.01078

Raw Image	e_{yy} Contour	TAG DIC 3
		e_{yy} (Point 0 = Top of Gage; Point 100 = Bottom of Gage)
		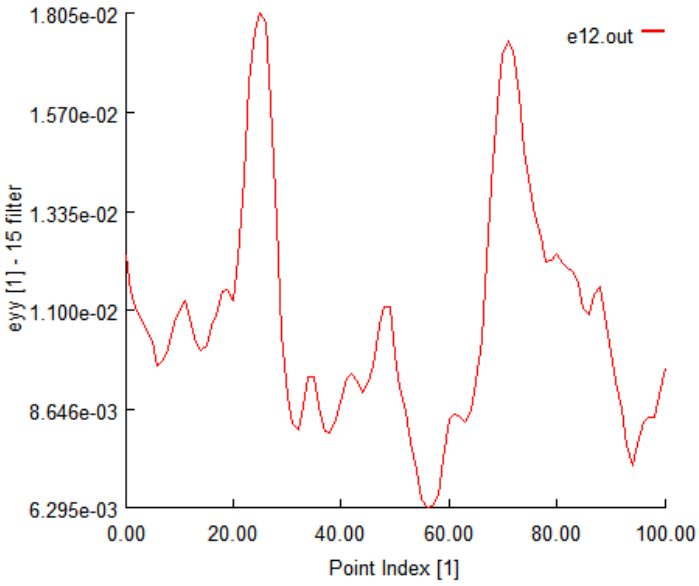
Load Step 12		T:706.7 lbf (3143N); σ: 142.5 ksi (982 Mpa) e_{EXT}: 0.01239
		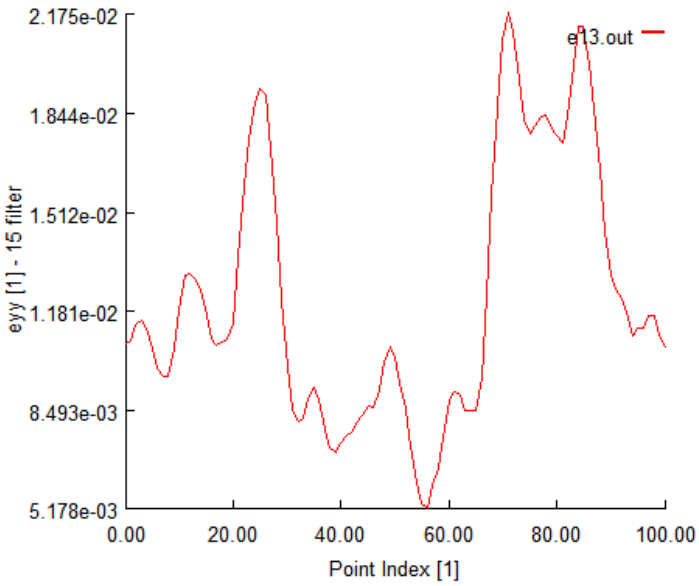
Load Step 13		T:709.0 lbf (3154N); σ: 142.9 ksi (985 Mpa) e_{EXT}: 0.01437

Raw Image	e_{yy} Contour	TAG DIC 3
		e_{yy} (Point 0 = Top of Gage; Point 100 = Bottom of Gage)
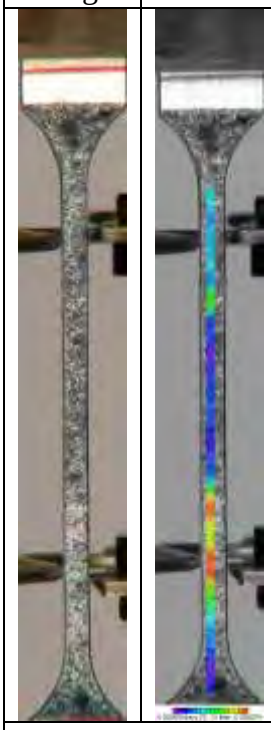		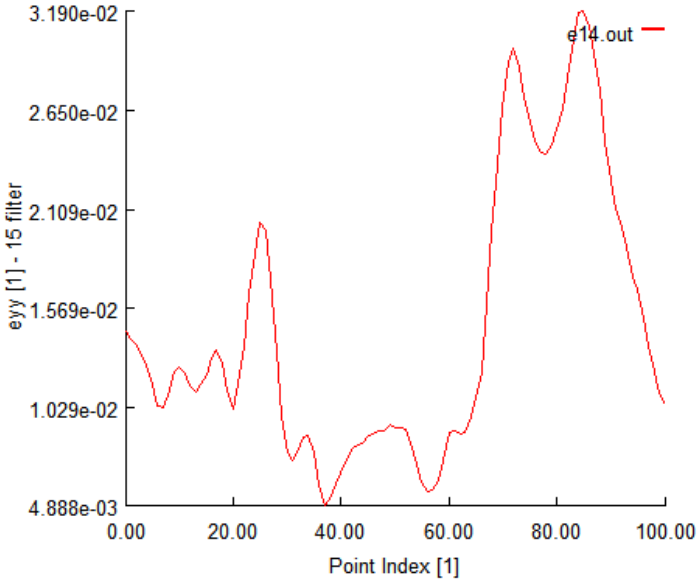
Load Step 14		T:710.3 lbf (3160N); σ: 143.2 ksi (987 Mpa) e_{EXT}: 0.01638
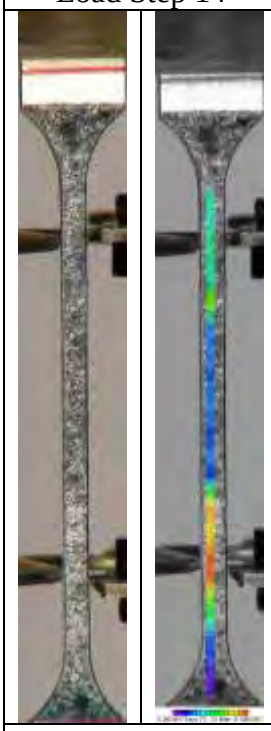		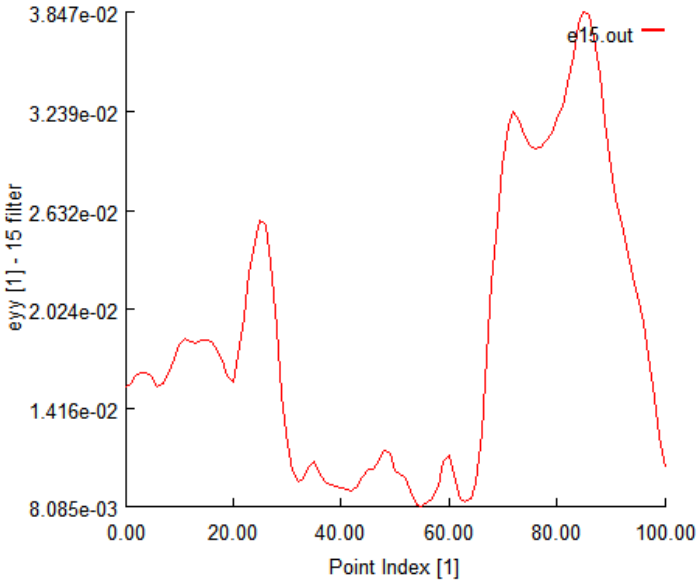
Load Step 15		T:712.0 lbf (3167N); σ: 143.6 ksi (990 Mpa) e_{EXT}: 0.01835

Raw Image	e_{yy} Contour	TAG DIC 3
		e_{yy} (Point 0 = Top of Gage; Point 100 = Bottom of Gage)
		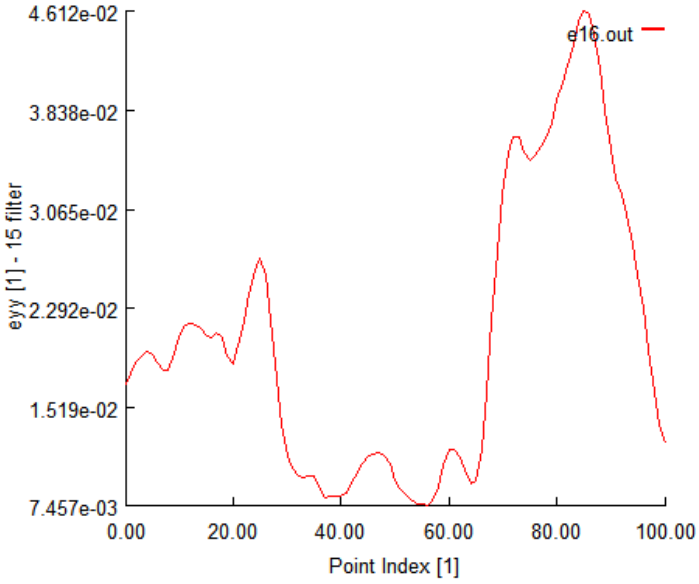
Load Step 16		T:713.4 lbf (3173N); σ: 143.8 ksi (992 Mpa) e_{EXT}: 0.02028
		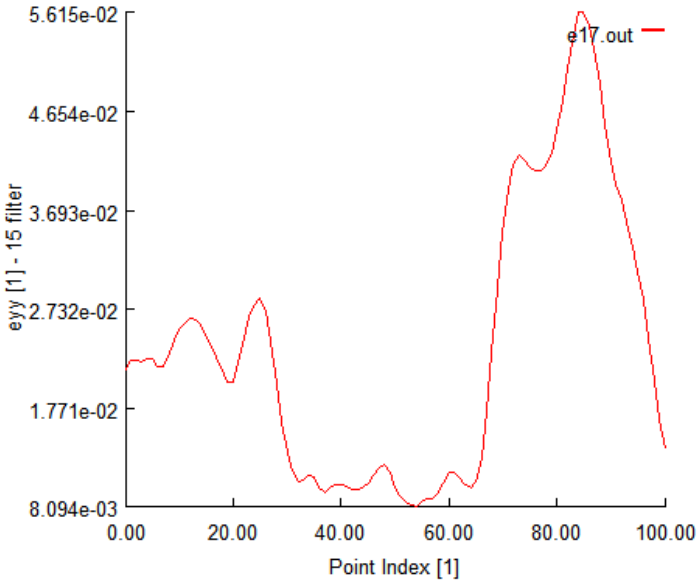
Load Step 17		T:715.0 lbf (3181N); σ: 144.2 ksi (994 Mpa) e_{EXT}: 0.02225

Raw Image	e_{yy} Contour	TAG DIC 3
		e_{yy} (Point 0 = Top of Gage; Point 100 = Bottom of Gage)
		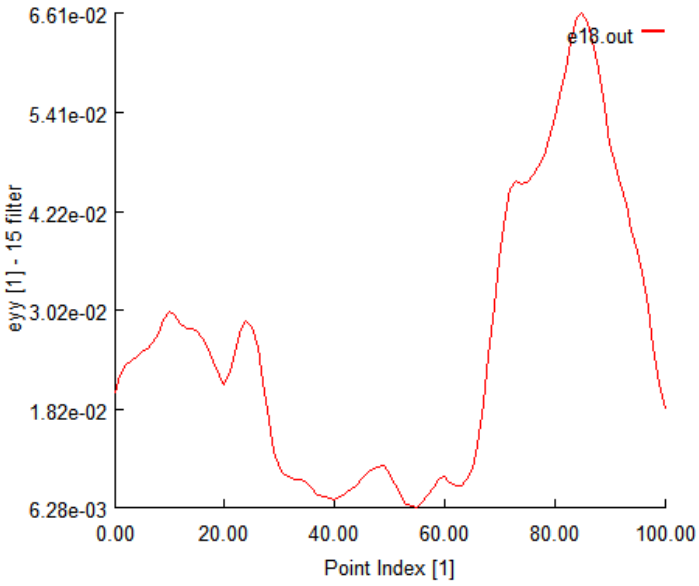
Load Step 18		T:716.1 lbf (3185N); σ: 144.4 ksi (995 Mpa) e_{EXT}: 0.02429
		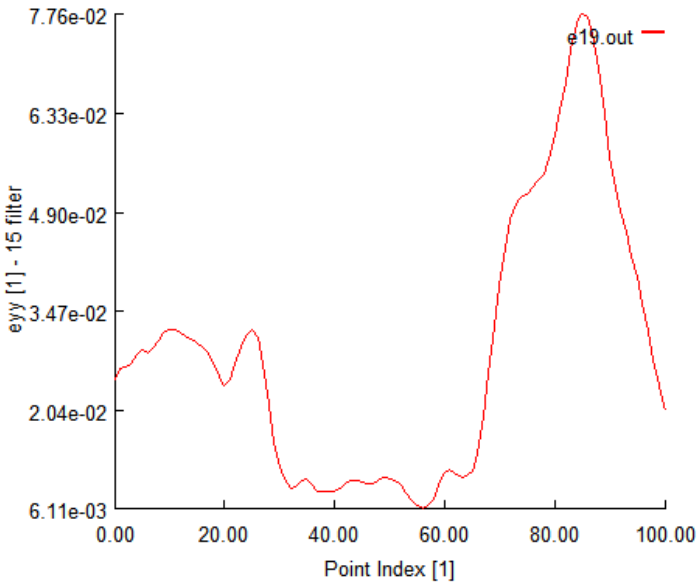
Load Step 19		T:716.8 lbf (3189N); σ: 144.5 ksi (996 Mpa) e_{EXT}: 0.02626

Raw Image	e_{yy} Contour	TAG DIC 3
		e_{yy} (Point 0 = Top of Gage; Point 100 = Bottom of Gage)
		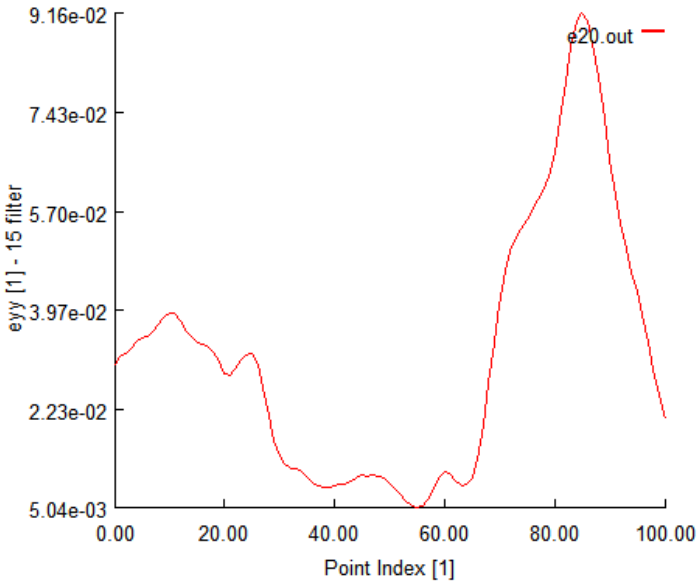
Load Step 20		T:716.3 lbf (3186N); σ: 144.4 ksi (996 Mpa) e_{EXT}: 0.02834
		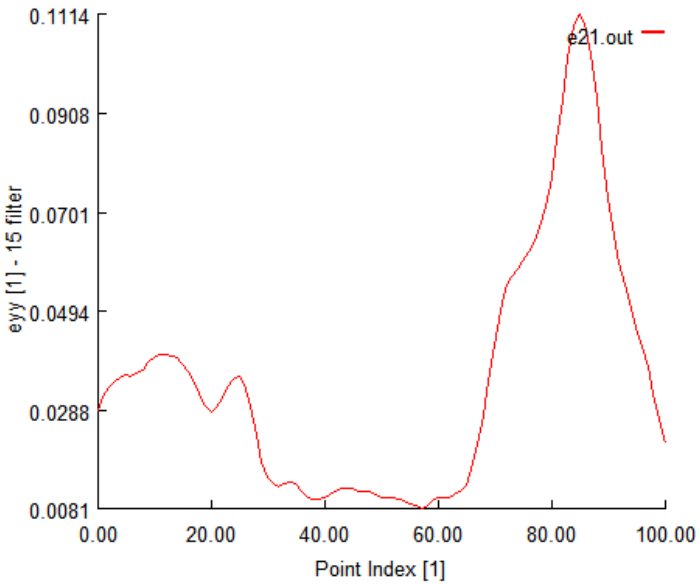
Load Step 21		T:713.9 lbf (3176N); σ: 143.9 ksi (992 Mpa) e_{EXT}: 0.03035

Raw Image	e_{yy} Contour	TAG DIC 3
		e_{yy} (Point 0 = Top of Gage; Point 100 = Bottom of Gage)
		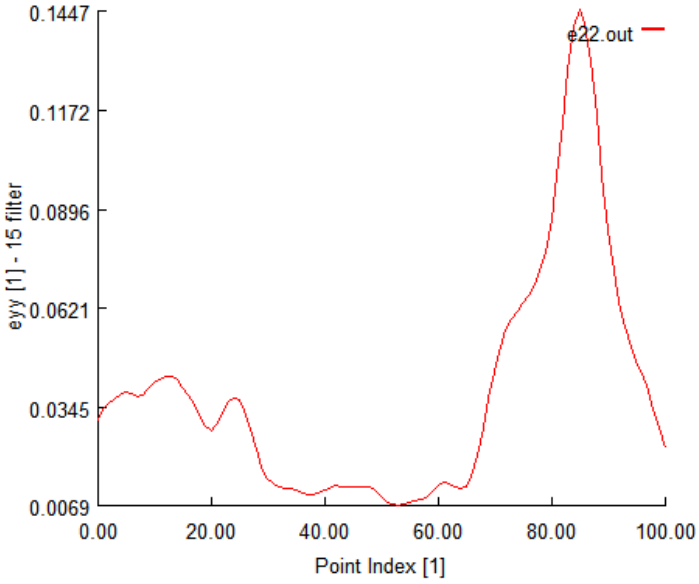
Load Step 22		T:707.3 lbf (3146N); σ: 142.6 ksi (983 Mpa) e_{EXT}: 0.03248
		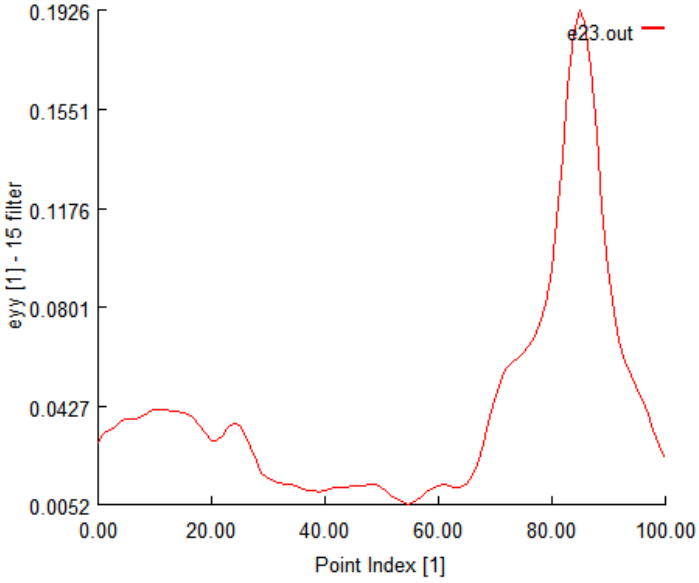
Load Step 23		T:691.2 lbf (3075N); σ: 139.4 ksi (961 Mpa) e_{EXT}: 0.03462

Raw Image	e_{yy} Contour	TAG DIC 3
		e_{yy} (Point 0 = Top of Gage; Point 100 = Bottom of Gage)
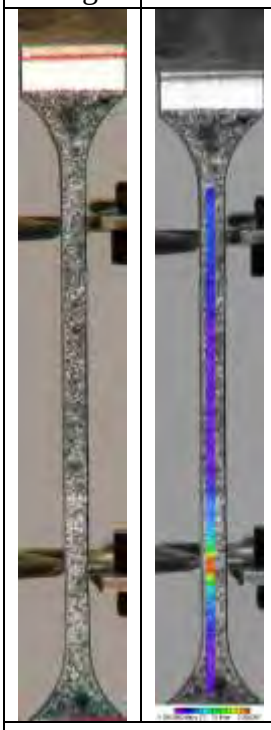		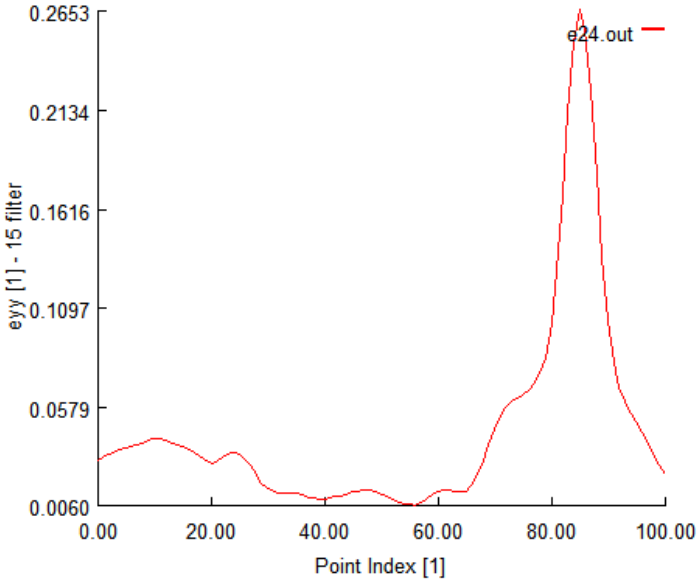
Load Step 24		T:664.5 lbf (2956N); σ: 134.0 ksi (924 Mpa) e_{EXT}: 0.03679
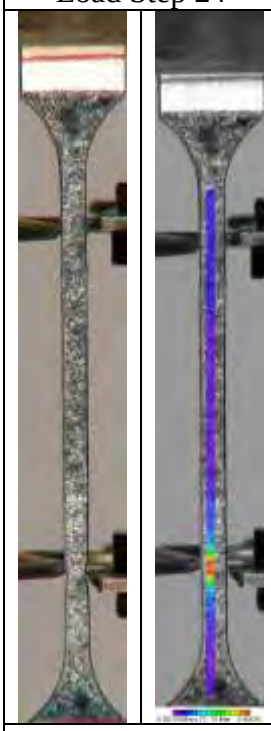		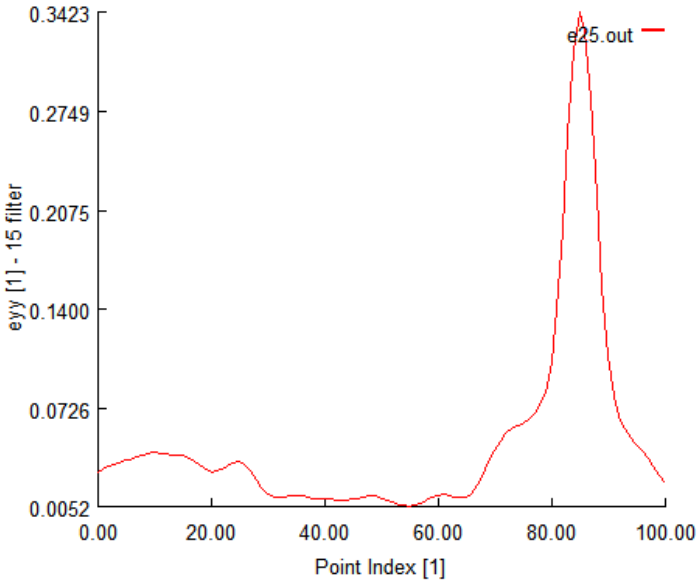
Load Step 25		T:628.4 lbf (2795N); σ: 126.7 ksi (874 Mpa) e_{EXT}: 0.03902

Raw Image	e_{yy} Contour	TAG DIC 3
		e_{yy} (Point 0 = Top of Gage; Point 100 = Bottom of Gage)
		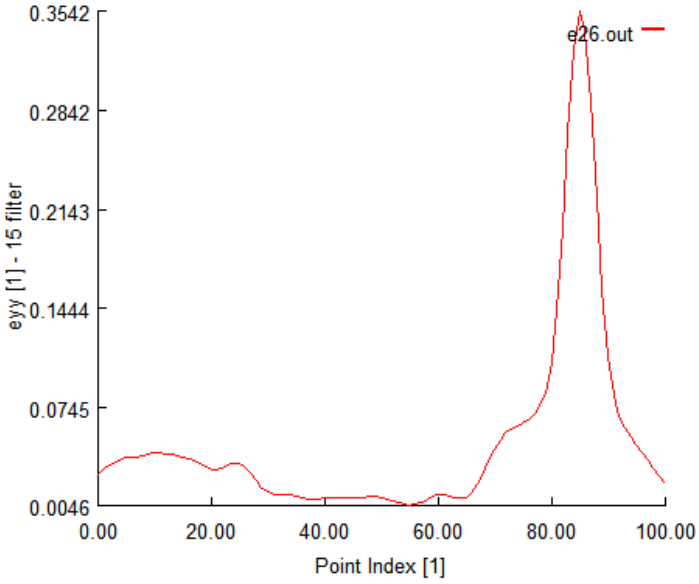
Load Step 26		T:603.2 lbf (2683N); σ: 121.6 ksi (838 Mpa) e_{EXT}: 0.03920

10. TAG DIC 4: test article F

Reference Image	Post Test Image	Global Stress Strain Behavior of Specimen
		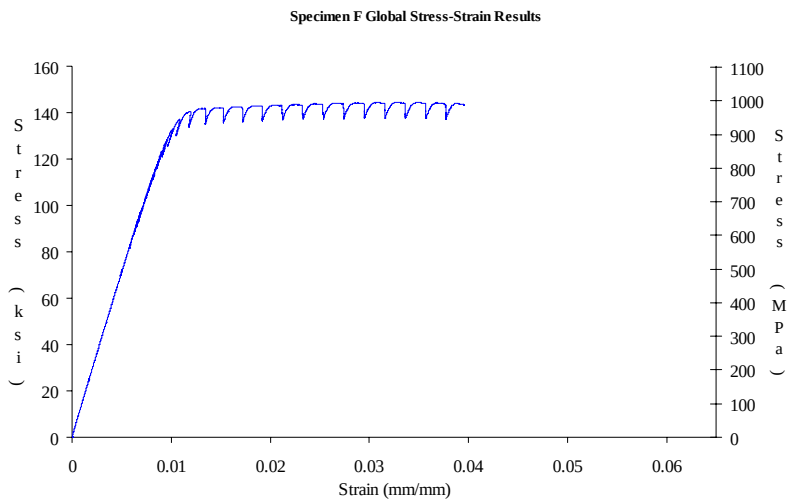 Reference Load (T): 124.6 lbf (554 N) Reference Stress (σ): 25.1 ksi (173 MPa) Reference Extensometer Strain (ε_{EXT}): 0.00172

Raw Image	e_{yy} Contour	TAG DIC 4
		e_{yy} (Point 0 = Top of Gage; Point 100 = Bottom of Gage)
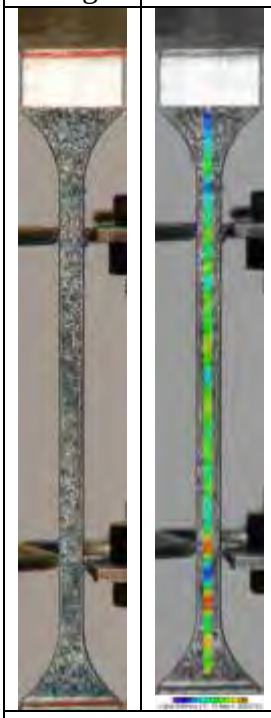		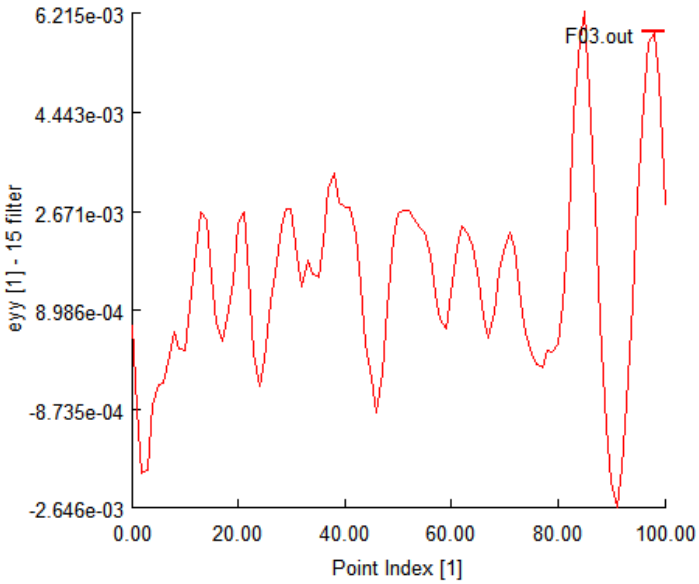
Load Step 3		T:249.6 lbf (1110N); σ: 50.3 ksi (347 Mpa) e_{EXT}: 0.00350
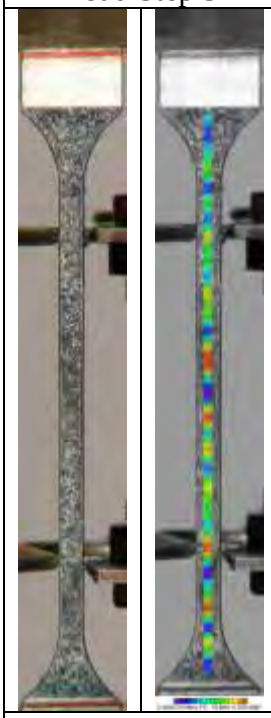		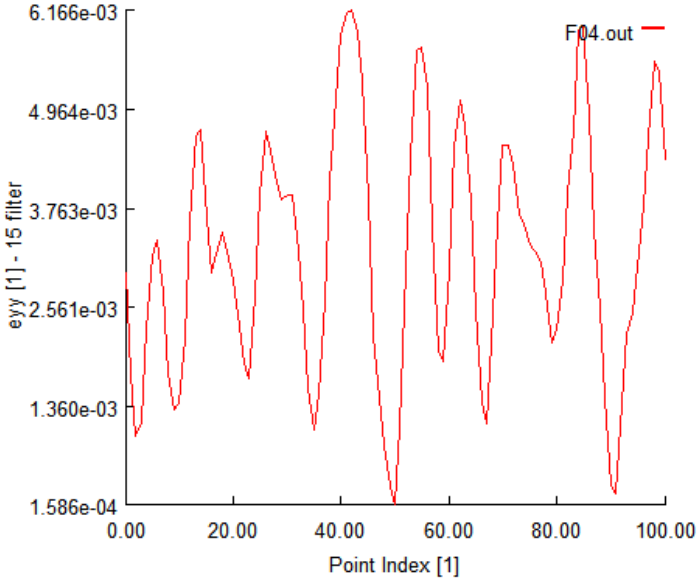
Load Step 4		T:358.2 lbf (1593N); σ: 72.2 ksi (498 Mpa) e_{EXT}: 0.00508

Raw Image	e_{yy} Contour	TAG DIC 4
		e_{yy} (Point 0 = Top of Gage; Point 100 = Bottom of Gage)
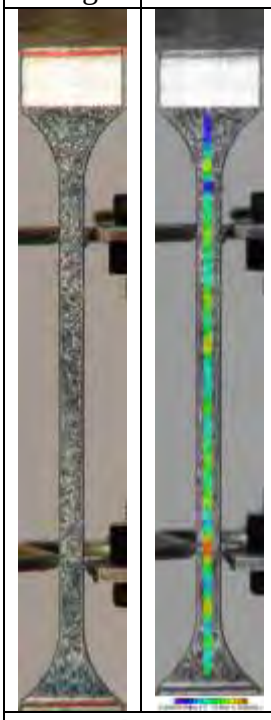		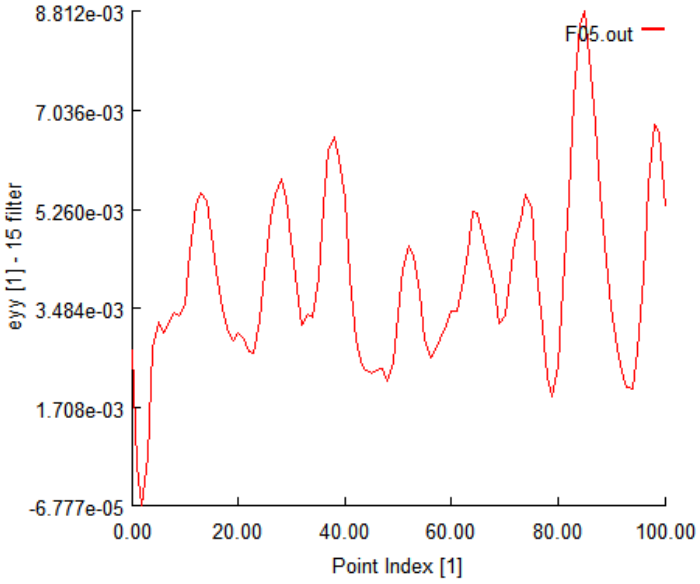
Load Step 5		T:432.0 lbf (1922N); σ: 87.1 ksi (601 Mpa) e_{EXT}: 0.00616
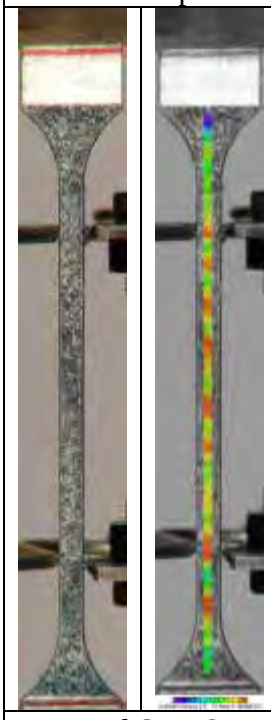		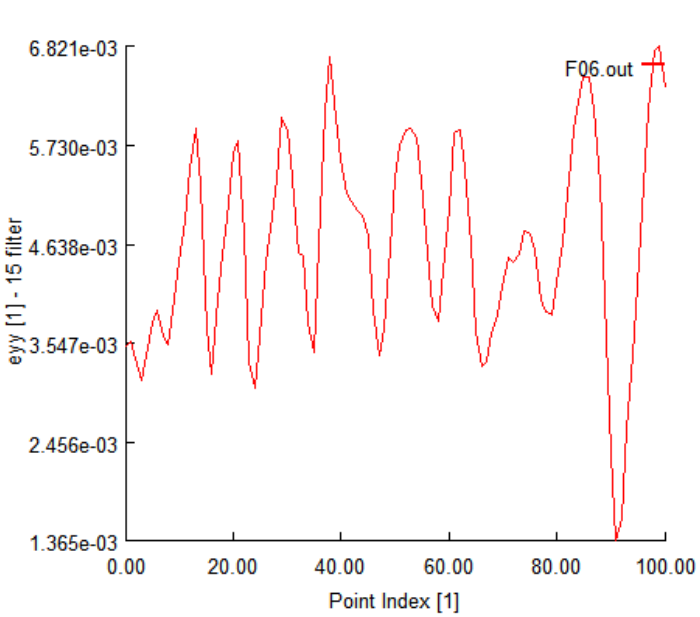
Load Step 6		T:466.7 lbf (2076N); σ: 94.1 ksi (649 Mpa) e_{EXT}: 0.00668

Raw Image	e_{yy} Contour	TAG DIC 4
		e_{yy} (Point 0 = Top of Gage; Point 100 = Bottom of Gage)
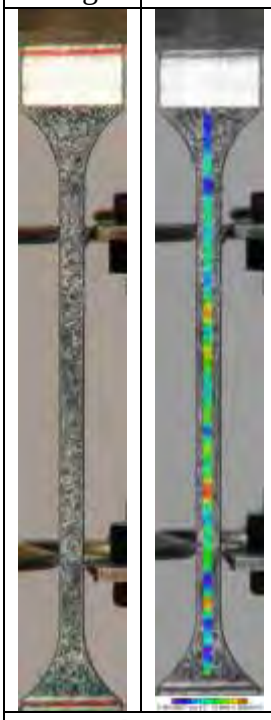		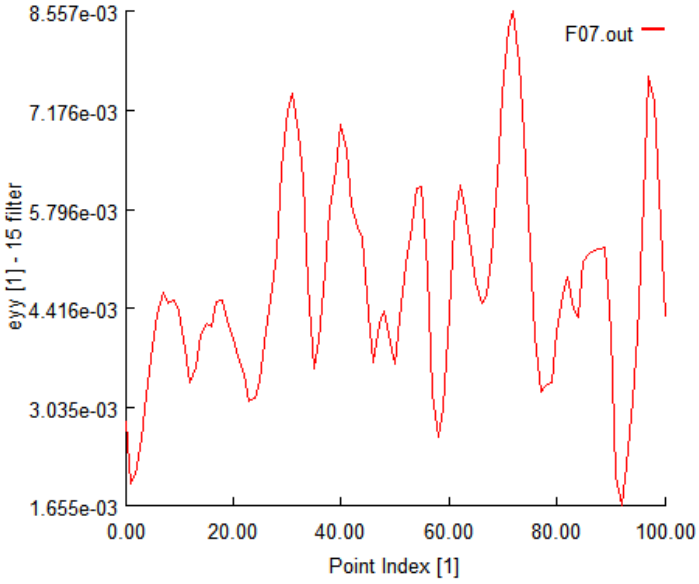
Load Step 7		T:479.7 lbf (2134N); σ: 96.7 ksi (667 Mpa) e_{EXT}: 0.00689
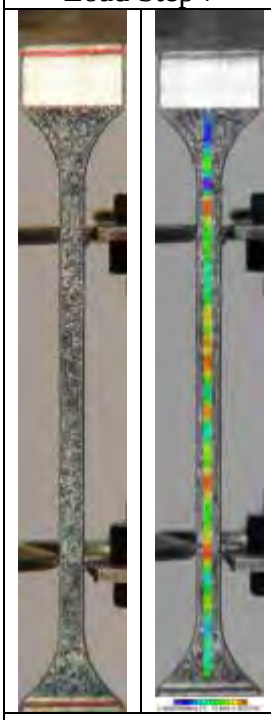		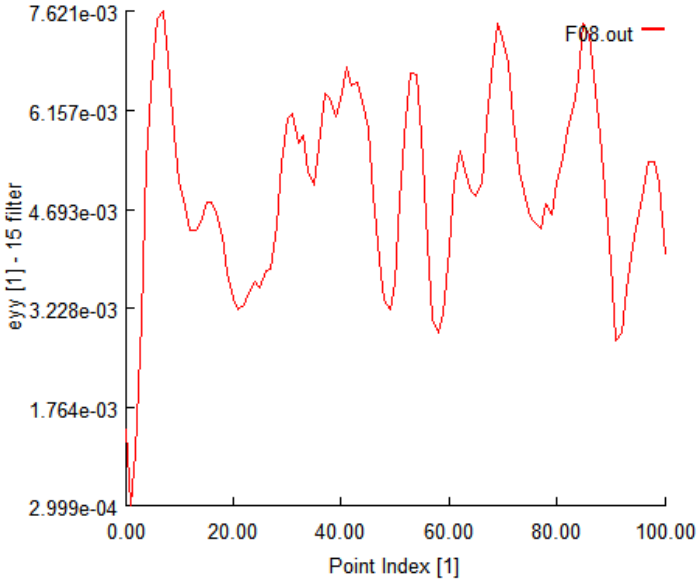
Load Step 8		T:488.1 lbf (2171N); σ: 98.4 ksi (679 Mpa) e_{EXT}: 0.00704

Raw Image	e_{yy} Contour	TAG DIC 4
		e_{yy} (Point 0 = Top of Gage; Point 100 = Bottom of Gage)
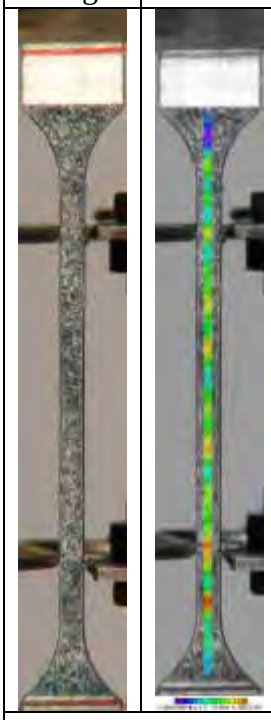		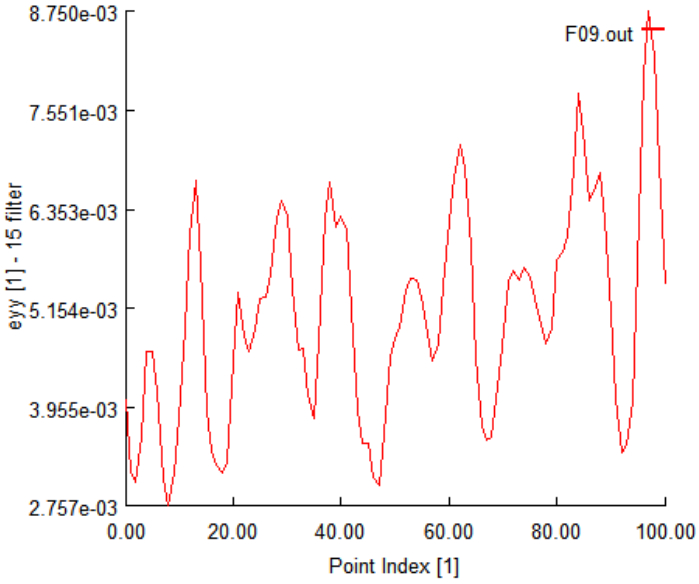
Load Step 9		T:510.0 lbf (2268N); σ: 102.8 ksi (709 Mpa) e_{EXT}: 0.00739
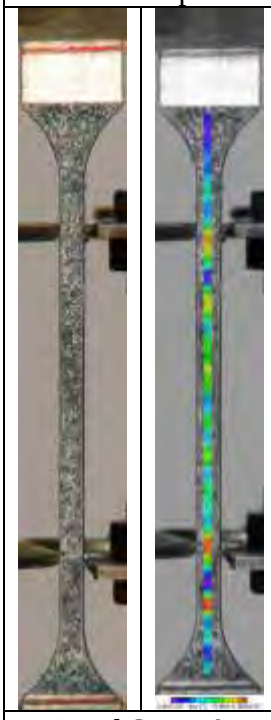		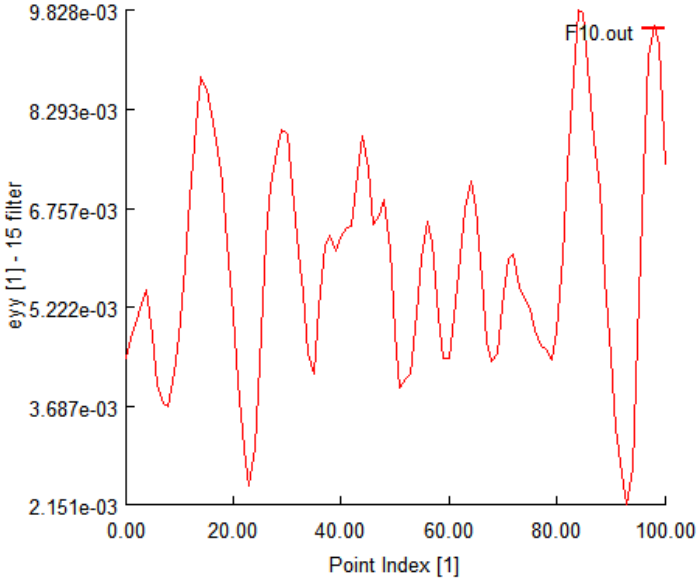
Load Step 10		T:534.4 lbf (2377N); σ: 107.8 ksi (743 Mpa) e_{EXT}: 0.00777

Raw Image	e_{yy} Contour	TAG DIC 4
		e_{yy} (Point 0 = Top of Gage; Point 100 = Bottom of Gage)
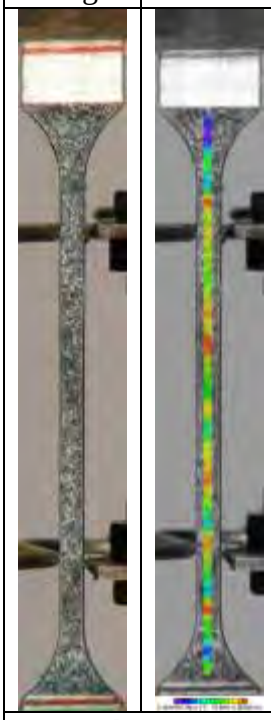		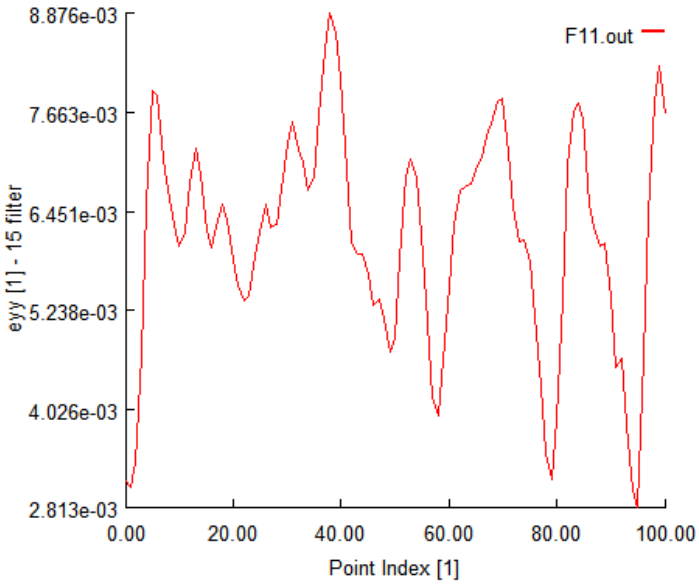
Load Step 11		T:560.7 lbf (2494N); σ: 113.0 ksi (779 Mpa) e_{EXT}: 0.00818
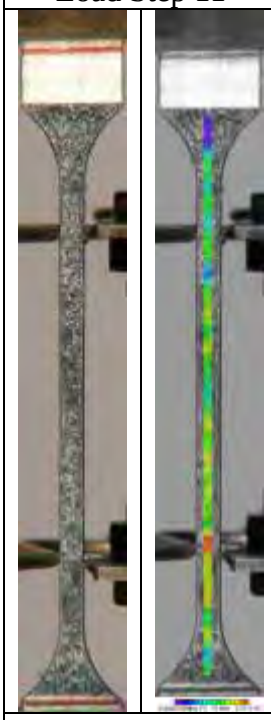		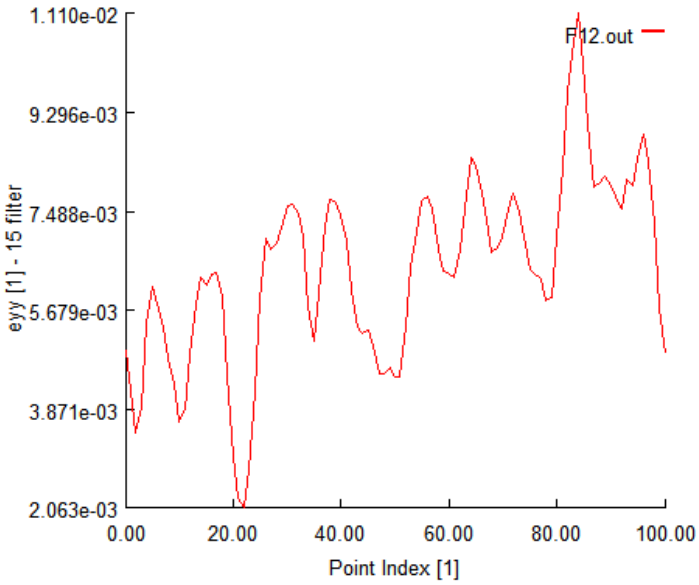
Load Step 12		T:587.2 lbf (2612N); σ: 118.4 ksi (816 Mpa) e_{EXT}: 0.00863

Raw Image	e_{yy} Contour	TAG DIC 4
		e_{yy} (Point 0 = Top of Gage; Point 100 = Bottom of Gage)
		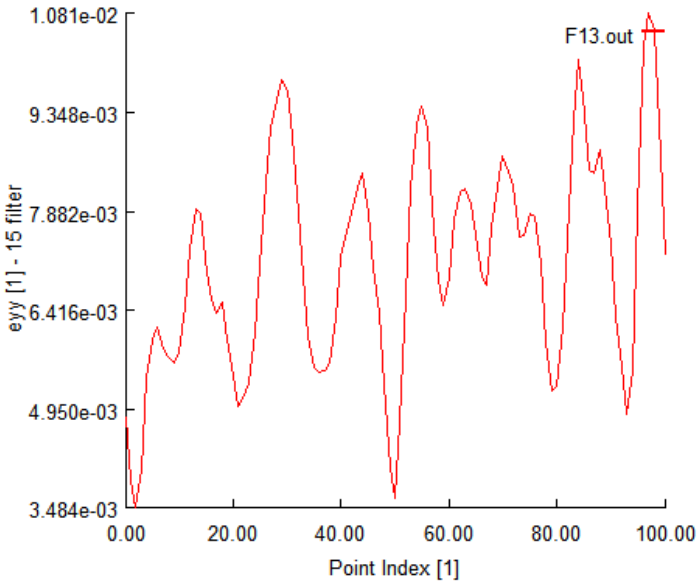
Load Step 13		T:611.4 lbf (2720N); σ: 123.3 ksi (850 Mpa) e_{EXT}: 0.00906
	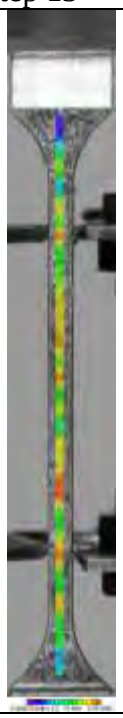	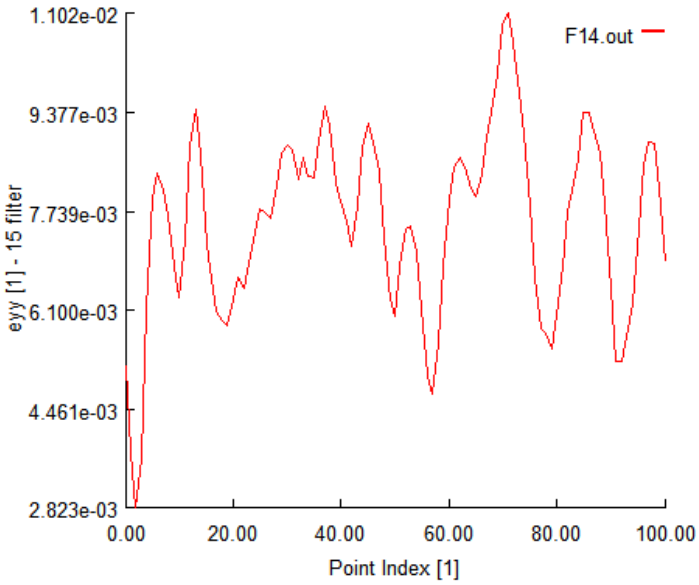
Load Step 14		T:636.3 lbf (2830N); σ: 128.3 ksi (884 Mpa) e_{EXT}: 0.00957

Raw Image	e_{yy} Contour	TAG DIC 4
		e_{yy} (Point 0 = Top of Gage; Point 100 = Bottom of Gage)
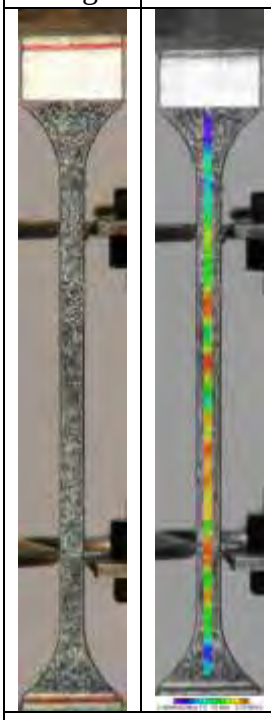		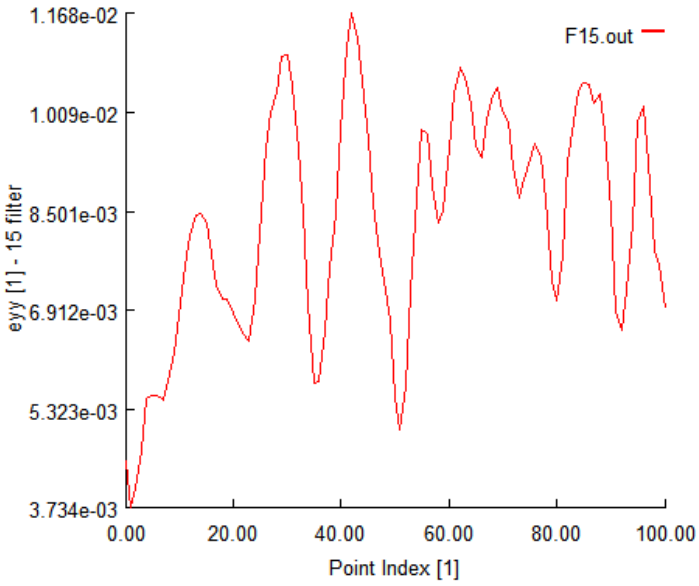
Load Step 15		T:659.2 lbf (2932N); σ: 132.9 ksi (916 Mpa) e_{EXT}: 0.01012
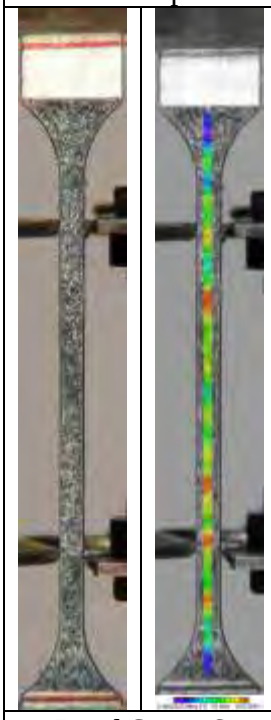		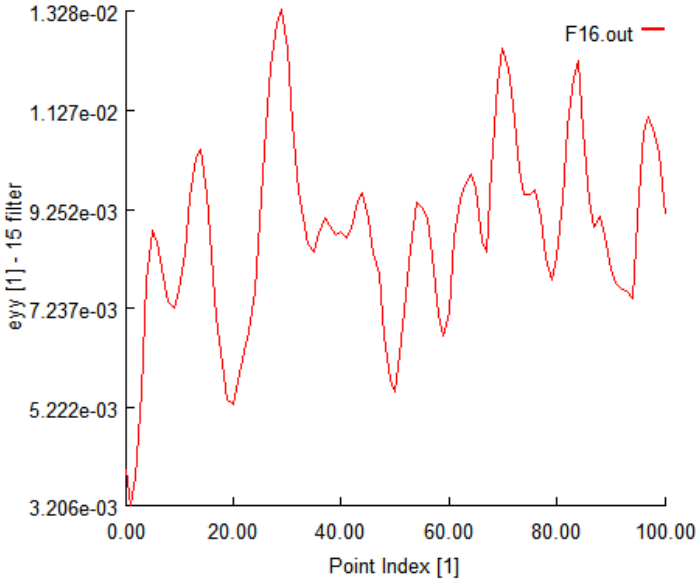
Load Step 16		T:680.4 lbf (3026N); σ: 137.2 ksi (946 Mpa) e_{EXT}: 0.01085

Raw Image	e_{yy} Contour	TAG DIC 4
		e_{yy} (Point 0 = Top of Gage; Point 100 = Bottom of Gage)
		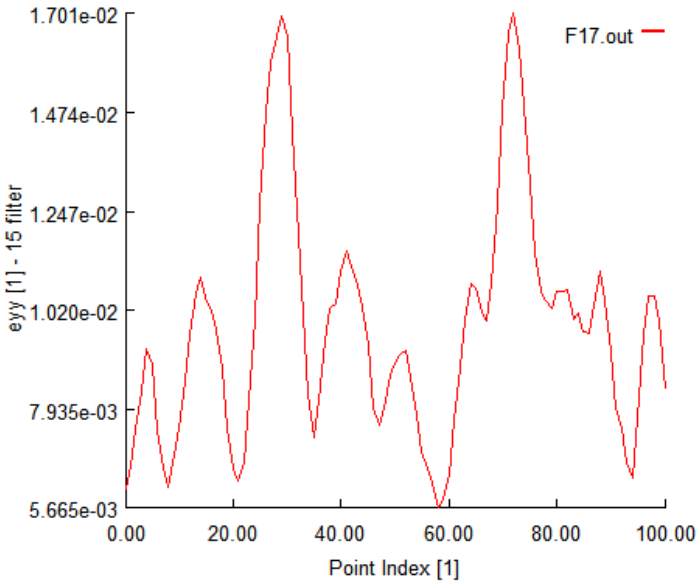
Load Step 17		T:697.3 lbf (3102N); σ: 140.6 ksi (969 Mpa) e_{EXT}: 0.01191
		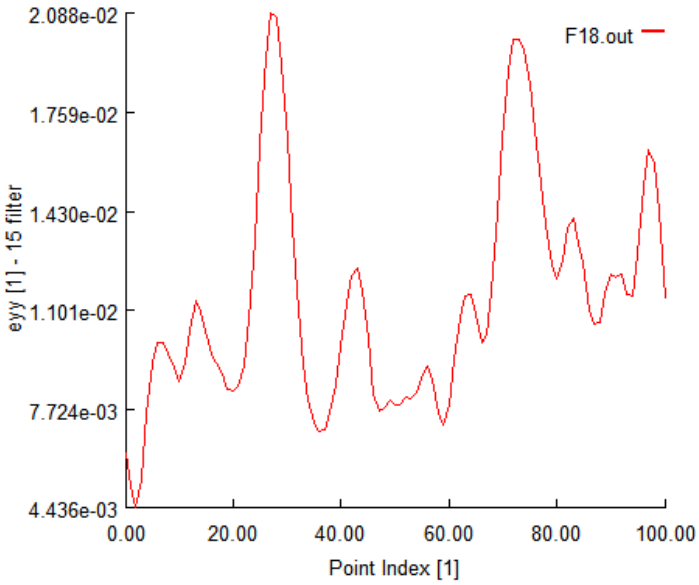
Load Step 18		T:703.3 lbf (3129N); σ: 141.8 ksi (978 Mpa) e_{EXT}: 0.01342

Raw Image	e_{yy} Contour	TAG DIC 4
		e_{yy} (Point 0 = Top of Gage; Point 100 = Bottom of Gage)
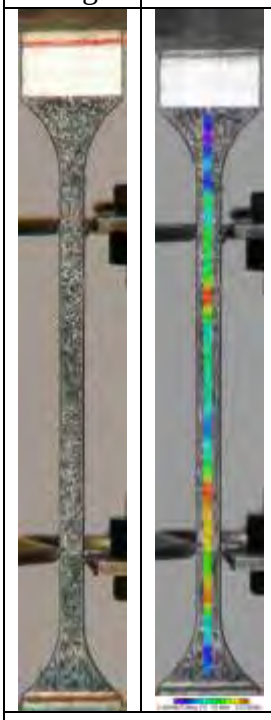		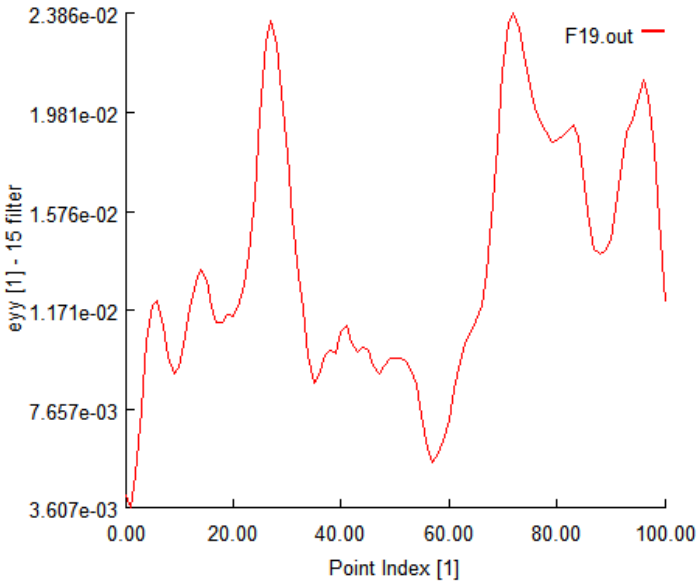
Load Step 19		T:704.3 lbf (3133N); σ: 142.0 ksi (979 Mpa) e_{EXT}: 0.01521
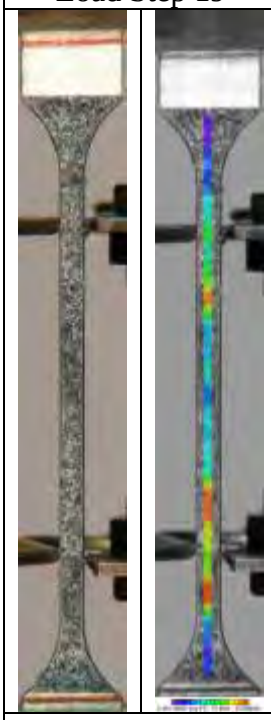		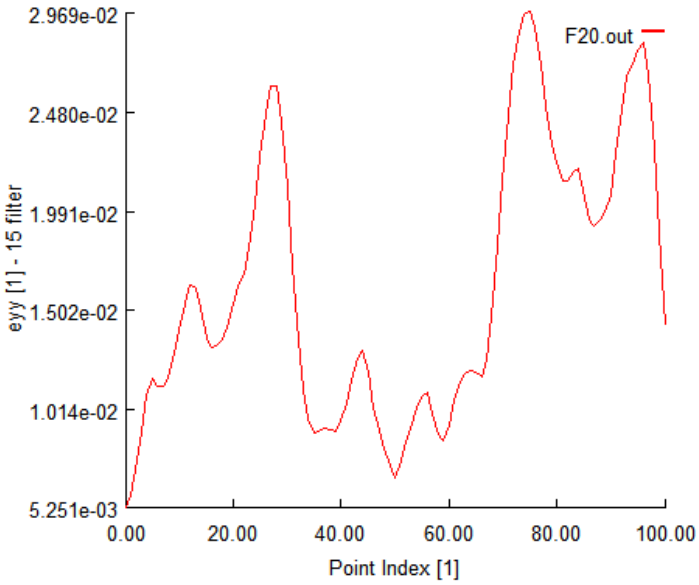
Load Step 20		T:706.3 lbf (3142N); σ: 142.4 ksi (982 Mpa) e_{EXT}: 0.01716

Raw Image	e_{yy} Contour	TAG DIC 4
		e_{yy} (Point 0 = Top of Gage; Point 100 = Bottom of Gage)
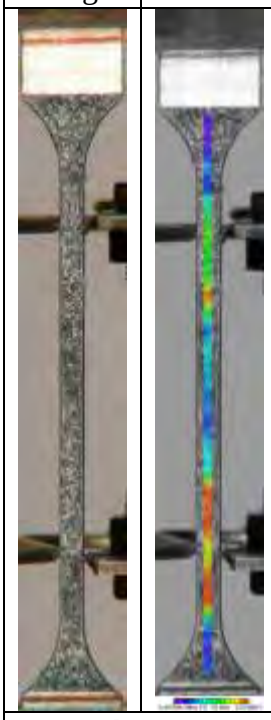		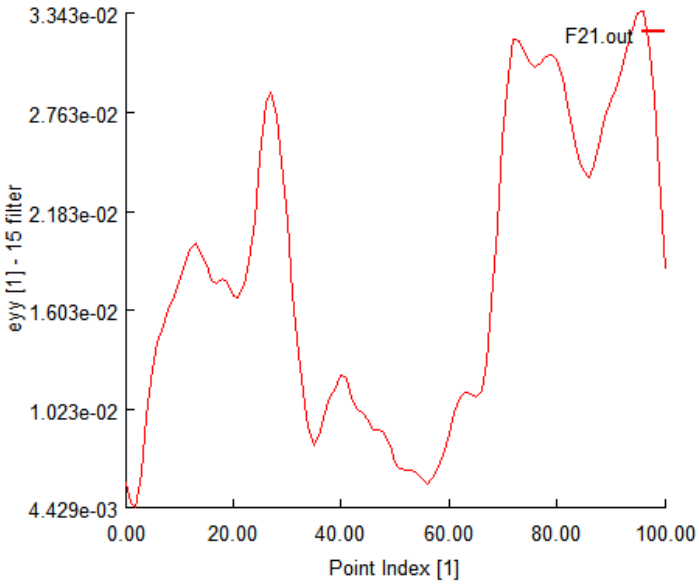
Load Step 21		T:708.2 lbf (3150N); σ: 142.8 ksi (984 Mpa) e_{EXT}: 0.01914
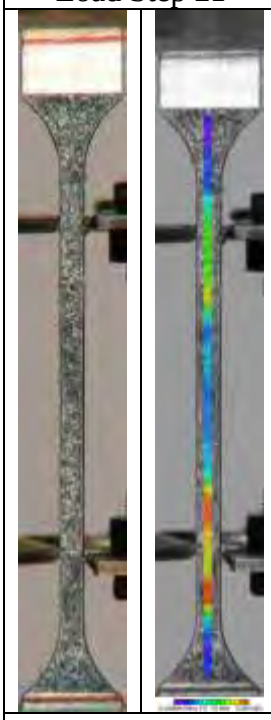		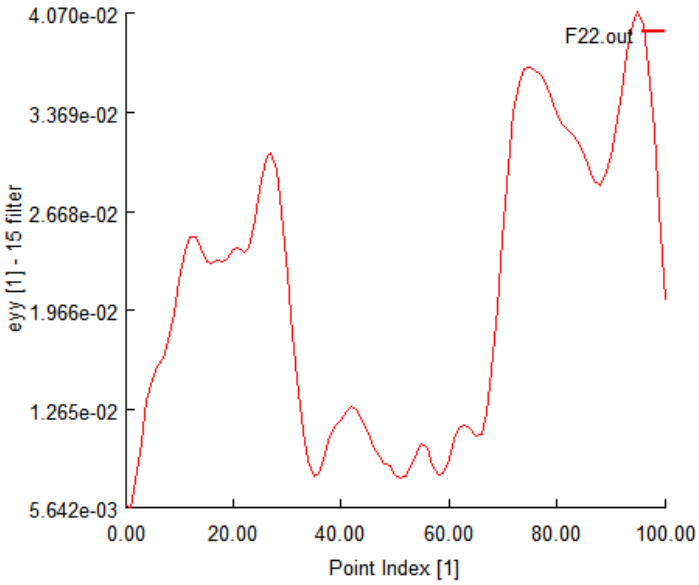
Load Step 22		T:709.5 lbf (3156N); σ: 143.0 ksi (986 Mpa) e_{EXT}: 0.02112

Raw Image	e_{yy} Contour	TAG DIC 4
		e_{yy} (Point 0 = Top of Gage; Point 100 = Bottom of Gage)
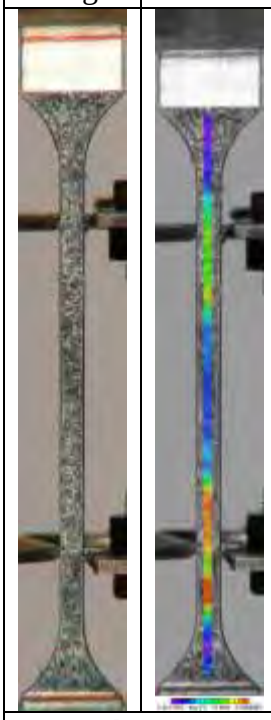		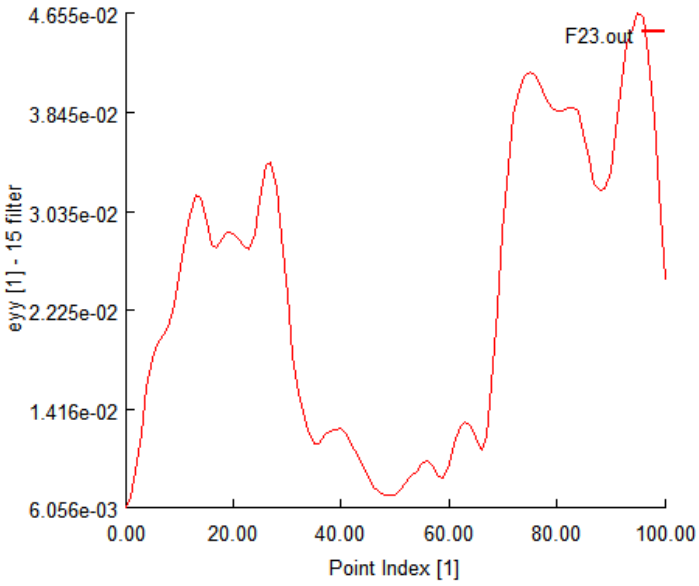
Load Step 23		T:711.2 lbf (3163N); σ: 143.4 ksi (989 Mpa) e_{EXT}: 0.02315
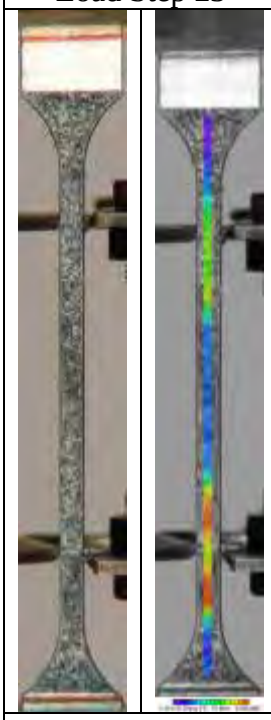		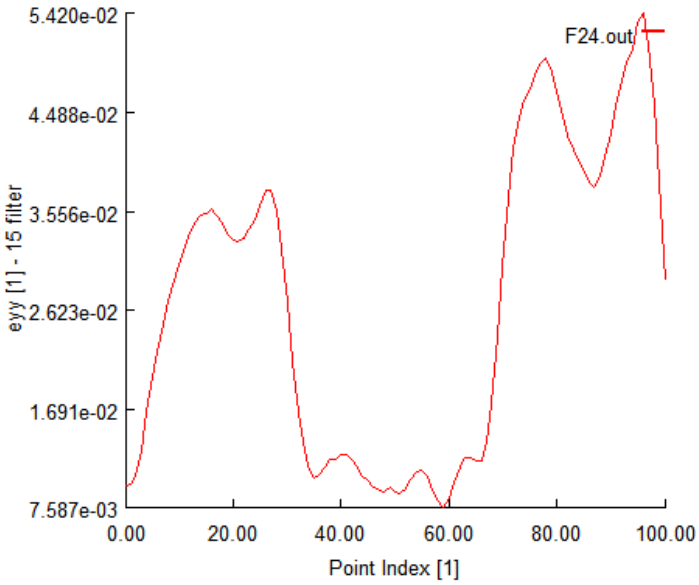
Load Step 24		T:712.7 lbf (3170N); σ: 143.7 ksi (991 Mpa) e_{EXT}: 0.02517

Raw Image	e_{yy} Contour	TAG DIC 4
		e_{yy} (Point 0 = Top of Gage; Point 100 = Bottom of Gage)
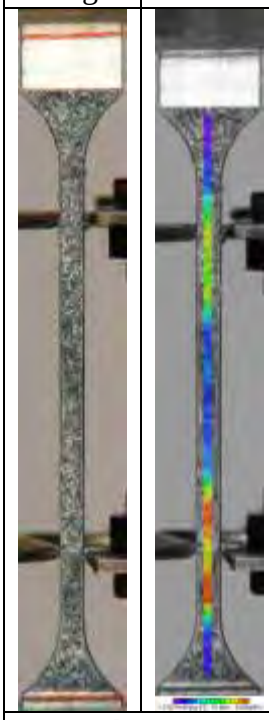		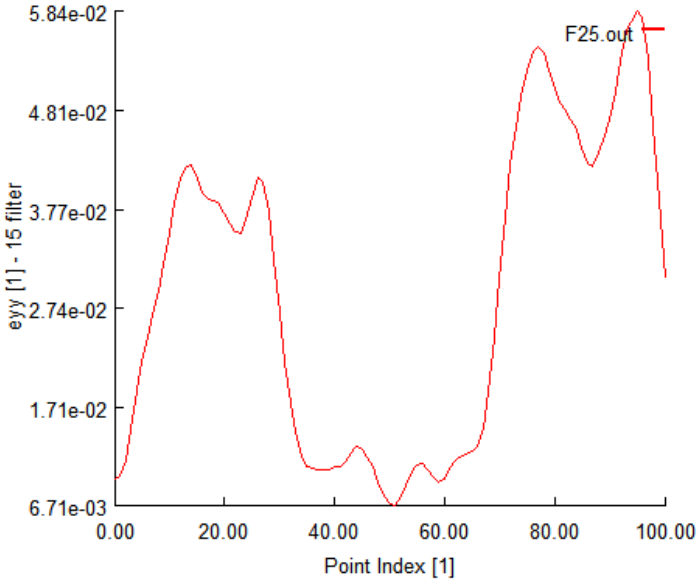
Load Step 25		T:713.7 lbf (3175N); σ: 143.9 ksi (992 Mpa) e_{EXT}: 0.02725
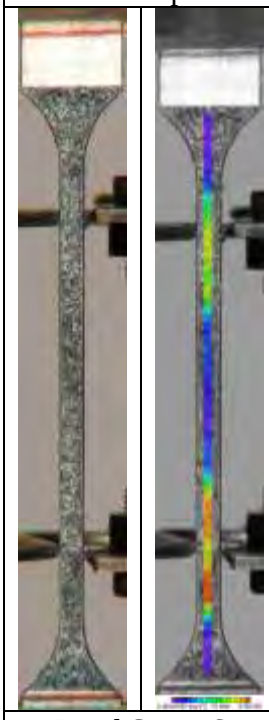		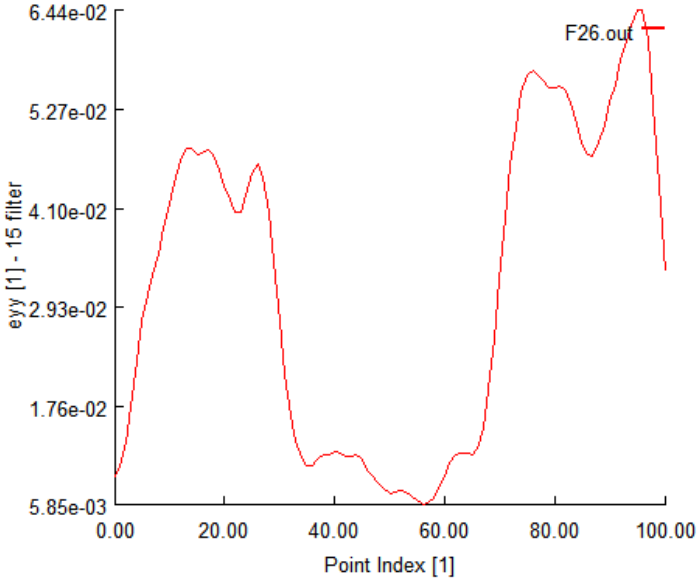
Load Step 26		T:714.3 lbf (3177N); σ: 144.0 ksi (993 Mpa) e_{EXT}: 0.02941

Raw Image	e_{yy} Contour	TAG DIC 4
		e_{yy} (Point 0 = Top of Gage; Point 100 = Bottom of Gage)
	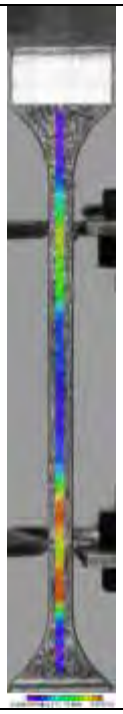	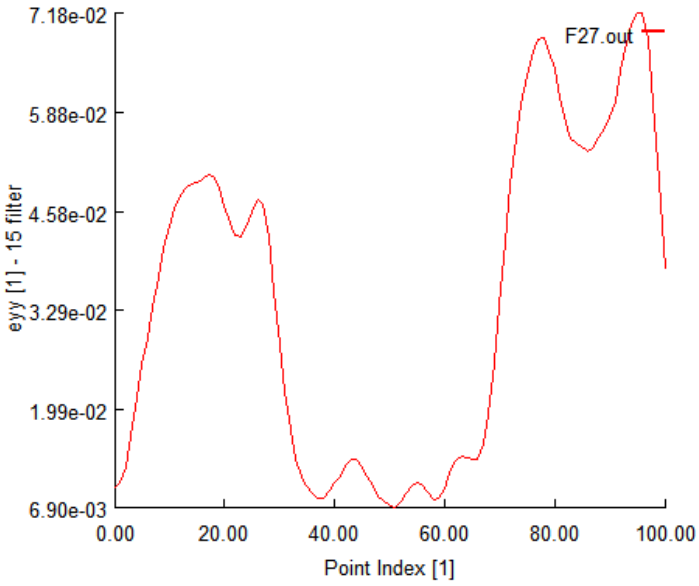
Load Step 27		T:714.9 lbf (3180N); σ: 144.1 ksi (994 Mpa) e_{EXT}: 0.03142
	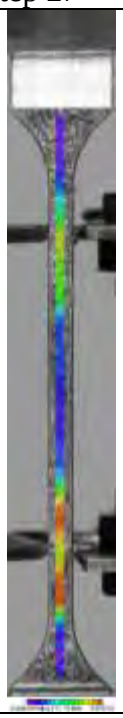	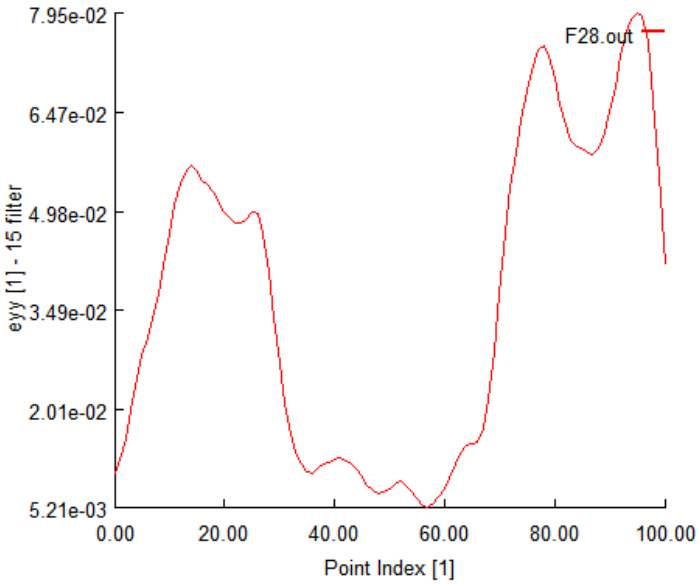
Load Step 28		T:714.8 lbf (3180N); σ: 144.1 ksi (994 Mpa) e_{EXT}: 0.03355

Raw Image	e_{yy} Contour	TAG DIC 4
		e_{yy} (Point 0 = Top of Gage; Point 100 = Bottom of Gage)
	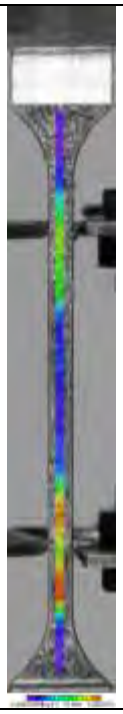	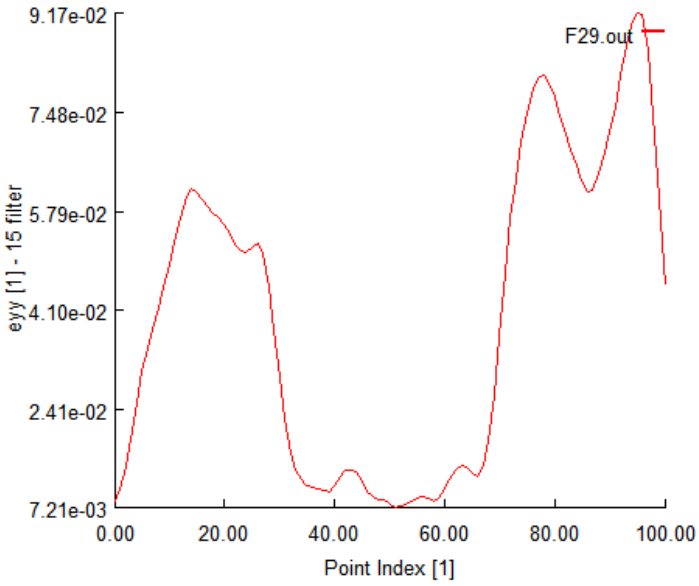
Load Step 29		T:714.2 lbf (3177N); σ: 144.0 ksi (993 Mpa) e_{EXT}: 0.03563
		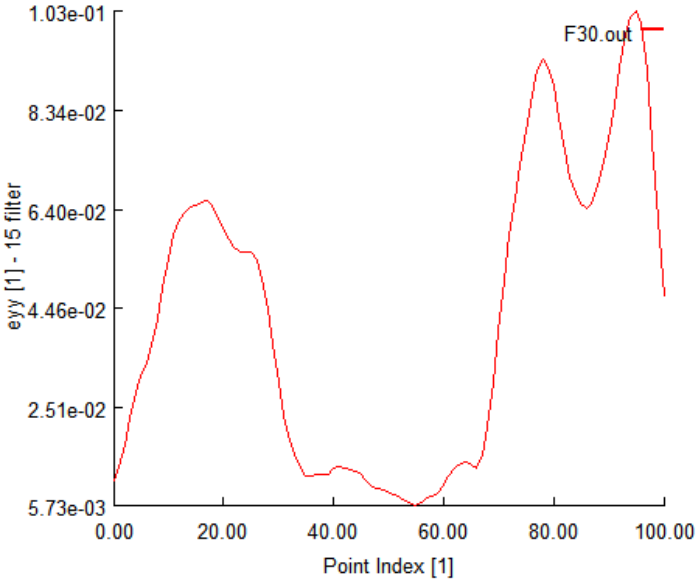
Load Step 30		T:713.1 lbf (3172N); σ: 143.8 ksi (991 Mpa) e_{EXT}: 0.03760

Raw Image	e_{yy} Contour	TAG DIC 4
		e_{yy} (Point 0 = Top of Gage; Point 100 = Bottom of Gage)
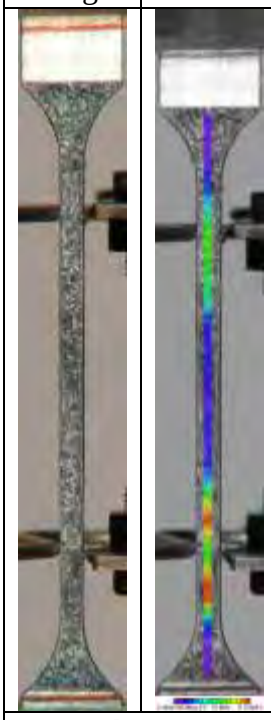		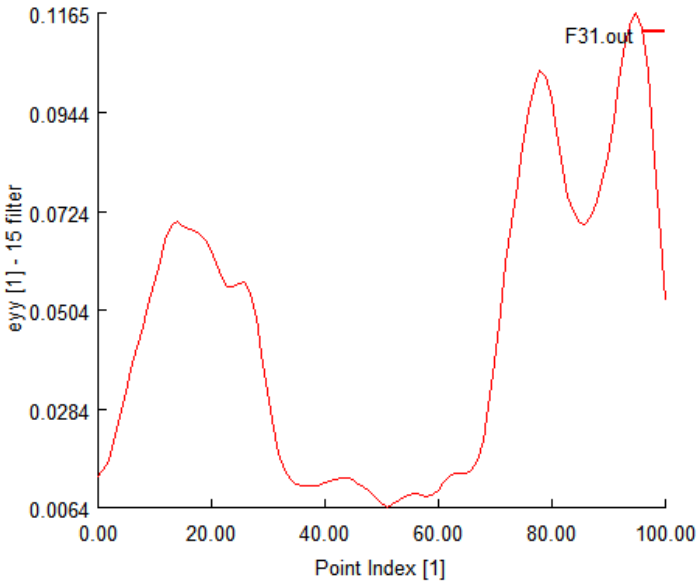
Load Step 31		T:711.3 lbf (3164N); σ: 143.4 ksi (989 Mpa) e_{EXT}: 0.03954
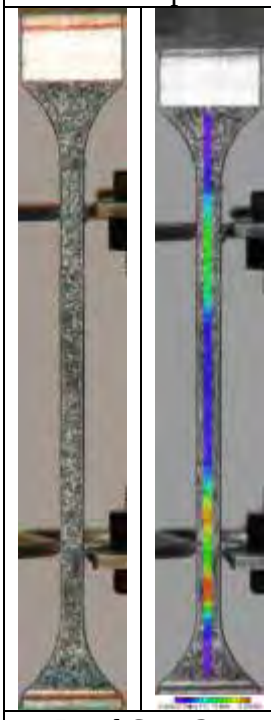		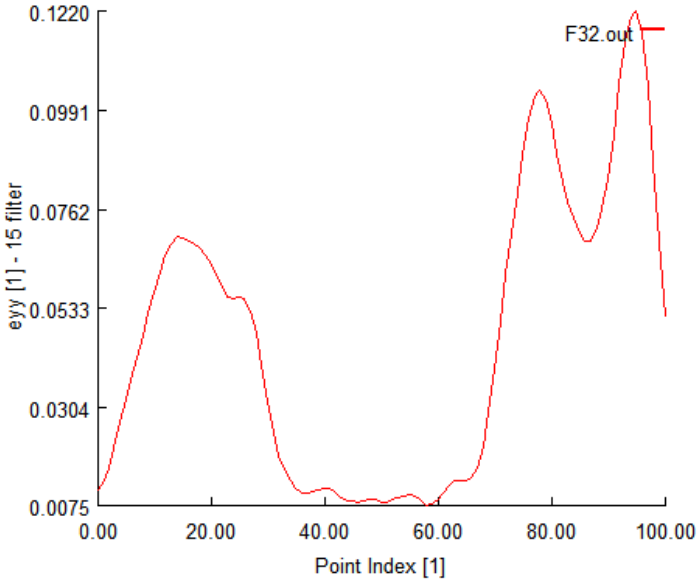
Load Step 32		T:711.1 lbf (3163N); σ: 143.4 ksi (988 Mpa) e_{EXT}: 0.03958

11. TAG DIC 5: test article G

Reference Image	Post Test Image	Global Stress-Strain Behavior of Specimen
		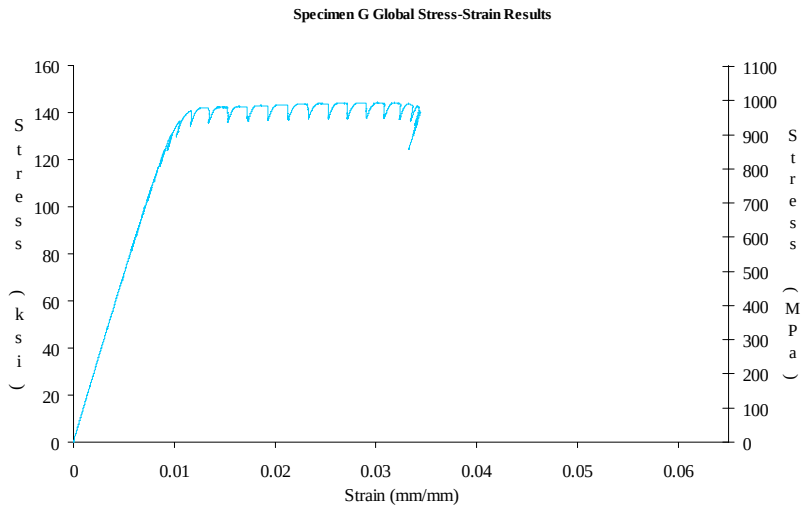 Reference Load (T): 244.1 lbf (1086 N) Reference Stress (σ): 49.2 ksi (339 MPa) Reference Extensometer Strain (ε_{EXT}): 0.00341

Raw Image	e_{yy} Contour	TAG DIC 5
		e_{yy} (Point 0 = Top of Gage; Point 100 = Bottom of Gage)
	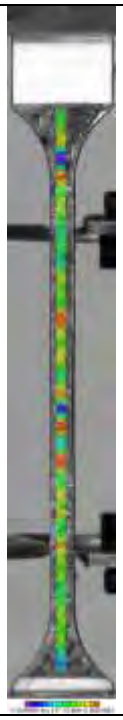	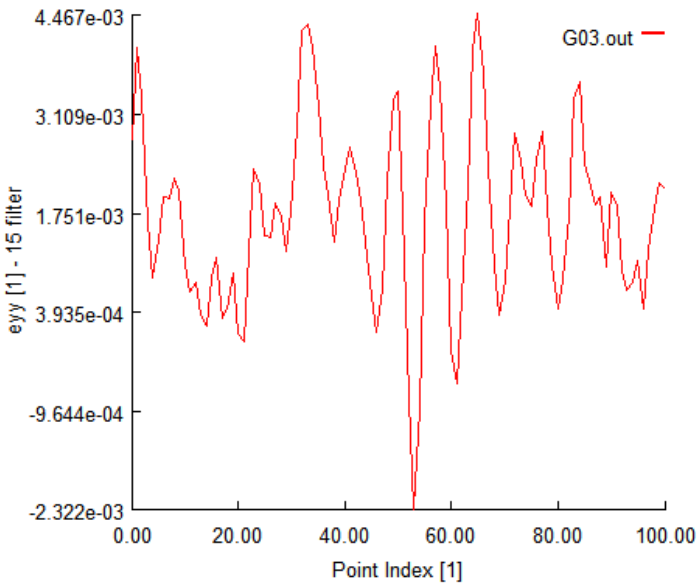
Load Step 3		T:244.1 lbf (1086N); σ: 49.2 ksi (339 Mpa) e_{EXT}: 0.00341
	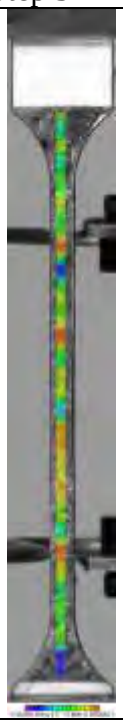	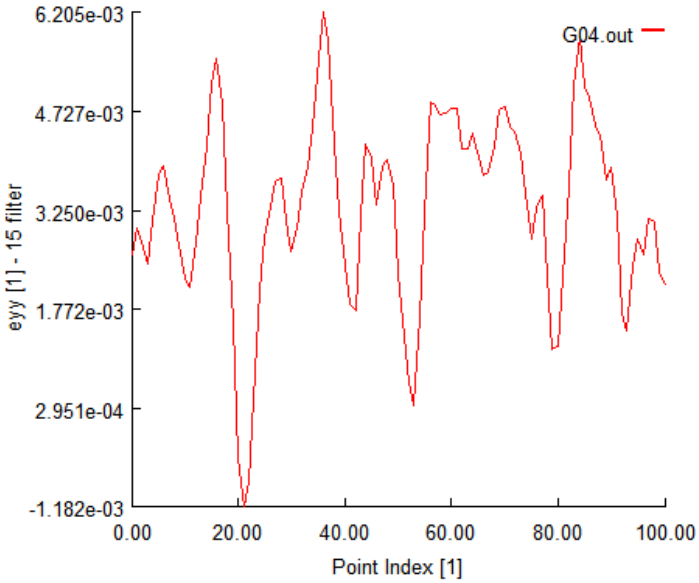
Load Step 4		T:353.2 lbf (1571N); σ: 71.2 ksi (491 Mpa) e_{EXT}: 0.00499

Raw Image	e_{yy} Contour	TAG DIC 5
		e_{yy} (Point 0 = Top of Gage; Point 100 = Bottom of Gage)
		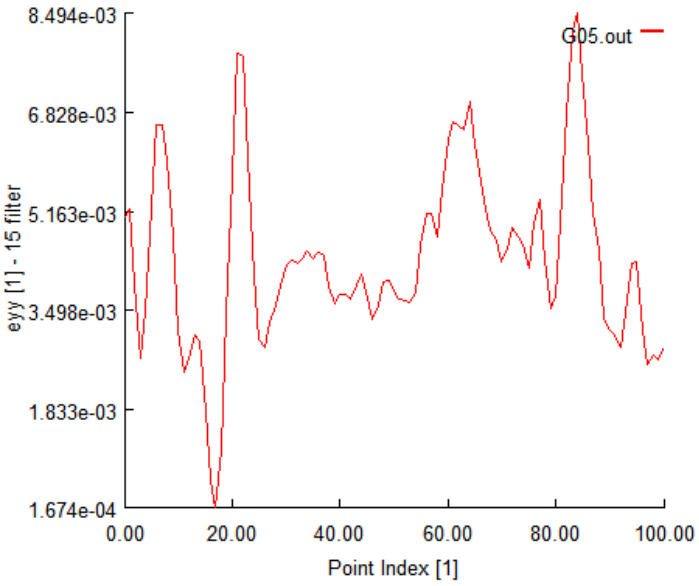
Load Step 5		T:430.1 lbf (1913N); σ: 86.7 ksi (598 Mpa) e_{EXT}: 0.00611
		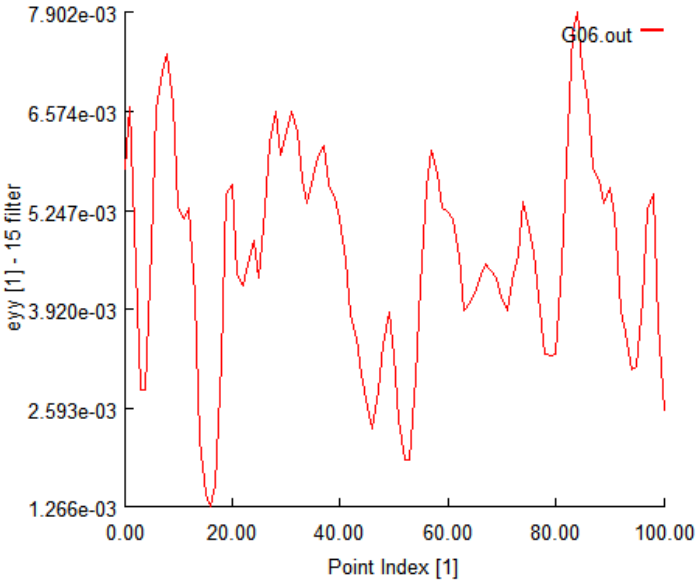
Load Step 6		T:463.6 lbf (2062N); σ: 93.5 ksi (644 Mpa) e_{EXT}: 0.00661

Raw Image	e_{yy} Contour	TAG DIC 5
		e_{yy} (Point 0 = Top of Gage; Point 100 = Bottom of Gage)
	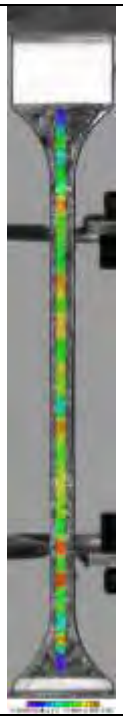	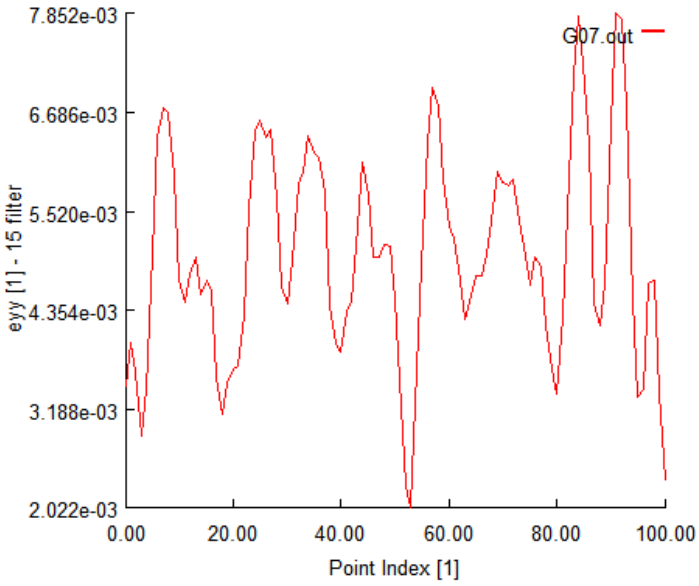
Load Step 7		T:497.2 lbf (2212N); σ: 100.2 ksi (691 Mpa) e_{EXT}: 0.00713
		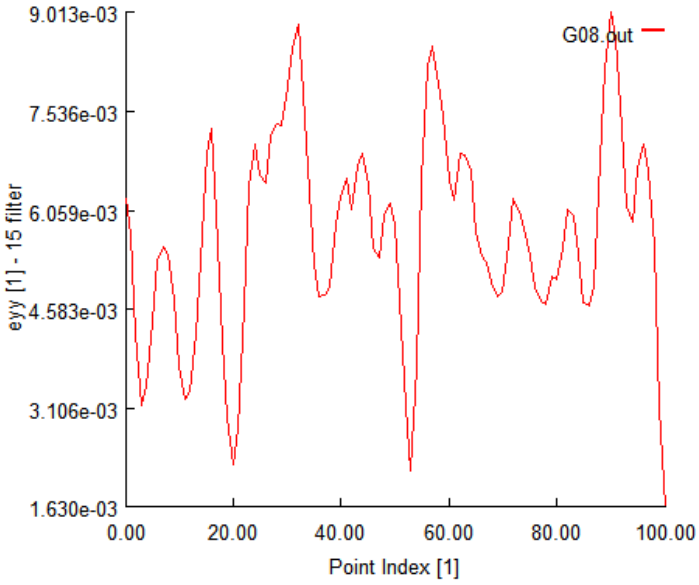
Load Step 8		T:538.6 lbf (2396N); σ: 108.6 ksi (749 Mpa) e_{EXT}: 0.00776

Raw Image	e_{yy} Contour	TAG DIC 5
		e_{yy} (Point 0 = Top of Gage; Point 100 = Bottom of Gage)
	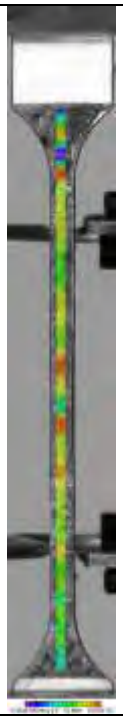	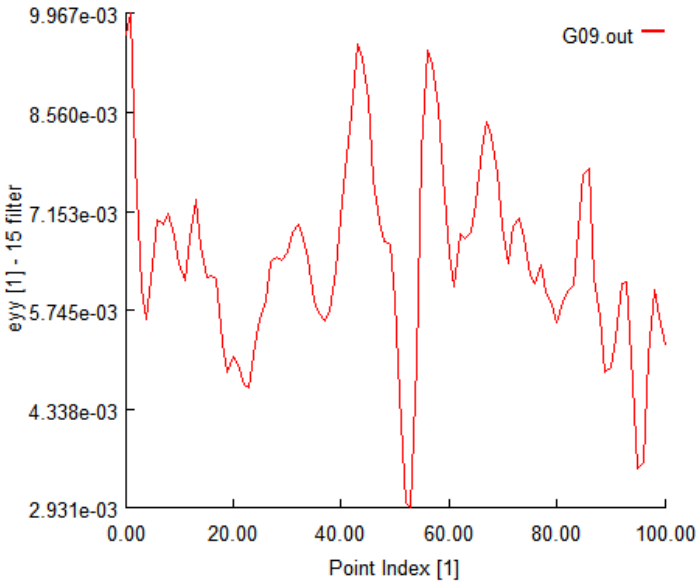
Load Step 9		T:579.2 lbf (2577N); σ: 116.8 ksi (805 Mpa) e_{EXT}: 0.00841
	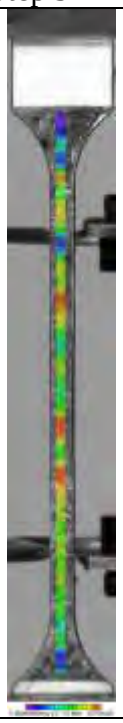	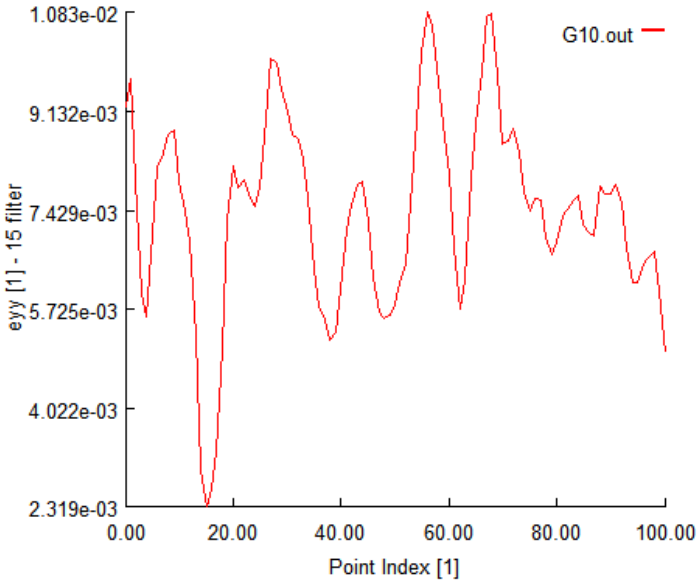
Load Step 10		T:616.3 lbf (2741N); σ: 124.3 ksi (857 Mpa) e_{EXT}: 0.00906

Raw Image	e_{yy} Contour	TAG DIC 5
		e_{yy} (Point 0 = Top of Gage; Point 100 = Bottom of Gage)
		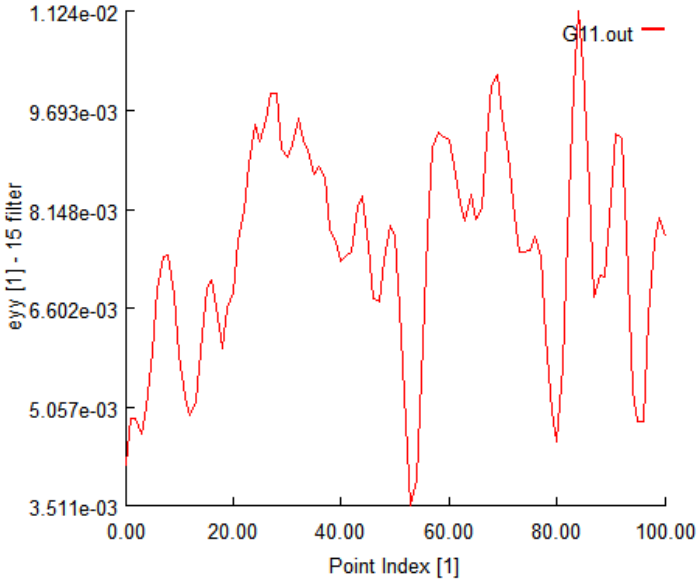
Load Step 11		T:649.3 lbf (2888N); σ: 130.9 ksi (903 Mpa) e_{EXT}: 0.00975
	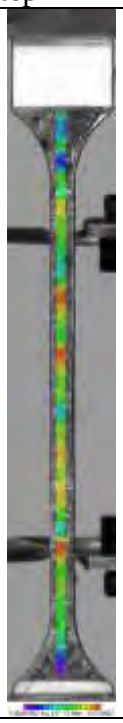	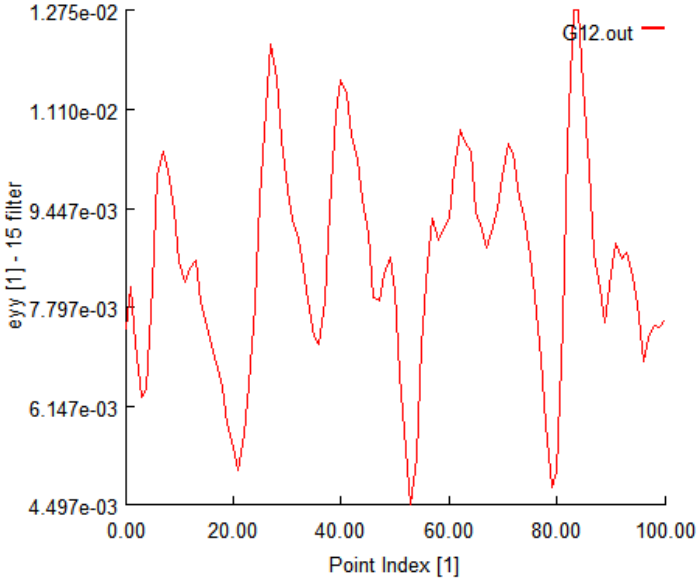
Load Step 12		T:676.5 lbf (3009N); σ: 136.4 ksi (940 Mpa) e_{EXT}: 0.01054

Raw Image	e_{yy} Contour	TAG DIC 5
		e_{yy} (Point 0 = Top of Gage; Point 100 = Bottom of Gage)
	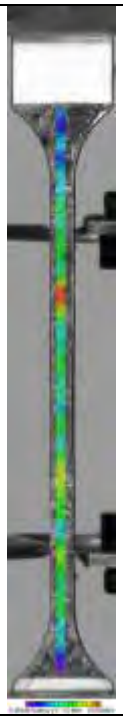	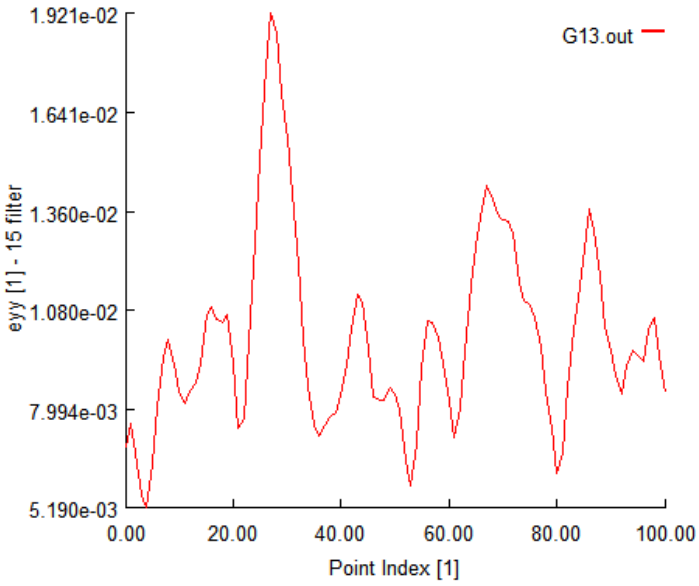
Load Step 13		T:697.7 lbf (3103N); σ: 140.7 ksi (970 Mpa) e_{EXT}: 0.01171
		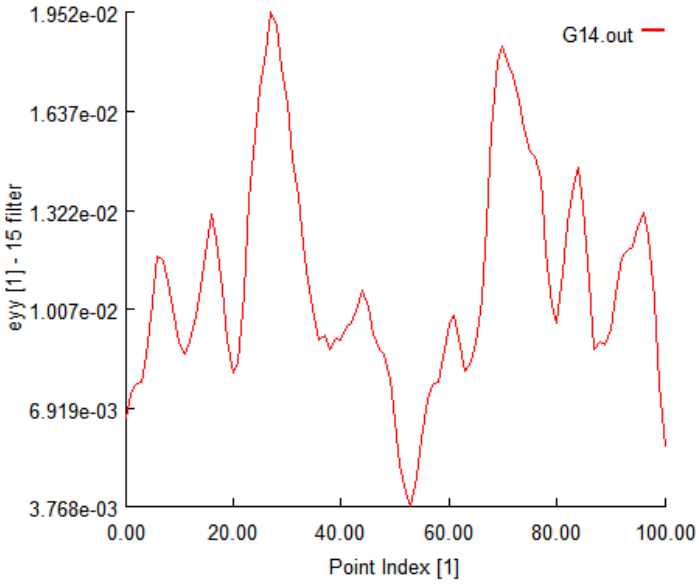
Load Step 14		T:705.0 lbf (3136N); σ: 142.1 ksi (980 Mpa) e_{EXT}: 0.01339

Raw Image	e_{yy} Contour	TAG DIC 5
		e_{yy} (Point 0 = Top of Gage; Point 100 = Bottom of Gage)
	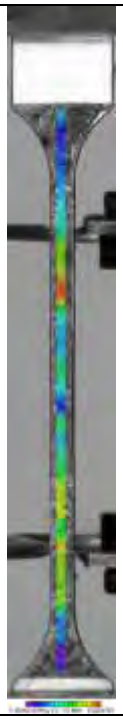	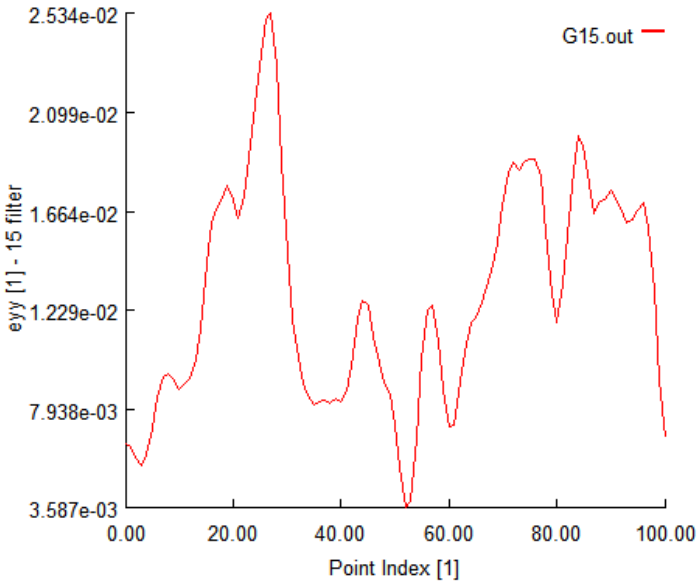
Load Step 15		T:705.5 lbf (3138N); σ: 142.2 ksi (981 Mpa) e_{EXT}: 0.01519
		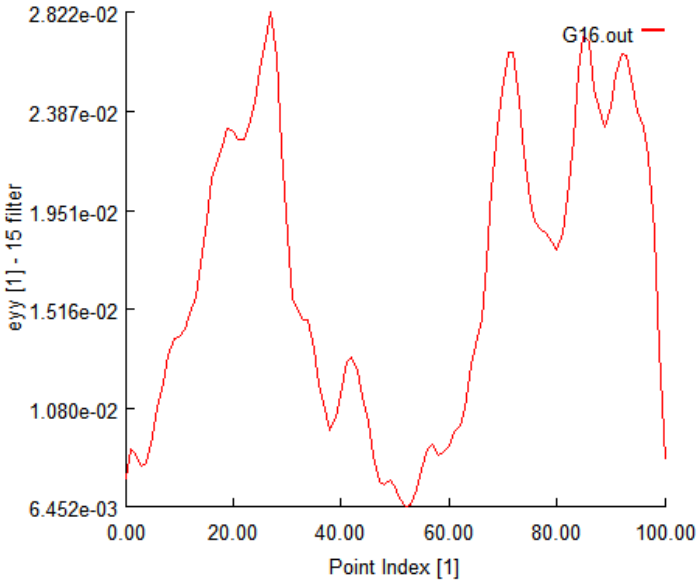
Load Step 16		T:706.9 lbf (3145N); σ: 142.5 ksi (983 Mpa) e_{EXT}: 0.01719

Raw Image	e_{yy} Contour	TAG DIC 5
		e_{yy} (Point 0 = Top of Gage; Point 100 = Bottom of Gage)
		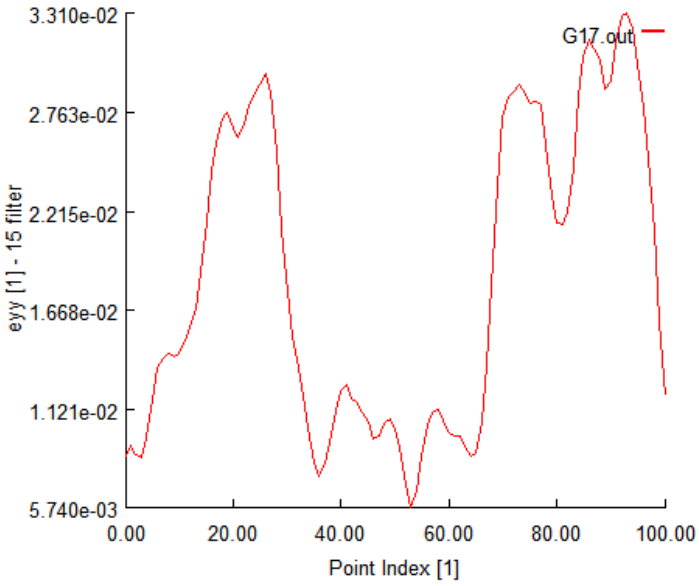
Load Step 17		T:708.9 lbf (3153N); σ: 142.9 ksi (985 Mpa) e_{EXT}: 0.01917
		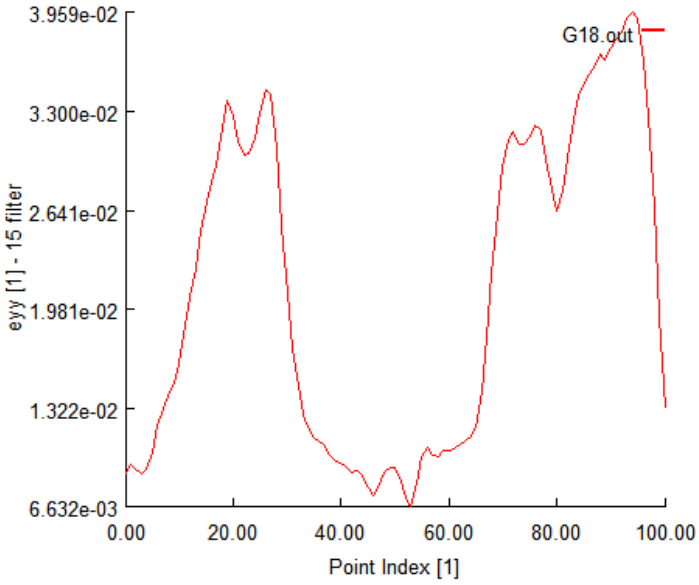
Load Step 18		T:710.2 lbf (3159N); σ: 143.2 ksi (987 Mpa) e_{EXT}: 0.02117

Raw Image	e_{yy} Contour	TAG DIC 5
		e_{yy} (Point 0 = Top of Gage; Point 100 = Bottom of Gage)
		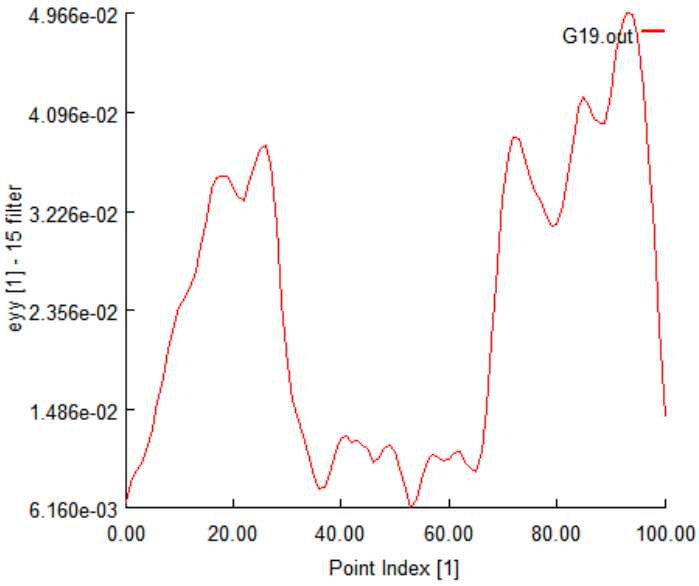
Load Step 19		T:711.8 lbf (3166N); σ: 143.5 ksi (989 Mpa) e_{EXT}: 0.02317
		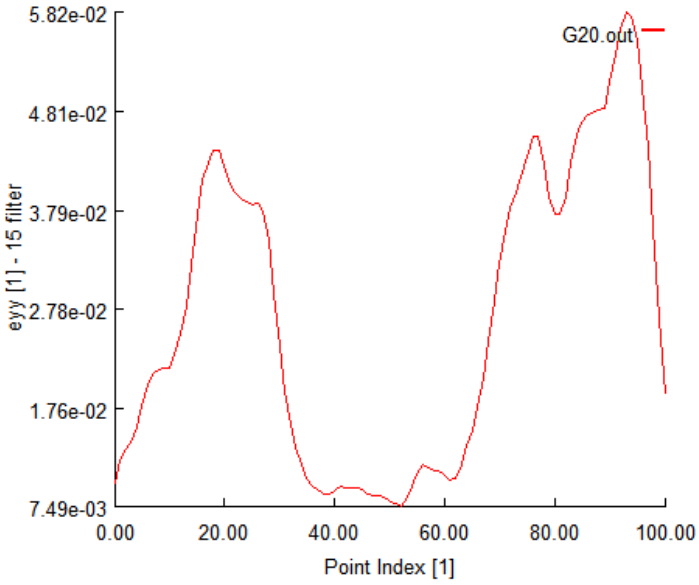
Load Step 20		T:712.7 lbf (3170N); σ: 143.7 ksi (991 Mpa) e_{EXT}: 0.02523

Raw Image	e_{yy} Contour	TAG DIC 5
		e_{yy} (Point 0 = Top of Gage; Point 100 = Bottom of Gage)
		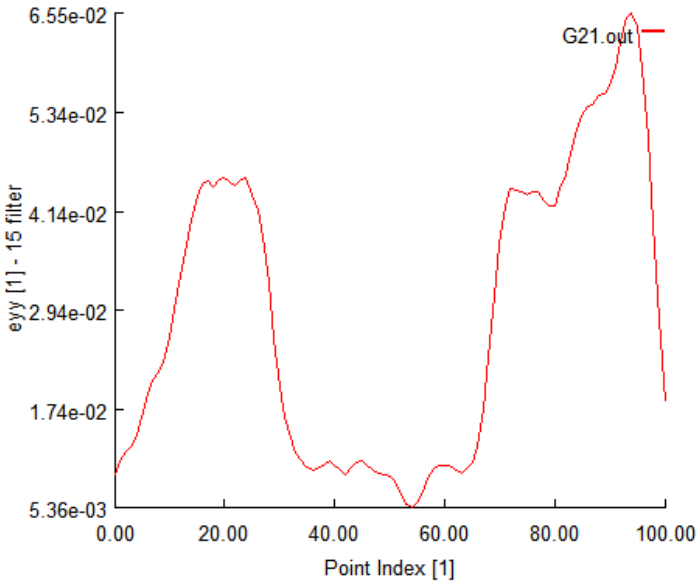
Load Step 21		T:713.4 lbf (3173N); σ: 143.8 ksi (992 Mpa) e_{EXT}: 0.02715
		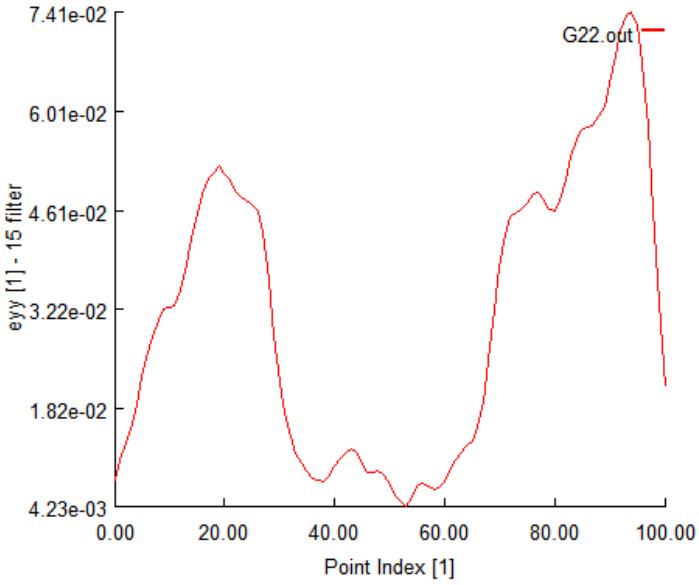
Load Step 22		T:713.9 lbf (3175N); σ: 143.9 ksi (992 Mpa) e_{EXT}: 0.02898

Raw Image	e_{yy} Contour	TAG DIC 5
		e_{yy} (Point 0 = Top of Gage; Point 100 = Bottom of Gage)
		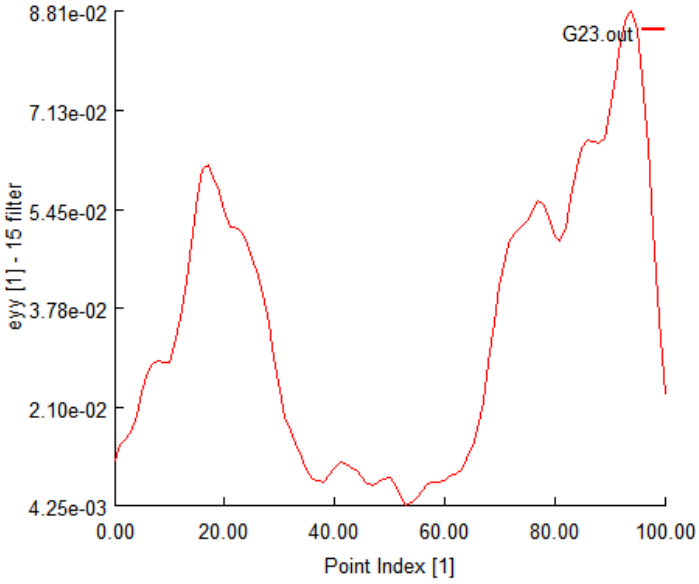
Load Step 23		T:713.3lbf (3173N); σ: 143.8 ksi (992 Mpa) e_{EXT}: 0.03084
		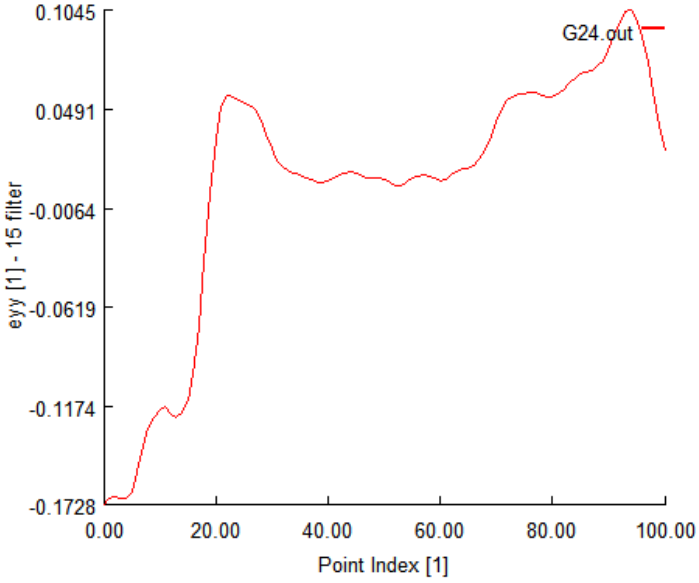
Load Step 24		T:712.8 lbf (3171N); σ: 143.7 ksi (991 Mpa) e_{EXT}: 0.03241

Raw Image	e_{yy} Contour	TAG DIC 5
		e_{yy} (Point 0 = Top of Gage; Point 100 = Bottom of Gage)
		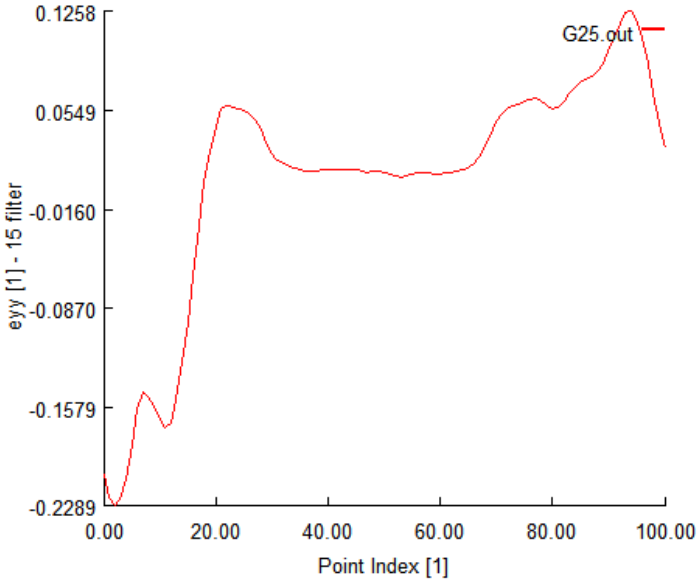
Load Step 25		T:709.0 lbf (3154N); σ: 142.9 ksi (986 Mpa) e_{EXT}: 0.03367
		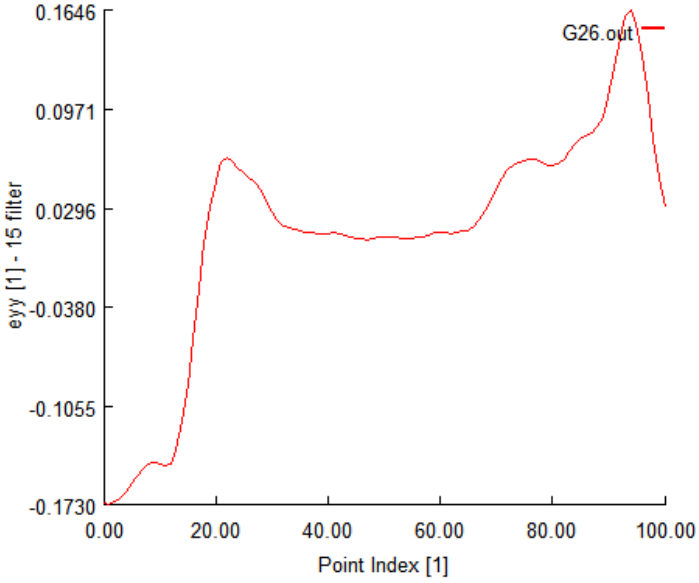
Load Step 26		T:699.3 lbf (3111N); σ: 141.0 ksi (972 Mpa) e_{EXT}: 0.03427

Raw Image	e_{yy} Contour	TAG DIC 5
		e_{yy} (Point 0 = Top of Gage; Point 100 = Bottom of Gage)
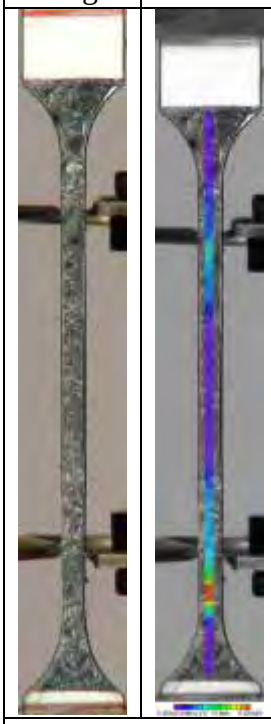		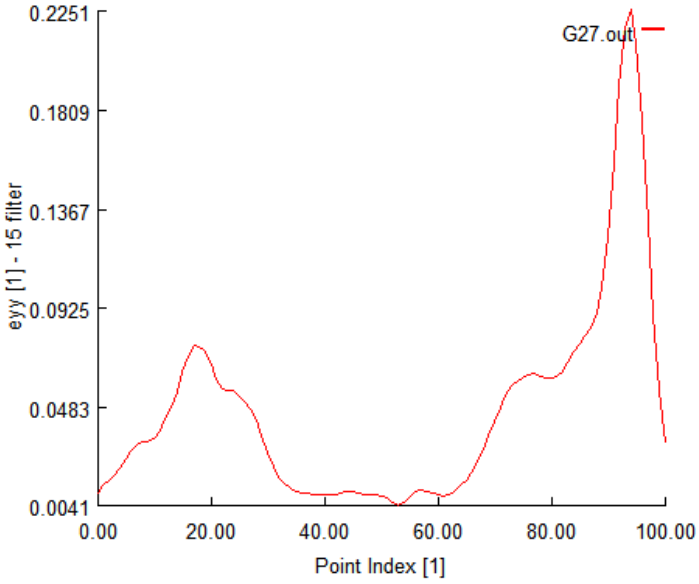
Load Step 27		T:677.4 lbf (3013N); σ: 136.6 ksi (942 Mpa) e_{EXT}: 0.03417
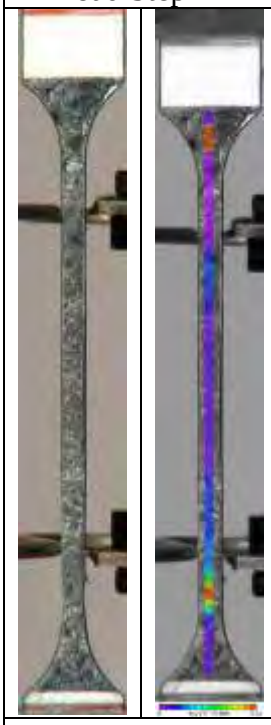		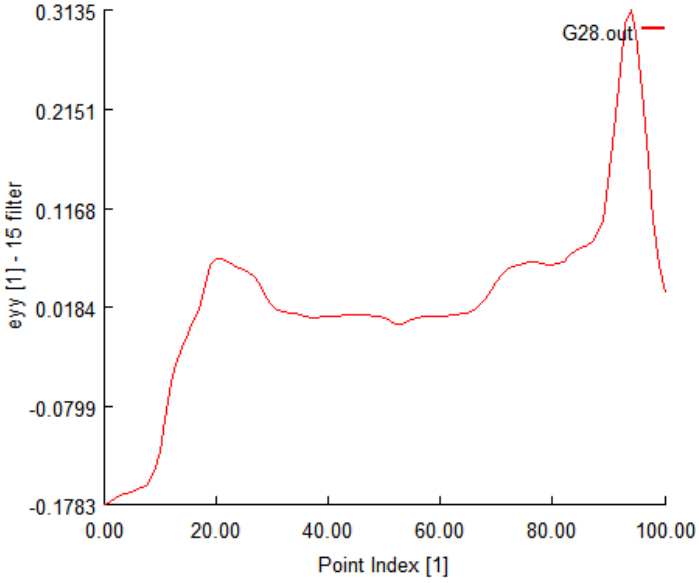
Load Step 28		T:645.5 lbf (2871N); σ: 130.1 ksi (897 Mpa) e_{EXT}: 0.03369

12. TAG DIC 6: test article J

Reference Image	Post Test Image	Global Stress-Strain Behavior of Specimen
		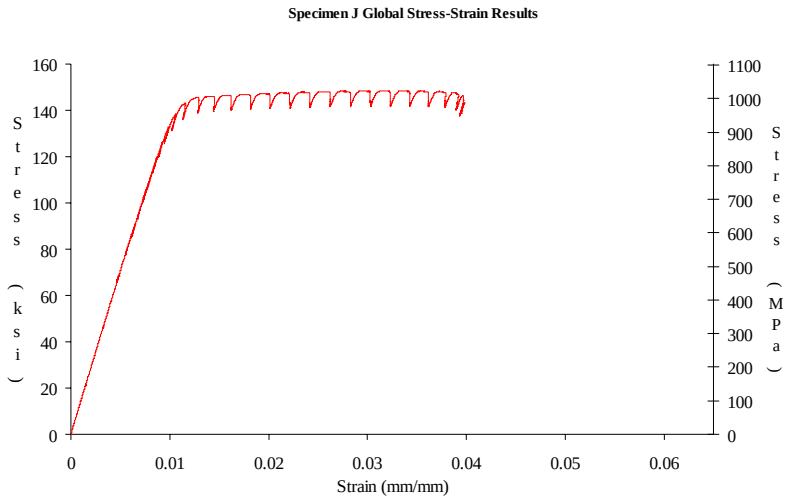 Reference Load (T): 232.9 lbf (1036 N) Reference Stress (σ): 47.0 ksi (324 MPa) Reference Extensometer Strain (ε_{EXT}): 0.00330

Raw Image	e_{yy} Contour	TAG DIC 6
		e_{yy} (Point 0 = Top of Gage; Point 100 = Bottom of Gage)
		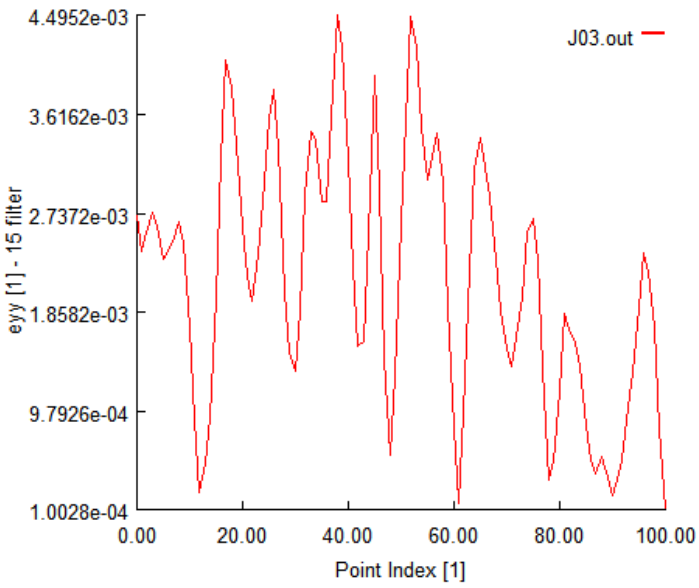
Load Step 3		T:232.9 lbf (1036N); σ: 47.0 ksi (324 Mpa) e_{EXT}: 0.00330
		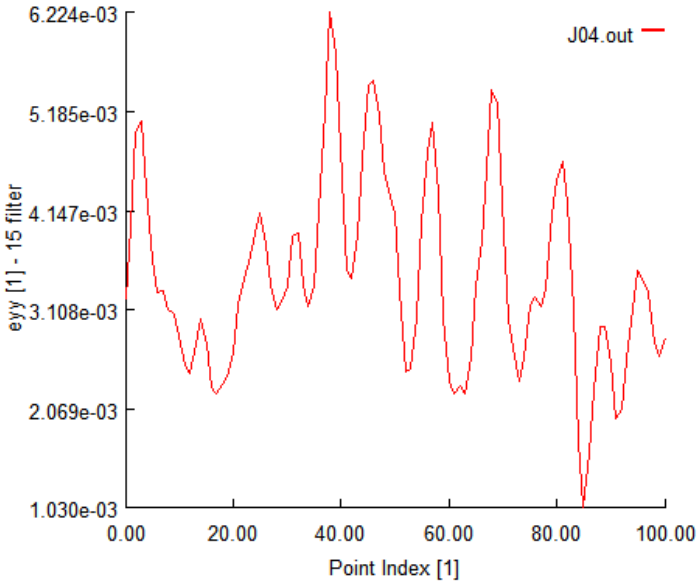
Load Step 4		T:341.5 lbf (1519N); σ: 68.8 ksi (475 Mpa) e_{EXT}: 0.00486

Raw Image	e_{yy} Contour	TAG DIC 6
		e_{yy} (Point 0 = Top of Gage; Point 100 = Bottom of Gage)
		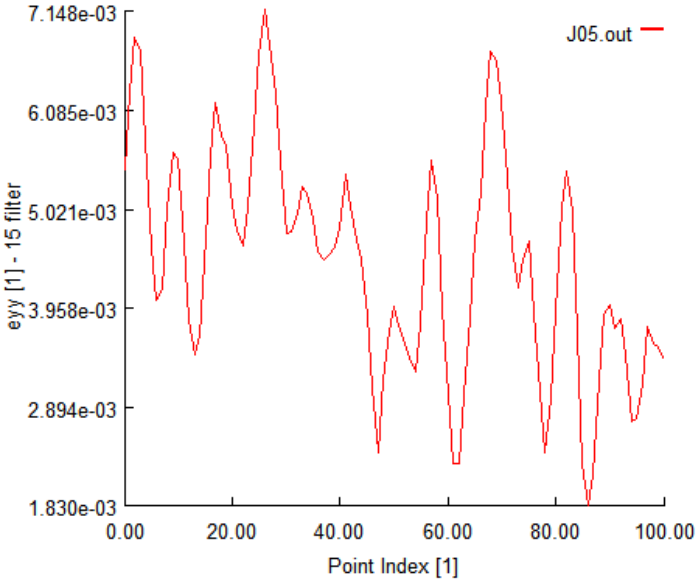
Load Step 5		T:411.7 lbf (1831N); σ: 83.0 ksi (572 Mpa) e_{EXT}: 0.00589
	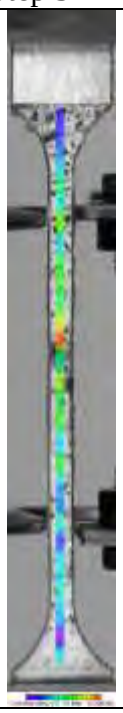	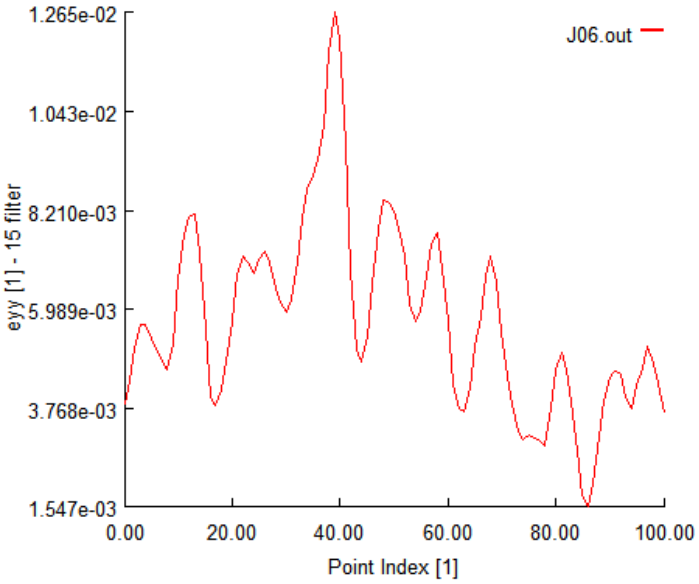
Load Step 6		T:450.4 lbf (2003N); σ: 90.8 ksi (626 Mpa) e_{EXT}: 0.00650

Raw Image	e_{yy} Contour	TAG DIC 6
		e_{yy} (Point 0 = Top of Gage; Point 100 = Bottom of Gage)
		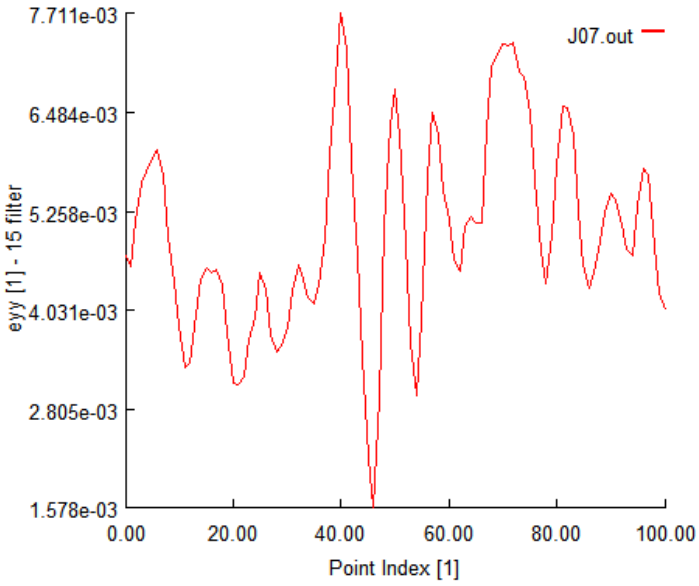
Load Step 7		T:491.4 lbf (2186N); σ: 99.1 ksi (683 Mpa) e_{EXT}: 0.00712
		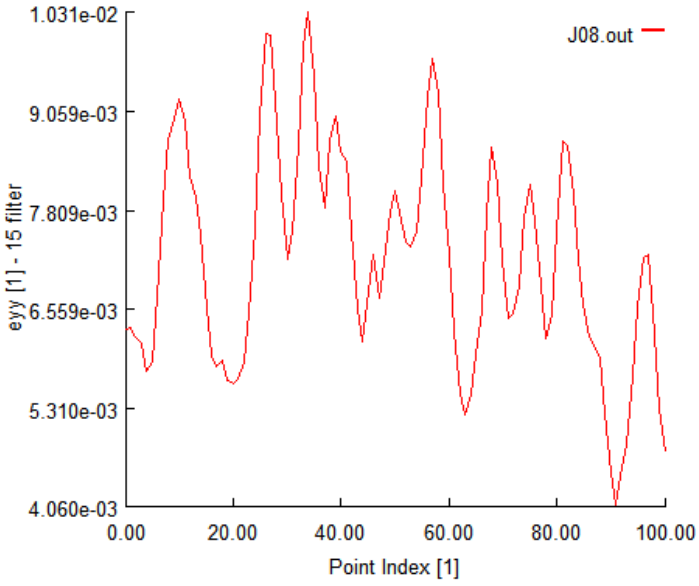
Load Step 8		T:529.2 lbf (2354N); σ: 106.7 ksi (736 Mpa) e_{EXT}: 0.00769

Raw Image	e_{yy} Contour	TAG DIC 6
		e_{yy} (Point 0 = Top of Gage; Point 100 = Bottom of Gage)
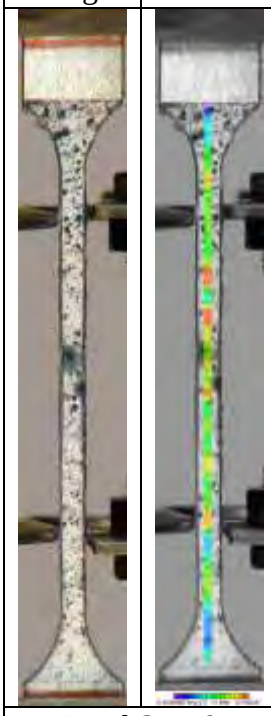		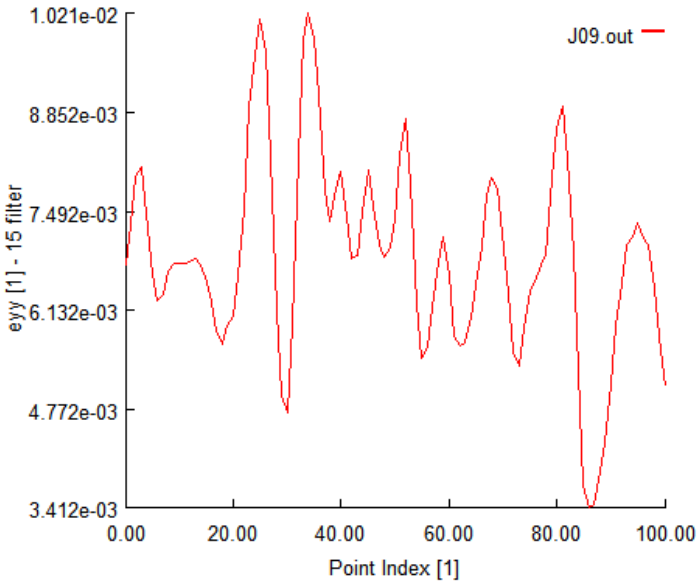
Load Step 9		T:563.6 lbf (2507N); σ: 113.6 ksi (783 Mpa) e_{EXT}: 0.00823
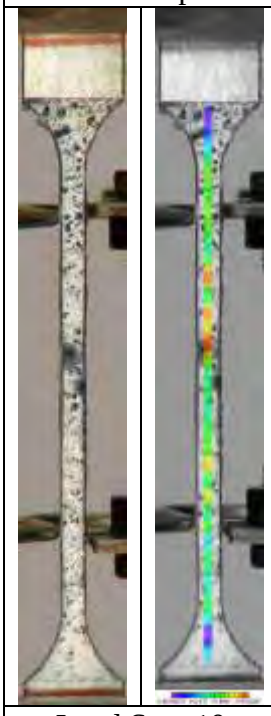		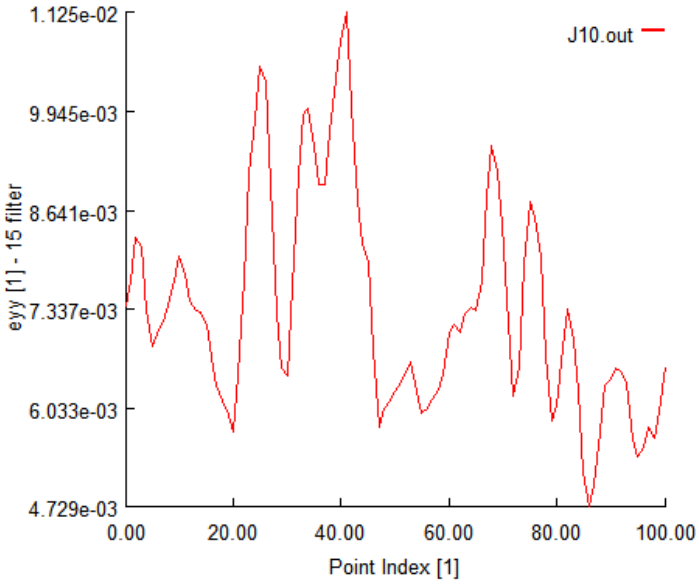
Load Step 10		T:594.0 lbf (2642N); σ: 119.8 ksi (826 Mpa) e_{EXT}: 0.00872

Raw Image	e_{yy} Contour	TAG DIC 6
		e_{yy} (Point 0 = Top of Gage; Point 100 = Bottom of Gage)
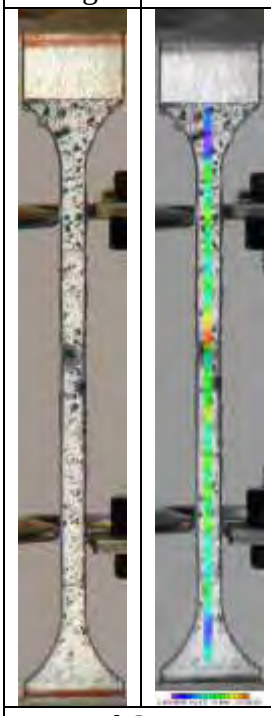		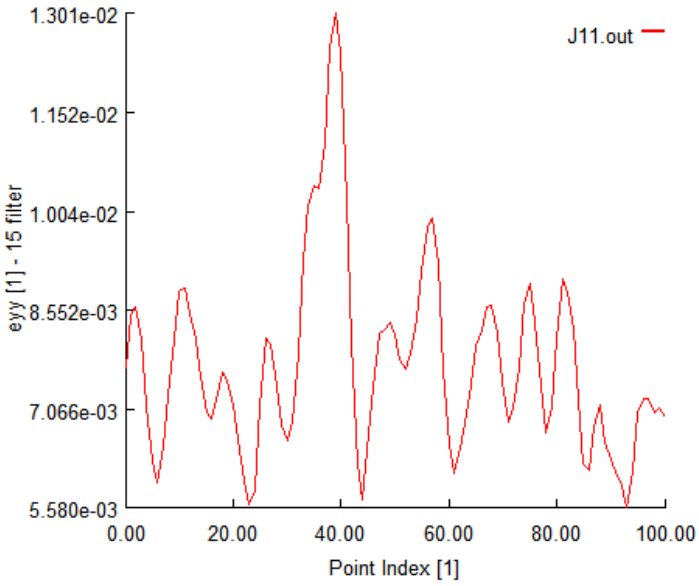
Load Step 11		T:626.9 lbf (2788N); σ: 126.4 ksi (871 Mpa) e_{EXT}: 0.00928
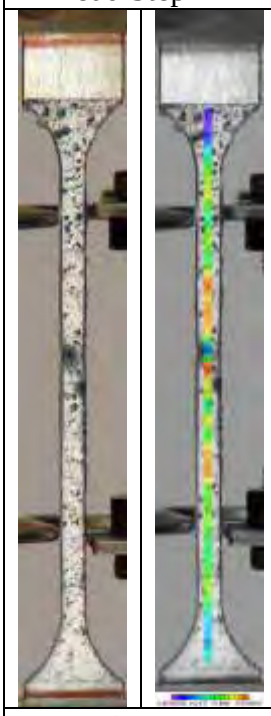		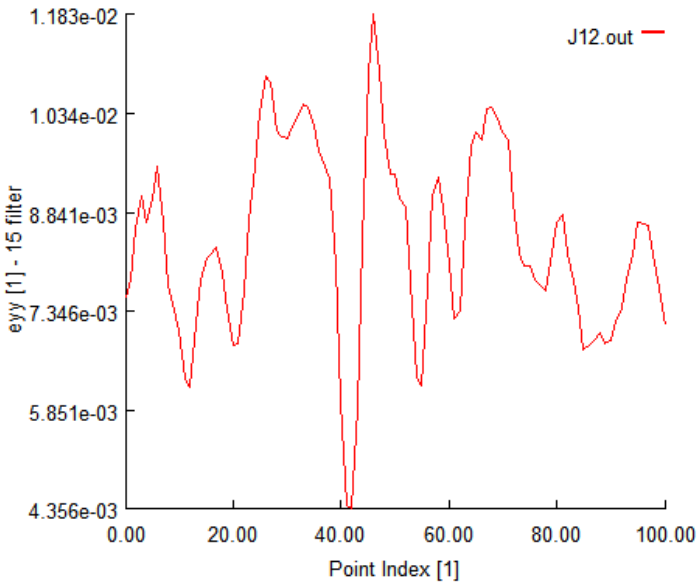
Load Step 12		T:658.3 lbf (2928N); σ: 132.7 ksi (915 Mpa) e_{EXT}: 0.00988

Raw Image	e_{yy} Contour	TAG DIC 6
		e_{yy} (Point 0 = Top of Gage; Point 100 = Bottom of Gage)
	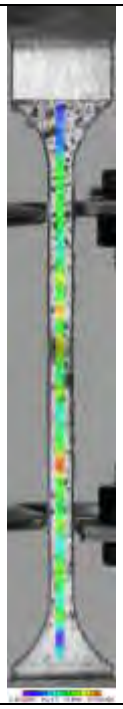	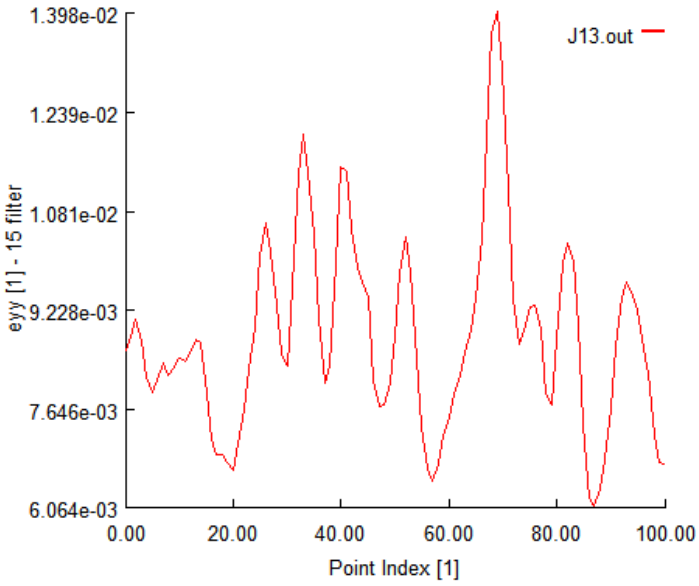
Load Step 13		T:686.9 lbf (3055N); σ: 138.5 ksi (955 Mpa) e_{EXT}: 0.01060
		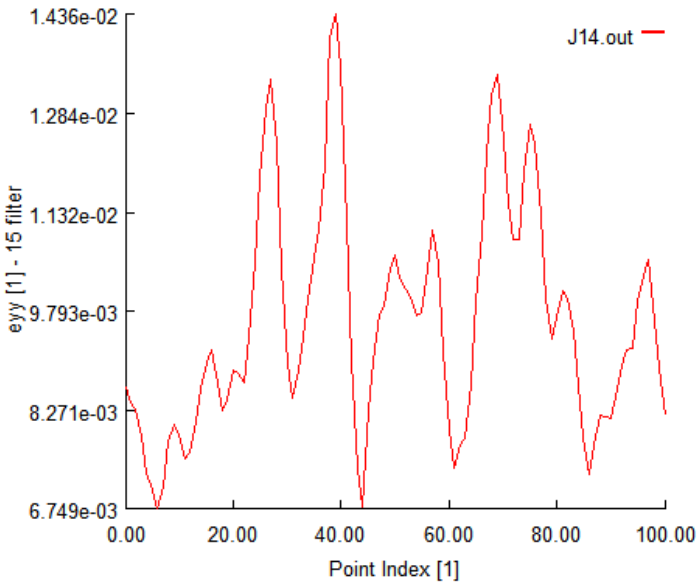
Load Step 14		T:710.4 lbf (3160N); σ: 143.2 ksi (987.5 Mpa) e_{EXT}: 0.01156

Raw Image	e_{yy} Contour	TAG DIC 6
		e_{yy} (Point 0 = Top of Gage; Point 100 = Bottom of Gage)
		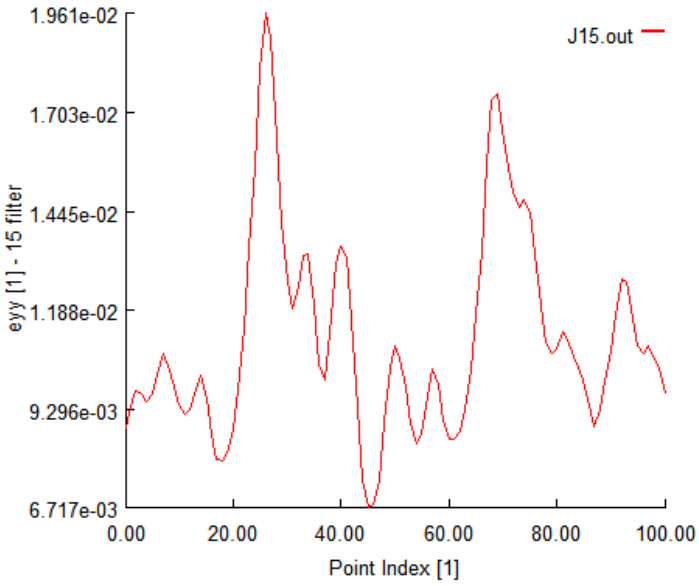
Load Step 15		T:722.1 lbf (3212N); σ: 145.6 ksi (1004 Mpa) e_{EXT}: 0.0129
	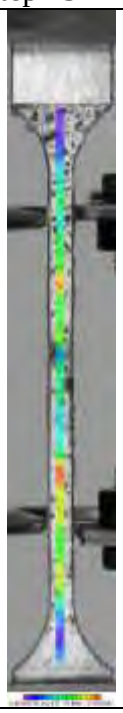	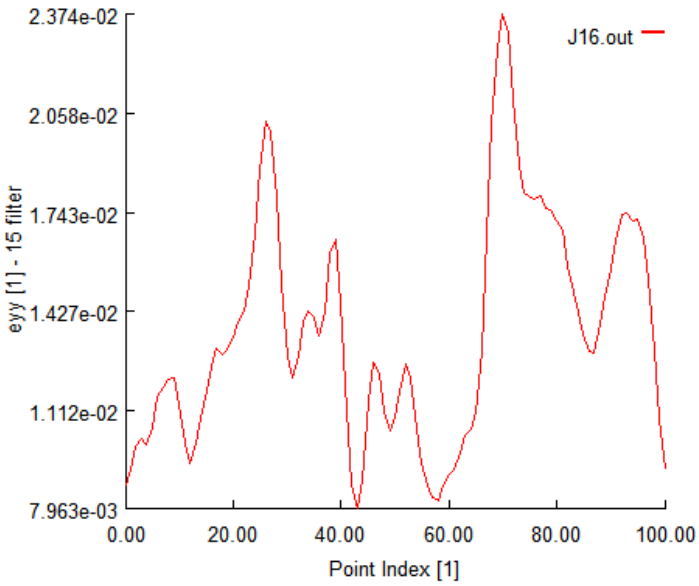
Load Step 16		T:724.1 lbf (3221N); σ: 146.0 ksi (1007 Mpa) e_{EXT}: 0.01447

Raw Image	e_{yy} Contour	TAG DIC 6
		e_{yy} (Point 0 = Top of Gage; Point 100 = Bottom of Gage)
		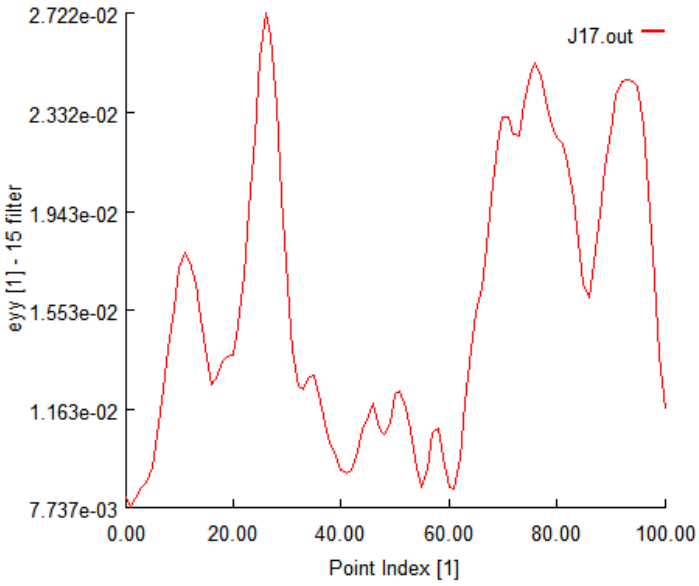
Load Step 17		T:726.1 lbf (3230N); σ: 146.4 ksi (1009 Mpa) e_{EXT}: 0.01617
		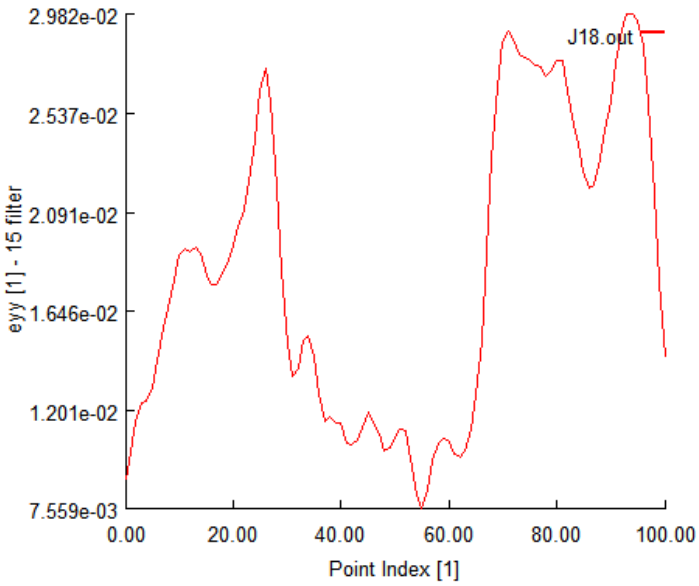
Load Step 18		T:727.6 lbf (3237N); σ: 146.7 ksi (1011Mpa) e_{EXT}: 0.01808

Raw Image	e_{yy} Contour	TAG DIC 6
		e_{yy} (Point 0 = Top of Gage; Point 100 = Bottom of Gage)
		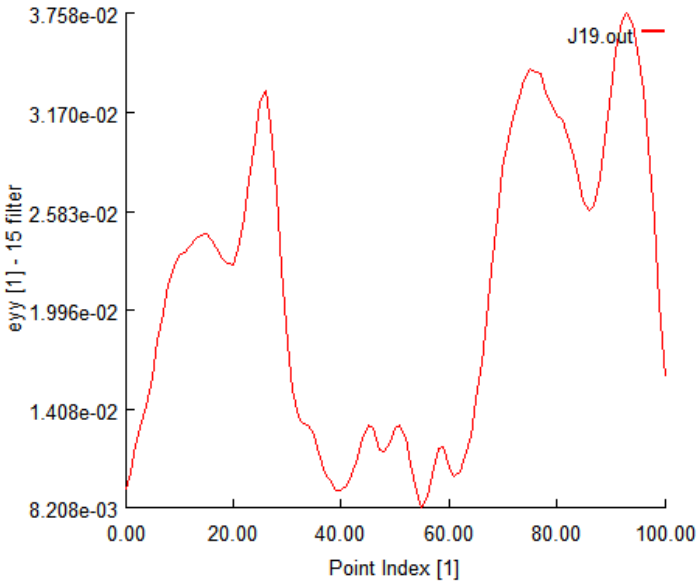
Load Step 19		T:729.5 lbf (3245N); σ: 147.1 ksi (1014 Mpa) e_{EXT}: 0.02002
		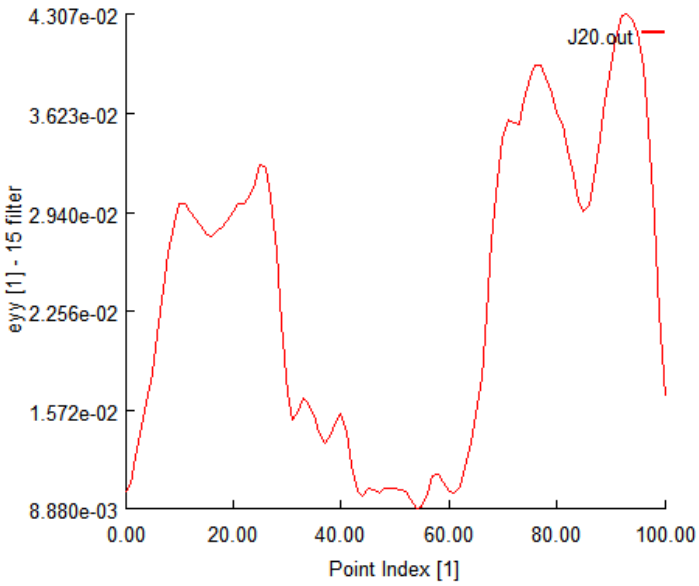
Load Step 20		T:731.1 lbf (3252N); σ: 147.4 ksi (1016 Mpa) e_{EXT}: 0.02200

Raw Image	e_{yy} Contour	TAG DIC 6
		e_{yy} (Point 0 = Top of Gage; Point 100 = Bottom of Gage)
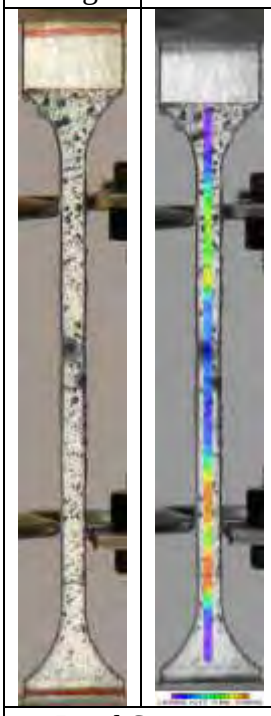		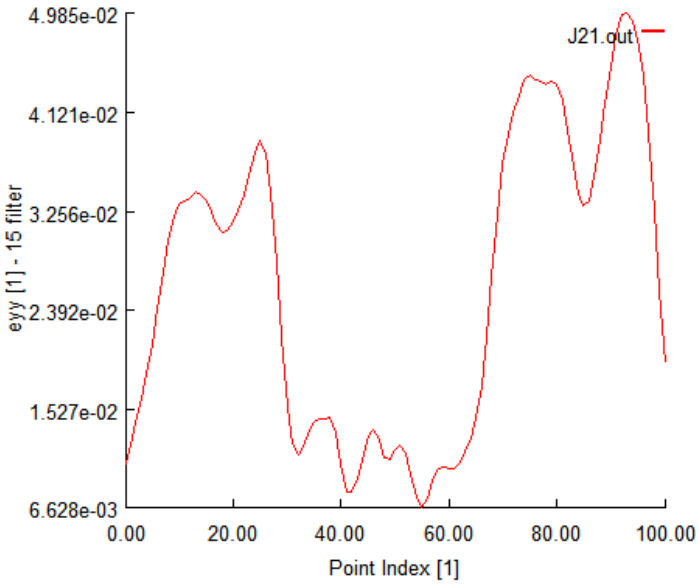
Load Step 21		T:732.6 lbf (3259N); σ: 147.7 ksi (1018 Mpa) e_{EXT}: 0.02402
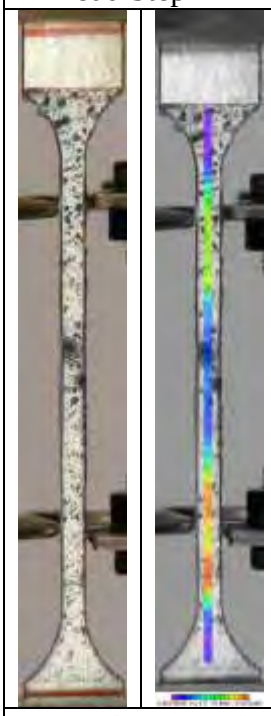		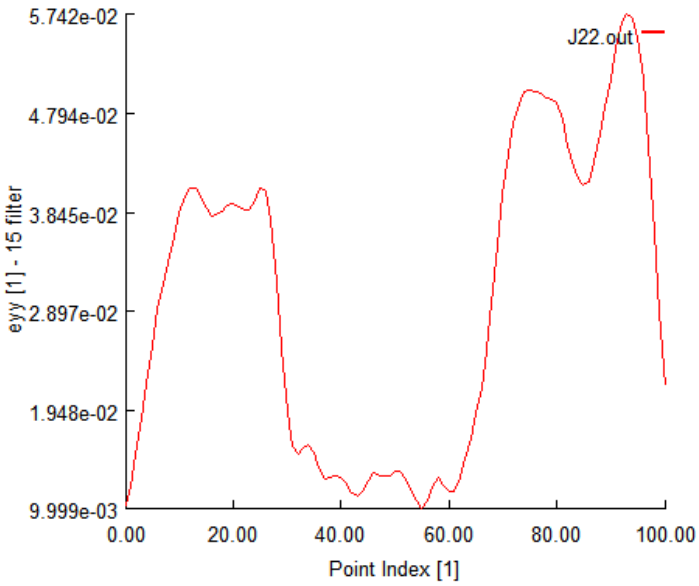
Load Step 22		T:733.8 lbf (3264N); σ: 147.9 ksi (1020 Mpa) e_{EXT}: 0.02608

Raw Image	e_{yy} Contour	TAG DIC 6
		e_{yy} (Point 0 = Top of Gage; Point 100 = Bottom of Gage)
		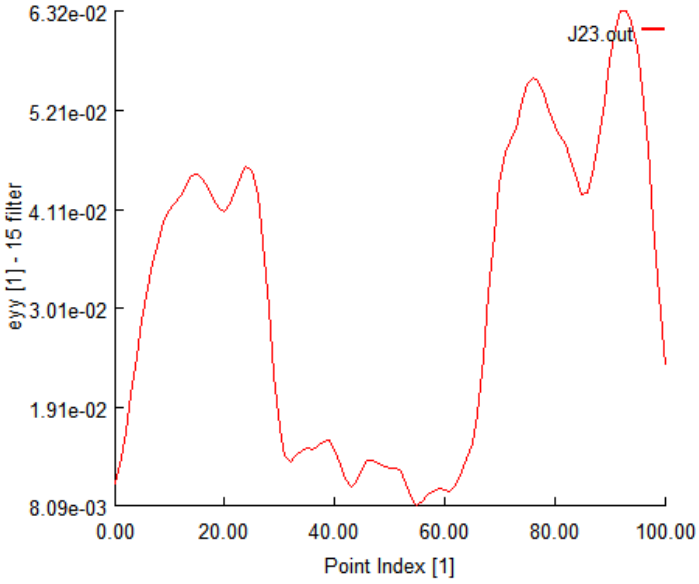
Load Step 23		T:734.9 lbf (3269N); σ: 148.2 ksi (1022 Mpa) e_{EXT}: 0.02811
		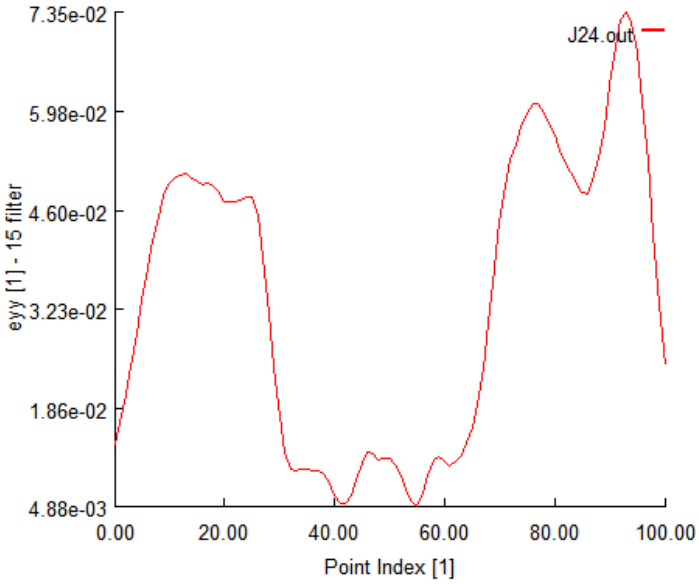
Load Step 24		T:735.3 lbf (3271N); σ: 148.2 ksi (1022 Mpa) e_{EXT}: 0.03025

Raw Image	e_{yy} Contour	TAG DIC 6
		e_{yy} (Point 0 = Top of Gage; Point 100 = Bottom of Gage)
		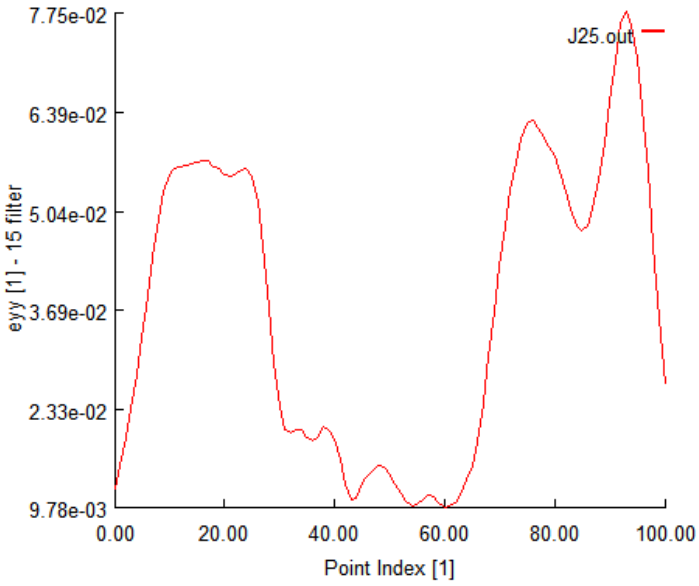
Load Step 25		T:735.3 lbf (3271N); σ: 148.2 ksi (1022 Mpa) e_{EXT}: 0.03221
		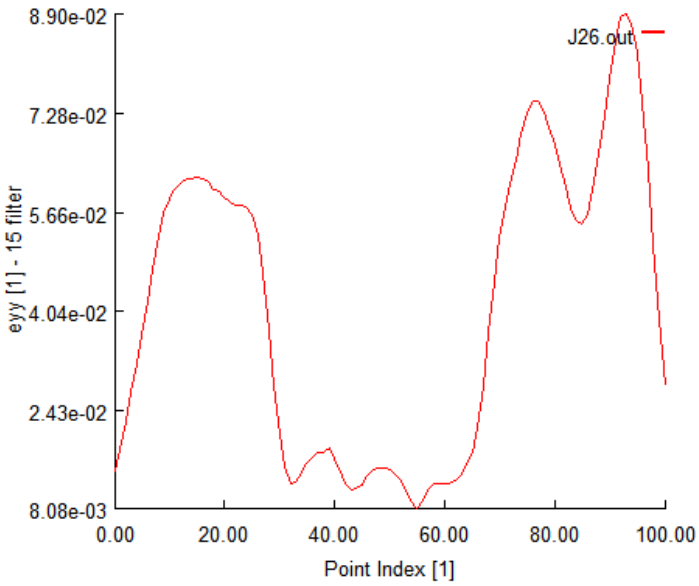
Load Step 26		T:735.3 lbf (3271N); σ: 148.2 ksi (1022 Mpa) e_{EXT}: 0.03416

Raw Image	e_{yy} Contour	TAG DIC 6
		e_{yy} (Point 0 = Top of Gage; Point 100 = Bottom of Gage)
		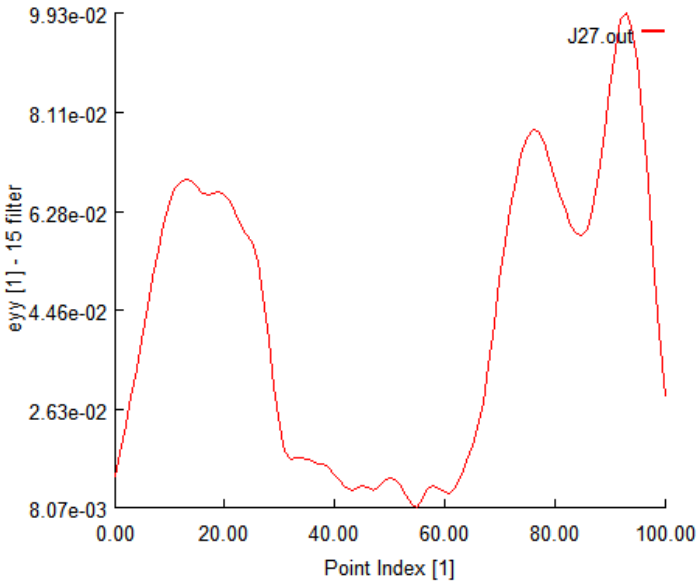
Load Step 27		T:734.2 lbf (3266N); σ: 148.0 ksi (1021 Mpa) e_{EXT}: 0.03609
		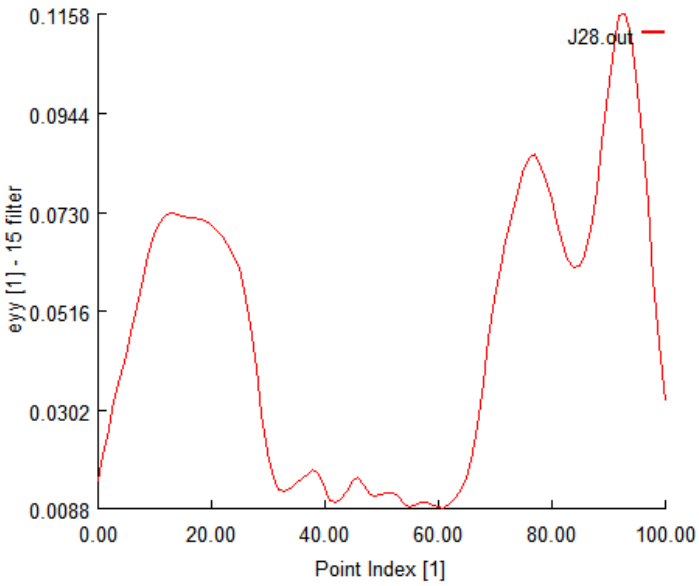
Load Step 28		T:732.4 lbf (3258N); σ: 147.7 ksi (1018 Mpa) e_{EXT}: 0.03783

Raw Image	e_{yy} Contour	TAG DIC 6
		e_{yy} (Point 0 = Top of Gage; Point 100 = Bottom of Gage)
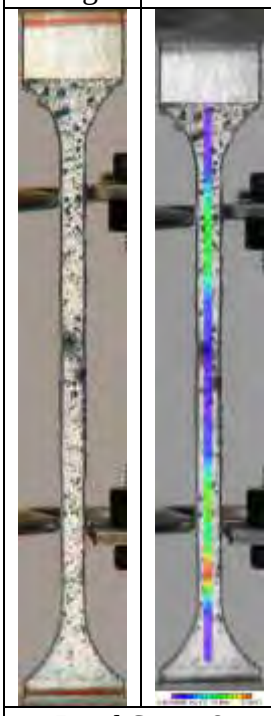		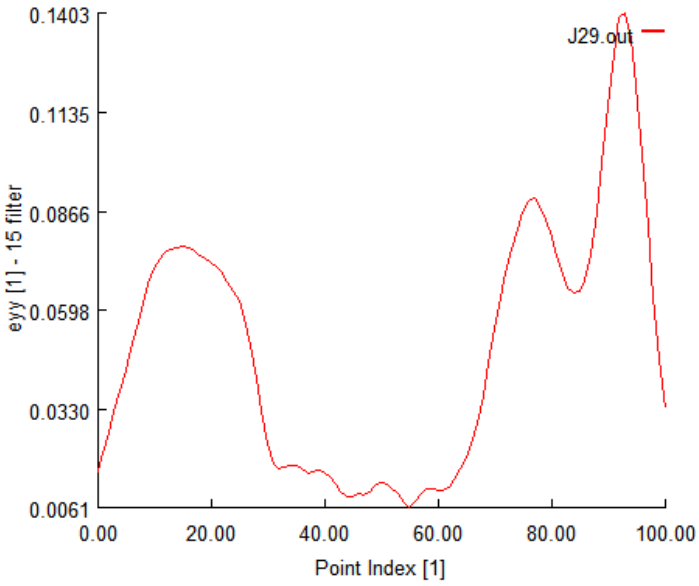
Load Step 29		T:728.4 lbf (3240N); σ: 146.9 ksi (1012 Mpa) e_{EXT}: 0.03918
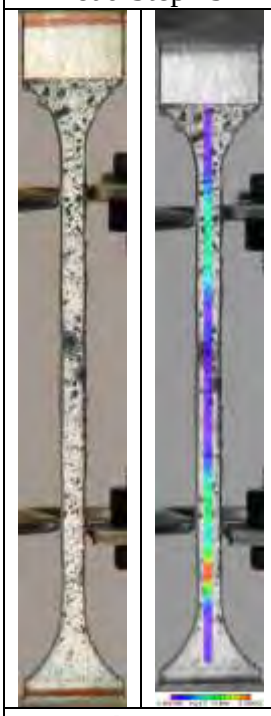		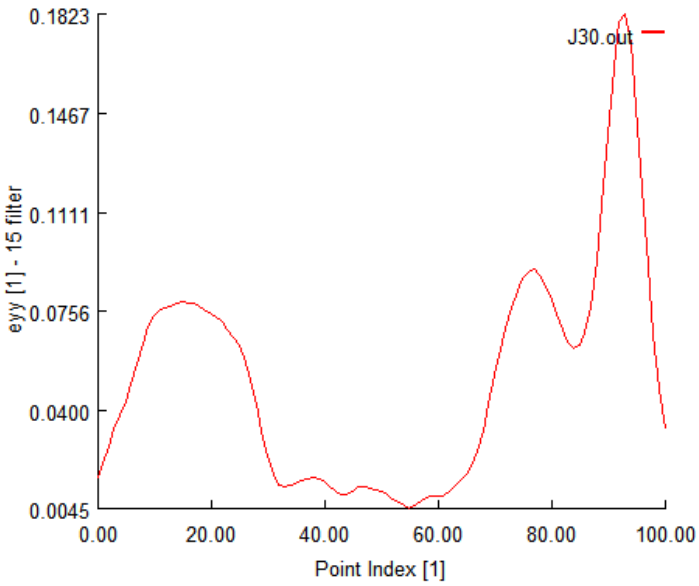
Load Step 30		T:714.9 lbf (3180N); σ: 144.1 ksi (994 Mpa) e_{EXT}: 0.03974

Raw Image	e_{yy} Contour	TAG DIC 6
		e_{yy} (Point 0 = Top of Gage; Point 100 = Bottom of Gage)
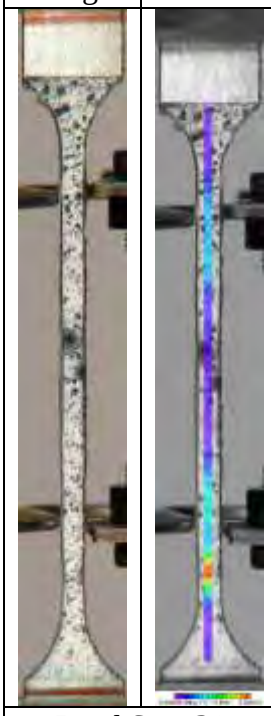		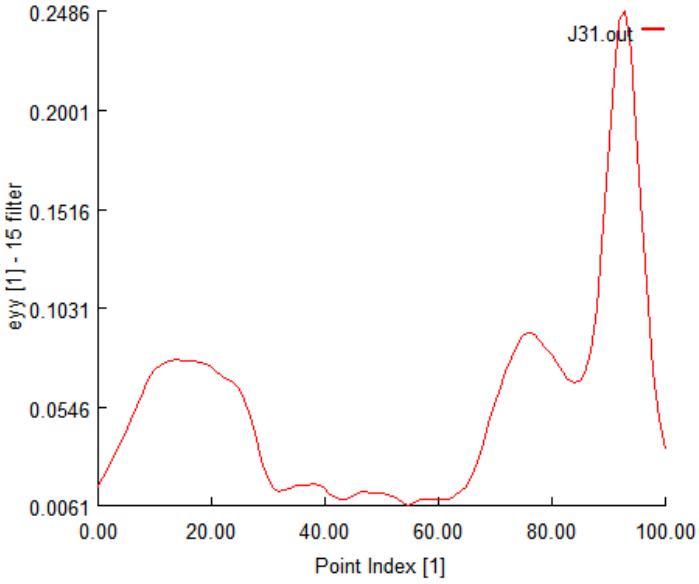
Load Step 31		T:689.0 lbf (3065N); σ: 138.9 ksi (958 Mpa) e_{EXT}: 0.03952
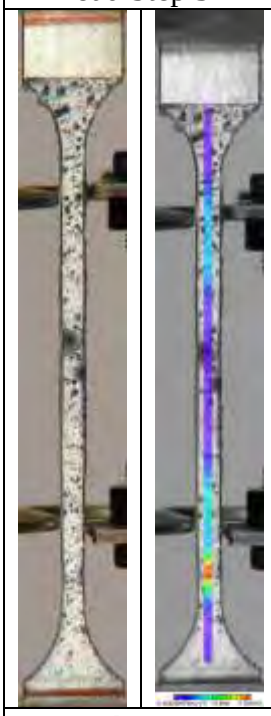		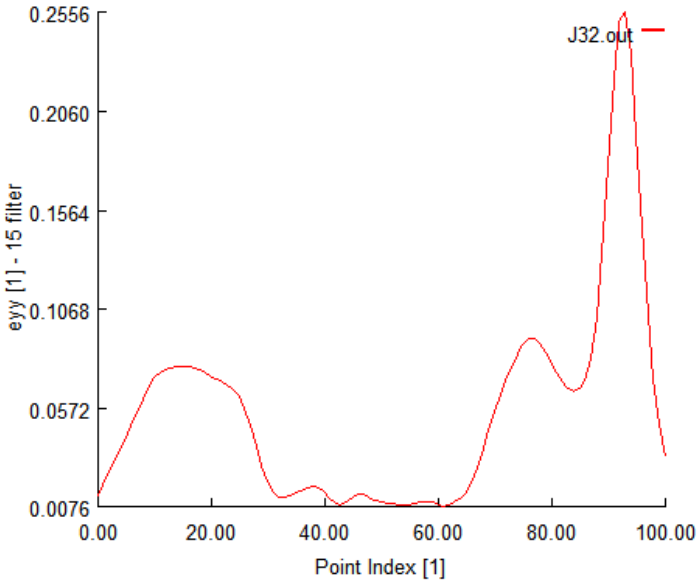
Load Step 32		T:687.9 lbf (3060N); σ: 138.7 ksi (956 Mpa) e_{EXT}: 0.03951

13. TAG DIC 7: test article K

Reference Image	Post Test Image	Global Stress-Strain Behavior of Specimen
		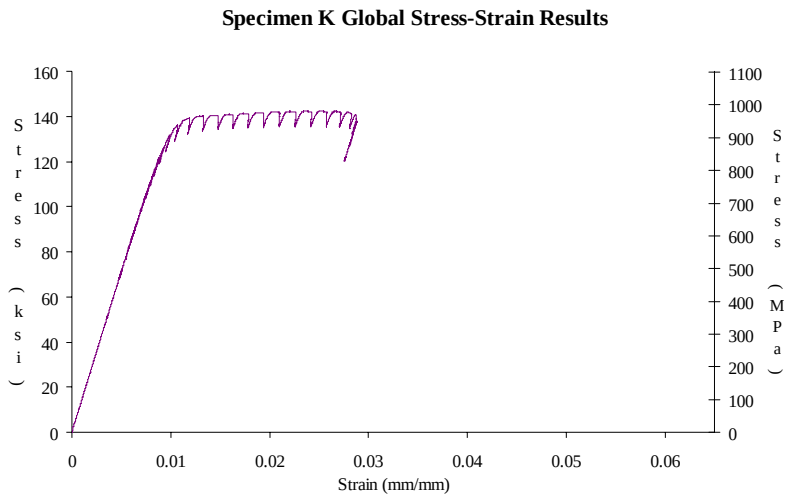 Reference Load (T): 257.6 lbf (1146 N) Reference Stress (σ): 51.9 ksi (358 MPa) Reference Extensometer Strain (ε_{EXT}): 0.00363

Raw Image	eyy Contour	TAG DIC 7
		e_{yy} (Point 0 = Top of Gage; Point 100 = Bottom of Gage)
		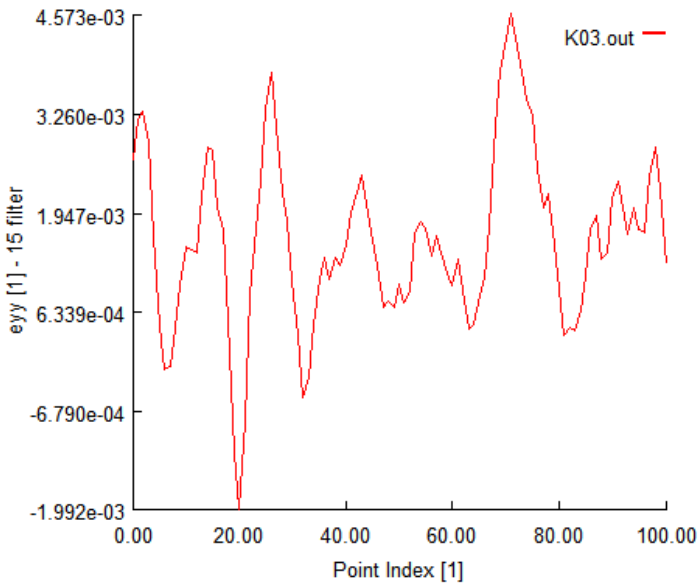
Load Step 3		T:257.6 lbf (1146N); σ: 51.9 ksi (358 Mpa) e_{EXT}: 0.00363
		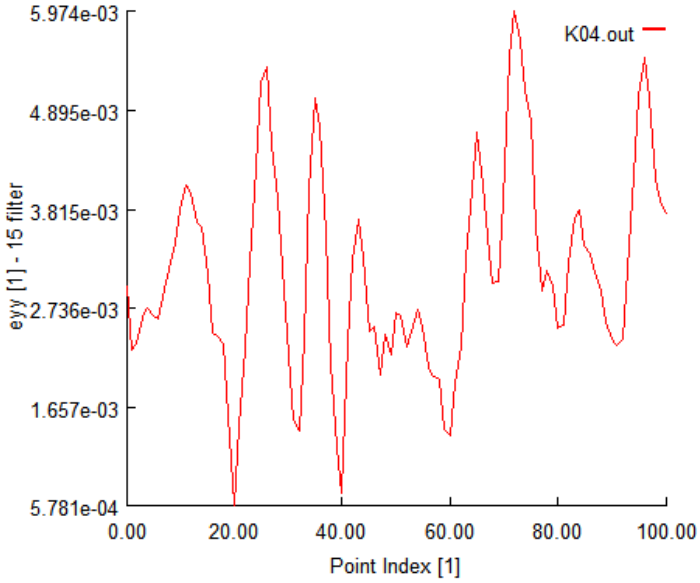
Load Step 4		T:358.4 lbf (1594N); σ: 72.2 ksi (498 Mpa) e_{EXT}: 0.00507

Raw Image	eyy Contour	TAG DIC 7
		e_{yy} (Point 0 = Top of Gage; Point 100 = Bottom of Gage)
		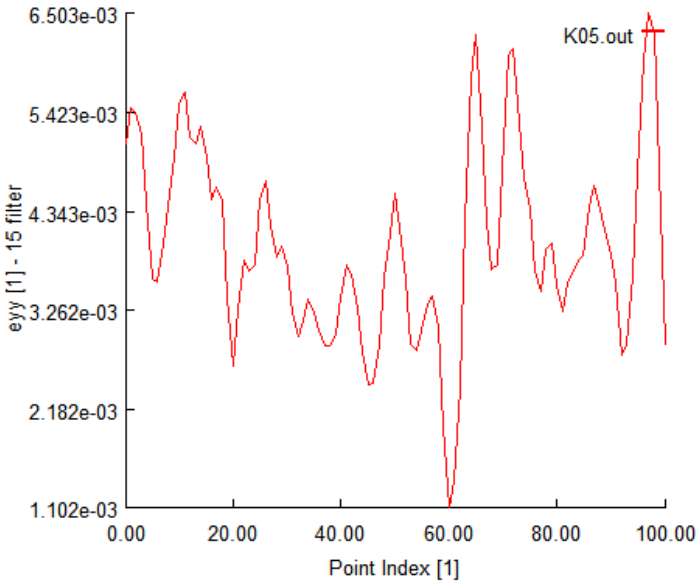
Load Step 5		T:412.0 lbf (1833N); σ: 83.1 ksi (573 Mpa) e_{EXT}: 0.00584
		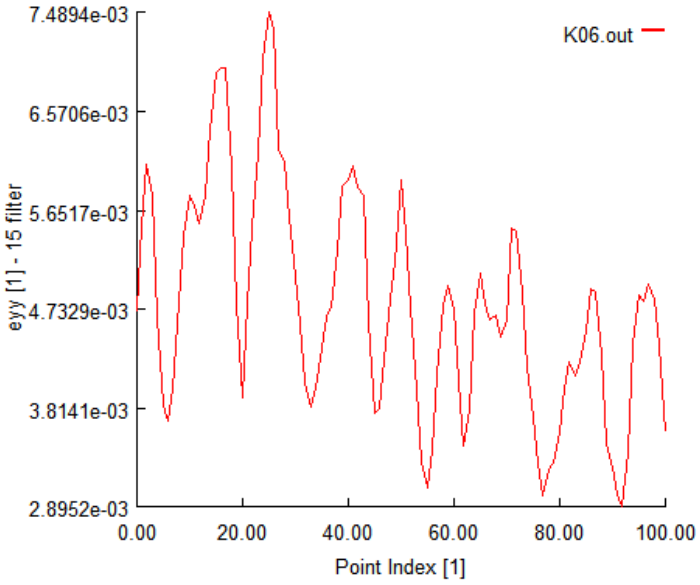
Load Step 6		T:428.1 lbf (1904N); σ: 86.3 ksi (595 Mpa) e_{EXT}: 0.00608

Raw Image	eyy Contour	TAG DIC 7
		e_{yy} (Point 0 = Top of Gage; Point 100 = Bottom of Gage)
		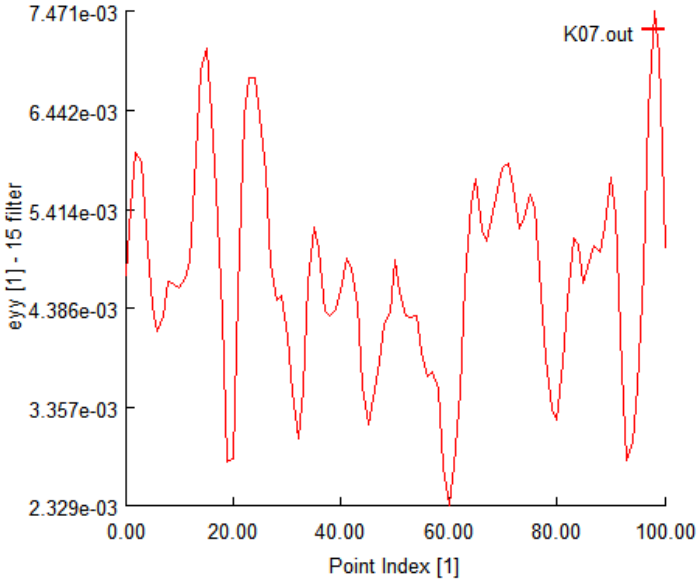
Load Step 7		T:459.5 lbf (2044N); σ: 92.6 ksi (639 Mpa) e_{EXT}: 0.00654
		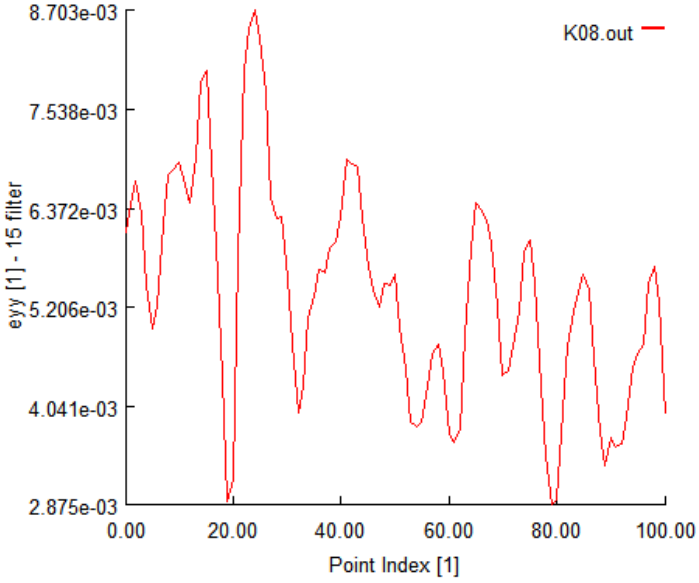
Load Step 8		T:493.1 lbf (2193N); σ: 99.4 ksi (685 Mpa) e_{EXT}: 0.00704

Raw Image	eyy Contour	TAG DIC 7
		e_{yy} (Point 0 = Top of Gage; Point 100 = Bottom of Gage)
		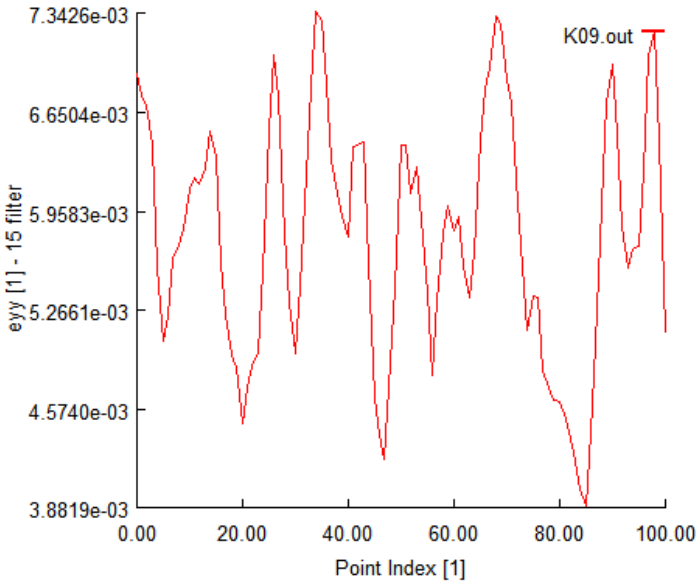
Load Step 9		T:524.7 lbf (2334N); σ: 105.8 ksi (729 Mpa) e_{EXT}: 0.00752
		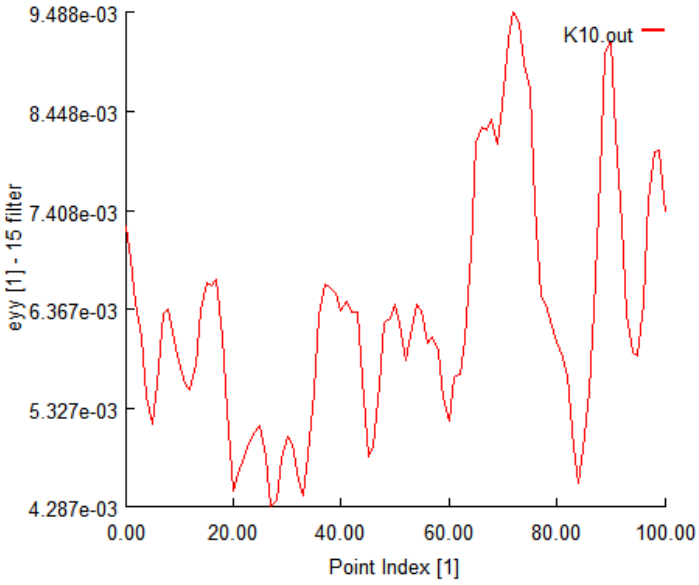
Load Step 10		T:553.5 lbf (2462N); σ: 111.6 ksi (769 Mpa) e_{EXT}: 0.00798

Raw Image	eyy Contour	TAG DIC 7
		e_{yy} (Point 0 = Top of Gage; Point 100 = Bottom of Gage)
		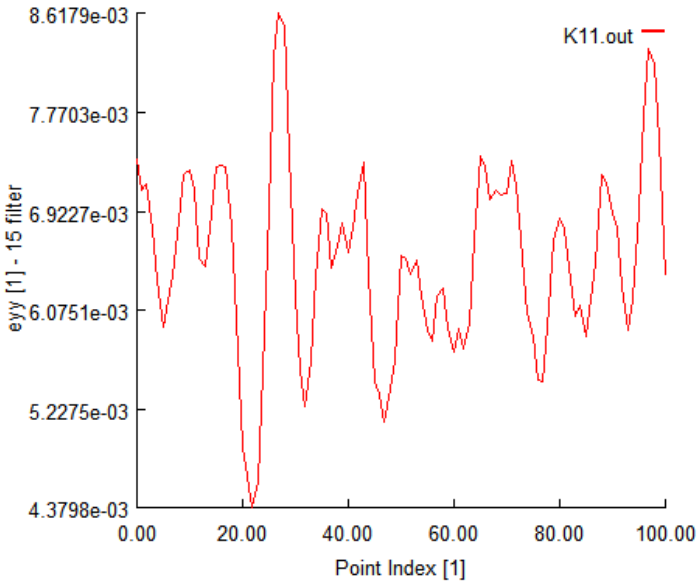
Load Step 11		T:580.8 lbf (2584N); σ: 117.1 ksi (807.4 Mpa) e_{EXT}: 0.00843
		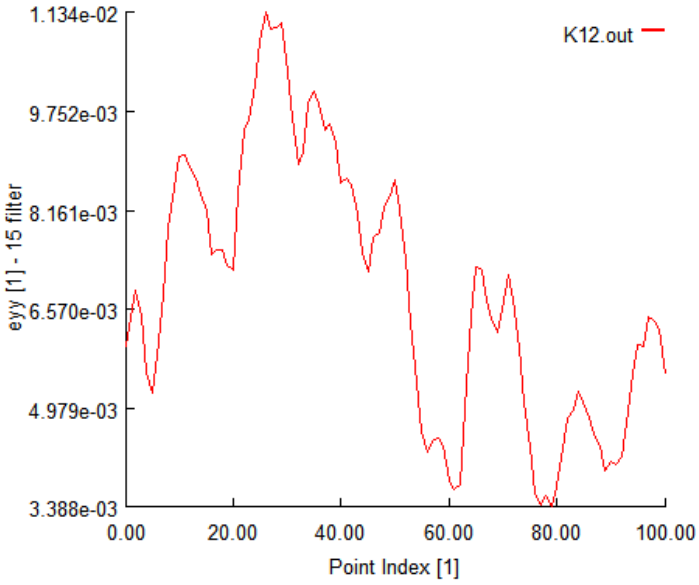
Load Step 12		T:604.3 lbf (2688N); σ: 121.8 ksi (840 Mpa) e_{EXT}: 0.00884

Raw Image	eyy Contour	TAG DIC 7
		e_{yy} (Point 0 = Top of Gage; Point 100 = Bottom of Gage)
		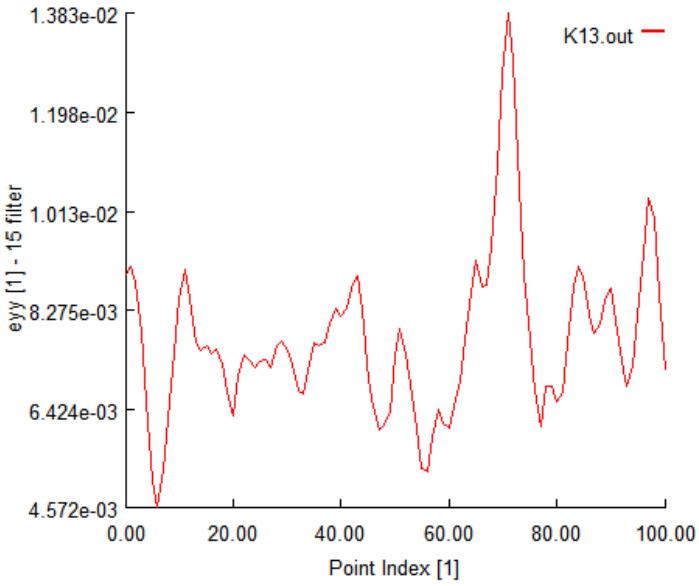
Load Step 13		T:626.5 lbf (2687N); σ: 126.3 ksi (871 Mpa) e_{EXT}: 0.00928
		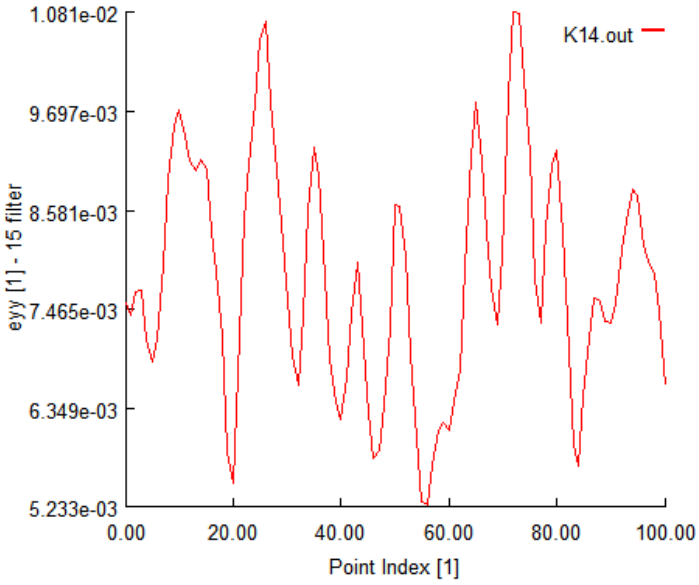
Load Step 14		T:653.4 lbf (2906N); σ: 131.7 ksi (908 Mpa) e_{EXT}: 0.00991

Raw Image	eyy Contour	TAG DIC 7
		e_{yy} (Point 0 = Top of Gage; Point 100 = Bottom of Gage)
		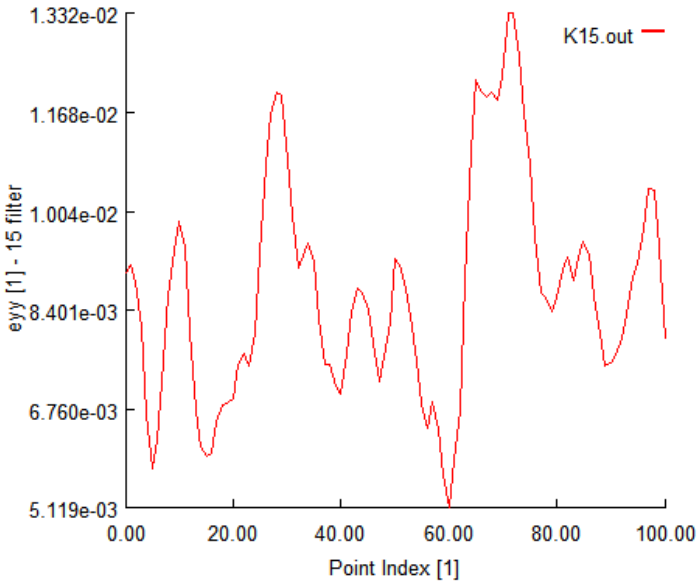
Load Step 15		T:675.8 lbf (3006N); σ: 136.3 ksi (939 Mpa) e_{EXT}: 0.01072
		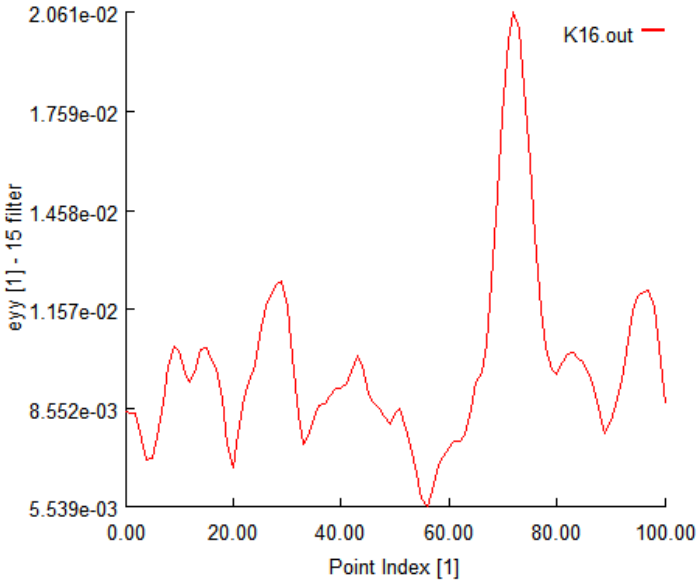
Load Step 16		T:691.0 lbf (3074N); σ: 139.3 ksi (961 Mpa) e_{EXT}: 0.01187

Raw Image	eyy Contour	TAG DIC 7
		e_{yy} (Point 0 = Top of Gage; Point 100 = Bottom of Gage)
		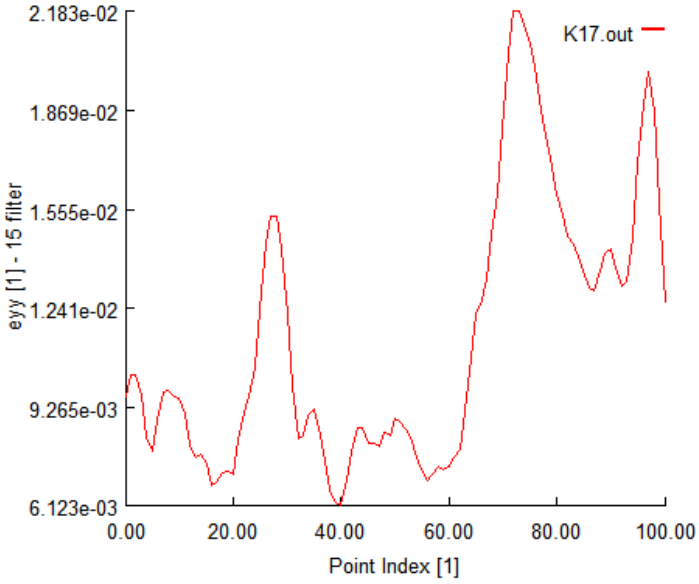
Load Step 17		T:695.1 lbf (3091N); σ: 140.1 ksi (966 Mpa) e_{EXT}: 0.01328
		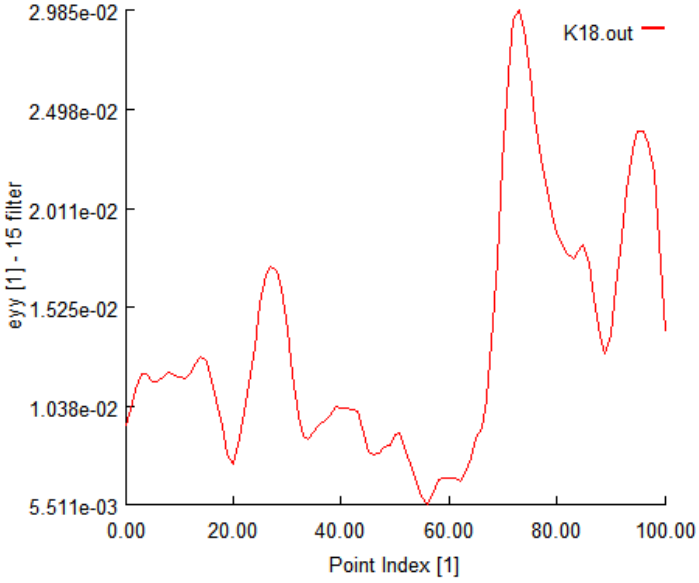
Load Step 18		T:696.9 lbf (3100N); σ: 140.5 ksi (969 Mpa) e_{EXT}: 0.01476

Raw Image	eyy Contour	TAG DIC 7
		e_{yy} (Point 0 = Top of Gage; Point 100 = Bottom of Gage)
		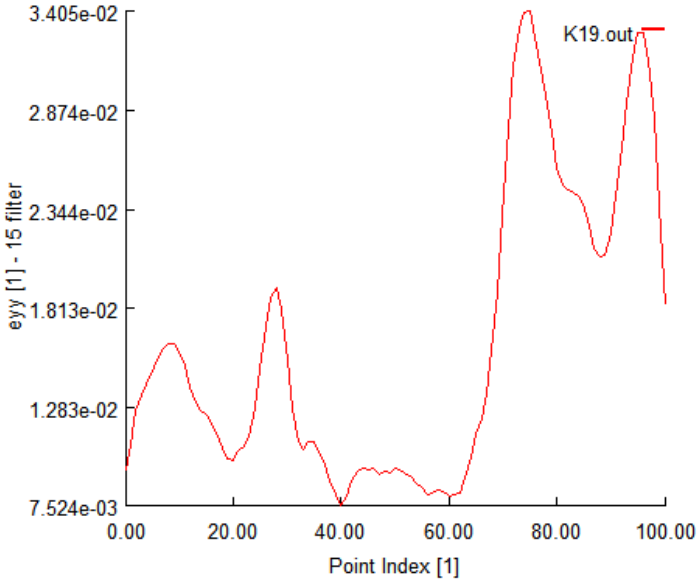
Load Step 19		T:699.0 lbf (3109N); σ: 140.9 ksi (972 Mpa) e_{EXT}: 0.01627
		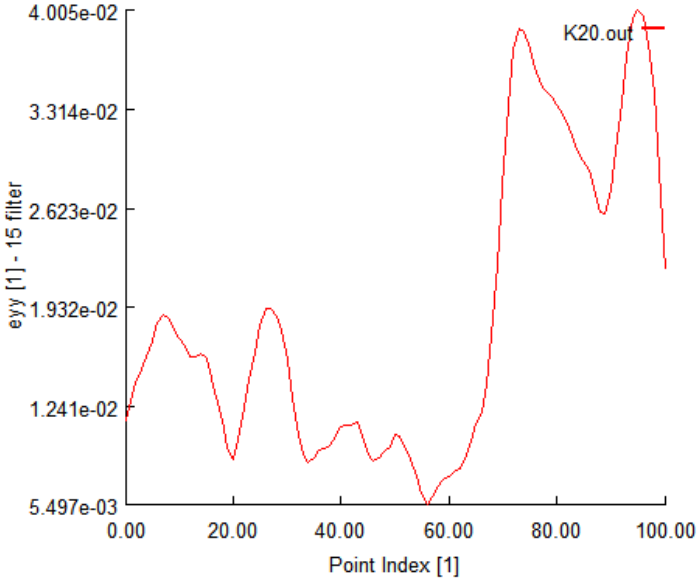
Load Step 20		T:700.2 lbf (3115N); σ: 141.2 ksi (973 Mpa) e_{EXT}: 0.01783

Raw Image	eyy Contour	TAG DIC 7
		e_{yy} (Point 0 = Top of Gage; Point 100 = Bottom of Gage)
		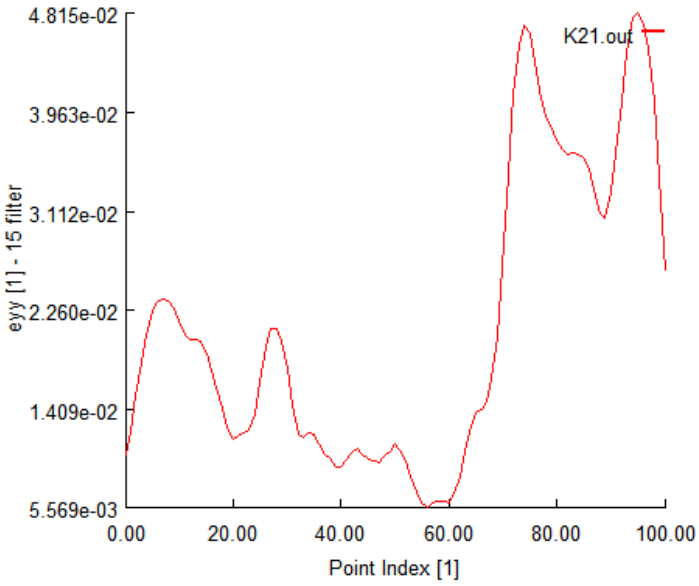
Load Step21		T:701.7 lbf (3121N); σ: 141.5 ksi (975 Mpa) e_{EXT}: 0.01937
		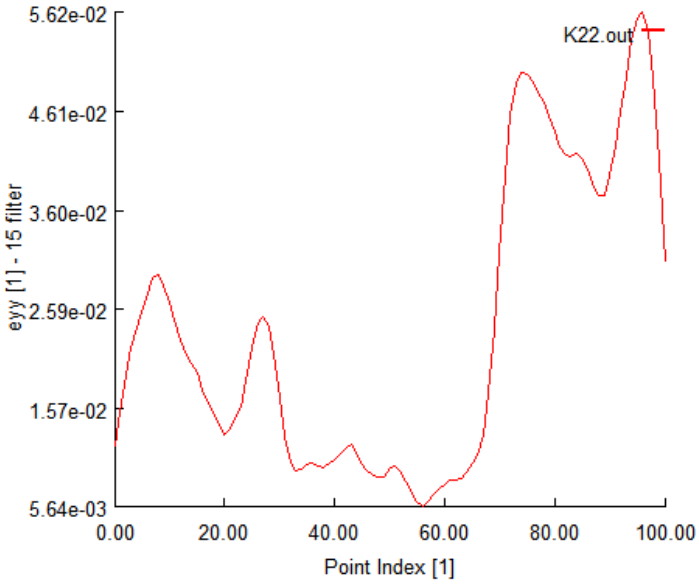
Load Step 22		T:703.1 lbf (3128N); σ: 141.7 ksi (977 Mpa) e_{EXT}: 0.02100

Raw Image	eyy Contour	TAG DIC 7
		e_{yy} (Point 0 = Top of Gage; Point 100 = Bottom of Gage)
		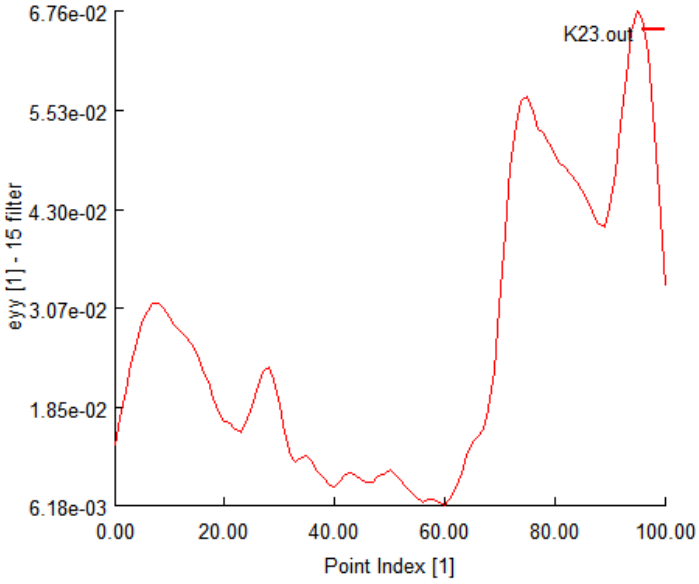
Load Step 23		T:704.2 lbf (3132N); σ: 142.0 ksi (979 Mpa) e_{EXT}: 0.02263
		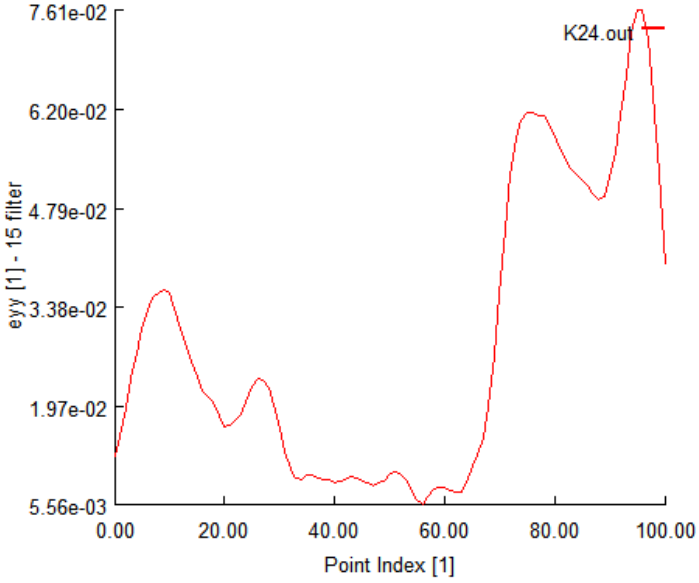
Load Step 24		T:704.6 lbf (3134N); σ: 142.1 ksi (979 Mpa) e_{EXT}: 0.02421

Raw Image	eyy Contour	TAG DIC 7
		e_{yy} (Point 0 = Top of Gage; Point 100 = Bottom of Gage)
	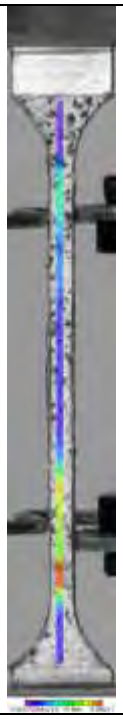	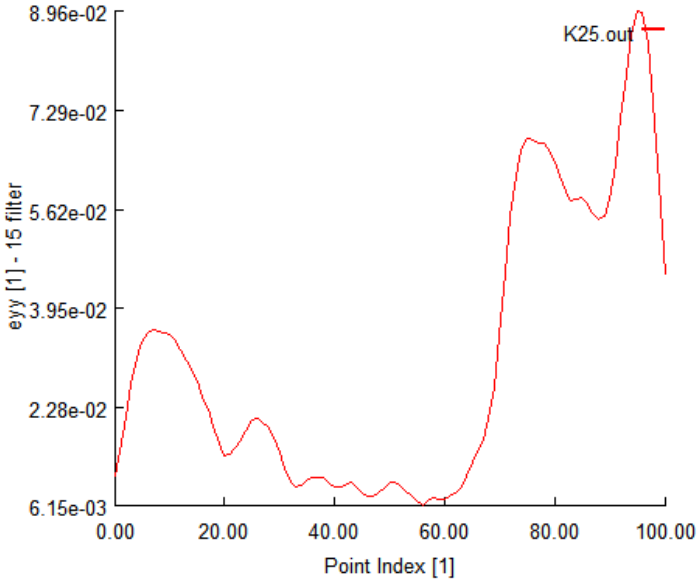
Load Step 25		T:704.2 lbf (3132N); σ: 142.0 ksi (979 Mpa) e_{EXT}: 0.02580
		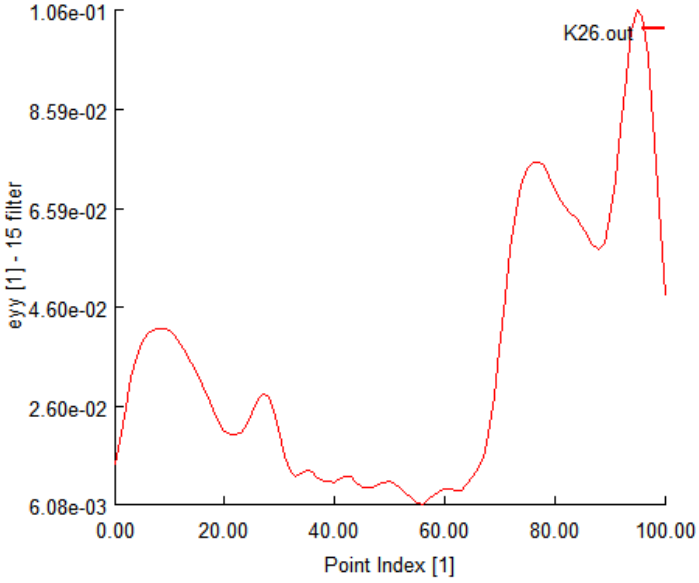
Load Step 26		T:703.0 lbf (3127N); σ: 141.7 ksi (977 Mpa) e_{EXT}: 0.02717

Raw Image	eyy Contour	TAG DIC 7
		e_{yy} (Point 0 = Top of Gage; Point 100 = Bottom of Gage)
	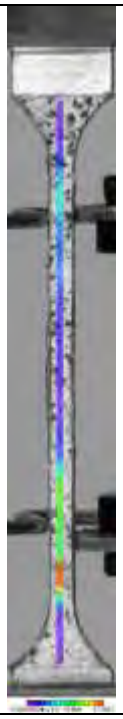	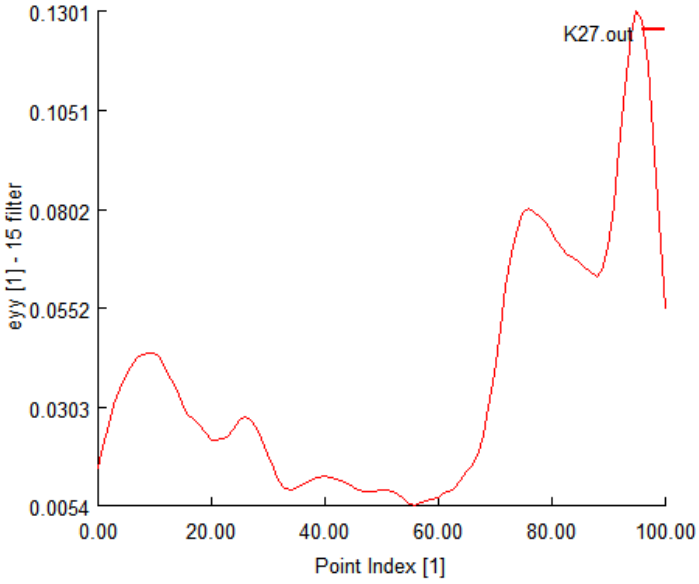
Load Step 27		T:699.1 lbf (3110N); σ: 141.0 ksi (972 Mpa) e_{EXT}: 0.02829
		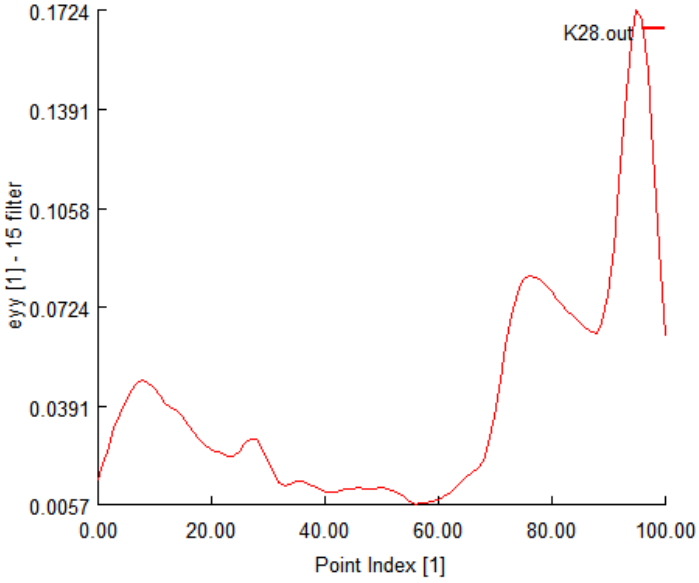
Load Step 28		T:686.7 lbf (3055N); σ: 138.5 ksi (955 Mpa) e_{EXT}: 0.02875

Raw Image	eyy Contour	TAG DIC 7
		e_{yy} (Point 0 = Top of Gage; Point 100 = Bottom of Gage)
		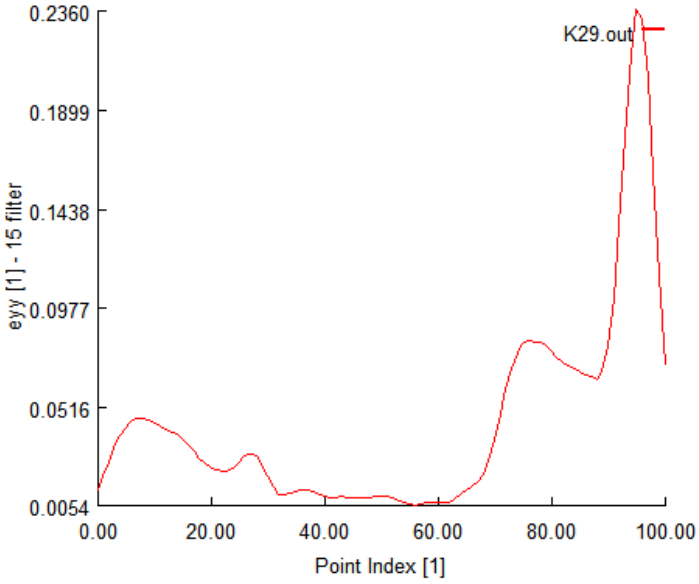
Load Step 29		T:661.5 lbf (2942N); σ: 133.4 ksi (920 Mpa) e_{EXT}: 0.02853
	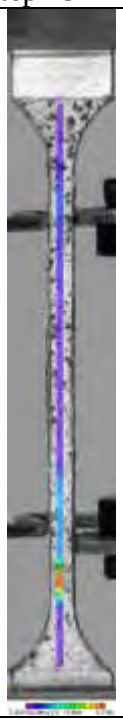	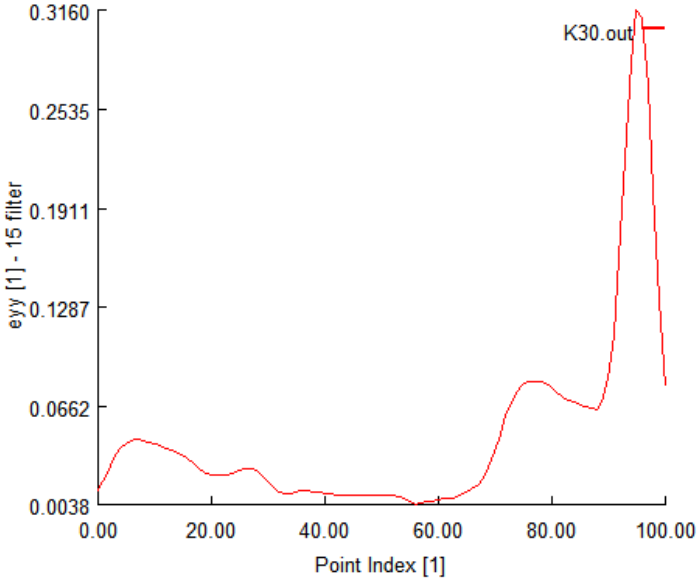
Load Step 30		T:626.8 lbf (2788N); σ: 126.4 ksi (871 Mpa) e_{EXT}: 0.02801

Raw Image	eyy Contour	TAG DIC 7
		e_{yy} (Point 0 = Top of Gage; Point 100 = Bottom of Gage)
		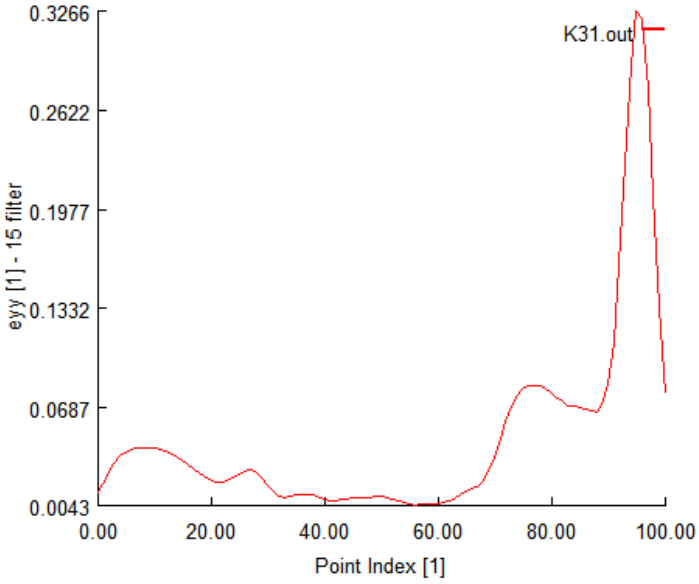
Load Step 31		T:596.9 lbf (2655N); σ: 120.3 ksi (830 Mpa) e_{EXT}: 0.02756

14. TAG DIC 8: test article L

Reference Image	Post Test Image	Global Stress-Strain Behavior of Specimen
		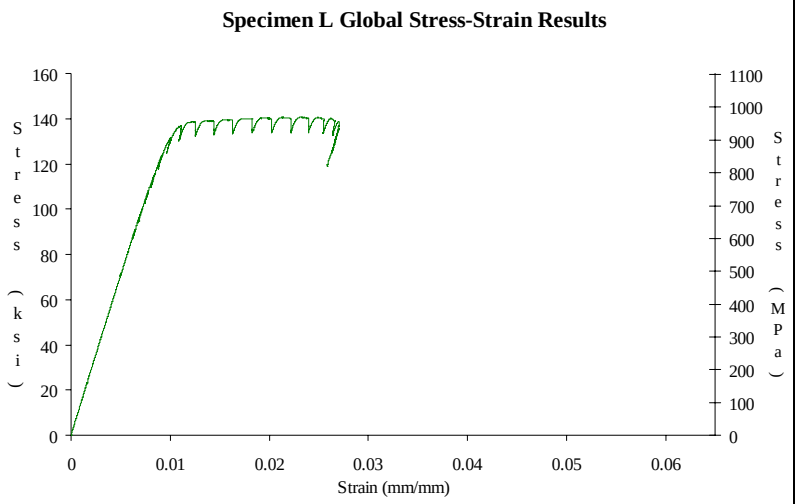 Reference Load (T): 239.3 lbf (1064 N) Reference Stress (σ): 48.2 ksi (333 MPa) Reference Extensometer Strain (ε_{EXT}): 0.00339

Raw Image	e_{yy} Contour	e_{xx} Contour	TAG DIC 8
			e_{yy} (Point 0 = Top of Gage; Point 100 = Bottom of Gage)
			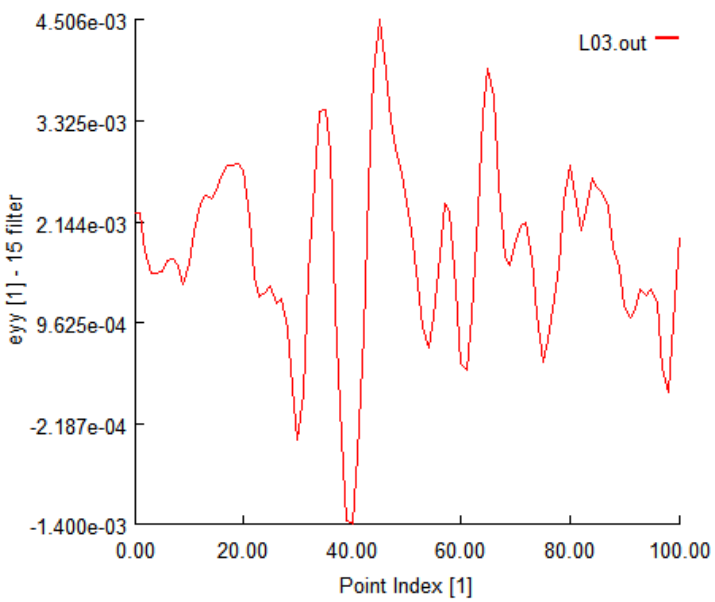
Load Step 3			T:115.9 lbf (516N); σ: 23.4 ksi (161 MPa) e_{EXT}: 0.00162
			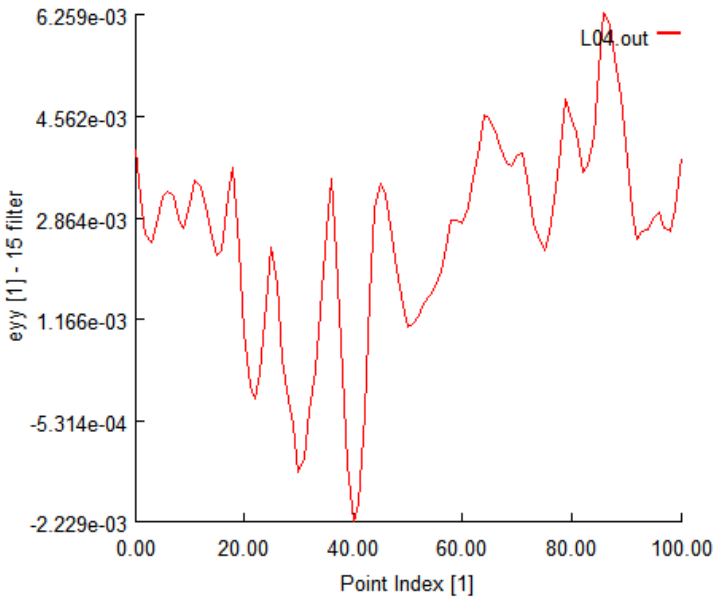
Load Step 4			T:239.3 lbf (1064N); σ: 48.2 ksi (333 MPa) e_{EXT}: 0.00339

Raw Image	e_{yy} Contour	e_{xx} Contour	TAG DIC 8
			e_{yy} (Point 0 = Top of Gage; Point 100 = Bottom of Gage)
			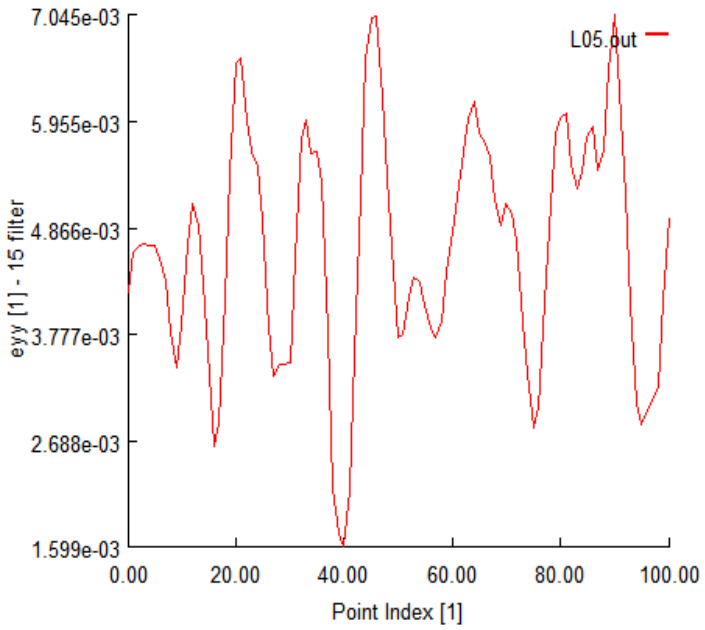
Load Step 5			T:355.9 lbf (1583N); σ: 71.8 ksi (495 MPa) e_{EXT}: 0.00507
			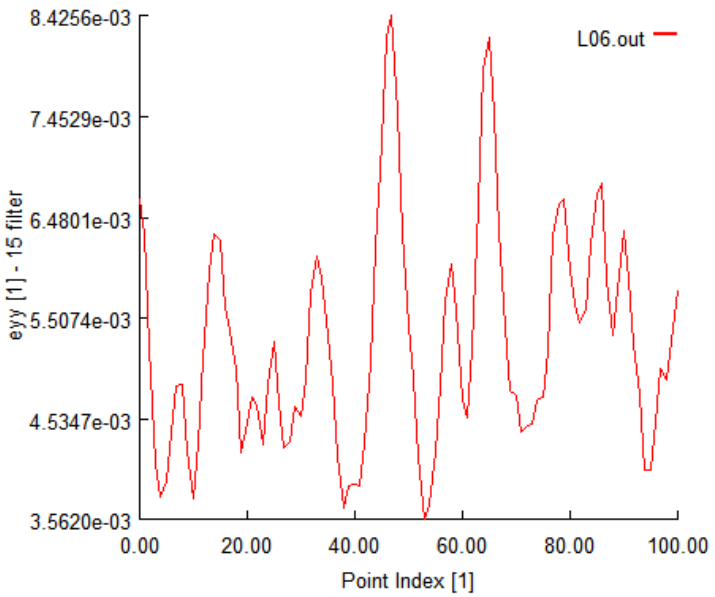
Load Step 6			T:451.8 lbf (2010N); σ: 91.1 ksi (628 MPa) e_{EXT}: 0.00648

Raw Image	e_{yy} Contour	e_{xx} Contour	TAG DIC 8
			e_{yy} (Point 0 = Top of Gage; Point 100 = Bottom of Gage)
	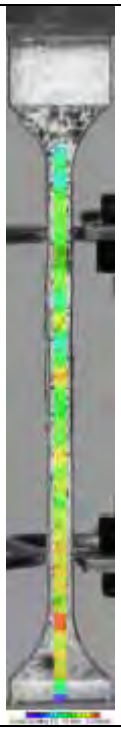		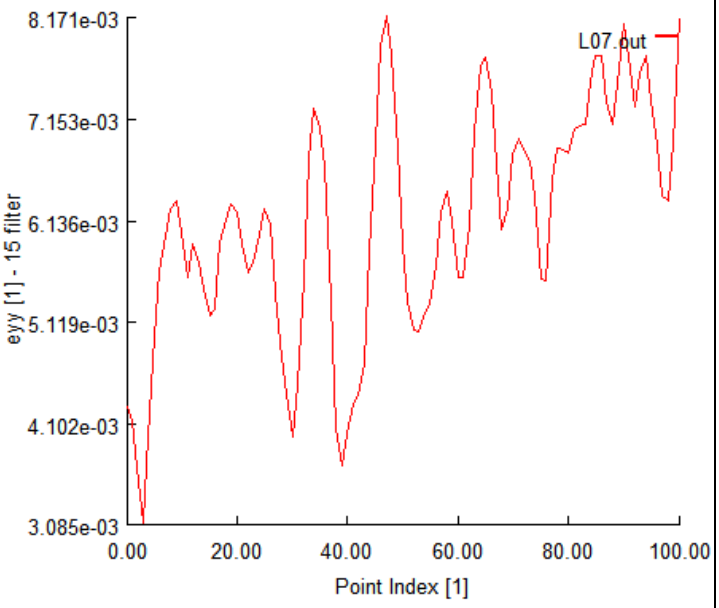
Load Step 7			T:497.6 lbf (2214N); σ: 100.3 ksi (692 MPa) e_{EXT}: 0.00719
			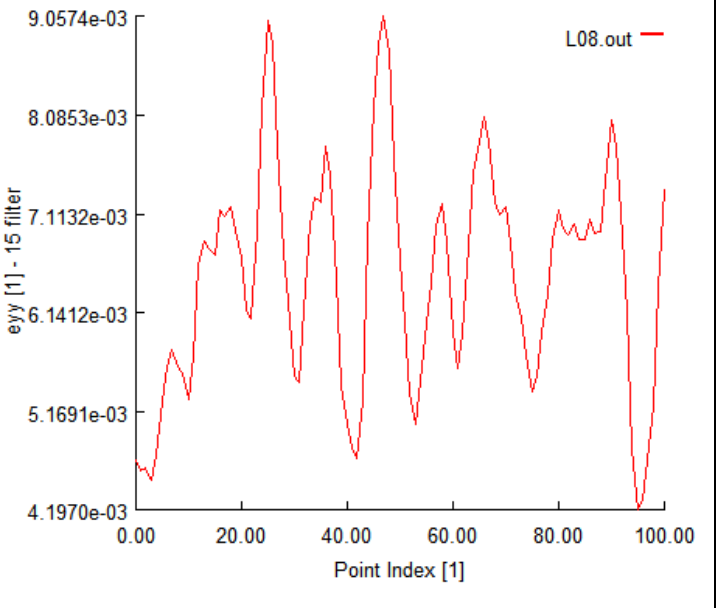
Load Step 8			T:536.9 lbf (2388N); σ: 108.2 ksi (746 MPa) e_{EXT}: 0.00782

Raw Image	e_{yy} Contour	e_{xx} Contour	TAG DIC 8
			e_{yy} (Point 0 = Top of Gage; Point 100 = Bottom of Gage)
			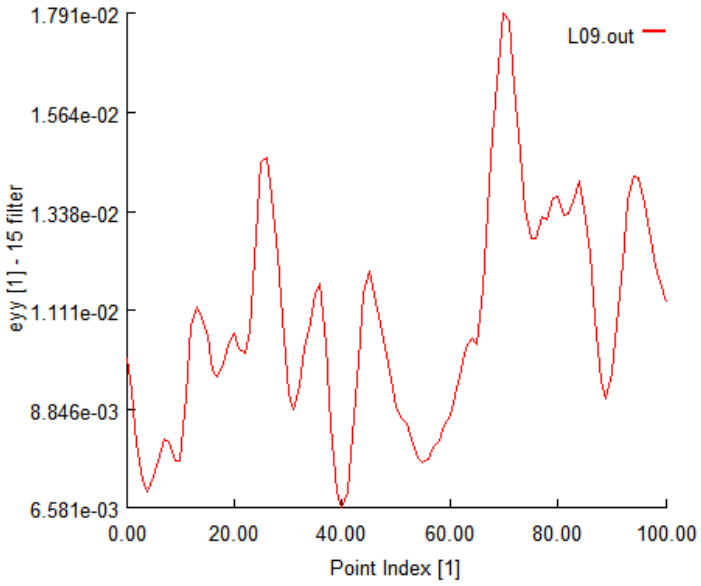
Load Step 9			T:574.7 lbf (2556N); σ: 115.9 ksi (799 MPa) e_{EXT}: 0.00845
			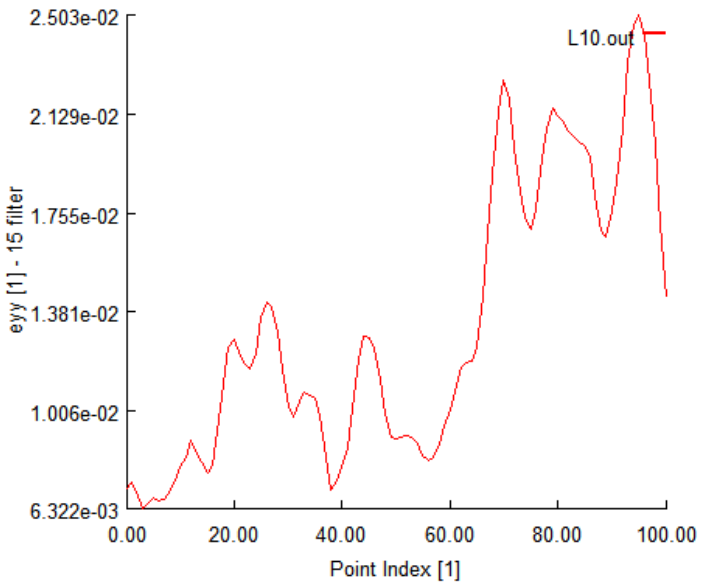
Load Step 10			T:614.8 lbf (2735N); σ: 124.0 ksi (854 MPa) e_{EXT}: 0.00916

Raw Image	e_{yy} Contour	e_{xx} Contour	TAG DIC 8
			e_{yy} (Point 0 = Top of Gage; Point 100 = Bottom of Gage)
			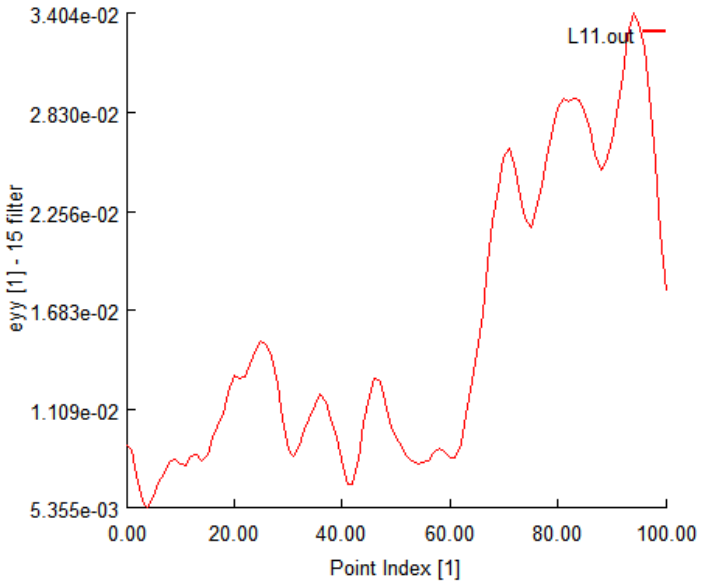
Load Step 11			T:652.6 lbf (2903N); σ: 131.6 ksi (907 MPa) e_{EXT}: 0.01002
			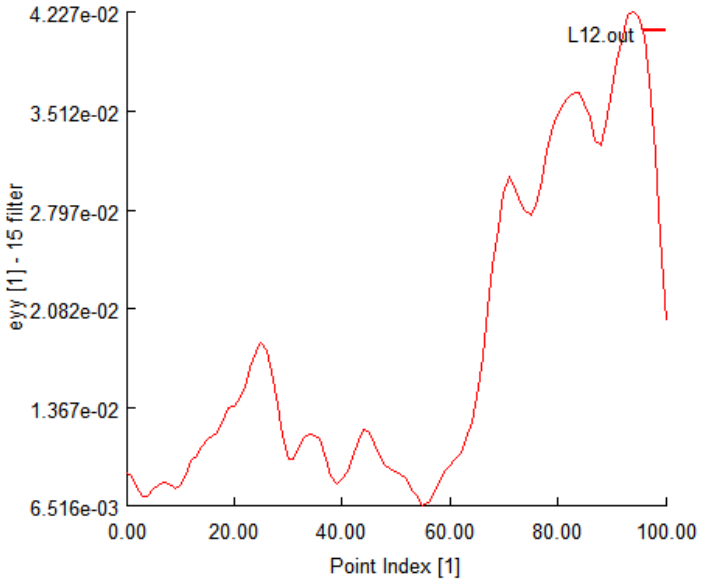
Load Step 12			T:678.9 lbf (3020N); σ: 136.9 ksi (944 MPa) e_{EXT}: 0.01110

Raw Image	e_{yy} Contour	e_{xx} Contour	TAG DIC 8
			e_{yy} (Point 0 = Top of Gage; Point 100 = Bottom of Gage)
			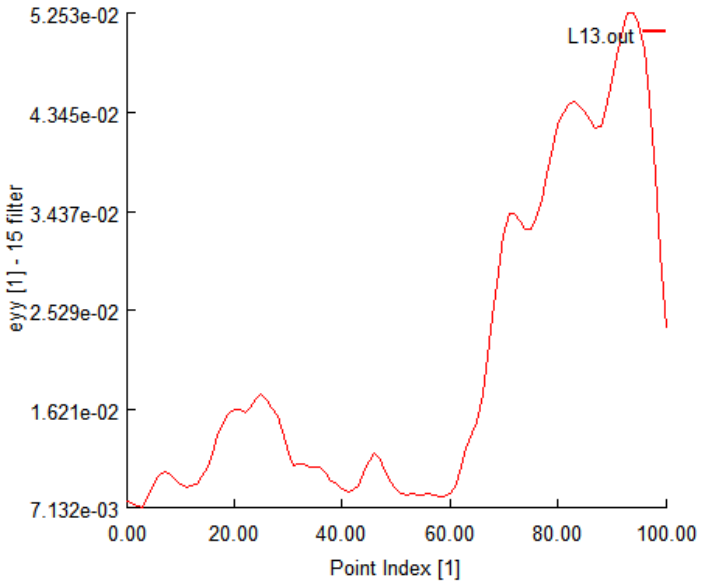
Load Step 13			T:687.3 lbf (3057N); σ: 138.6 ksi (955 MPa) e_{EXT}: 0.01253
			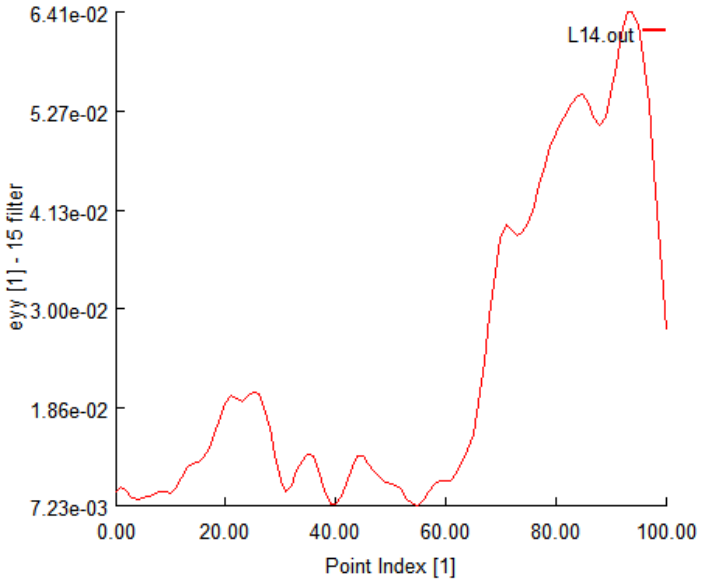
Load Step 14			T:689.0 lbf (3065N); σ: 138.9 ksi (958 MPa) e_{EXT}: 0.01437

Raw Image	e_{yy} Contour	e_{xx} Contour	TAG DIC 8
			e_{yy} (Point 0 = Top of Gage; Point 100 = Bottom of Gage)
			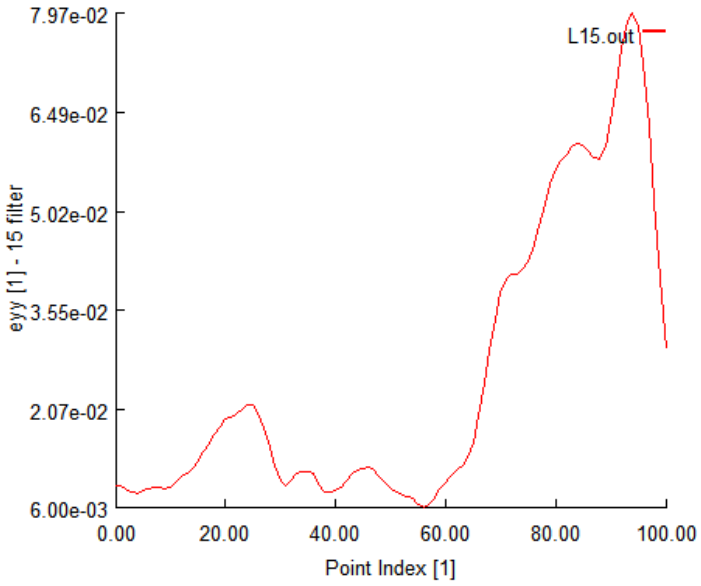
Load Step 15			T:691.5 lbf (3076N); σ: 139.4 ksi (961 MPa) e_{EXT}: 0.01623
			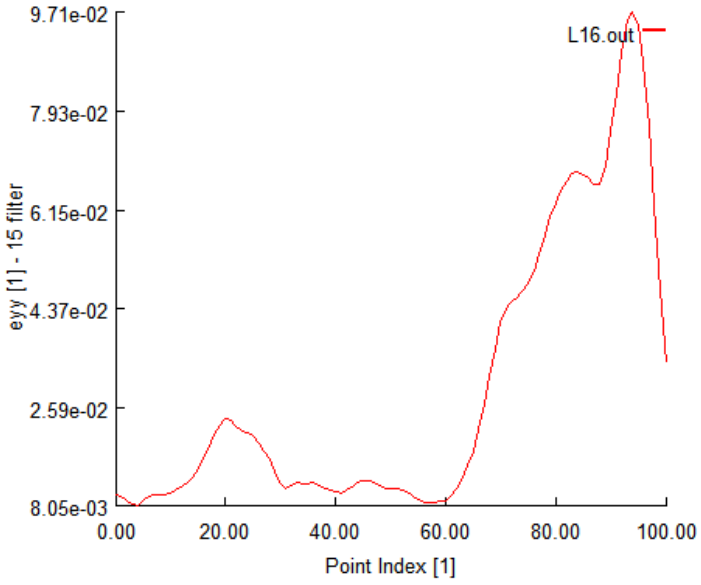
Load Step 16			T:693.4 lbf (3085N); σ: 139.8 ksi (964 MPa) e_{EXT}: 0.01824

Raw Image	e_{yy} Contour	e_{xx} Contour	TAG DIC 8
			e_{yy} (Point 0 = Top of Gage; Point 100 = Bottom of Gage)
			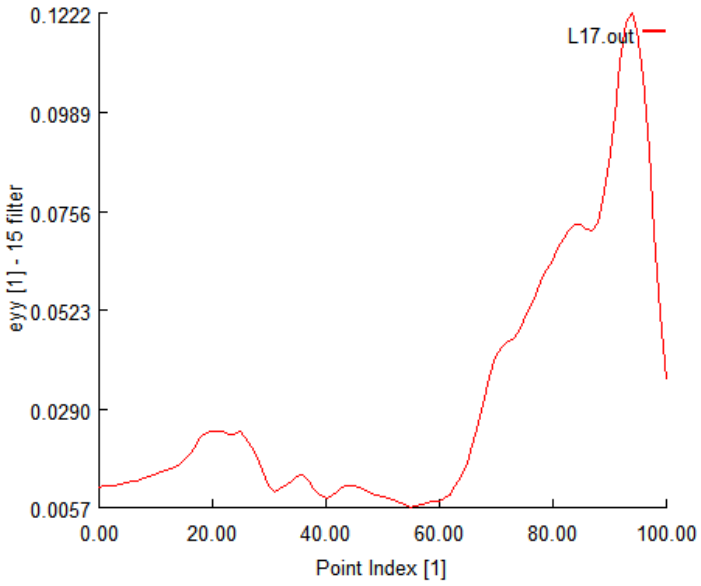
Load Step 17			T:694.7 lbf (3090N); σ: 140.1 ksi (966 MPa) e_{EXT}: 0.02017
			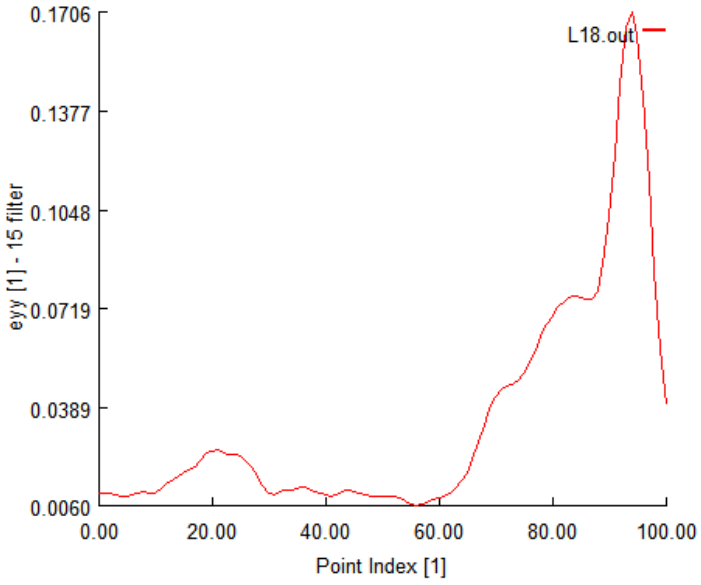
Load Step 18			T:695.5 lbf (3094N); σ: 140.2 ksi (967 MPa) e_{EXT}: 0.02208

Raw Image	e_{yy} Contour	e_{xx} Contour	TAG DIC 8
			e_{yy} (Point 0 = Top of Gage; Point 100 = Bottom of Gage)
			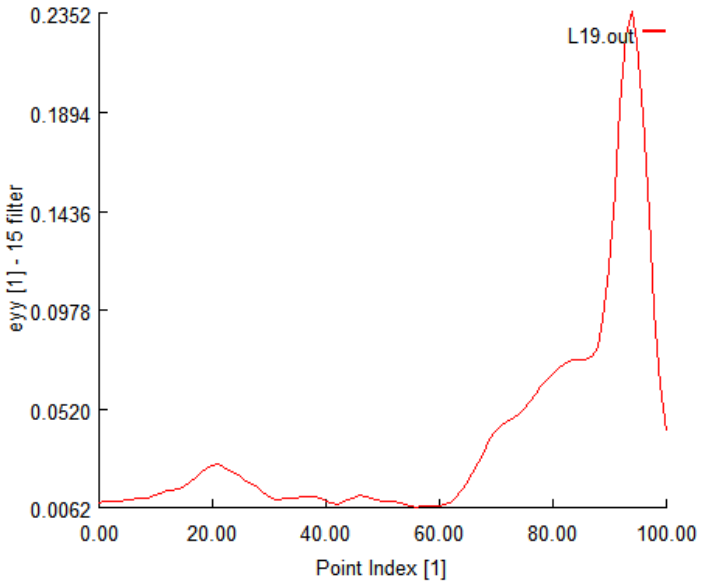
Load Step 19			T:695 lbf (3093N); σ: 140.2 ksi (966 MPa) e_{EXT}: 0.02394
			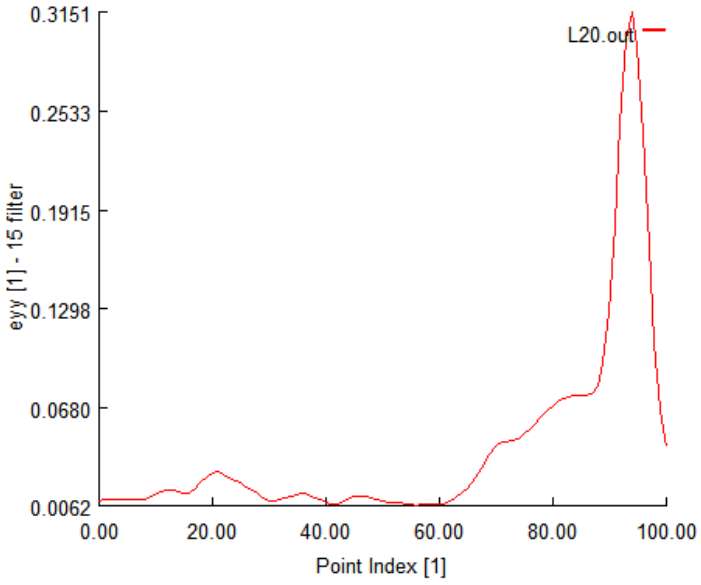
Load Step 20			T:694.0 lbf (3087N); σ: 139.9 ksi (965 MPa) e_{EXT}: 0.02548

Raw Image	e_{yy} Contour	e_{xx} Contour	TAG DIC 8
			e_{yy} (Point 0 = Top of Gage; Point 100 = Bottom of Gage)
			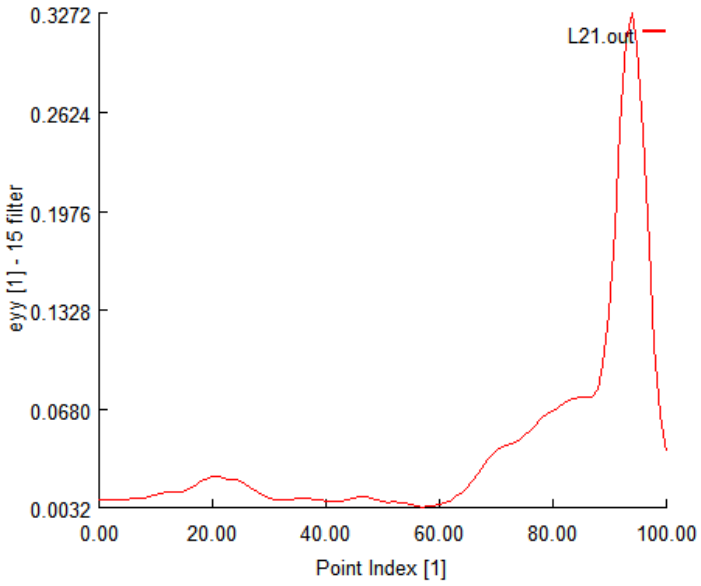
Load Step 21			T:689.4 lbf (3066N); σ: 139.0 ksi (958 MPa) e_{EXT}: 0.02662

Appendix B: Moiré Interferometry Data

1. TAG MS 0: test article 2

The second of the prepared moiré specimens was used primarily for purposes of alignment and verification of the experimental apparatus. Following successful placement of the camera stage and mirror, alignment of the collimated beams, determination of camera and collimated beam focus, and verification of camera connectivity to the image collection computer, the specimen was successively loaded in arbitrary steps in order to evaluate general fringe behavior as a function of loading. Panning along the length of the gage was accomplished to explore and validate procedural steps in the process of capturing sequential images. The images captured for test article 2 were primarily intended to confirm data acquisition and to provide a basis for establishment of data reduction procedure. Unfortunately, no surface marking was made at the weld boundaries, so it was impossible to determine the imaging location on the specimen surface. Even when under significant load, random and arbitrary panning across the gage surface failed to capture distinct strain localizations as a means of helping to identify particular weld regions, with the exception of the image of the necking behavior at the point of. Post-test evaluation determined this necking occurred within the parent material just outside of the retreating weld boundary.

Figure B-1: TAG MS 0 showing visible necking at failure point outside of retreating weld boundary

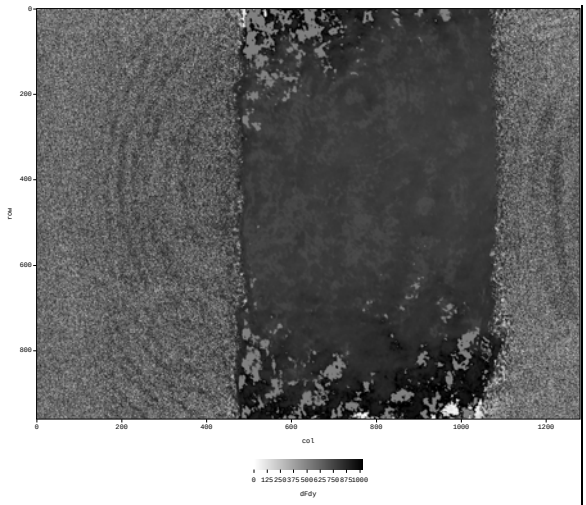

(a) Load: null; Location: undetermined

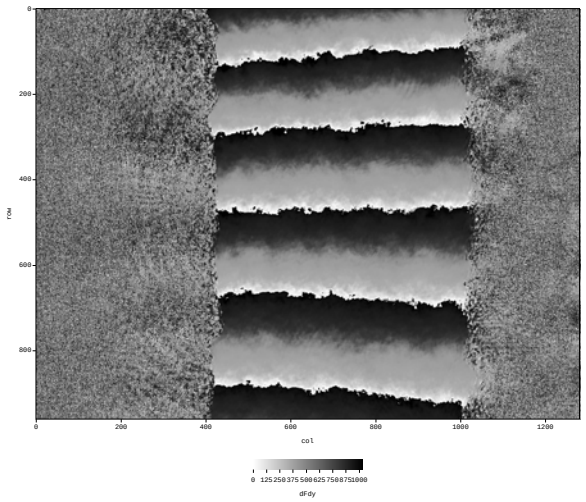

(b) Load: unknown; Location: undetermined

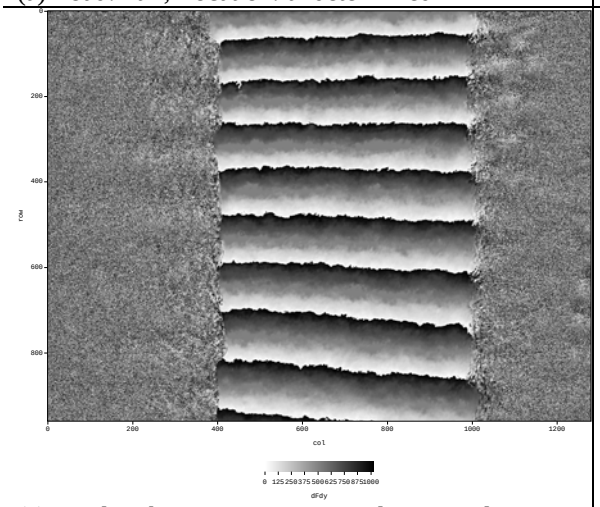

(c) Load: unknown; Location: undetermined

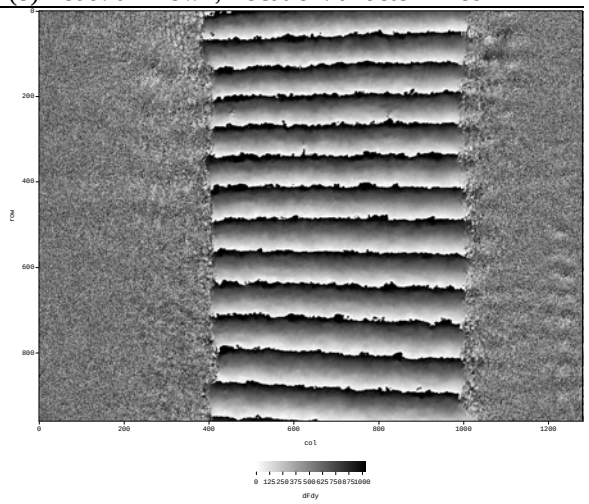

(d) Load: unknown; Location: undetermined

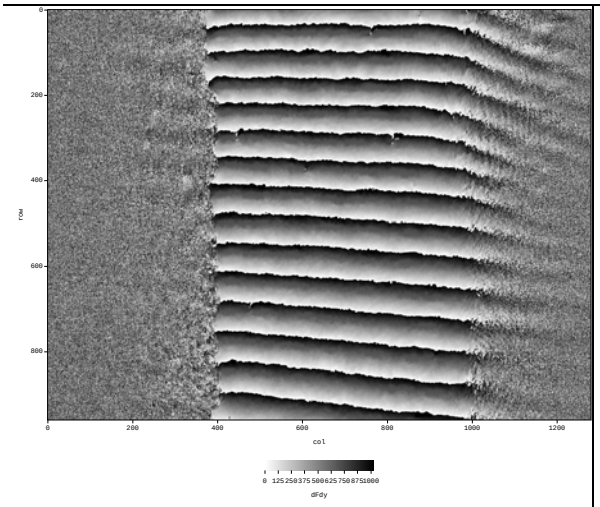

(e) Load: unknown; Location: undetermined

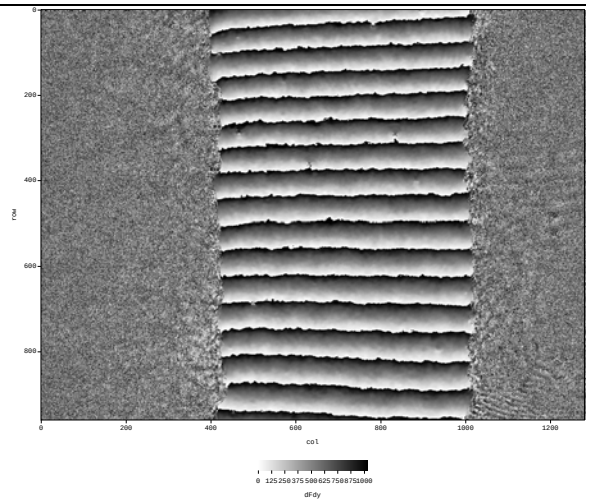

(f) Load: unknown; Location: undetermined

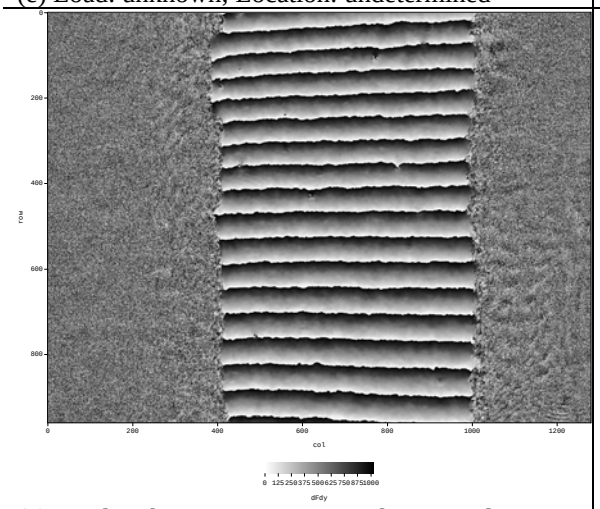

(g) Load: unknown; Location: undetermined

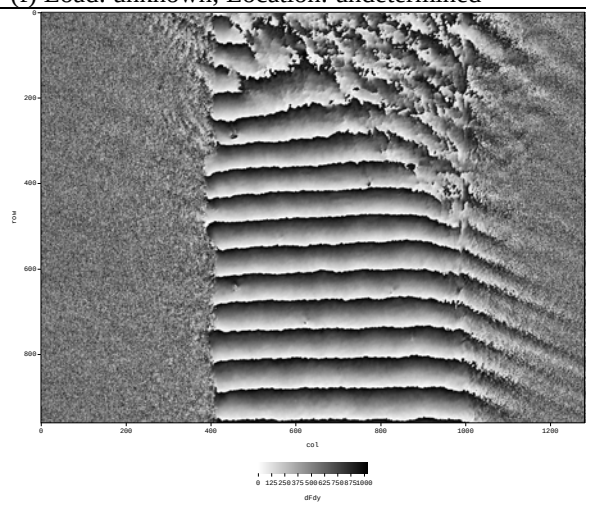

(h) Load: unknown; Location: undetermined

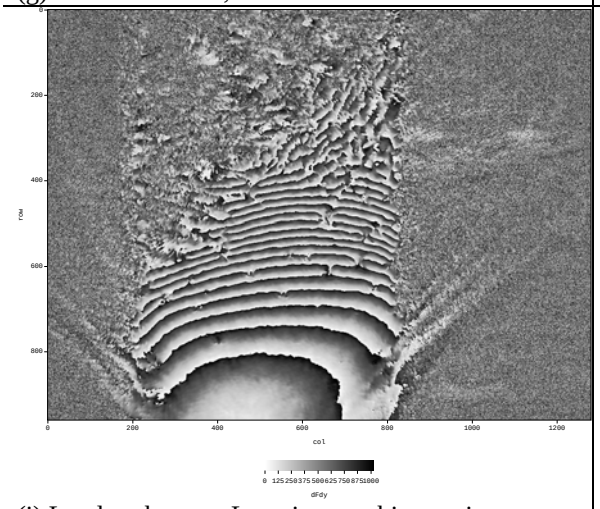

(i) Load: unknown; Location: necking region

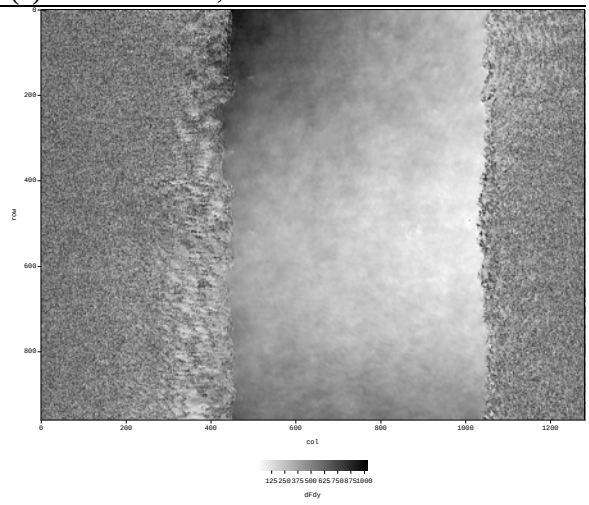

(j) Load: unloaded; Location: undetermined

Figure B-2: TAG MS 0 image data

2. TAG MS 1: test article 3

Moiré specimen 3 was the first specimen used for dedicated test data. The primary objective of the third specimen test was to identify and quantify developing localized axial strain in the vicinity of the retreating weld boundary. Figure B-5 shows the strain development in the vicinity of the retreating weld boundary for a series of loading and subsequent unloading steps along with reduced strain data gathered from each of the images. Figure B-3 is a stress-strain plot generated from these test results showing variations in the strain at different regions around the weld.

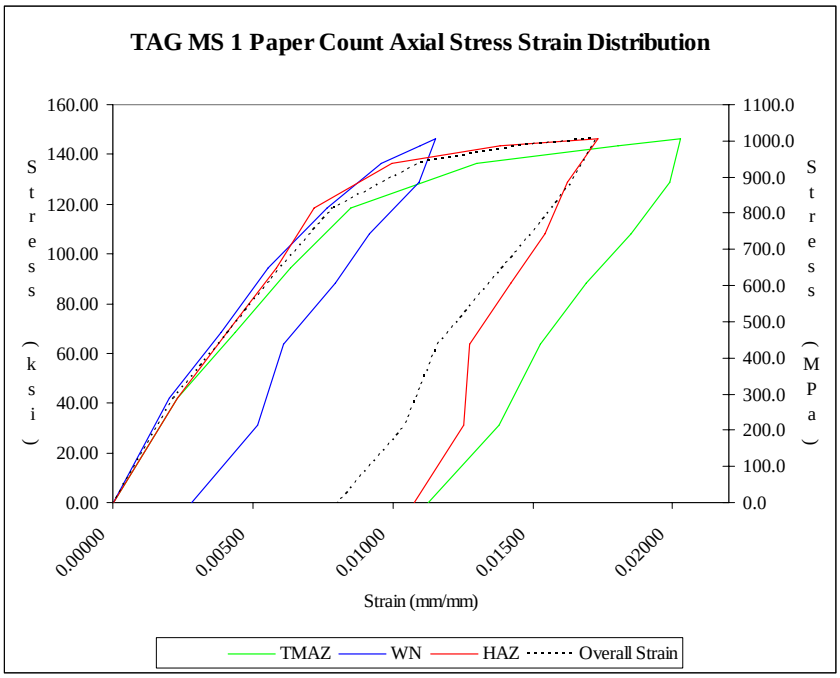

Figure B-3: TAG MS 1 stress-strain distribution

Figure B-4: TAG MS 1 post-test image – no visible necking

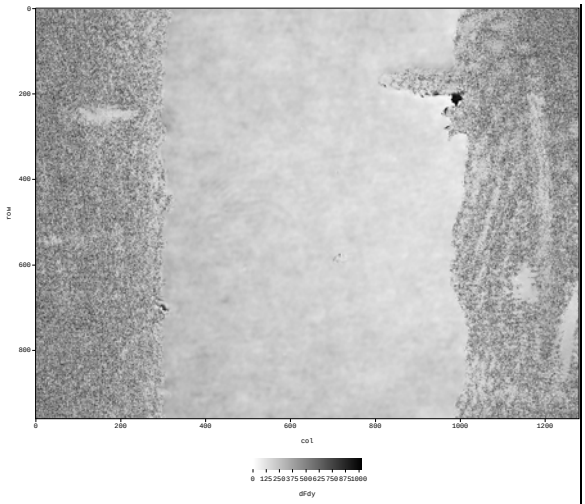

(a) Load Step 1
Indicated Load = null
Area = 0.0051 in^2 (3.26 mm^2)

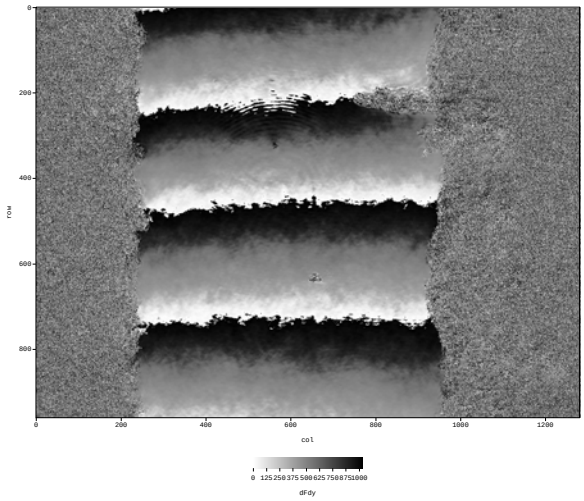

(b) Load Step 2 (Increasing Load)
- Indicated Load = 211.0 lbf (939 N)
- Stress = 41.8 ksi (288 MPa)
- Overall Strain = 0.00220
 -- PM Strain = N/A
 -- HAZ Strain = 0.00229
 -- TMAZ Strain = 0.00232
 -- WN Strain = 0.00203

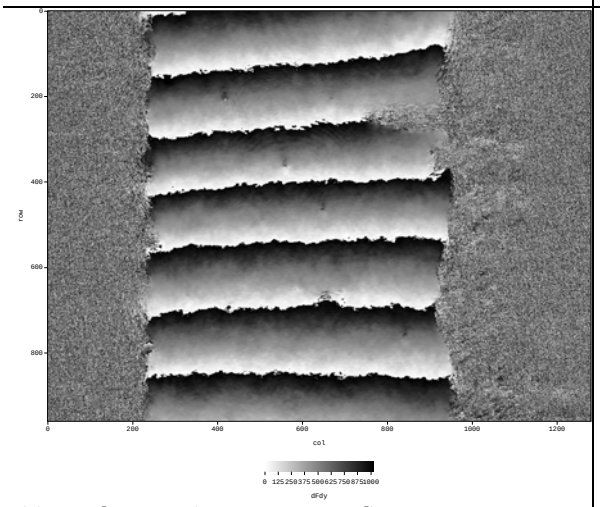

(c) Load Step 3 (Increasing Load)
- Indicated Load = 345.3 lbf (1536 N)
- Stress = 68.5 ksi (472 MPa)
- Overall Strain = 0.00411
 -- PM Strain = N/A
 -- HAZ Strain = 0.00407
 -- TMAZ Strain = 0.00436
 -- WN Strain = 0.00387

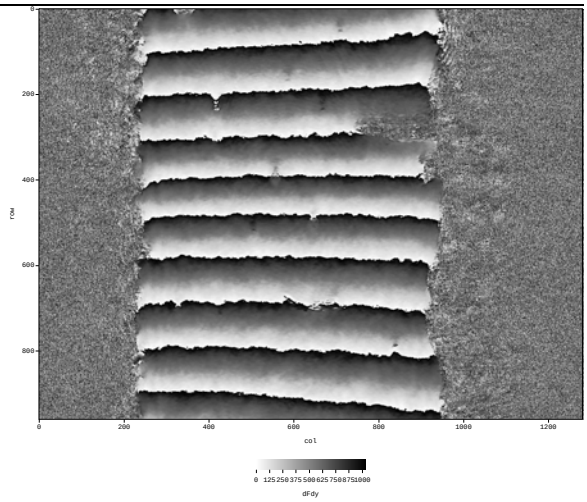

(d) Load Step 4 (Increasing Load)
- Indicated Load = 475.9 lbf (2117 N)
- Stress = 94.3 ksi (650.4 MPa)
- Overall Strain = 0.00596
 -- PM Strain = N/A
 -- HAZ Strain = 0.00583
 -- TMAZ Strain = 0.00636
 -- WN Strain = 0.00557

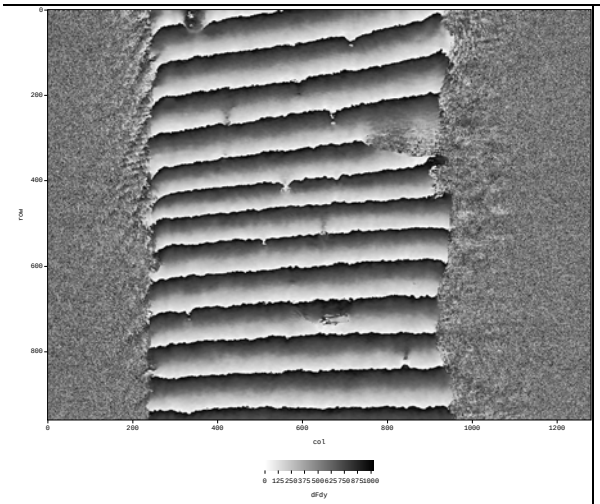

(d) Load Step 5 (Increasing Load)
- Indicated Load = 596.6 lbf (2654 N)
- Stress = 118.3 ksi (815 MPa)
- Overall Strain = 0.00785
 -- PM Strain = N/A
 -- HAZ Strain = 0.00721
 -- TMAZ Strain = 0.00851
 -- WN Strain = 0.00767

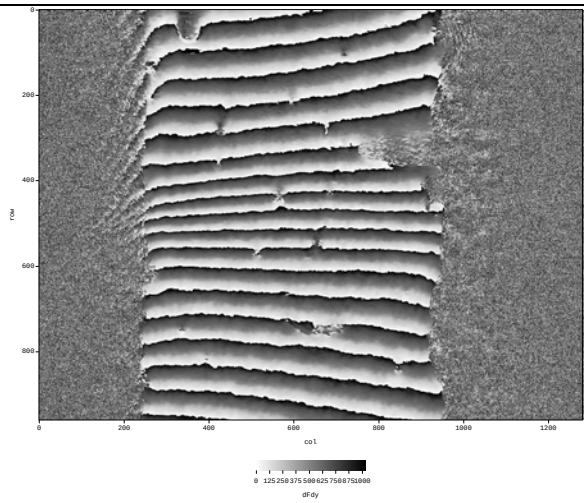

(e) Load Step 6 (Increasing Load)
- Indicated Load = 688.6 lbf (3063 N)
- Stress = 136.5 ksi (941 MPa)
- Overall Strain = 0.01102
 -- PM Strain = N/A
 -- HAZ Strain = 0.00996
 -- TMAZ Strain = 0.01300
 -- WN Strain = 0.00961

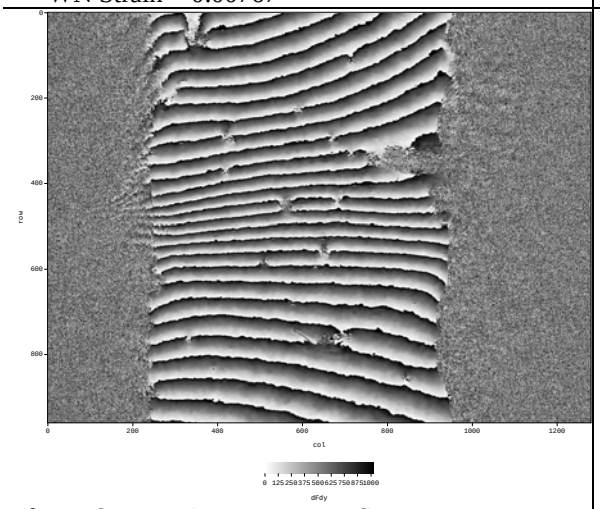

(f) Load Step 7 (Increasing Load)
- Indicated Load = 723.4 lbf (3218 N)
- Stress = 143.4 ksi (989 MPa)
- Overall Strain = 0.01482
 -- PM Strain = N/A
 -- HAZ Strain = 0.01384
 -- TMAZ Strain = 0.01803
 -- WN Strain = 0.01099

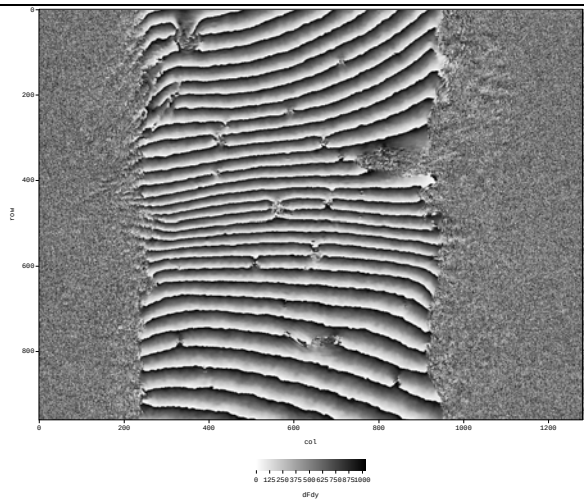

(g) Load Step 8 (Increasing Load)
- Indicated Load = 737.1 lbf (2379 N)
- Stress = 146.1 ksi (1007 MPa)
- Overall Strain = 0.01721
 -- PM Strain = N/A
 -- HAZ Strain = 0.01732
 -- TMAZ Strain = 0.02028
 -- WN Strain = 0.01155

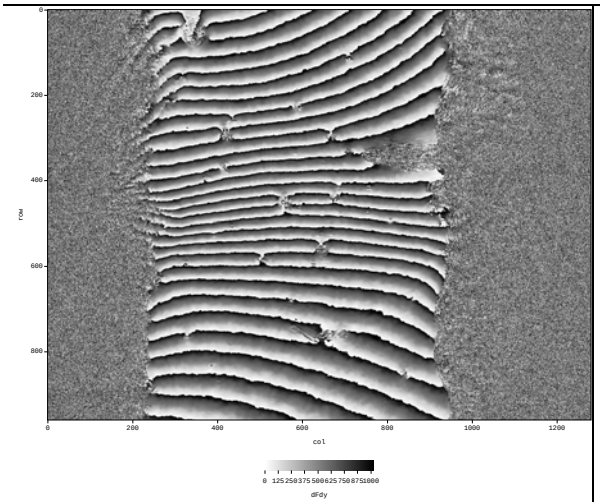

(h) Load Step 9 (Decreasing Load)
- Indicated Load = 650.0 lbf (3279 N)
- Stress = 128.9 ksi (888 MPa)
- Overall Strain = 0.01634
 -- PM Strain = N/A
 -- HAZ Strain = 0.01622
 -- TMAZ Strain = 0.01992
 -- WN Strain = 0.01095

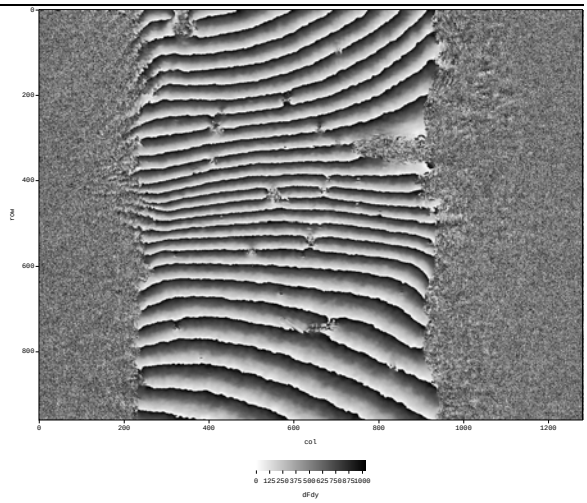

(i) Load Step 10 (Decreasing Load)
- Indicated Load = 545.6 lbf (2427 N)
- Stress = 108.1 ksi (746 MPa)
- Overall Strain = 0.01492
 -- PM Strain = N/A
 -- HAZ Strain = 0.01542
 -- TMAZ Strain = 0.01851
 -- WN Strain = 0.00918

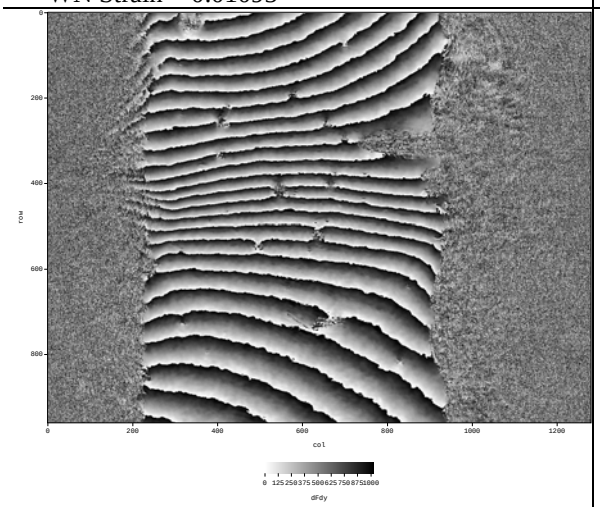

(j) Load Step 11 (Decreasing Load)
- Indicated Load = 446.1 lbf (1984 N)
- Stress = 88.4 ksi (610 MPa)
- Overall Strain = 0.01342
 -- PM Strain = N/A
 -- HAZ Strain = 0.01424
 -- TMAZ Strain = 0.01691
 -- WN Strain = 0.00794

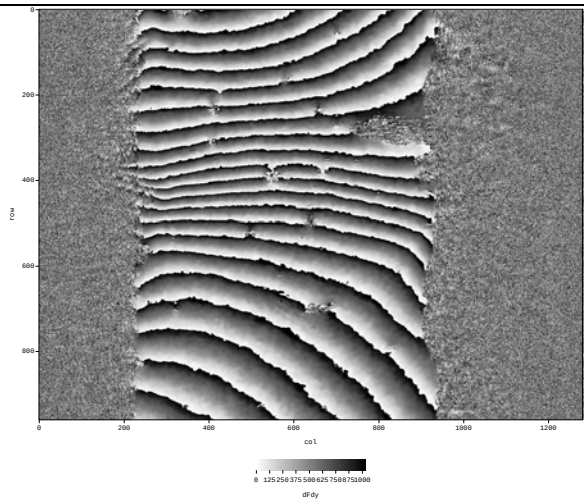

(k) Load Step 12 (Decreasing Load)
- Indicated Load = 321.7 lbf (1431 N)
- Stress = 63.8 ksi (440 MPa)
- Overall Strain = 0.01158
 -- PM Strain = N/A
 -- HAZ Strain = 0.01275
 -- TMAZ Strain = 0.01528
 -- WN Strain = 0.00610

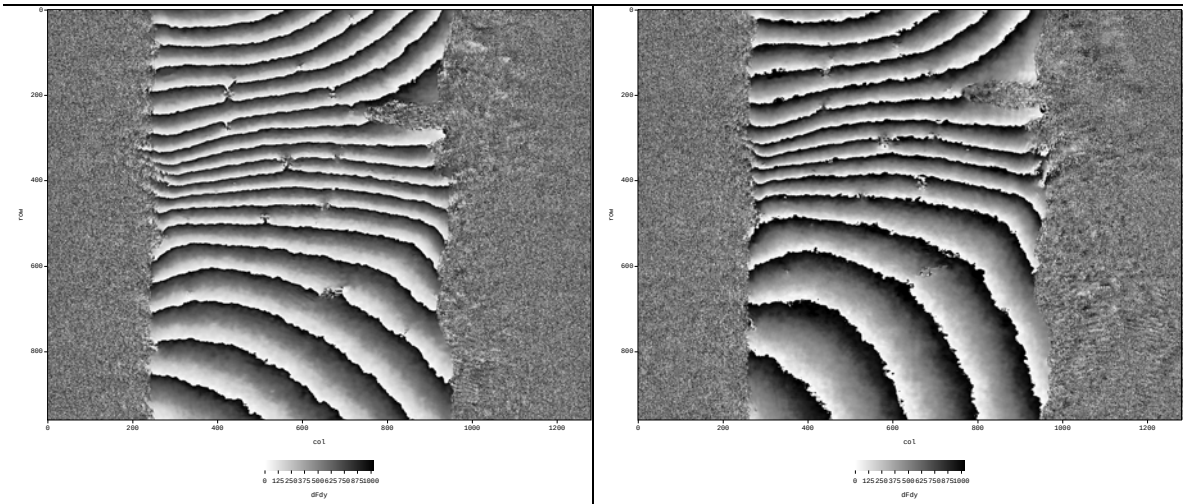

(l) Load Step 13 (Decreasing Load)
- Indicated Load = 157.5 lbf (701 N)
- Stress = 31.2 ksi (215 MPa)
- Overall Strain = 0.01038
 -- PM Strain = N/A
 -- HAZ Strain = 0.01252
 -- TMAZ Strain = 0.01379
 -- WN Strain = 0.00517

(m) Load Step 14 (Decreasing Load)
- Indicated Load = 0.81 lbf (4 N)
- Stress = 0.2 ksi (1.1 MPa)
- Overall Strain = 0.00800
 -- PM Strain = N/A
 -- HAZ Strain = 0.01078
 -- TMAZ Strain = 0.01128
 -- WN Strain = 0.00280

Figure B-5: TAG MS 1 image and associated load and strain data

As apparent from the moiré images, strain localization first occurs just inside the weld less than 0.0197 in (0.5 mm) from the visible weld boundary. Distinct localization begins at approximately 120 ksi (830 MPa), shown in (d), and continues uniformly through increasing load up to approximately 146 ksi (1000 MPa). As the specimen was gradually unloaded, distinct variations in residual strain developed to a final condition shown in (m). These variations in strain response through loading and unloading reflect variations in material properties across the weld zone. The stress-strain curve shown in Figure B-3, shows distinct differences in yield strength as well as plastic response in each of the three weld regions examined.

3. TAG MS 2: test article 4

The specific objective of moiré test article 4 was to further explore the localized strain behavior in the region of the weld interface and examine the necking material to quantify the maximum observed strain. Figure B-7 shows the strain development in the vicinity of the retreating weld boundary for a series of loading steps along with reduced strain data gathered from each of the images. Figure B-6 is a stress-strain plot generated from these test results showing variations in the strain at different regions around the weld.

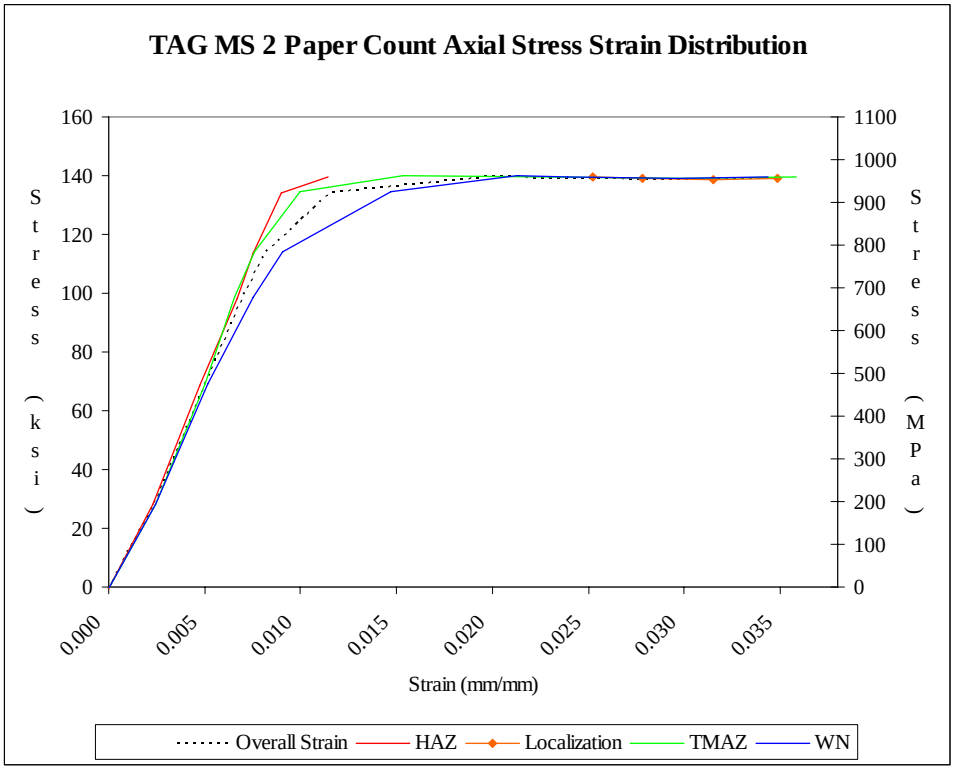

Figure B-6: TAG MS 2 stress-strain distribution

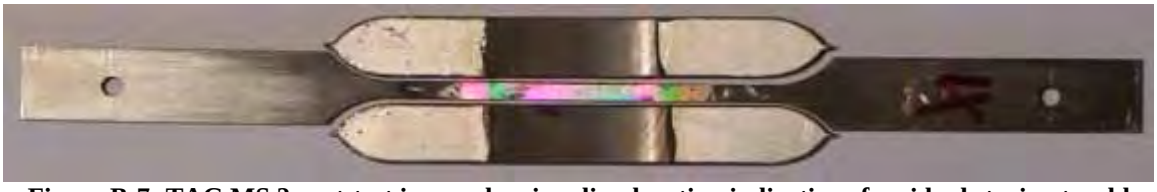

Figure B-7: TAG MS 2 post-test image showing discoloration indicative of residual strain at weld boundaries

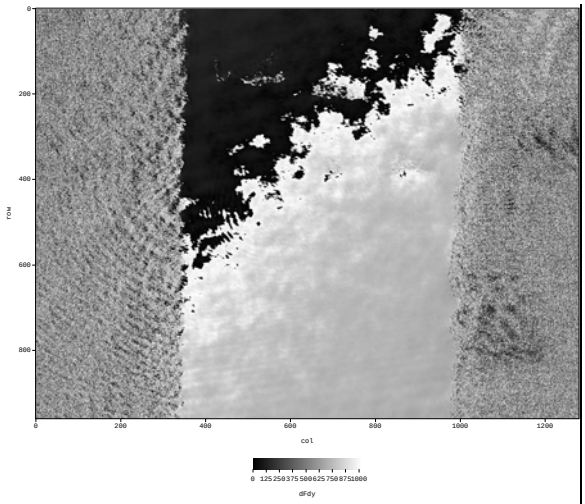

(a) Load Step 1
Indicated Load = null
Area = 0.0051 in^2 (3.26 mm^2)

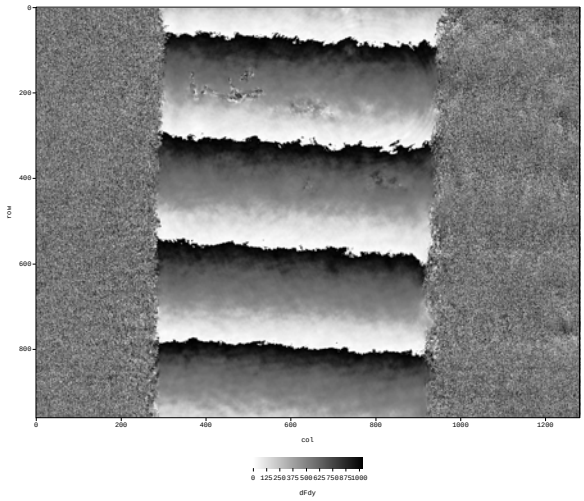

(b) Load Step 2 (Increasing Load)
- Indicated Load = 141.4 lbf (629 N)
- Stress = 28.0 ksi (193 MPa)
- Overall Strain = 0.00238
 -- PM Strain = N/A
 -- HAZ Strain = 0.00229
 -- TMAZ Strain = 0.00241
 -- WN Strain = 0.00242

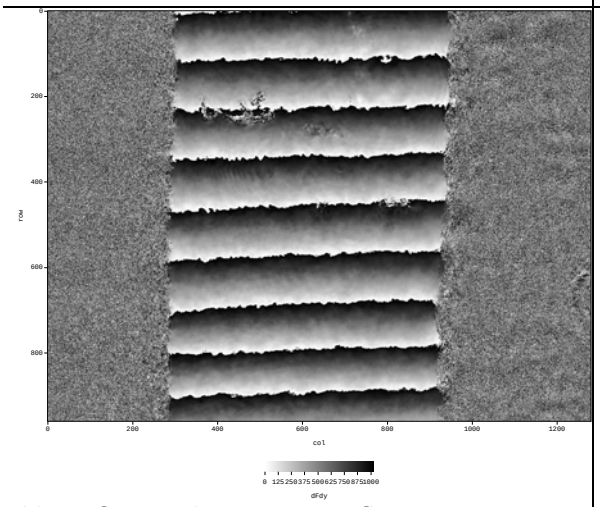

(c) Load Step 3 (Increasing Load)
- Indicated Load = 346.6 lbf (1542 N)
- Stress = 68.7 ksi (474 MPa)
- Overall Strain = 0.00502
 -- PM Strain = N/A
 -- HAZ Strain = 0.00472
 -- TMAZ Strain = 0.00504
 -- WN Strain = 0.00519

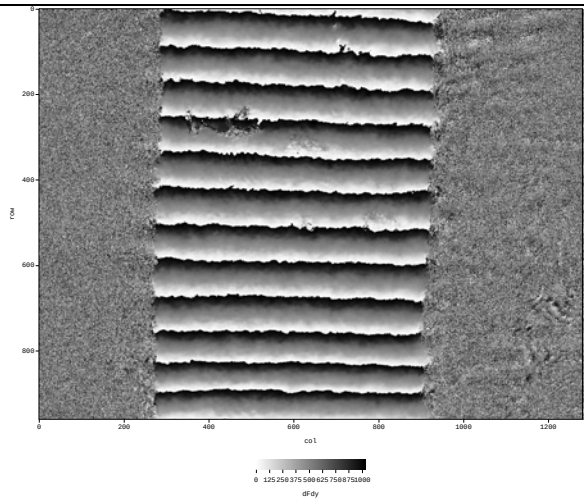

(d) Load Step 4 (Increasing Load)
- Indicated Load = 495.8 lbf (2205 N)
- Stress = 98.3 ksi (678 MPa)
- Overall Strain = 0.00696
 -- PM Strain = N/A
 -- HAZ Strain = 0.00671
 -- TMAZ Strain = 0.00657
 -- WN Strain = 0.00755

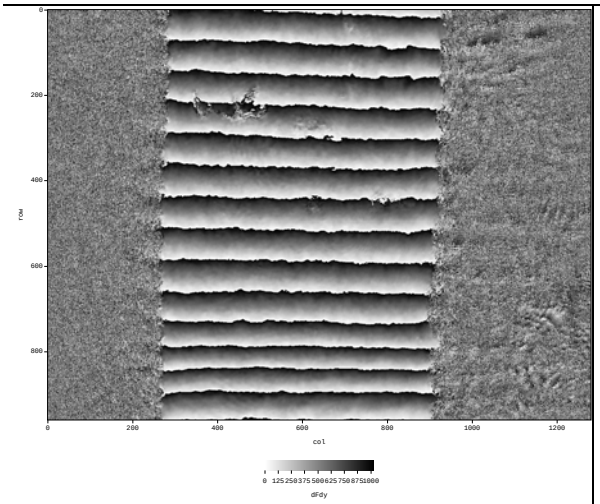

(d) Load Step 5 (Increasing Load)
- Indicated Load = 574.2 lbf (2554 N)
- Stress = 113.8 ksi (785 MPa)
- Overall Strain = 0.00816
 -- PM Strain = N/A
 -- HAZ Strain = 0.00756
 -- TMAZ Strain = 0.00760
 -- WN Strain = 0.00904

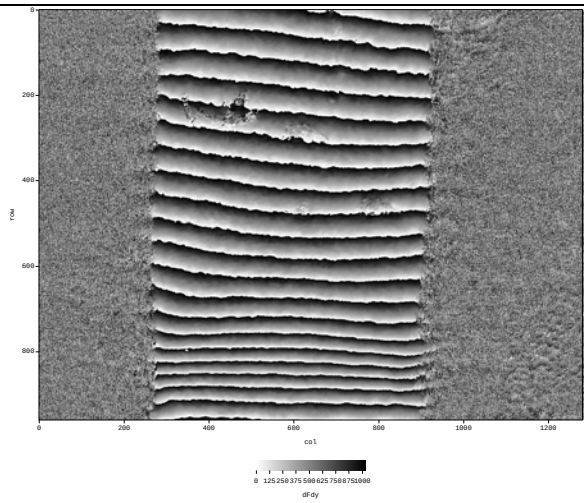

(e) Load Step 6 (Increasing Load)
- Indicated Load = 677.4 lbf (3013 N)
- Stress = 134.3 ksi (926 MPa)
- Overall Strain = 0.01158
 -- PM Strain = N/A
 -- HAZ Strain = 0.00897
 -- TMAZ Strain = 0.01000
 -- WN Strain = 0.01471

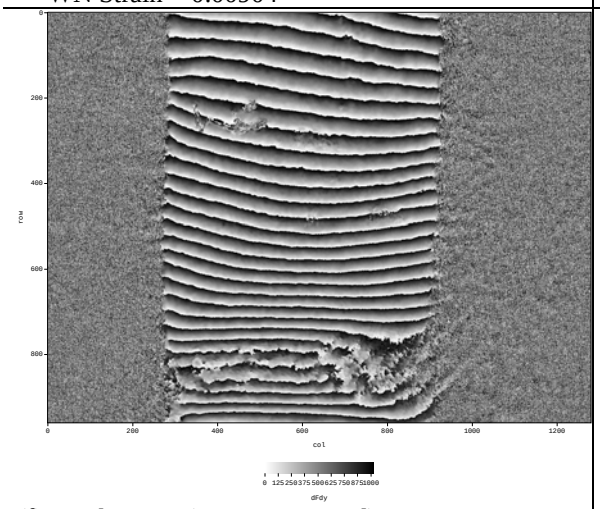

(f) Load Step 7 (Increasing Load)
- Indicated Load = 703.5 lbf (3129 N)
- Stress = 139.5 ksi (961 MPa)
- Overall Strain = 0.01978
 -- PM Strain = N/A
 -- HAZ Strain = 0.01147
 -- TMAZ Strain = 0.01531
 -- WN Strain = 0.02126

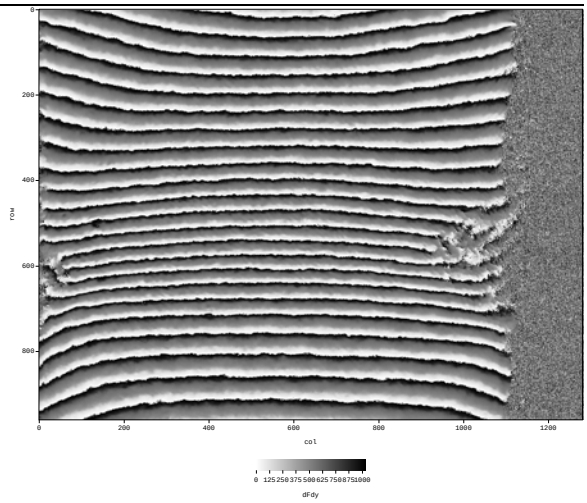

(g) Load Step 7z (Increasing Load)
- Indicated Load = 703.5 lbf (3129 N)
- Stress = 139.5 ksi (961 MPa)
- Overall Strain = 0.01978
 -- PM Strain = N/A
 -- HAZ Strain = 0.01147
 -- TMAZ Strain = 0.01531
 -- WN Strain = 0.02126; Neck Strain = 0.02523

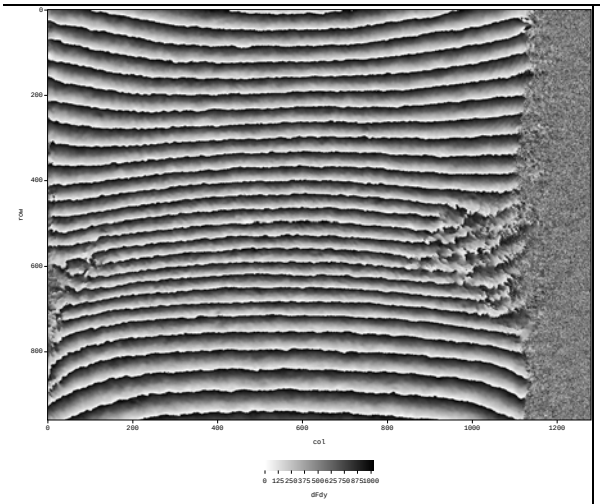

(h) Load Step 8 Magnified (Increasing Load)
- Indicated Load = 702.3 lbf (3124 N)
- Stress = 139.2 ksi (960 MPa)
- Overall Strain = 0.02380
 -- PM Strain = N/A
 -- HAZ Strain = N/A
 -- TMAZ Strain = 0.02292
 -- WN Strain = 0.02392; Neck Strain = 0.02781

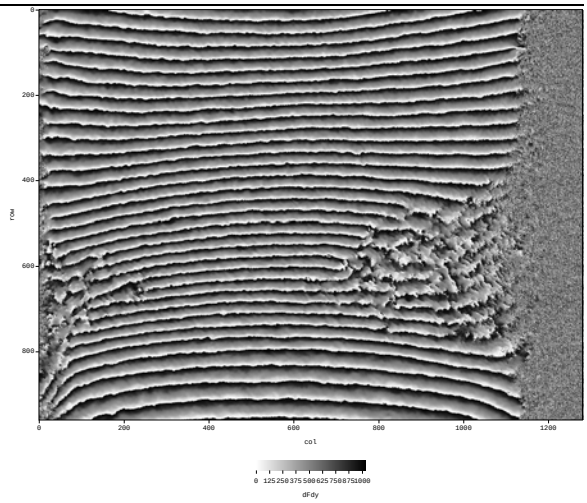

(i) Load Step 9 Magnified (Increasing Load)
- Indicated Load = 700.0 lbf (3113 N)
- Stress = 138.7 ksi (956 MPa)
- Overall Strain = 0.02973
 -- PM Strain = N/A
 -- HAZ Strain = N/A
 -- TMAZ Strain = 0.02996
 -- WN Strain = 0.02964; Neck Strain = 0.03153

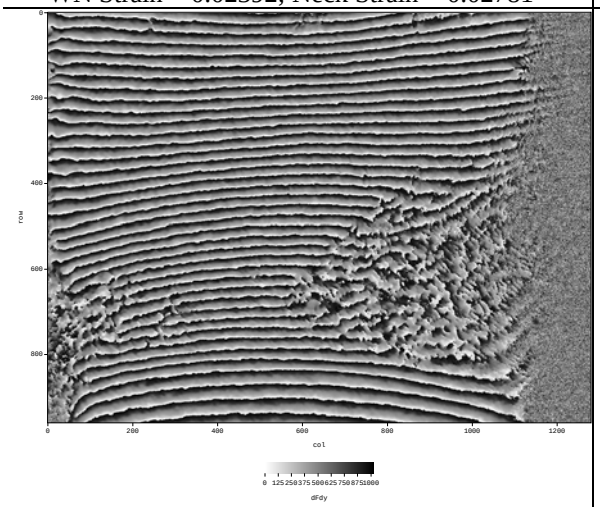

(j) Load Step 10 Magnified (Increasing Load)
- Indicated Load = 446.1 lbf (1984 N)
- Stress = 88.4 ksi (610 MPa)
- Overall Strain = 0.03480
 -- PM Strain = N/A
 -- HAZ Strain = N/A
 -- TMAZ Strain = 0.03587
 -- WN Strain = 0.03437; Neck Strain = 0.03488

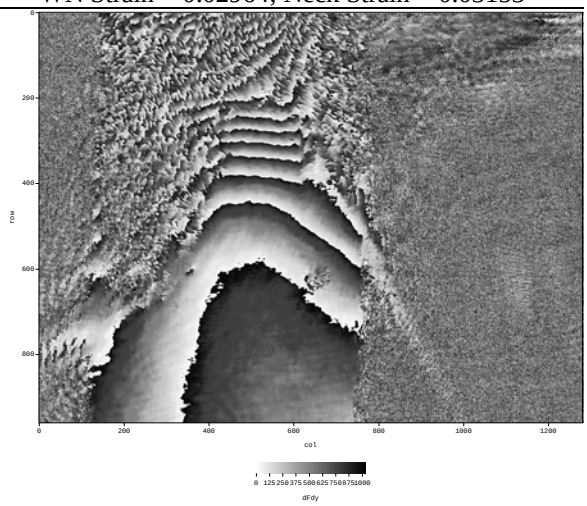

(k) Load Step 11 (Null Load)
- Indicated Load = null
- Stress = null

No strain values determined

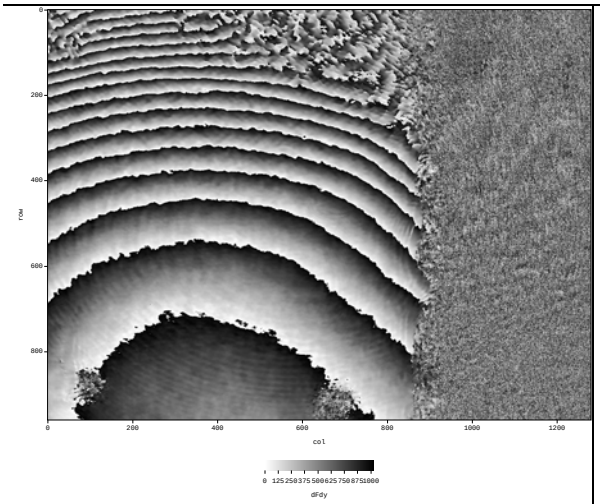

(l) Load Step 11 Magnified (Null Load)
- No remaining reference to determine strain locale or value.

Figure B-8: TAG MS 2 image and associated load and strain data

Test data from this specimen showed strain localization first occurred deeper inside the weld boundary than the previous specimen; approximately 0.0787 in (2.0 mm) inside the visible weld boundary. Figure B-7 shows the post-test specimen with the relative location of the weld boundaries shown along the specimen gage. Distinct localization began at significantly lower stress in this specimen than in TAG MS 1; approximately 68.7 ksi (474 MPa) vs 120 ksi (830 MPa). This strain localization increased in relative intensity as the load increased with fringe indication necking occurring at approximately 140 ksi (961 MPa). With the advent of necking and the associated increase in fringe frequency, a higher image resolution was required to clearly resolve the moiré fringes. This can be seen in the comparison between images (f) and (g), where a change in the image magnification level brought the previously unresolved necking region into discernable focus. The remainder of the specimen images was captured at the increased magnification in order to examine the strain response within the area of localization.

The stress-strain distribution shown in Figure B-6 appears contrary to the previous distribution because of the unusual location of initial necking inside the weld in the region quantified as the weld nugget (WN). The standard for this research is to consider the weld nugget as beginning 0.039 in (1.0 mm) inside the visible weld boundary, though this is not entirely accurate as the entire weld region spans roughly 0.630 in (16 mm) which requires examination of the moiré fringe data closer to the center of the weld region. For this test, only one group of panned images was captured, shown in Figure B-9, which shows the fringe spacing increasing further into the WN. This indicates the anomaly of the necking location is not indicative of a general increase in strain behavior across the region of the WN. Figure B-6 appears to represent this behavior due to limited area of fringe sampling in the WN.

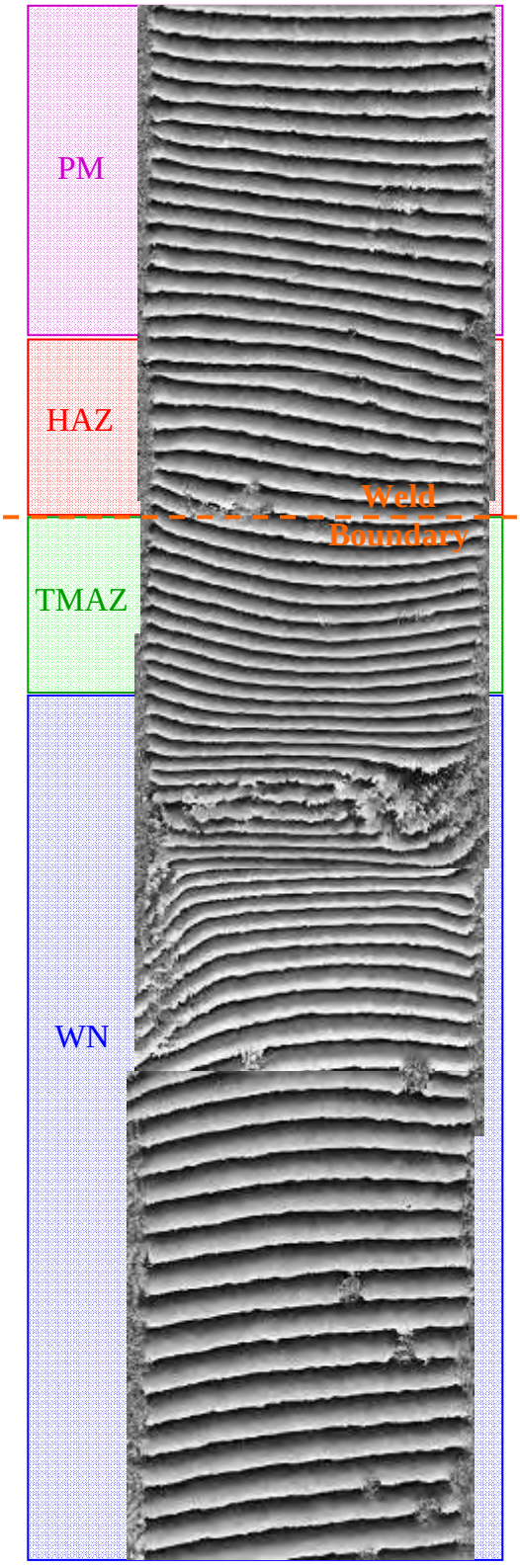

Figure B-9: TAG MS 2 composite image at Load Step 7 = 139.5 ksi (961 MPa)

4. TAG MS 3: test article 5

The specific objective of moiré test article 5 was to explore both the axial and transverse strain behavior around the weld interface. Figure B-12 shows the strain development in the vicinity of the retreating weld boundary for a series of loading steps along with reduced strain data gathered from each of the images. Figure B-10 is a stress-strain plot generated from these test results showing variations in the strain at different regions around the weld.

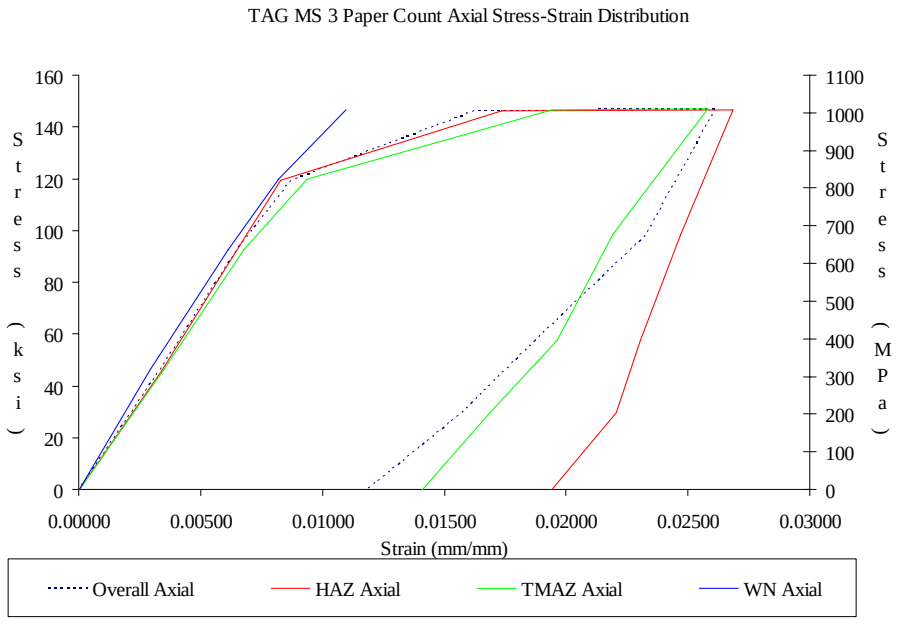

Figure B-10: TAG MS 3 Stress-Strain Plot

Figure B-11: TAG MS 3 post-test image

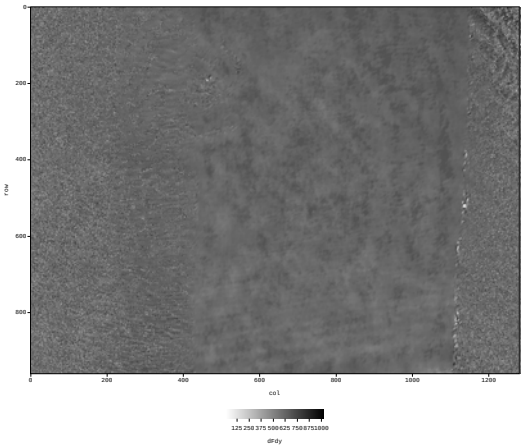

(a) Load Step 1: axial (v-field), retreating side
- Load = null

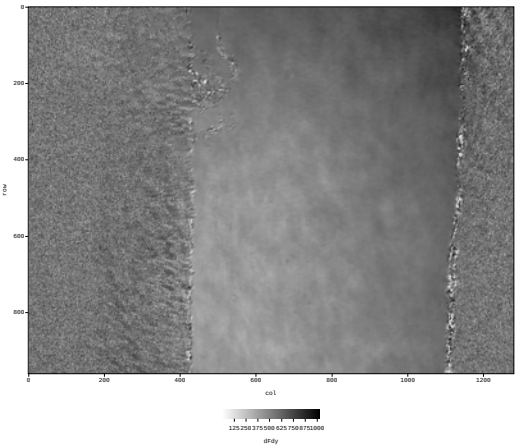

(b) Load Step 1: transverse (u-field), retreating side

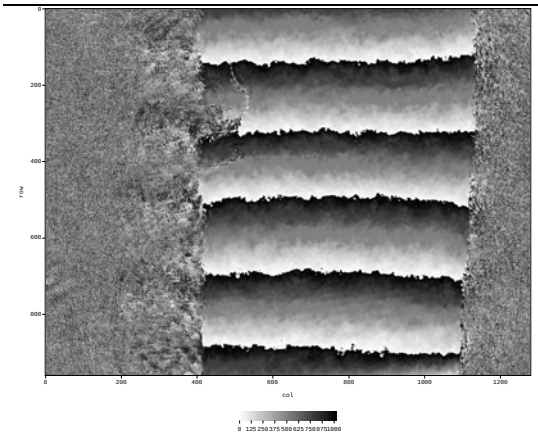

(c) Load Step 2: axial (v-field), retreating side
- Indicated Load = 232.2 lbf (1032 N)
- Overall e_{yy} = 0.00330

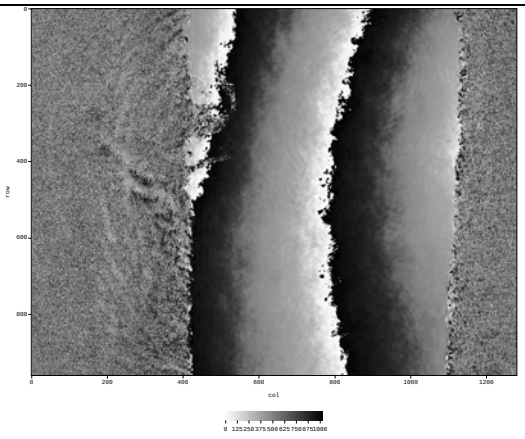

(d) Load Step 2: transverse (u-field), retreating side
- Stress = 46.0 ksi (317 MPa)
- Average e_{xx} = 0.00167
- Average ν = 0.5

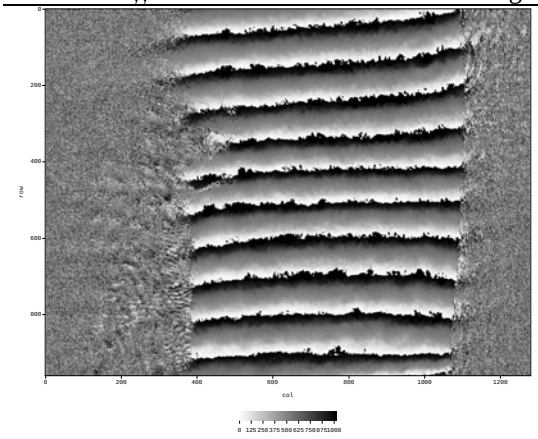

(e) Load Step 3: axial (v-field), retreating side
- Indicated Load = 466.0 lbf (2072 N)
- Overall e_{yy} = 0.00649

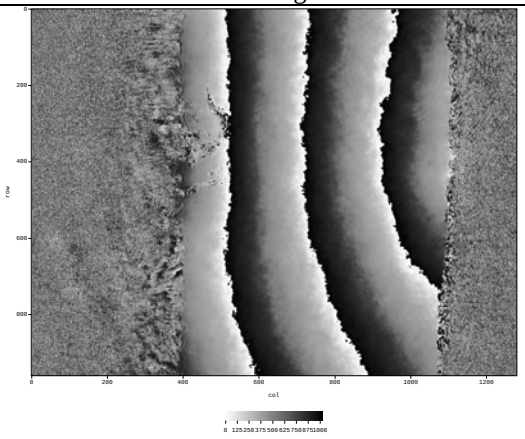

(f) Load Step 3: transverse (u-field), retreating side
- Stress = 92.4 ksi (637 MPa)
- Average e_{xx} = 0.00257
- Average ν = 0.40

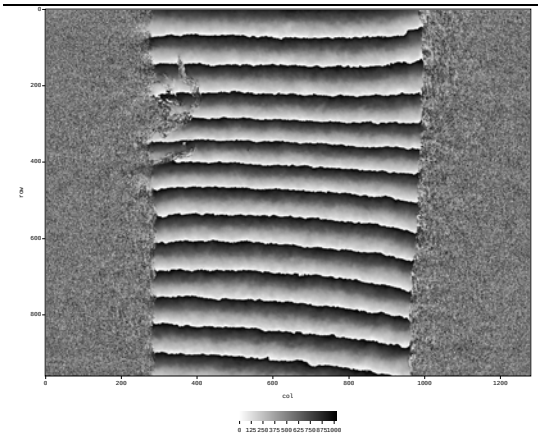

(g) Load Step 4: axial (v-field), retreating side
- Indicated Load = 602.8 lbf (2681 N)
- Overall e_{yy} = 0.00874

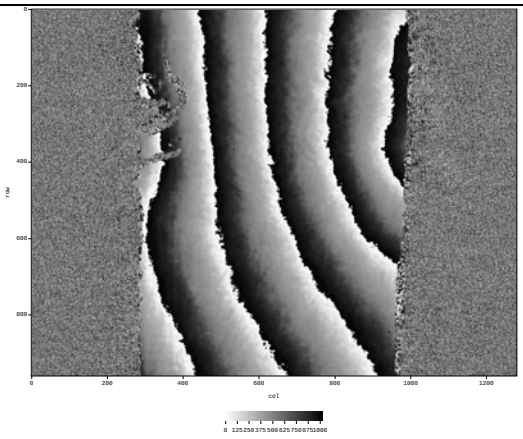

(h) Load Step 4: transverse (u-field), retreating side
- Stress = 119.5 ksi (824 MPa)
- Average e_{xx} = 0.00338
- Average ν = 0.39

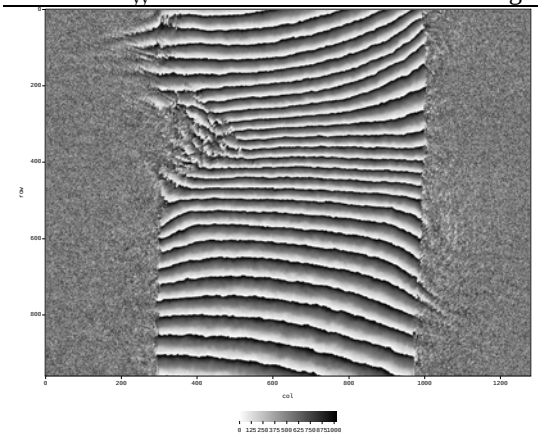

(i) Load Step 5: axial (v-field), retreating side
- Indicated Load = 737.1 lbf (3279 N)
- Overall e_{yy} = 0.01628

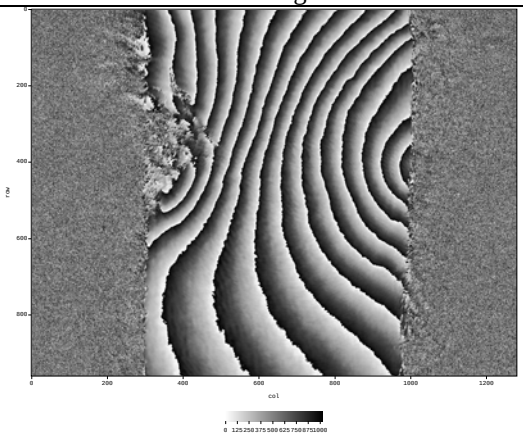

(j) Load Step 5: transverse (u-field), retreating side
- Stress = 146.1 ksi (1007 MPa)
- Average e_{xx} = 0.00852
- Average ν = 0.52*

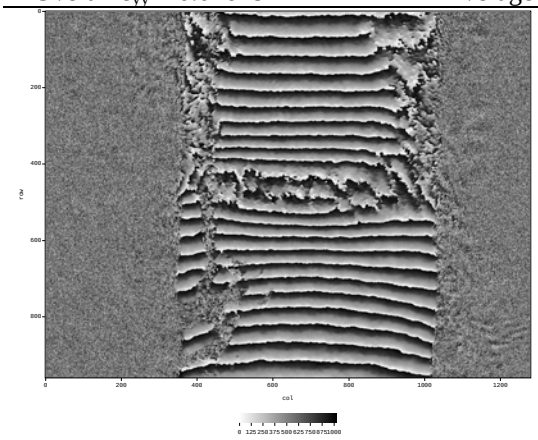

(k) Load Step 5: axial (v-field), advancing side
- Overall e_{yy} = 0.01628

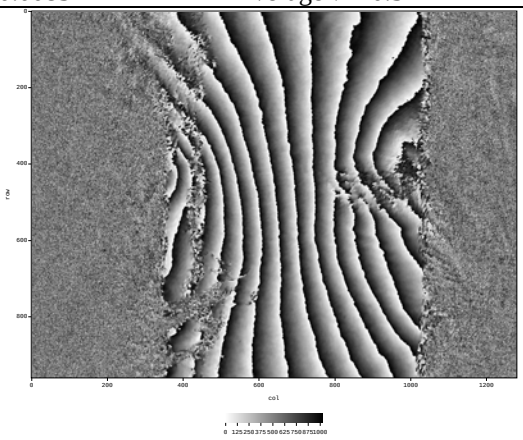

(l) Load Step 5: transverse (u-field), advancing side
- Average e_{xx} = 0.00865
- Average ν = 0.53*

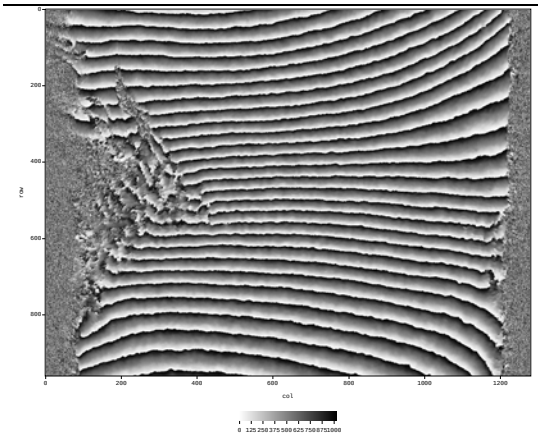

(m) Load Step 6z: axial (v-field), retreating side
- Indicated Load = 739.6 lbf (3290 N)
- Overall e_{yy} = 0.02608

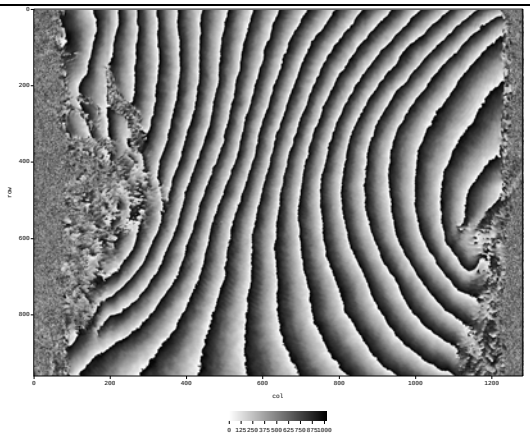

(n) Load Step 6z: transverse (u-field), retreating side
- Stress = 146.6 ksi (1011 MPa)
- Average e_{xx} = 0.01277
- Average ν = 0.49

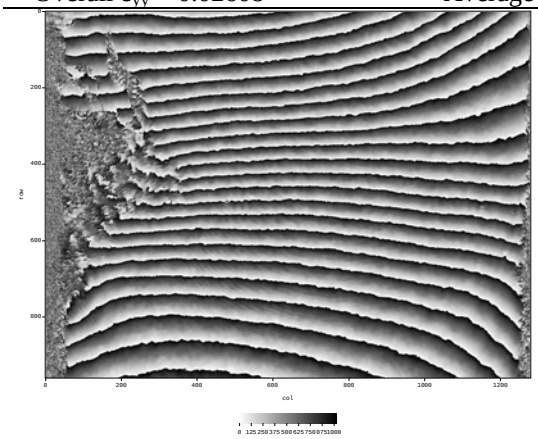

(o) Load Step 7z:axial (v-field), retreating side
- Indicated Load = 495.8 lbf (2205 N)
- Overall e_{yy} = 0.02324

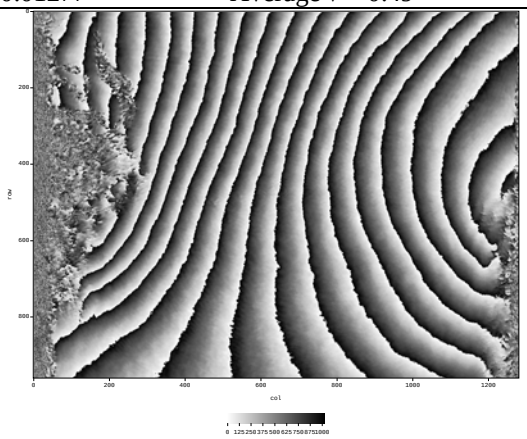

(p) Load Step 7z: transverse (u-field), retreating side
- Stress = 98.3 ksi (678 MPa)
- Average e_{xx} = 0.01112
- Average ν = 0.48

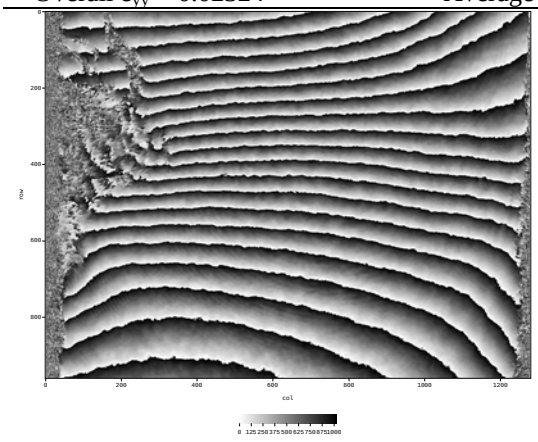

(q) Load Step 8z: axial (v-field), retreating side
- Indicated Load = 290.6 lbf (1293 N)
- Overall e_{yy} = 0.01868

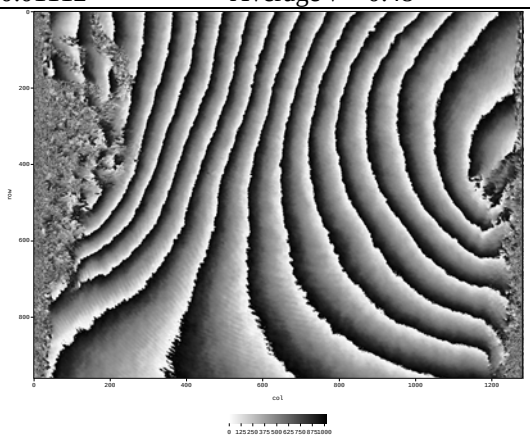

(r) Load Step 8z: transverse (u-field), retreating side
- Stress = 57.6 ksi (397 MPa)

Average e_{xx} = 0.00939

Average ν = 0.50

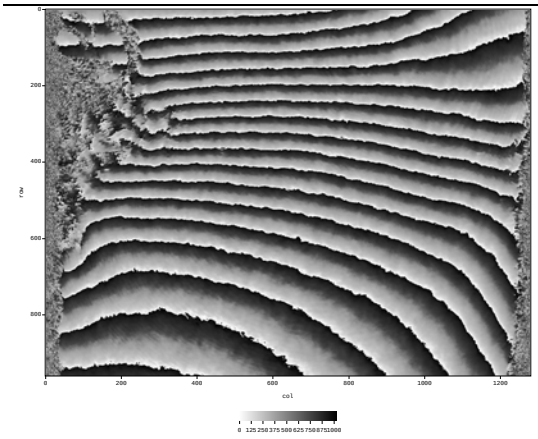

(s) Load Step 9z: axial (v-field), retreating side
- Indicated Load = 148.8 lbf (662 N)
- Overall e_{yy} = 0.01567

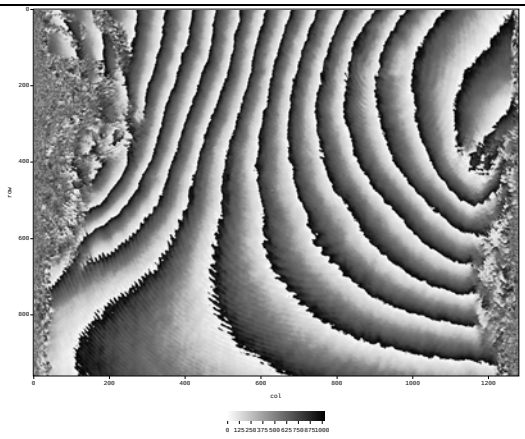

(t) Load Step 9z: transverse (u-field), retreating side
- Stress = 29.5 ksi (203 MPa)
- Average e_{xx} = 0.00882
- Average ν = 0.56*

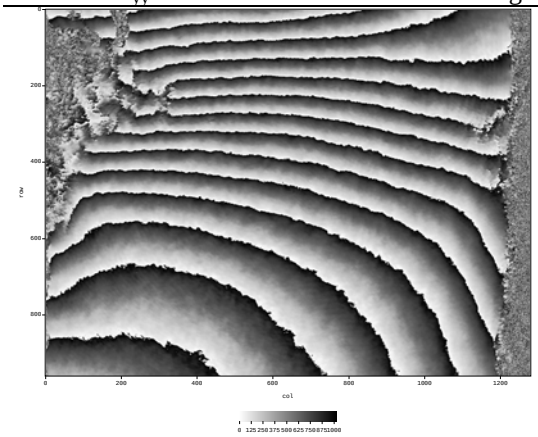

(u) Load Step 10z: axial (v-field), retreating side
- Indicated Load = fully unloaded
- Overall e_{yy} = 0.01176

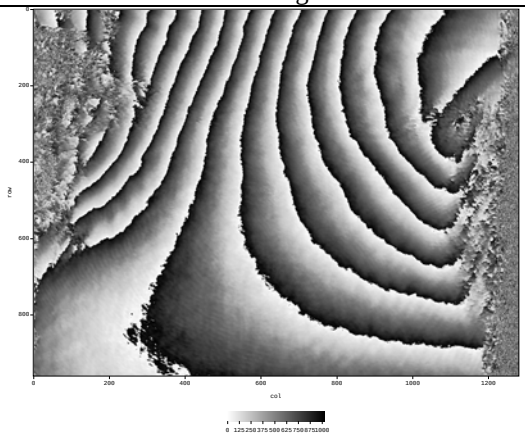

(v) Load Step 10z: transverse (u-field), retreating side
- Average e_{xx} = 0.00167
- Average ν = 0.69*

Figure B-12: TAG MS 3 image and associated load and strain data

The addition of u-field fringe imagery, as shown in Figure B-12, presented substantial additional qualitative information about the strain behavior of the specimen. The necking behavior manifested only as tighter spaced fringes in v-field, which can be somewhat difficult to determine when only slightly closer spaced than the surrounding fringes. The u-field imagery manifested more distinctly in a curved and "pinched" fringe pattern. These patterns become particularly visible in (i) and (j). The calculated values of

Poisson's ratio for this specimen do not show strong accord with expected results, nor are they consistent with the theoretical Poisson's ratio limit of 0.50. This research presented no explanation for this inconsistency.

TAG MS 4: test article 6

The specific objective of moiré test article 6 was to explore the strain behavior along the full length of the weld at loads approaching yielding. Figure B-15 shows the strain development in the vicinity of the retreating weld boundary for a series of loading steps along with reduced strain data gathered from each of the images. Figure B-13 is a stress-strain plot generated from these test results showing variations in the strain at different regions around the weld. As PM fringe data was only collected for two load steps, only a small portion of the PM curve is shown.

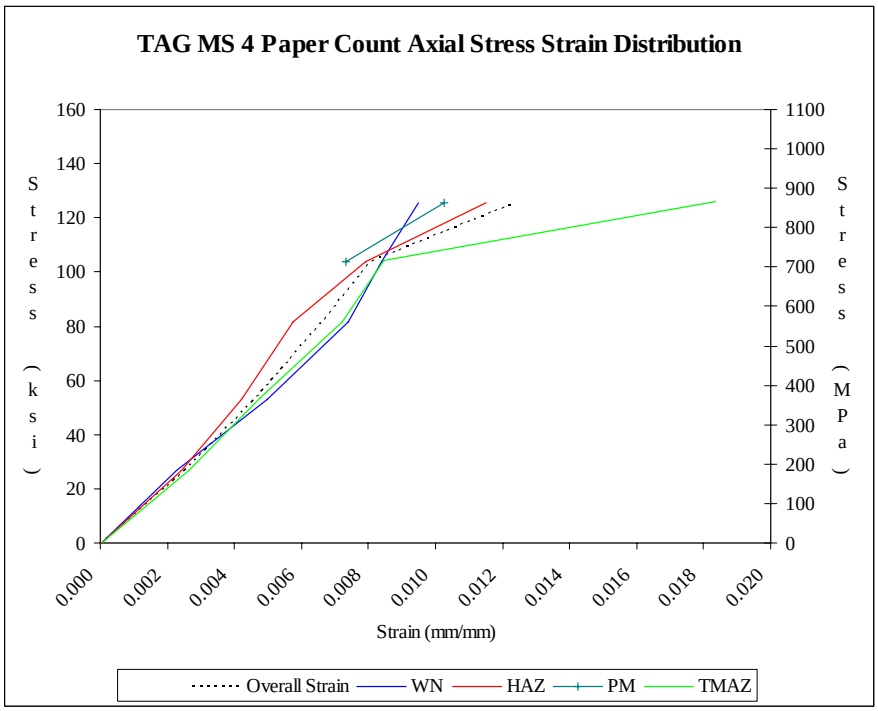

Figure B-13: TAG MS 4 stress-strain plot

Figure B-14: TAG MS 4 post-test image

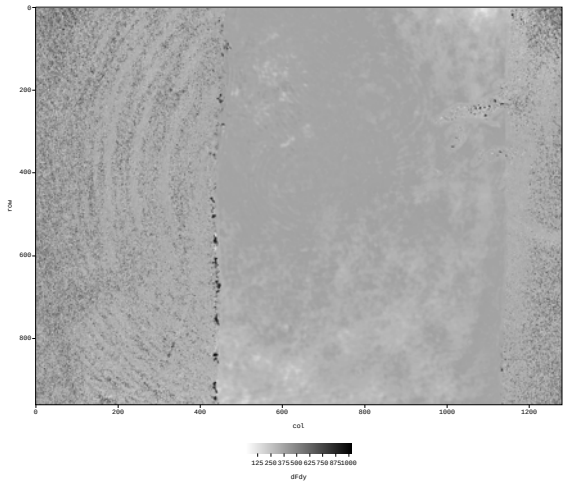

(a) Load Step 1
Indicated Load = null
Area = 0.0051 in^2 (3.26 mm^2)

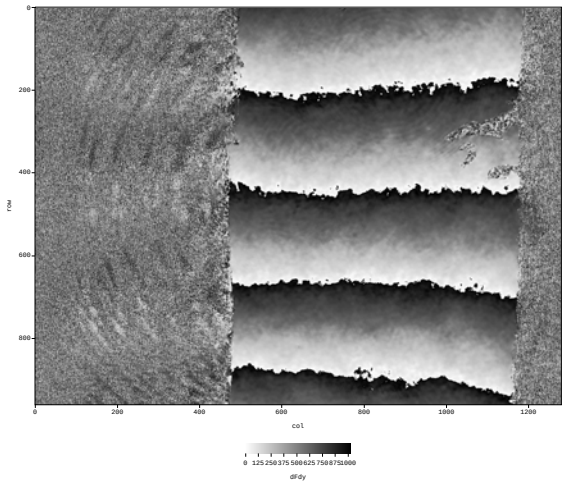

(b) Load Step 2 (Retreating Side)
- Indicated Load = 133.9 lbf (596 N)
- Stress = 26.5 ksi (183 MPa)
- Overall Strain = 0.0025
 -- PM Strain = N/A
 -- HAZ Strain = 0.00242
 -- TMAZ Strain = 0.00264
 -- WN Strain = 0.00226

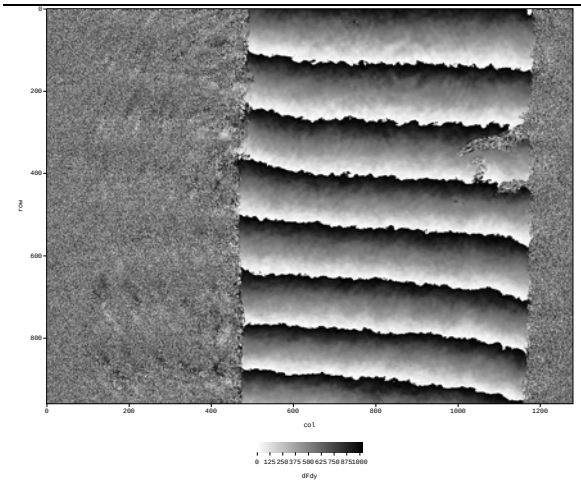

(c) Load Step 3 (Retreating Side)
- Indicated Load = 268.2 lbf (1193 N)
- Stress = 53.2 ksi (367 MPa)
- Overall Strain = 0.0046
 -- PM Strain = N/A
 -- HAZ Strain = 0.00442
 -- TMAZ Strain = 0.00478
 -- WN Strain = 0.00497

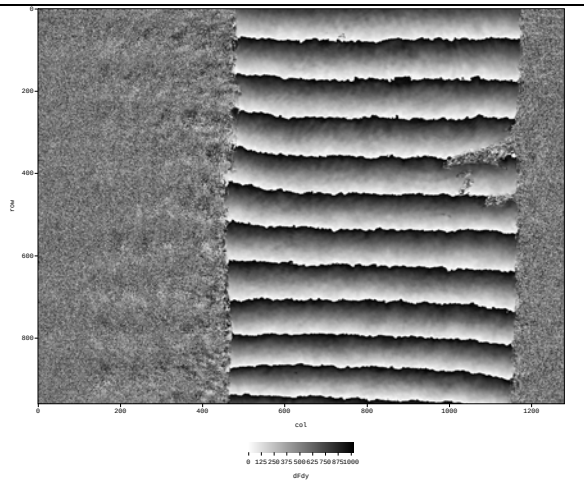

(d) Load Step 4 (Retreating Side)
- Indicated Load = 411.2 lbf (1829 N)
- Stress = 81.5 ksi (562 MPa)
- Overall Strain = 0.00696
 -- PM Strain = N/A
 -- HAZ Strain = 0.00573
 -- TMAZ Strain = 0.00722
 -- WN Strain = 0.00741

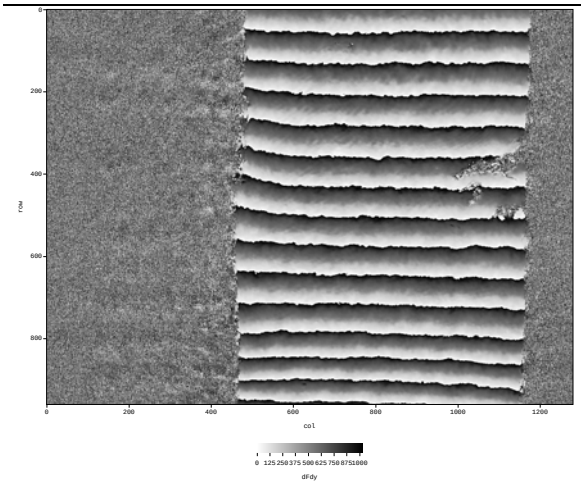

(d) Load Step 5 (Retreating Side)
- Indicated Load = 524.4 lbf (2333 N)
- Stress = 104.0 ksi (717 MPa)
- Overall Strain = 0.00620
 -- PM Strain = 0.00734
 -- HAZ Strain = 0.00792
 -- TMAZ Strain = 0.00847
 -- WN Strain = 0.00837

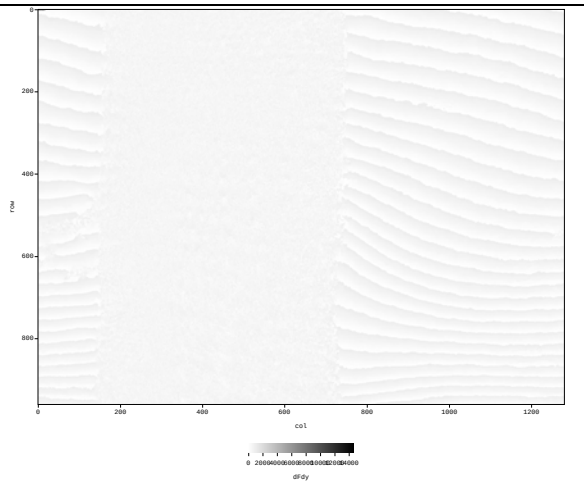

(e) Load Step 6 (Retreating Side)
- Indicated Load = 633.9 lbf (2820 N)
- Stress = 125.6 ksi (866 MPa)
- Overall Strain = 0.01240
 -- PM Strain = 0.01026
 -- HAZ Strain = 0.01150
 -- TMAZ Strain = 0.01833
 -- WN Strain = 0.00947

NOTE image data for load step 6 corrupted, but fringe values still able to be counted

Figure B-15: TAG MS 4 image and associated load and strain data

TAG MS 4 was not carried into plastic loading as far as the previous test articles, primarily due to the fundamental test goal of demonstrating strain localization across the entire weld region having been met at load step 6. Unfortunately, the data for load step 6 was corrupted and the imagery, while marginally countable, was far from optimal. The two composite full weld images captured at load steps 5 and 6 are shown in Figure B-16.

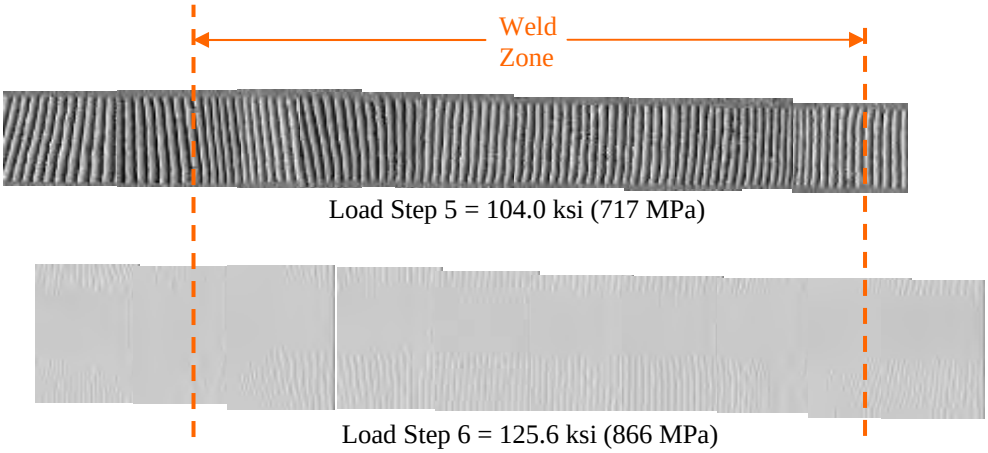

Figure B-16: comparison of TAG MS 4 clean and corrupted data

5. TAG MS 5: test article 7

The specific objective of moiré test article 7 was to again explore the strain behavior along the full length of the weld at a series of loads spanning elasticity, plasticity, and back to fully unloaded. Figure B-19 shows the strain development in the vicinity of the retreating weld boundary for a series of loading steps along with reduced strain data gathered from each of the images. Figure B-17 is a stress-strain plot generated from these test results showing variations in the strain at different regions around the weld. As both PM and WN fringe data was only collected for limited load steps, only small portions of the PM and WN curve are shown. The general choppiness of the curves is due to the relatively small areas available for fringe sampling and strain calculations for all regions except the HAZ and TMAZ. Figure B-18 is a post-test image of TAG MS 5 showing visible necking outside of the weld boundary on the retreating side (lefthand side of image).

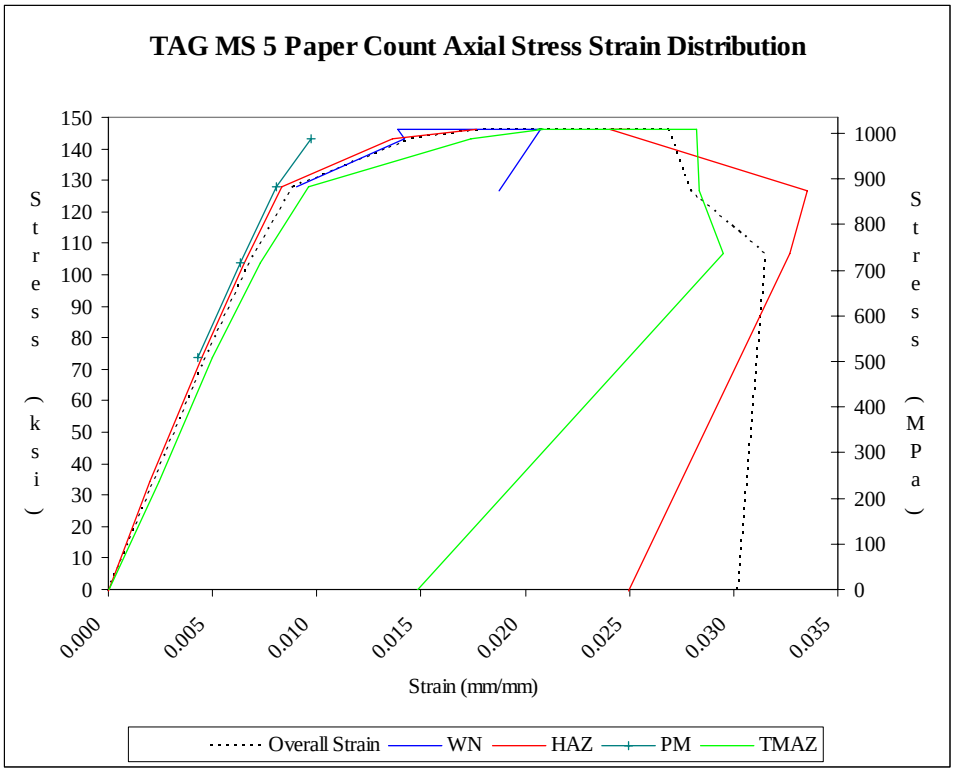

Figure B-17: TAG MS 5 stress-strain plot

Figure B-18: TAG MS 5 post-test image

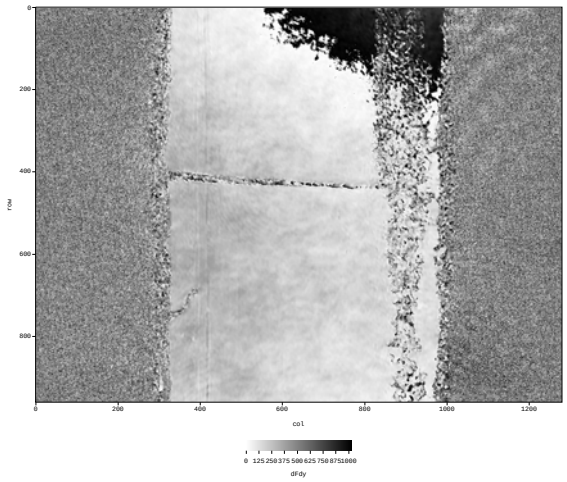

(a) Load Step 1
Indicated Load = null
Area = 0.0051 in^2 (3.26 mm^2)

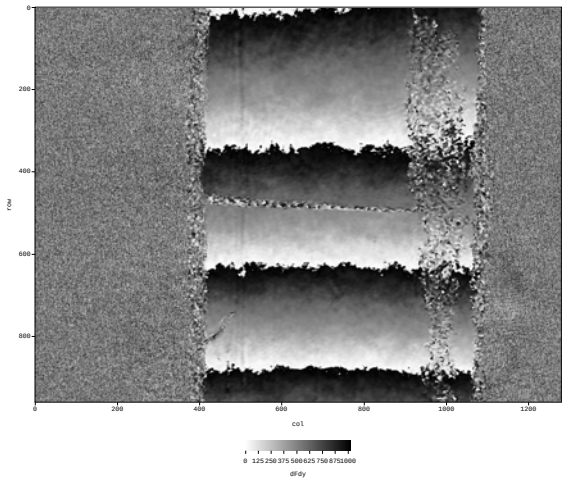

(b) Load Step 2 (Increasing Load)
- Indicated Load = 173.7.4 lbf (773 N)
- Stress = 34.4 ksi (237 MPa)
- Overall Strain = 0.00219
 -- PM Strain = N/A
 -- HAZ Strain = 0.00199
 -- TMAZ Strain = 0.00240
 -- WN Strain = N/A

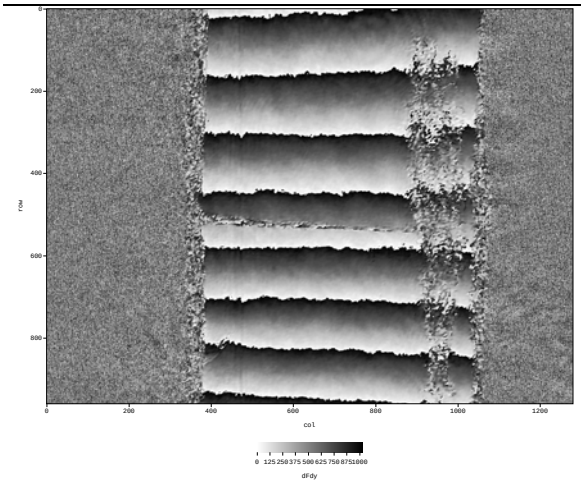

(c) Load Step 3 (Increasing Load)
- Indicated Load = 371.4 lbf (1652 N)
- Stress = 73.6 ksi (508 MPa)
- Overall Strain = 0.00466
 -- PM Strain = 0.00429
 -- HAZ Strain = 0.00447
 -- TMAZ Strain = 0.00500
 -- WN Strain = N/A

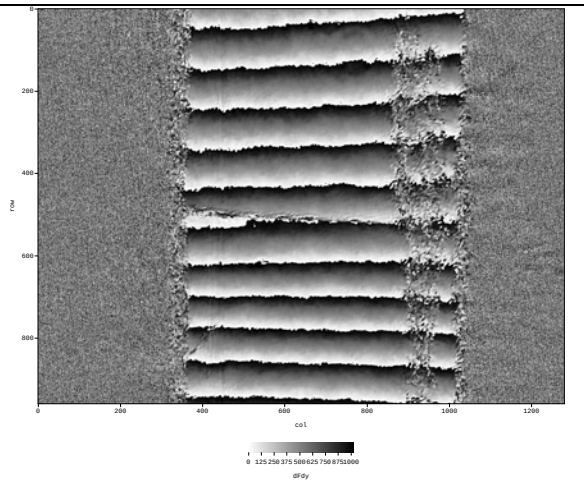

(d) Load Step 4 (Increasing Load)
- Indicated Load = 523.2 lbf (2327 N)
- Stress = 103.7 ksi (715 MPa)
- Overall Strain = 0.00681
 -- PM Strain = 0.00633
 -- HAZ Strain = 0.00650
 -- TMAZ Strain = 0.00729
 -- WN Strain = N/A

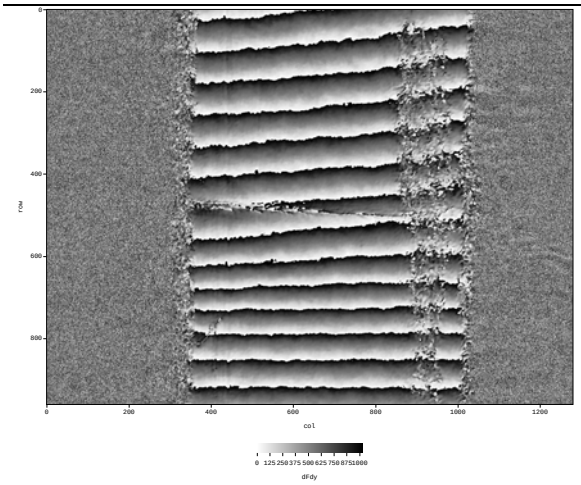

(d) Load Step 5 (Increasing Load)
- Indicated Load = 646.3 lbf (2875 N)
- Stress = 128.1 ksi (883 MPa)
- Overall Strain = 0.00887
 -- PM Strain = 0.00806
 -- HAZ Strain = 0.00834
 -- TMAZ Strain = 0.00958
 -- WN Strain = 0.00904

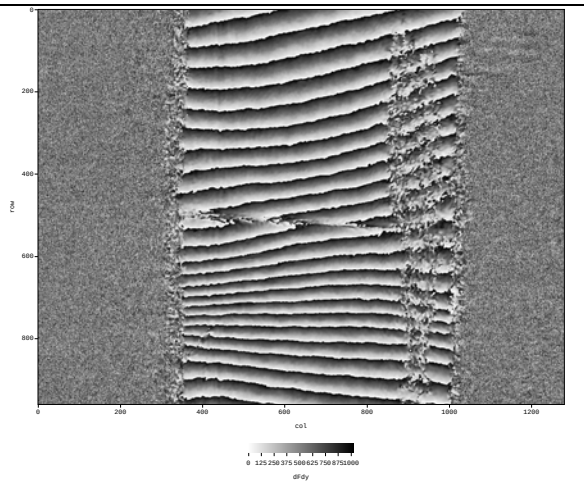

(e) Load Step 6 (Increasing Load)
- Indicated Load = 723.4 lbf (3218 N)
- Stress = 143.4 ksi (989 MPa)
- Overall Strain = 0.01451
 -- PM Strain = 0.00975
 -- HAZ Strain = 0.01362
 -- TMAZ Strain = 0.01742
 -- WN Strain = 0.01418

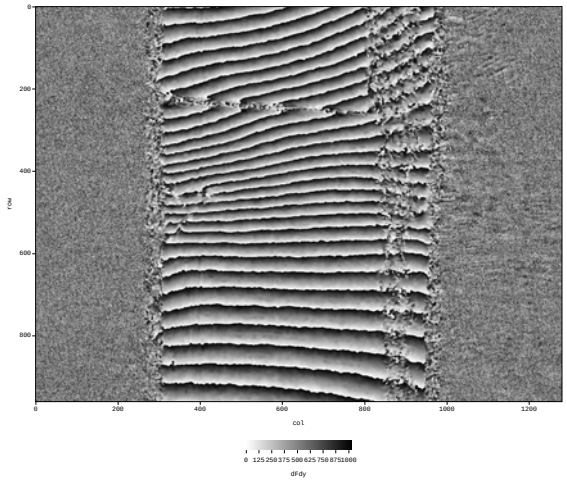

(f) Load Step 7 (Increasing Load)
- Indicated Load = 738.3 lbf (3284 N)
- Stress = 146.4 ksi (1009 MPa)
- Overall Strain = 0.01805
 -- PM Strain = N/A
 -- HAZ Strain = 0.01767
 -- TMAZ Strain = 0.02084
 -- WN Strain = 0.01391

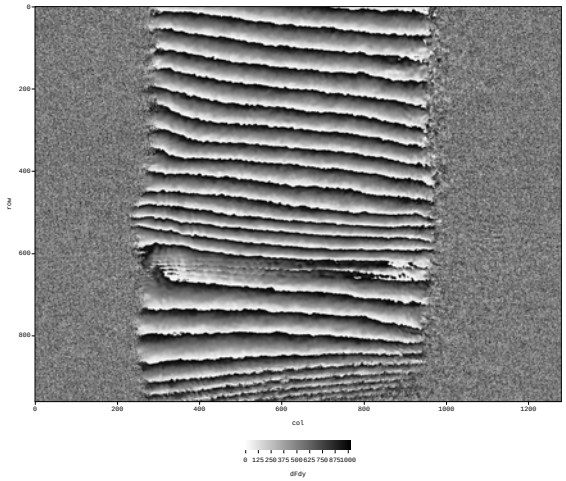

(g) Load Step 7 (Advancing Side)
- Indicated Load = 738.3 lbf (3284 N)
- Stress = 146.4 ksi (1009 MPa)
- Strains not calculated

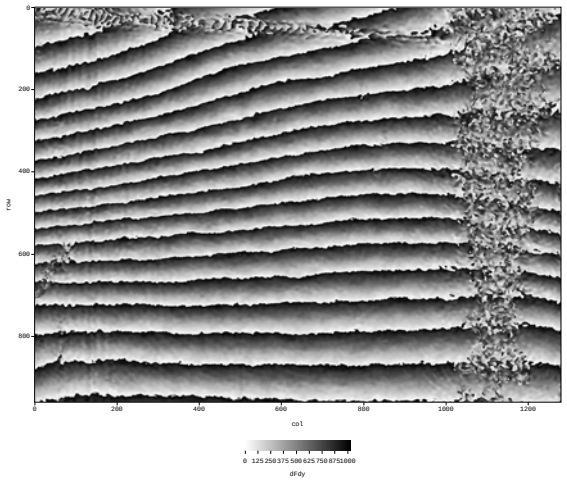

(h) Load Step 8z (Retreating Side)
- Indicated Load = 738.3 lbf (3284 N)
- Stress = 146.4 ksi (1009 MPa)
- Overall Strain = 0.01966
 -- PM Strain = N/A
 -- HAZ Strain = N/A
 -- TMAZ Strain = 0.02063
 -- WN Strain = 0.01522

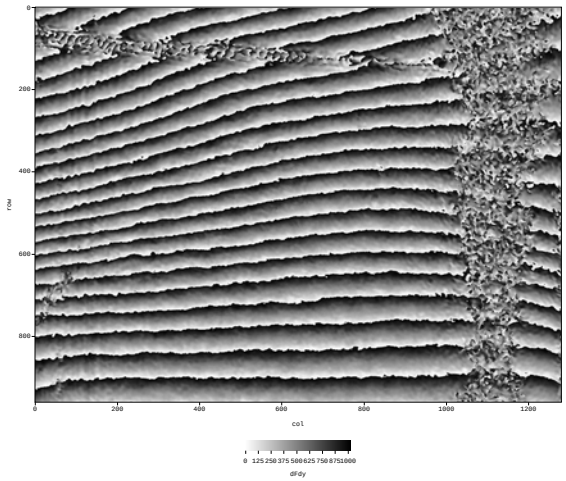

(i) Load Step 9z (Retreating Side)
- Indicated Load = 738.3 lbf (3284 N)
- Stress = 146.4 ksi (1009 MPa)
- Overall Strain = 0.02664
 -- PM Strain = N/A
 -- HAZ Strain = 0.02504
 -- TMAZ Strain = 0.02509
 -- WN Strain = 0.01736

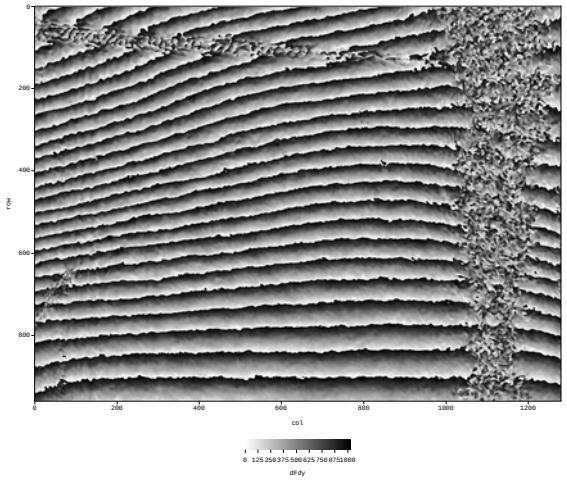

(j) Load Step 10z (Retreating Side)
- Indicated Load = 738.3 lbf (3284 N)
- Stress = 146.4 ksi (1009 MPa)
- Overall Strain = 0.02690
 -- PM Strain = N/A
 -- HAZ Strain = 0.02404
 -- TMAZ Strain = 0.02821
 -- WN Strain = 0.02076

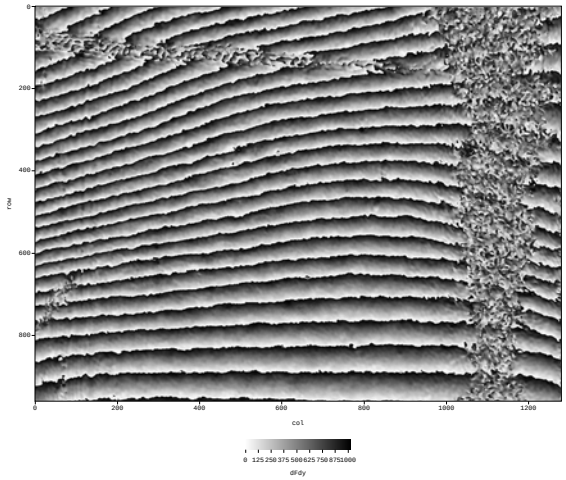

(k) Load Step 11z (Retreating Side)
- Indicated Load = 638.8 lbf (2842 N)
- Stress = 126.6 ksi (873 MPa)
- Overall Strain = 0.02789
 -- PM Strain = N/A
 -- HAZ Strain = 0.03355
 -- TMAZ Strain = 0.02833
 -- WN Strain = 0.01872

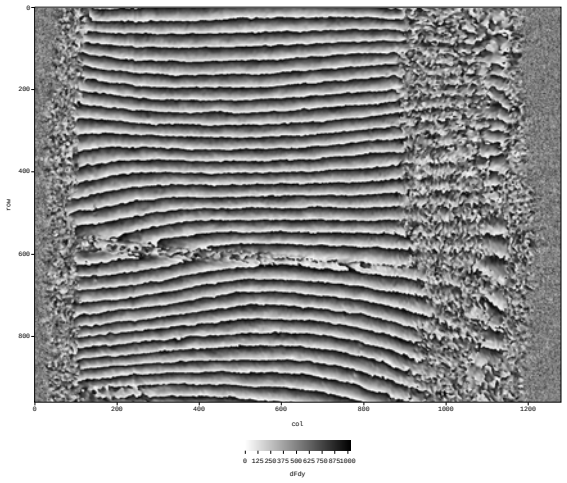

(l) Load Step 12 (Retreating Side)
- Indicated Load = 539.3 lbf (2399 N)
- Stress = 106.9 ksi (737 MPa)
- Overall Strain = 0.03151
 -- PM Strain = N/A
 -- HAZ Strain = 0.03267
 -- TMAZ Strain = 0.02951
 -- WN Strain = N/A

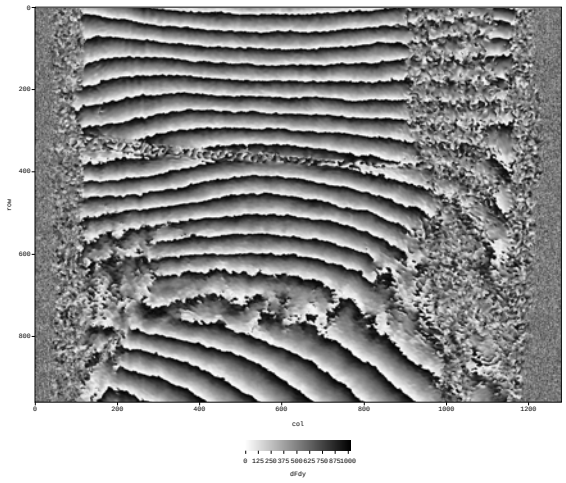

(m) Load Step 13 (Retreating Side)
- Indicated Load = -2.92 lbf (-13 N)
- Stress = -0.6 ksi (-4 MPa)
- Overall Strain = 0.03012
 -- PM Strain = N/A
 -- HAZ Strain = 0.2497
 -- TMAZ Strain = 0.01476
 -- WN Strain = N/A

Figure B-19: TAG MS 5 image and associated load and strain data

The fundamental goal of this test article was to demonstrate variations in strain behavior across the full region of the weld. This was accomplished in the composite image of the fully unloaded test article shown in Figure B-20. Note the region of the WN shows neither distinct fringe patterns nor patterns of recognizable contrast – this is due to the phase shifting which arbitrarily selected which portion of a fringe will be dark vs light. This was typical for all images, though did not present significant ambiguity in images with multiple fringes per frame. The value of Figure B-20 is in providing a nearly complete image of the full-field strain behavior, residual in this case, across nearly the full length of the specimen gage.

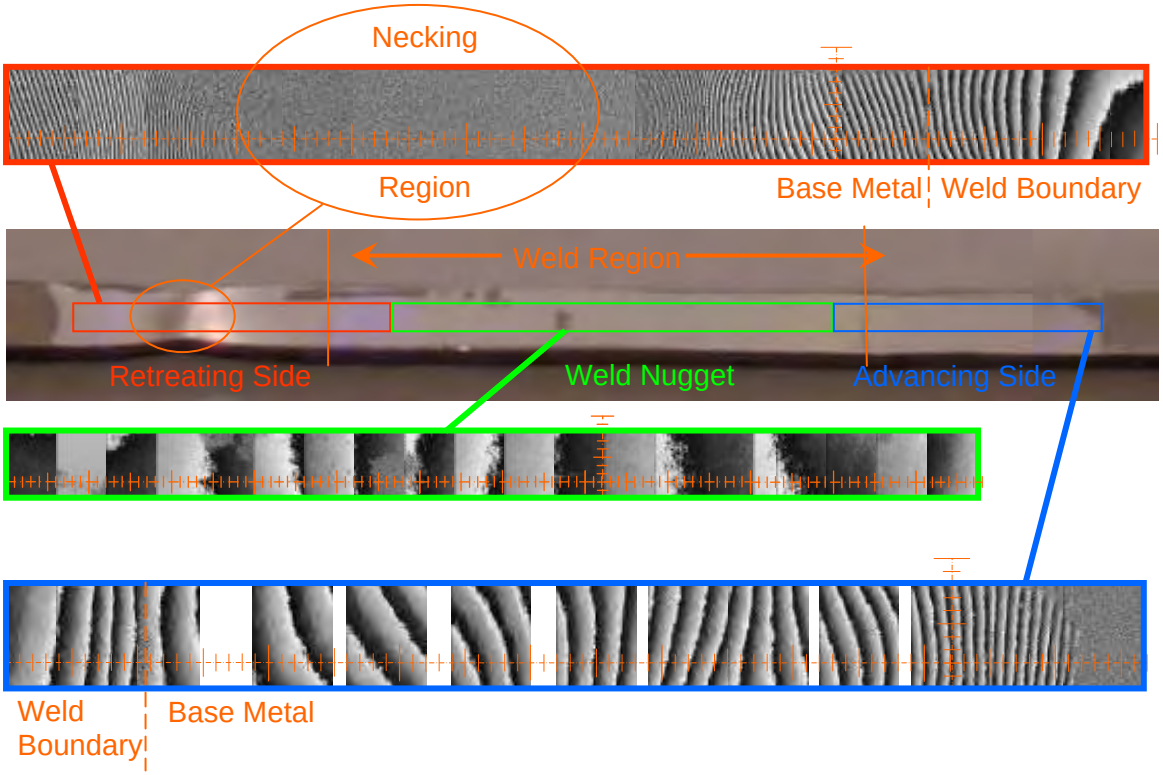

Figure B-20: TAG MS 5 composite image of fringe pattern along gage length

6. TAG MS 6: test article 8

The specific objective of moiré test article 8 was to again explore both the axial and transverse strain behavior along a greater span of the weld at an abbreviated series of loads focusing on plasticity. Figure B-22 shows the strain development in the vicinity of the retreating weld boundary for a series of loading steps along with reduced strain data gathered from each of the images. As only a small number of load step images were captured, no stress-strain plot was produced. Figure B-21 is a post-test image of TAG MS 6 showing visible necking just outside of the weld boundary on the retreating side (lefthand side of image).

Figure B-21: TAG MS 6 post-test image

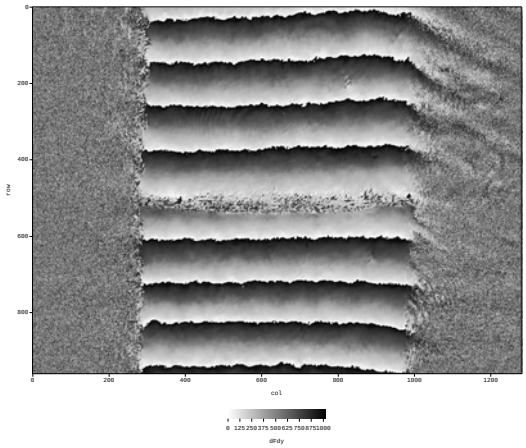

(a) Load Step 1: axial (v-field), retreating side
- Indicated Load = 388.9 lbf (1730 N)
- Overall e_{yy} = 0.0055

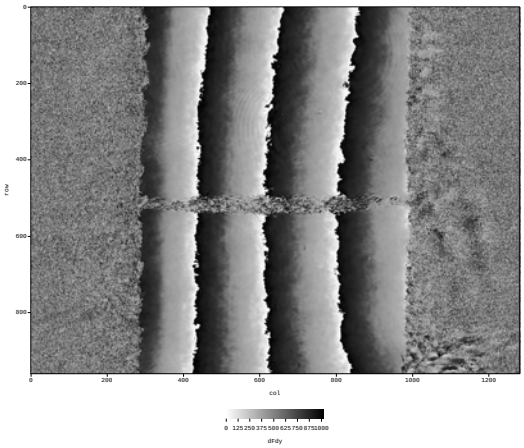

(b) Load Step 1: transverse (u-field), retreating side
- Stress = 77.1 ksi (531 MPa)
- Average e_{xx} = 0.0032
- Average ν = 0.58

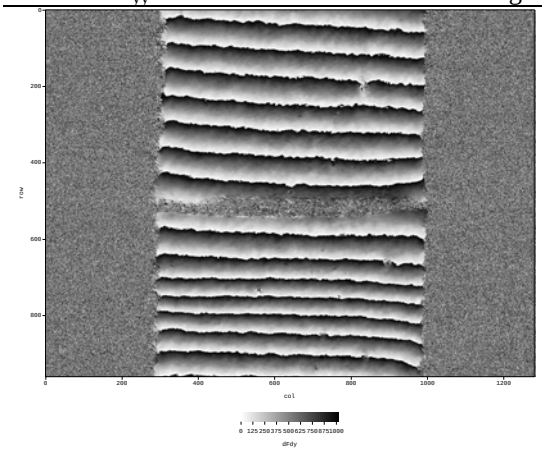

(c) Load Step 2: axial (v-field), retreating side
- Indicated Load = 626.3 lbf (2919 N)
- Overall e_{yy} = 0.0098

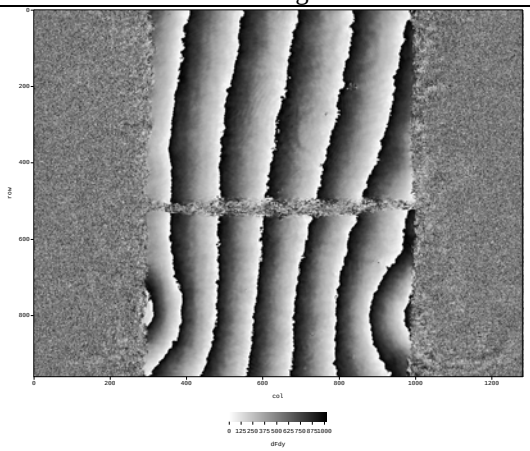

(d) Load Step 2: transverse (u-field), retreating side
- Stress = 130.1 ksi (897 MPa)
- Average e_{xx} = 0.0046
- Average ν = 0.47

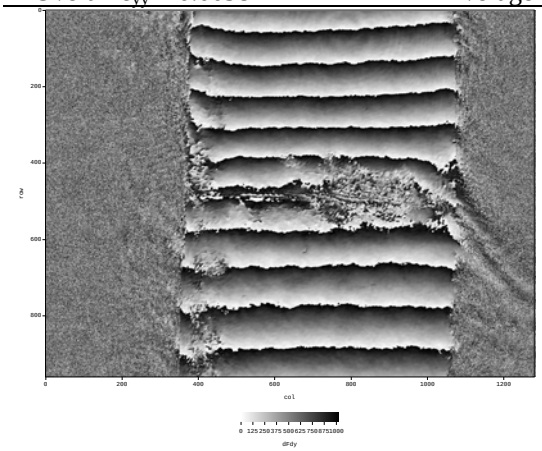

(e) Load Step 2: axial (v-field), advancing side

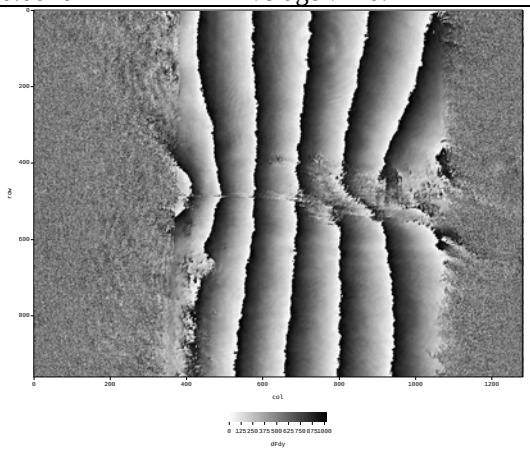

(f) Load Step 2: transverse (u-field), advancing side

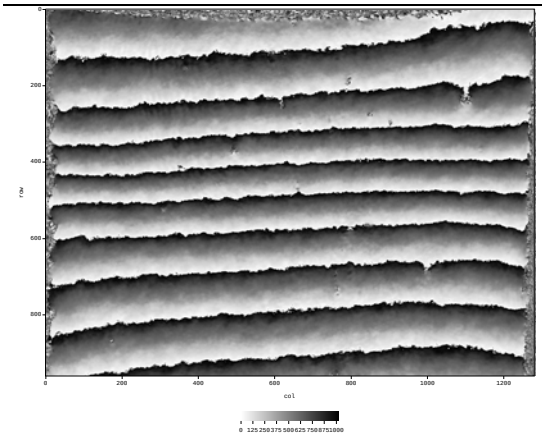

(g) Load Step 2z: axial (v-field), retreating side

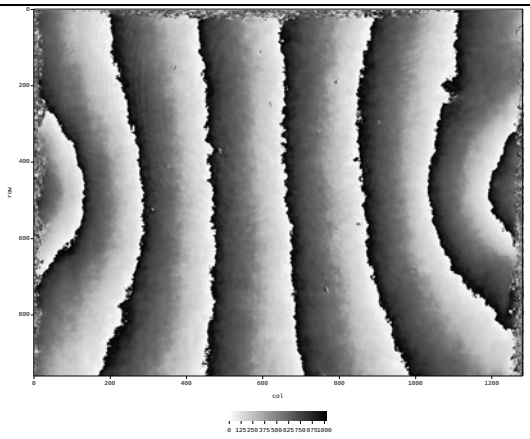

(h) Load Step 2z: transverse (u-field), retreating side

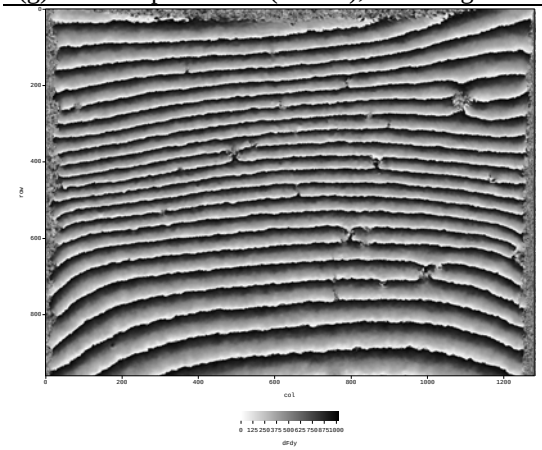

(i) Load Step 3z: axial (v-field), retreating side
- Indicated Load = 720.1 (3207 N)
- Overall e_{yy} = 0.0265

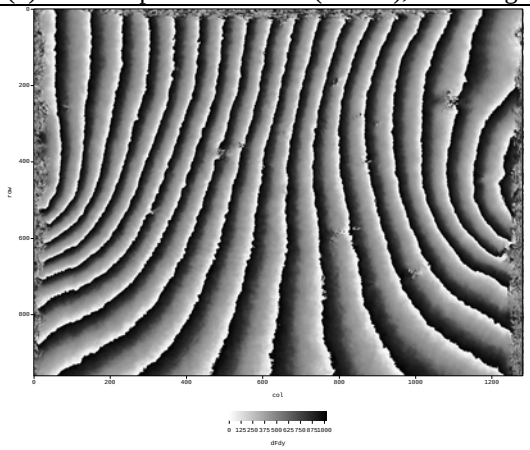

(j) Load Step 3z: transverse (u-field), retreating side
- Stress = 142.9 ksi (985 MPa)
- Average e_{xx} = 0.0108
- Average ν = 0.41

Figure B-22: TAG MS 6 image and associated load and strain data

The full range of retreating side weld regions for three load steps are shown in Figure B-23, Figure B-24, and Figure B-25. The sequence of images begins at a load below the ultimate plateau showing strain localization developed at the weld boundary. The next image shows an extension of the strain localization across a larger span of the weld interface to the parent material. The final image shows the location of ultimate failure developed just outside of the weld boundary – note the area of unresolved fringes indicative of fringe spacing too tight to be captured with the available lens.

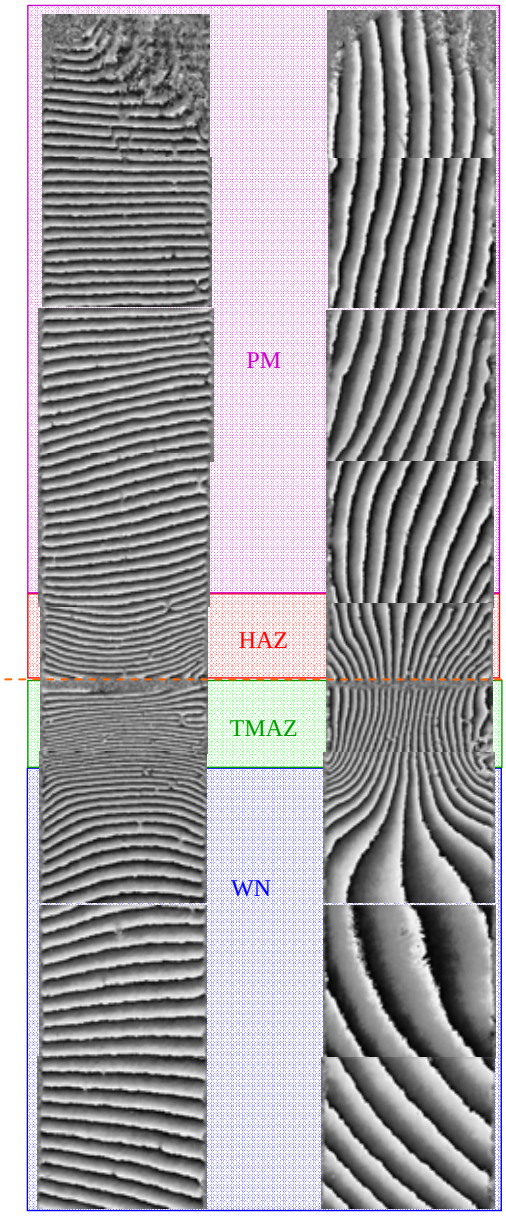

Figure B-23: TAG MS 6 retreating side weld detail step 1

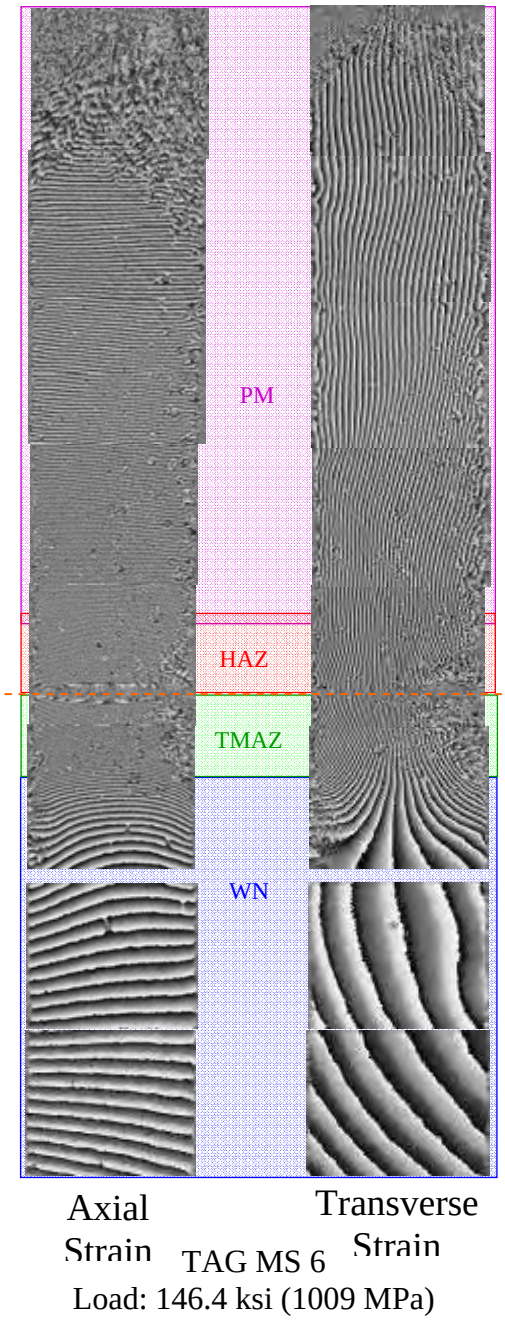

Figure B-24: TAG MS 6 retreating side weld detail step 2

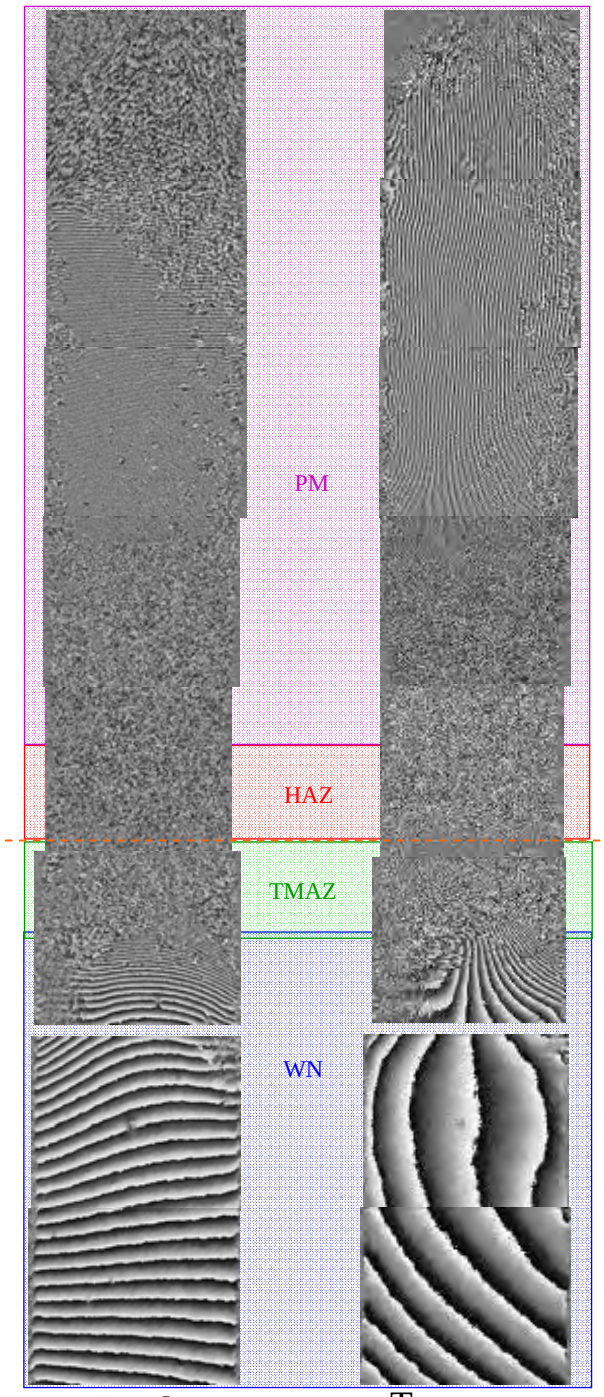

Figure B-25: TAG MS 6 retreating side weld detail step 3